aero-elastic modeling of floating wind turbines with vortex methods

Rémi Corniglion

▶ **To cite this version:**

Rémi Corniglion. aero-elastic modeling of floating wind turbines with vortex methods. Mechanical engineering [physics.class-ph]. École des Ponts ParisTech, 2022. English. NNT : 2022ENPC0015 . tel-03901284

HAL Id: tel-03901284
https://pastel.hal.science/tel-03901284v1

Submitted on 15 Dec 2022

HAL is a multi-disciplinary open access archive for the deposit and dissemination of scientific research documents, whether they are published or not. The documents may come from teaching and research institutions in France or abroad, or from public or private research centers.

L'archive ouverte pluridisciplinaire **HAL**, est destinée au dépôt et à la diffusion de documents scientifiques de niveau recherche, publiés ou non, émanant des établissements d'enseignement et de recherche français ou étrangers, des laboratoires publics ou privés.

École des Ponts ParisTech

THÈSE DE DOCTORAT

de l'École des Ponts ParisTech

Modélisation aéro-élastique des éoliennes flottantes avec des méthodes vortex

École doctorale N°531, Sciences, Ingénierie et Environnement, SIE

Mécanique des fluides

Thèse préparée au Laboratoire d'Hydraulique Saint-Venant (Ecole des Ponts ParisTech et EDF R&D) et au Laboratoire Nationale d'Hydraulique et Environnement (EDF R&D)

Thèse soutenue le 21/06/2022, par
Rémi CORNIGLION

Composition du jury:

Grégory PINON Professeur des universités, Université du Havre	*Rapporteur, Président du Jury*
Alberto ZASSO Full Professor, Politecnico di Milano	*Rapporteur*
Sandrine AUBRUN Professeure des universités, Ecole Centrale de Nantes	*Examinatrice*
Axelle VIRÉ Associate Professor, TU Delft	*Examinatrice*
Jeffrey HARRIS Chargé de recherche, Ecole des Ponts ParisTech	*Directeur de thèse*
Christophe PEYRARD Ingénieur, chercheur expert, EDF R&D - LNHE	*Encadrant*
Matteo CAPALDO Docteur, Total Energies	*Invité*
Christine DE JOUETTE Docteure, EDF Renouvelables	*Invité*

Thèse effectuée au sein du **Laboratoire d'Hydraulique Saint-Venant**

de l'Ecole des Ponts ParisTech

6, quai Watier

BP 49

78401 Chatou cedex

France

CIFRE n°2018/1790

Résumé

Les éoliennes flottantes sont placées sur un flotteur, libre de bouger sous l'effet combiné du vent et des vagues. Cela induit un mouvement relatif entre l'éolienne et le vent incident. La méthode Blade Element Momentum largement utilisée pour l'étude aérodynamique des éoliennes utilise des corrections empiriques pour modéliser ces conditions instationnaires de fonctionnement. Dans cette thèse, des modèles aérodynamiques de niveau intermédiaire sont utilisés pour améliorer la compréhension des forces aérodynamiques instationnaires sur une éolienne en mouvement. En particulier, le phénomène de Dynamic Inflow est étudié pour les éoliennes flottantes. Des mouvements de translation imposés sont d'abord étudiés avec un modèle vortex à ligne portante ainsi qu'un modèle Actuator Line. L'aérodynamique d'une éolienne après trois perturbations est étudiée : un changement de l'angle d'orientation des pâles, un changement de la vitesse de rotation et un changement de la vitesse de translation du rotor. La méthode Free Vortex Wake à ligne portante et un modèle hélicoïdale analytique basé sur le modèle de rotor de Joukowsky sont utilisés pour étudier le comportement dynamique de la vitesse induite par le sillage au niveau des pâles. Pour approfondir l'étude de l'aérodynamique des éoliennes flottantes, un modèle Free Vortex Wake à ligne portante est couplé à un code hydro-servo-élastique pour étudier les éoliennes flottantes dans des conditions réelles de fonctionnement. Une méthode de simplification du sillage est proposée pour pouvoir réaliser des simulations de temps physique long à un coût de calcul raisonnable. Le code couplé est validé par comparaison à des résultats expérimentaux et numériques. Le code aero-hydro-servo-élastique est utilisé pour évaluer l'influence du modèle aérodynamique sur les dommages dus à la fatigue pour une éolienne flottante de taille industrielle.

Mots-clé:

Eolienne flottante, Aéro-élasticité, Vortex

Aero-elastic modeling of floating wind turbines with vortex methods

Abstract

Floating offshore wind turbines are set on a foundation free to move under the effect of the winds and waves. This induces a relative motion between the wind turbine rotor and the incoming wind. The Blade Element Momentum Theory, widely used to study the aerodynamics of wind turbines, relies on empirical corrections to model these unsteady conditions. In this thesis, medium fidelity aerodynamic models are used to provide more insight into the unsteady aerodynamic loads on a moving wind turbine rotor. In particular, the phenomenon of dynamic inflow is studied with regard to floating wind turbines. Imposed surge motions are first explored with a lifting line free vortex wake model and an actuator line model. The aerodynamics of a wind turbine after three perturbations are studied: a blade pitch step; a rotor speed step; and a surge velocity step. The Free Vortex Wake method and an analytical helical vortex model based on the Joukowsky rotor model are used to study the dynamic behavior of the induced velocity at the blades. To improve upon the imposed motions cases, a Free Vortex wake code is coupled to a hydro-servo-elastic code to study floating wind turbines in real metocean conditions. A wake simplification model is proposed to enable long simulations at a reasonable computational cost. The coupled code is validated against experimental and numerical data. The aero-hydro-servo-elastic code is used to evaluate the influence of the aerodynamic models on the computed damage of an industrial scale floating wind turbine.

Keywords:

Floating Wind Turbine, Wind Energy, Free Vortex Wake, Dynamic Inflow

Remerciements

La thèse est un long chemin qui ne se parcourt jamais seul. Je tiens en premier lieu à remercier mon directeur de thèse Jeffrey Harris et Christophe Peyrard de m'avoir accompagné sur ce chemin. Je vous remercie en particulier pour votre disponibilité de chaque instant et la grande confiance que vous m'avez donnée.

Je remercie mes rapporteurs Grégory Pinon et Alberto Zasso ainsi que mes examinatrices Sandrine Aubrin et Axelle Viré d'avoir accepté de faire partie de mon jury de thèse. Je remercie également Christine de Jouette d'avoir participé à mon jury de thèse.

Le chemin qui mène à une thèse est rempli de rencontres. Pour moi, cela a tout d'abord été Jean-Philipe, Mathieu et Stéphane, qui ont éveillé ma curiosité pour le travail de thèse. Et puis il y a eu Paul, Norbert, Panos, Bastien, Felix, Laurent et surtout Vladimir qui m'ont fait découvrir le monde des éoliennes. Vous avez éveillé en moi l'envie de faire une thèse et m'avez ouvert le monde des éoliennes.

J'ai du mal à croire qu'une thèse puisse se passer dans de meilleures conditions qu'à Chatou. Merci à tous les collègues et doctorant du bâtiment I et D et en particulier à tous les joueurs d'ultimate pour tous ces bons moments passés ensemble. Matteo et Anais, malgré la distance entre Chatou et Saclay, c'était un plaisir de travailler avec vous.

Ces trois années ne se seraient pas passées aussi bien sans mes fantastiques co-bureaux : Daniel, Paul, Jiaze, Sunnil et mes presques co-bureaux Antoine, Teddy et Elie. Et puis la vie, c'est aussi tous ses amis qui ne font pas de thèse. Merci à vous pour tous les bons moments qu'on a partagés.

Merci à ma famille pour tout son soutien.

Papa et Maman, Etienne, je vous remercie pour la curiosité que vous m'avez transmise. Elle m'a servie tous les jours pendant ces trois années. Je vous aime. Merci aux Dulong de m'avoir accueilli comme un nouveau membre de la famille. Merci à toi Aurélie de bien vouloir partager ta vie avec moi.

Contents

List of Figures

List of Tables

Chapter 1

State of the art

Dans ce chapitre, un état de l'art du dévelopement des éoliennes flottantes est réalisé. Les méthodes numériques utilisées pour la simulation des éoliennes flottantes sont présentés. En particulier, les avantages et limites de chaque approche sont abordés. La méthode Blade Element Momentum, qui est le plus couramment utilisée, a recours à plusieurs corrections empiriques pour modéliser des phénomènes qui ne sont pas pris en compte par le modèle. Les connaissances existantes du comportement aérodynamique des éoliennes flottantes sont présentées. En mouvement de cavalement imposés, les simulations numériques montrent une augmentation de la puissance moyenne et une diminution de la poussée moyenne sur l'éolienne. Les expériences réalisées sur des modèles réduits d'éolienne flottantes en présence de vent et de vagues montrent l'intéractions des efforts aérodynamique et hydrodynamique sur le mouvement des éoliennes flottantes. L'influence du controlleur sur la dynamique globale du système est particulièrement mise en avant, ce qui montre l'importance des outils de simulations aéro-hydro-servo-élastique pour l'étude et la conception des éoliennes flottantes. Dans ce cadre, la méthode Free Vortex Wake se montre pertinente pour l'étude aéro-hydro-servo-élastique de la dynamique des éoliennes flottantes car elle permet un bon compromis entre coup de calcul et description de l'écoulement d'air sur l'éolienne.

1.1 Wind turbines

1.1.1 Harvesting offshore wind energy

The fight against global warming requires global changes in society. Together with the reduction of energy consumption, renewable energies contribute to the reduction of fossil fuel use and greenhouse gas emission. Among the renewable energy sources, offshore wind is now seen as a reliable and cost effective electricity production source. As an example, the first zero-subsidy bottom fixed offshore wind farm is to be built in the Netherlands in 2022 [214], showing that offshore wind is now a cost effective renewable electricity source. The International Energy Agency (IEA) has shown that offshore wind energy has the technical potential to provide more than 10 times the global electricity demand in 2040 [81], with 78% of the technical potential being in deeper water, more than 60 m of depth, for which bottom fixed wind turbines are impractical. Instead, floating wind turbines are a way to access these large energy resources in deep waters. They also reduce the impact of foundations on the seabed - floating wind turbine moorings have a lower footprint of the seabed than bottom-fixed turbines. They could therefore have an environmental interest even for shallow waters compared to bottom-fixed turbines.

1.1.2 Horizontal axis wind turbines

Horizontal axis wind turbines extract kinetic energy from the wind and convert it into electricity. Most current horizontal axis wind turbine designs are lift-based wind turbines. The blades have a specific airfoil profile that leads to a lift force on the blade due to the wind. These lift forces lead to the rotation of the rotor and generate a torque on the axis that is converted into electricity by a generator.

The geometry of a typical wind turbine is shown in Fig. 1.1. An actuator placed at the bottom of the nacelle enables control of the wind turbine yaw angle and aligns the wind turbine with the inflow wind. Actuators placed at the root of the blades control the blade pitch. They are used to adapt the orientation of the blade to the incoming wind. At low wind speed, below the so-called “rated wind speed” of the wind turbine, the blade pitch is set so that as much power as possible is extracted from the wind. The rated wind speed is the lowest wind speed for which the wind turbine is able to generate its rated electric power output. Above the rated wind speed, the generator is not able to convert more mechanical power into electric power because it has reached its limit. Therefore, the blades are feathered to reduce to force of the wind on the blades. When the turbine is not rotating, either due to the lack of wind, to a storm, or for maintenance operations, the blades are aligned with the incoming wind to prevent rotation.

The performance of a wind turbine is often assessed in terms of thrust T and power P.

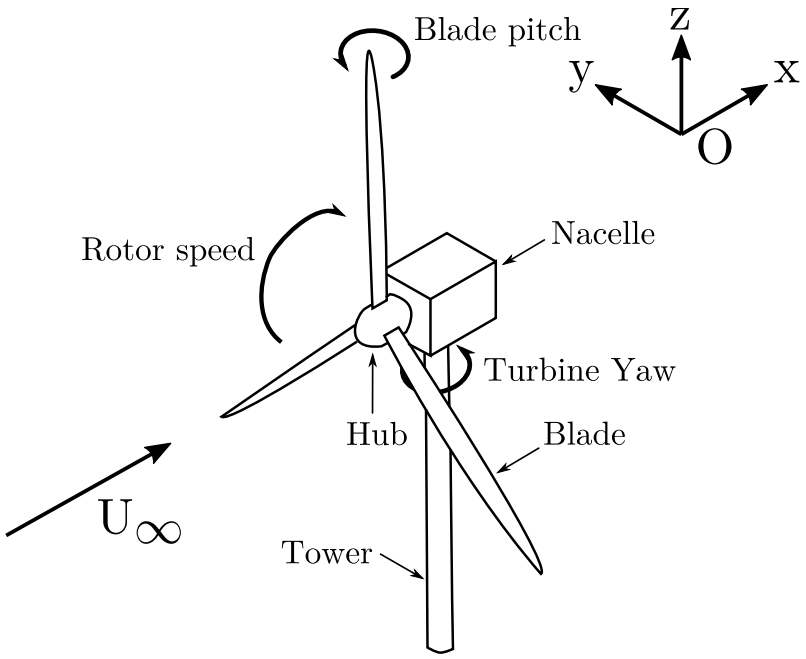

Figure 1.1: Notations for a horizontal axis wind turbine, with incoming wind speed U_∞.

The thrust coefficient, C_T, and the power coefficient, C_P, are defined from the thrust T and power P:

$$C_T = \frac{T}{\frac{1}{2}\rho\pi R^2 U_\infty^2} \tag{1.1}$$

$$C_P = \frac{P}{\frac{1}{2}\rho\pi R^2 U_\infty^3} \tag{1.2}$$

where R is the radius of the rotor, ρ is the air density, and U_∞ is the undisturbed inflow velocity upstream of the rotor. The power coefficient represents the power extracted from the wind compared to the available power in the wind passing through the rotor.

1.1.3 Floating wind turbines

The idea of erecting wind turbines on floating substructure to access wind resources in deep waters can be traced back to the 1970s [188] with the design of Bill Heronemus. The industrial development of offshore wind energy started in Denmark, where bottom-fixed wind turbines are feasible and became the de facto standard. The design of floating wind turbines followed the design of bottom-fixed offshore wind turbines. Various floater design have been proposed, with one or more wind turbines per floater [133]. Butterfield et al. [36] have classified wind turbine floating platforms in three categories based on the way static stability is provided to the floater: ballast, mooring line tension and buoyancy

stabilization. Wind turbine floater use a combination of these three stabilization methods.

The most common floating wind turbine concepts are shown in Fig. 1.2. The spar buoy uses the ballast stabilization method. Ballast placed at the bottom of the floater provides a righting moment that stabilizes the floating platform. A spar requires a large draft to provide the righting moment and is thus not adapted to shallow waters. The tension leg platform (TLP) is stabilized by its mooring line tension. The barge concept uses buoyancy for stabilization. Other concept such as semi-submersibles use a combination of ballast and buoyancy to provide stability to the system.

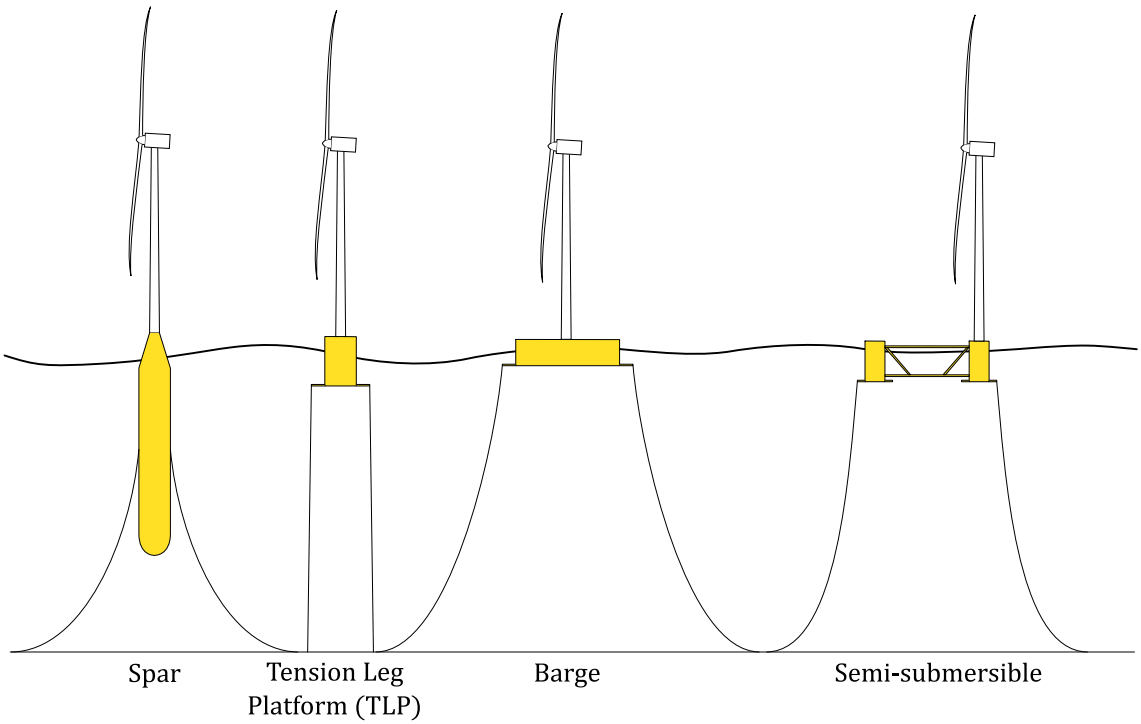

Figure 1.2: Common types of wind turbine floaters.

The first floating wind turbine prototype of 80 kW was installed in Italy by Blue H and used a Tension Leg Platform floating foundation [1]. The first industrial scale wind turbine, Hywind, was installed off the cost of Norway. It is a 2.3 MW wind turbine on a spar buoy. Another floating wind turbine, the WindFloat, was installed off the cost of Portugal and started operating in December 2011 [204] on a semi-submersible floater based on the design presented by Roddier et al. [158]. No floater design has yet imposed itself as the standard. The world first floating wind farm, Hywind Scotland, is composed of five 6 MW wind turbines on spar floaters [3], while the only two other operating wind farms, WindFloat Atlantic and Kincardine, use semi-submersibles. The Provence Grand Large pilot wind farm in France is going to be built using TLPs. Wind farm projects depend on the local conditions such as, for example, the meteorological conditions, the depth, and the available local ports, so different floater designs might be more or less

adapted depending on the project sites.

The action of wind and waves on floating wind turbines induces motions of the system. For floating wind turbines, the same terminology as that used for ships is used. These motions are shown in Fig. 1.3. There are three rotational degree of freedom: pitch, yaw and roll; and three translational degree of freedom: heave, sway and surge.

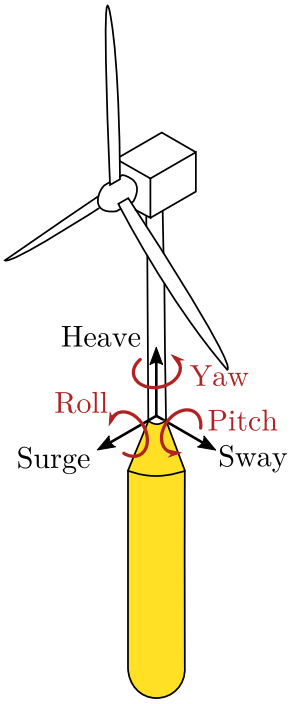

Figure 1.3: Terminology of the motions of a floating wind turbine, following ship terminology.

1.2 Numerical modeling of wind turbine aerodynamics

Numerical methods are an important tool for the design and operation of wind turbines. They are an additional tool to experiments and enable one to explore more configurations both in terms of wind turbine design and operating conditions. Numerical methods differ in the equations that are used to model the wind turbine and the airflow around it. Models that take into account more physical phenomena usually have a higher computational cost and can therefore not be used for the same purpose as a simpler one. Fig. 1.4 shows a classification of the main methods used to model the aerodynamics of wind turbines. They are classified according to their representation of the flow on the wind turbine and their computational cost. Results for a steady production case are obtained in less than a second with the Blade Element Momentum theory (BEM) while it takes several hours with blade-resolved computational fluid dynamics (CFD). The theory behind each method, their differences, and limits will be presented next in increasing computational cost order, to be able to better analyze the results obtained with these methods in the literature and the present work.

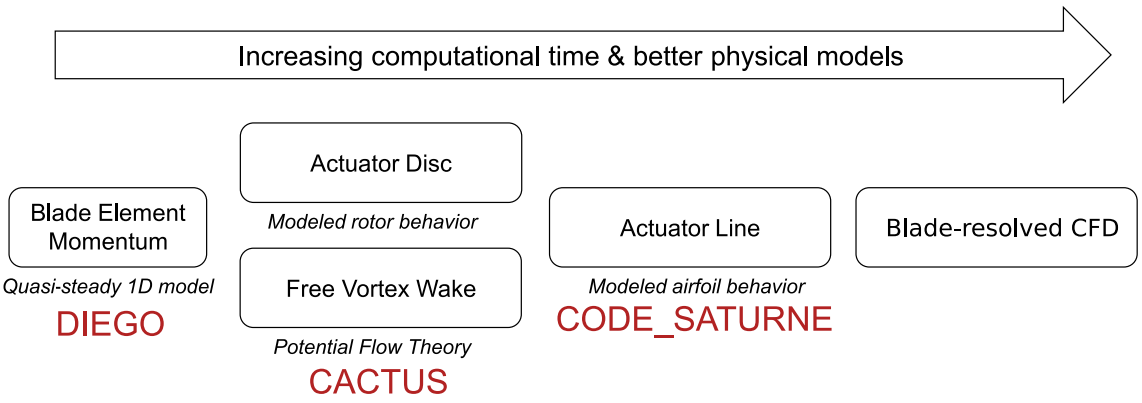

Figure 1.4: Wind turbine numerical methods. The codes that were used in the presented work are shown in orange.

The numerical methods can be separated into two categories that differ in the way they model the aerodynamic forces on the wind turbine blades:

- The first kind of model considers the blade as a combination of blade elements for which the aerodynamic properties are based on their airfoil profiles. The aerodynamic forces, lift, drag and pitching moment of each blade element are obtained from airfoil polars depending on the angle of attack. These tabulated airfoil polars are obtained from experiments or numerical models. Correction models are used to enhance the accuracy of the approach to take into account dynamic effects such as dynamic stall or 3D rotational effects.
- The second kind of model solves the flow around the geometry of the blades and

computes the lift, drag and pitching moment from the integration of the forces around the blade.

1.2.1 Blade element momentum theory

1.2.1.1 Quasi-steady theory

The blade element momentum theory (BEM, see Burton et al. [35]) is based on the Rankine-Froude axial momentum theory. Only the rotor is considered, and it is modeled as an actuator disc, a concept that was introduced by Froude [60]. The aerodynamic forces applied on the blades are assumed to be evenly distributed on the actuator disc representing the rotor. The flow is assumed to be inviscid and incompressible. Rankine-Froude theory studies the stream-tube passing by the edges of the actuator disc represented on Figure 1.5.

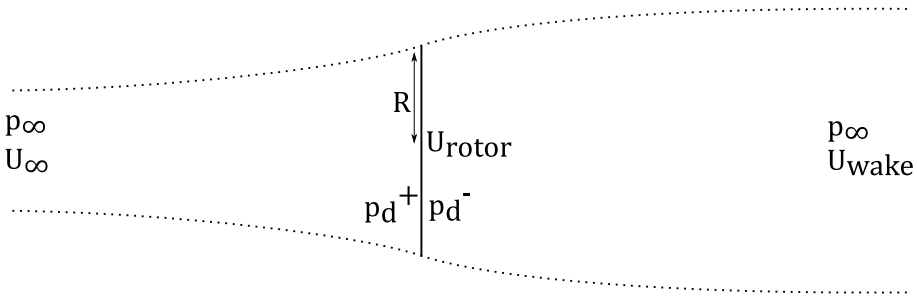

Figure 1.5: Stream-tube and actuator disc, with far-field pressure p_∞, inflow velocity U_∞, flow velocity at the rotor U_{rotor}, flow velocity in the far-wake U_{wake} and p_d^+ and p_d^- the pressures just upstream and downstream of the rotor disc.

If p_{d^+} and p_{d^-} are the pressures just upstream and downstream of the actuator disc, the thrust T acting on the rotor (the axial force) is the difference of the integrated pressure on the actuator disc:

$$T = \pi R^2 (p_{d^+} - p_{d^-})$$

Bernouilli's equation applied upstream and downstream of the rotor links the pressure drop at the actuator disc to the fluid velocities far upstream, U_∞, and far downstream, U_{wake}:

$$T = \frac{\rho \pi R^2}{2} (U_\infty^2 - U_{wake}^2) \tag{1.3}$$

The axial induction factor, a, quantifies the axial velocity deficit at the rotor :

$$U_{rotor} = U_\infty (1 - a) \tag{1.4}$$

The momentum balance equation applied on the stream-tube gives another expression of the thrust and allows the downstream velocity in the wake to be written as a function of

the upstream velocity, U_∞, and the axial induction factor, a:

$$T = \dot{m}(U_\infty - U_{wake}) \text{ where } \dot{m} = \rho U_{rotor}\pi R^2 = \rho U_\infty(1-a)\pi R^2 \tag{1.5}$$

Using the expressions of the thrust obtained with Bernouilli's equation (i.e. Eq. 1.3) and with the momentum balances (Eq. 1.5) gives an expression for the velocity in the chosen far-wake plane:

$$U_{wake} = U_\infty(1-2a)$$

and the thrust on the rotor:

$$T = 2\rho\pi R^2 U_\infty^2 a(1-a) \tag{1.6}$$

By now dividing the stream-tube into a set of annular stream-tubes, the same process can be applied to express the elemental thrust dT applied on an annulus of radial extension dr and radius r of the actuator disc:

$$dT = 4\pi\rho r U_\infty^2 a(1-a)dr \tag{1.7}$$

The actuator disc rotating at the angular speed Ω extracts a torque from the wind, therefore it generates an angular velocity in the flow after the disc. This induced angular velocity ω is expressed from the tangential induction factor a' as $\omega = 2\Omega a'$. The balance of momentum density on a stream-tube between the front and the back of the rotor gives the following expression of the torque of a blade element, dQ:

$$dQ = 4\pi\rho\Omega a' r^3 U_\infty(1-a)dr \tag{1.8}$$

The expression of the projection of the lift of the blade element in the axial and tangential direction as shown on Figure 1.6 gives the two following expressions for the elemental thrust dT and torque dQ:

$$dT = \frac{1}{2}n_b c\rho W^2 C_L \cos\varphi dr \tag{1.9}$$

$$dQ = \frac{1}{2}n_b cr\rho W^2 C_L \sin\varphi dr \tag{1.10}$$

where W is the relative velocity of the wind on the blade, n_b is the number of blades, c is the chord of the blade element, C_L is the lift coefficient and φ is the inflow angle between the relative velocity and the rotor plane which is equal to the sum of the blade twist, blade pitch and angle of attack α. By combining both formulations of thrust and torque, one

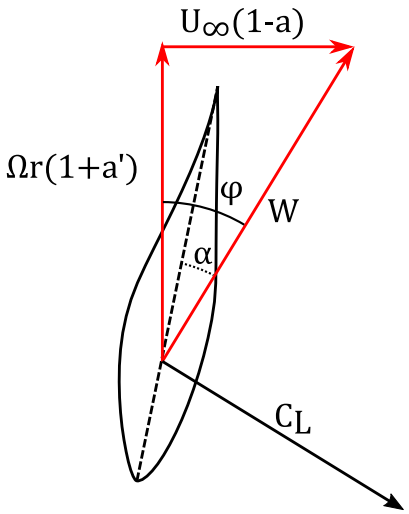

Figure 1.6: Relative velocity and inflow angle, φ, between the relative velocity and rotor plane on a typical wind turbine airfoil.

can derive the following expressions :

$$\frac{a}{1-a} = \frac{\sigma C_L \cos\varphi}{4\sin^2\varphi} \tag{1.11}$$

$$\frac{a'}{1+a'} = \frac{\sigma C_L}{4\cos\varphi} \tag{1.12}$$

where $\sigma = \frac{n_b c}{2\pi r}$ is the solidity at radius r, that is, the fraction of the rotor plane taken by the blade elements.

Solving these equations for the axial and tangential induction factor then gives an expression for the elemental thrust and torque on the considered blade section. However, this set of equations cannot be solved in this form since both the inflow angle and the lift coefficient, C_L, are functions of induction factors as can be seen in Fig. 1.6. The induction factors are usually found using an iterative process. A first guess value is chosen for the induction factors and an updated value is computed from this initial guess. The iterations are stopped when a convergence condition is reached.

The Blade Element Momentum theory suffers from its lack of representation of the actual wind flow on the wind turbine. The different blade sections are totally independent and therefore have no influence on each other. It is a quasi-steady theory and is therefore well suited to study steady operating conditions. A large set of correction models have been developed by different authors to alleviate the short-comings the blade element momentum theory. They are critical and the BEM method is almost never used without them. The analysis of each correction is important to assess the reliability of the results obtained with the BEM method.

1.2.1.2 Tip and Hub Losses

Tip and hub loss models were developed to take into account the fact that the rotor has a finite number of blades. The original model was devised by Prandtl [148] and modified by Glauert as presented in [62] (p. 263-268). It expresses the fact that only a fraction, F, of the flow between two adjacent vortex sheets emitted by the blades in the wake is affected by the movement of the sheets. It is written as follows by Glauert:

$$F = \frac{2}{\pi} \arccos\left(\exp\left(-\frac{n_b(R-r)\sqrt{1+\lambda^2}}{2R}\right)\right) \tag{1.13}$$

where $\lambda = \Omega R/U_\infty$ is the tip speed ratio. It is equivalent to:

$$F = \frac{2}{\pi} \arccos\left(\exp\left(-\frac{n_b(R-r)}{2R\sin\phi_{tip}}\right)\right)$$

where ϕ_{tip} is the flow angle at the tip of the blade considering that the vortex sheet is a perfect screw. In [62] Glauert suggests to use the local values $r\sin\phi$ instead of $R\sin\phi_{tip}$ in the expression of F for practicality in BEM computations. F becomes:

$$F = \frac{2}{\pi} \arccos\left(\exp\left(-\frac{n_b(R-r)}{2r\sin\phi}\right)\right) \tag{1.14}$$

Other corrections have been proposed. For example, Shen et al. [172] presented a modification of this model adding a factor g in the exponential which is a function of the number of blades and the tip speed ratio.

The tip and hub loss model induces a reduction of the predicted aerodynamic forces near the root and the tip of the blades.

1.2.1.3 Turbulent Wake State

For highly loaded rotors, i.e., when the induction factor a becomes higher than 0.5, the momentum theory predicts that the thrust coefficient decreases. However, thrust coefficients higher than 1 have been measured experimentally. This shows that the momentum balance assumption is broken: the wake behind the rotor is energized by a transfer of kinetic energy from outside of the rotor stream-tube. To model the evolution of the thrust coefficient for high values of the induction factor a, empirical corrections built from experimental data are used.

Burton et al. [35] gives the following formula for the thrust coefficient:

$$C_T(a) = C_T(a=1) - 4(\sqrt{C_T(a=1)} - 1)(1-a) \tag{1.15}$$

It is a linear model for which the value at $a = 1$ is fixed and which is tangential to the parabolic formulation given by the momentum balance assumption. The value of the thrust coefficient for total blockage of the inflow $C_T(a = 1)$ can be taken equal to 1.816 as recommended by Burton et al. [35]. The transition between the expression of the thrust coefficient from the momentum balance assumption and the empirical expression is done at:

$$a_{transition} = 1 - \frac{1}{2}\sqrt{C_T(a = 1)}$$

giving $a_{transition} = 0.326$ for $C_T(a = 1) = 1.816$. Burton et al. state that others authors such as Wilson and Lissaman suggest $C_T(a = 1) = 1.6$. Other corrections exist: Buhl [34] presents the formulation of Eggleston and Stoddard (Eq. 1.16) as well as his own formulation (Eq. 1.17) that takes into account the tip loss correction factor F. The different models are plotted on Figures 1.7a and 1.7b for tip loss correction factors of $F = 1.0$ and $F = 0.8$ respectively.

Eggleston and Stoddard proposed:

$$C_T = 0.889 - \frac{0.0203 - (a - 0.143)^2}{0.6427} \tag{1.16}$$

while Buhl [34] proposed:

$$C_T = \frac{8}{9} + \left(4F - \frac{40}{9}\right) a + \left(\frac{50}{9} - 4F\right) a^2 \tag{1.17}$$

1.2.1.4 3D effects and rotational augmentation

An increase in the lift of airfoils in rotation has first been described by Himmelskamp in 1947 [76]. This effect is called rotational augmentation and is due to radial flow in the blade boundary layer [52]. H. Snel [68] proposed a correction of 2D airfoil polar lift coefficient to account for the rotational augmentation. The model is written:

$$C_{l,3D}(\alpha) = C_{l,2D}(\alpha) + f_l \left(2\pi \sin(\alpha - \alpha_0) - C_{l,2D}(\alpha)\right) \tag{1.18}$$

where α_0 is the angle of attack for which the airfoil produces no lift. The lift is corrected by the difference between the inviscid lift of a flat plate and the 2D lift with a factor f_l expressed as a fonction of chord, c, and section radius, r, by Snel as:

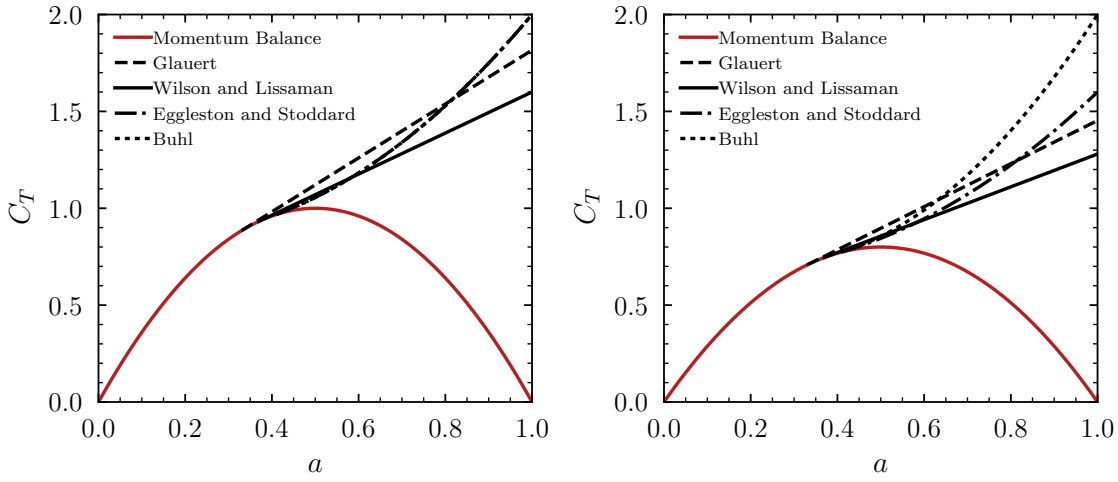

(a) $F = 1$ (b) $F = 0.8$

Figure 1.7: Empirical correction models for turbulent wake state. The Eggleston and Stoddard and Buhl [34] model overlap for tip loss correction factor $F = 1$.

$$f_l = 3\left(\frac{c}{r}\right)^2 \tag{1.19}$$

Following this process, other authors have recommended other expression of the correction factor f_l. Du and Selig [52] studied the position of the separation point along the chord of the airfoil with integral boundary layer equations. They showed that the tip speed ratio λ, the Reynolds number and the ratio of chord over local radial position c/r, delay the separation when they are increased, with the latter parameter having the highest effect. By processing the data from Navier-Stokes simulations of a NACA 63-2-15 airfoil, Chaviaropoulos and Hansen [39] proposed a model similar to Snel's model with an added dependency on the local twist of the airfoil. Dumitrescu et al. [53] explain the increased lift by the presence of a spanwise vortex on the inboard part of the blade. They model the increased lift along the span by a coefficient related to the viscous decay of this vortex.

Some of these models, such as Snel's formulation, can be applied a priori to the 2D airfoil polars knowing the radial position where a blade element will be located. Polars specifically adapted for each radial position are then used in numerical methods.

1.2.1.5 Unsteady airfoil aerodynamics and dynamic stall

In polar-based methods, the forces on an airfoil section are obtained from tabulated forces corresponding to different angle of attack. These forces correspond to quasi-steady forces for a fixed angle of attack. When using this approach, a change in the angle of attack leads to a direct change of the aerodynamic forces. The complex evolution of the flow around the airfoil is not taken into account. In particular, the attached unsteady airfoil

aerodynamics and the dynamic stall are not accounted for, thus models were developed to take into account these effects into account when using polar-base methods.

When an airfoil experiences a rapid change of its angle of attack, the variation of the lift does not adjust instantaneously. In the pioneering work of Theodorsen [195], he expressed analytically the variation of the forces and moments on a flat plate in attached conditions when it is plunging (translating normally to the inflow) and pitching. He divided the contribution to the forces into circulatory and non-circulatory parts, showing that rapid angle of attack variations lead to a delay in the variation of the lift, and this changes slower than the quasi-steady behavior both for an increase and for a decrease of the angle of attack. This specifically is important for floating wind turbines since the motions of the floater can induced cyclic variations of the angle of attack on the airfoils.

Additional flow features appear when the angle of attack is large enough to cause flow separation and thus stall conditions. The rapid transition in and out of the stall conditions and the related flow phenomena is called dynamic stall. A detailed description of the flow during dynamic stall was done by Lee and Gerontakos [101], with experimental measurements and flow visualization. For an airfoil oscillating beyond static stall, they highlighted two flow features increasing the maximum lift compared to the static case. First, a reversed flow is spreading from the trailing edge towards the leading edge. Then a turbulent breakdown occurs and a leading edge vortex travels downstream at a near constant convection velocity along the suction side of the airfoil. This vortex produces an increase of the maximum lift compared to the static case when it travels along the airfoil.

The harmonic pitching motion of an airfoil is characterized by the reduced frequency:

$$k = \frac{\omega c}{2V} \tag{1.20}$$

where c is the local chord of the blade, ω is the angular frequency of the perturbation and $V = \sqrt{U_\infty^2 + (r\Omega)^2}$ is the velocity of the inflow wind.

A secondary vortex traveling from the leading edge is observed when the airfoil is pitching down from stall for large reduced frequencies, producing a slight increase of the lift coefficient even after stall. The stall itself is also delayed for higher reduced frequencies and therefore occurs for higher angles of attack.

Modeling efforts of the dynamic stall have been made, starting for helicopters or other rotorcraft in order to capture the delay of the stall and the increased maximum lift before stalls, using a differential equation such as in the ONERA model [198]. The models most commonly used for wind turbines are variations of the Beddoes-Leishman [103] model, such as the one of Hansen et al. [73]. The Beddoes-Leishman model includes the effects of both dynamic stall and attached unsteady airfoil aerodynamics.

1.2.1.6 Dynamic Inflow

The loads on the blades of a wind turbine do not change instantly when a change of the pitching angle of the blades occurs. In addition to the effects related to the unsteady airfoil aerodynamics detailed in section 1.2.1.5, there is a delay linked to the development of the wake of the rotor. The near wake is due to the previous flow conditions, therefore the induced velocities at the blade are still affected by the previous operating conditions as they influence the blockage of the wind turbine. The blockage is the reduction of the wind speed in front of the wind turbine due to the presence of the wind turbine and its wake. The new operating conditions take their full effect on the loads when the wake is developing and the part of the wake generated by the previous operating conditions is convected far-enough downwind. Models such as the actuator disc, actuator line, free vortex wake, and blade-resolved CFD (see Fig. 1.4) take into account the wake and thus inherently take into account the dynamic effects due to the development of the wake.

The BEM method does not consider the development of the wake. The loads react instantly to variation of inflow conditions if no modeling of dynamic inflow effects is done. Various dynamic inflow models have thus been developed to reproduce the delay in induced velocities due to the wake development.

One such model is the model developed by Stig Øye and explained in [178] and [48]. It consists of two consecutive first-order filters. Writing $u_{i,qs}$ as the quasi-steady induced velocity computed with the BEM, $u_{i,int}$ the intermediate induced velocity used for the model, and u_i the modeled induced velocity, the model is:

$$\begin{aligned}
&\frac{du_{i,int}}{dt} + \frac{1}{\tau_1} u_{i,int} = k\frac{du_{i,qs}}{dt} + \frac{1}{\tau_1} u_{i,qs} \\
&\frac{du_i}{dt} + \frac{1}{\tau_2} u_i = \frac{1}{\tau_2} u_{i,int} \\
&\tau_1 = \frac{1.1}{1 - 1.3a}\frac{R}{U_\infty} \\
&\tau_2 = \left(0.39 - 0.26\left(\frac{r}{R}\right)^2\right)\tau_1
\end{aligned} \tag{1.21}$$

with $k = 0.6$ and a the global induction factor of the wind turbine as defined in Eq. 1.4, where τ_1 and τ_2 are the time constants of the model. In this model, the delay increases when the loading is higher, and it decreases near the tip of the blades.

Another type of dynamic inflow model is based on the theory developed by Pitt and Peters [147] for helicopters. It is based on a pressure distribution around a disc that is a solution to the Laplace equation and is discontinuous at the rotor plane. It links the thrust coefficient to the induced velocity by a first order differential equation in time on

the induced velocity. This type of formulation, including an apparent mass, m_A, was later applied in the framework of the BEM for an annulus of inner radius r and radial extension dr as follows:

$$m_A \frac{da}{dt} + 4\pi\rho r U_\infty^2 a(1-a)dr = C_T \tag{1.22}$$

The second term is the quasi-static behavior. The first term is the dynamic contribution including the apparent mass m_A. Tuckerman [203] computed the apparent mass for a disc of radius R with potential flow theory and found: $m_A = 8/3\rho R^3$. The apparent mass of the considered annulus is then expressed as [178]:

$$m_A = \frac{8}{3}\rho\left((r+dr)^3 - r^3\right) \tag{1.23}$$

The new loading of the rotor takes some time to be applied to the apparent mass of fluid the rotor is acting upon, and it causes a delay.

These models are often tested against measurements done on the Tjæreborg wind turbine [180] for pitching blades and gusts of wind. They found dynamic effects for ramps of blade pitch while almost no dynamic effects were seen in the case of wind gusts. The wind gusts had a slower variation than the blade pitches, and it could therefore explain some of the differences observed.

The unsteady airfoil aerodynamics model presented in section 1.2.1.5 and the dynamic inflow model add a dynamic behavior to the otherwise quasi-steady BEM theory.

1.2.1.7 Yawed Inflow

A yawed inflow modifies the geometry of the wake. As the BEM is developed for an axial flow, some corrections have to be used for a yawed inflow. The main models used to take into account yawed inflows are the models of Glauert [63] and Schepers [163]. The Glauert model for skewed wakes expresses a sinusoidal variation of the induction factor a over the rotor disc. It can be written [28]:

$$\frac{a}{a_{average}} = 1 + \frac{15\pi}{32}\frac{r}{R}\tan\frac{\chi}{2}\cos\psi \tag{1.24}$$

where ψ is the azimuth angle over the rotor disc, χ is the skew angle of the wake and $a_{average}$ is the average induction factor for the considered annular stream-tube. With this model, the induction factor is higher in the downwind part of the rotor than in the upwind part. A new kind of model based on the work of Schepers [163] was presented by Rahimi et al. [151]. It is written:

$$\frac{a}{a_{average}} = 1 - A_1 \cos(\psi - \psi_1) - A_2 \cos(2\psi - \psi_2) \tag{1.25}$$

where A_1, A_2, ψ_1 and ψ_2 are functions of the tip speed ratio λ, the radius r, and the skew angle χ. The functions where expressed through data fitting with results from actuator line simulations. The axial induction factor obtained with this model has similar amplitude and phase with azimuth than the actuator line method but the mean value is different. The authors state that it might be due to the tip and root loss corrections used in the BEM.

Yawed inflow models are of interest for floating wind turbines since both the pitch and yaw movement of the floating platform can result in non-axial inflows.

1.2.2 Free Vortex Wake

The Free Vortex Wake method (FVW) consists of tracking the vorticity emitted by the blades in the flow with discrete vortex elements, and computing the velocity field from the set of vorticity elements. It is therefore a Lagrangian method. There exists a large range of free vortex wake methods (see Branlard [32]) that mainly differ in the choice of the discrete vorticity elements (particle, lines, high-order panels) and their method of emission of vorticity in the flow (lifting-line or paneled blade).

The method most commonly used for wind turbines is the lifting-line free vortex wake using vortex line elements [84, 100, 105, 169, 209–211]. The lifting-line approach seems well adapted to the slender geometry of current wind turbine blade designs. However, it fails to take into account the effect of the deformation of the blade airfoil profiles on the aerodynamic forces.

A potential flow is considered, in which vorticity is limited to discrete vortex segments (also called vortex lines). The vorticity elements are convected by the potential flow and the velocity induced by the set of vorticity elements is called the wake self-induced velocity. The velocity at a point $\mathbf{x_p}$ is computed as:

$$\mathbf{u}(\mathbf{x_p}, t) = \mathbf{U}_\infty(\mathbf{x_p}, t) + \sum_n \mathbf{u_{\Gamma,n}}(\mathbf{x_p}, t) \tag{1.26}$$

where $\mathbf{U}_\infty$ is the inflow and $\mathbf{u_{\Gamma,n}}$ is the velocity induced by the vortex element of index n. With the notations of Fig. 1.8, it can be written (see Katz and Plotkin [93]):

$$\mathbf{u_\Gamma}(\mathbf{x_p}) = \frac{\Gamma}{4\pi} \frac{\mathbf{r_1} \times \mathbf{r_2}}{|\mathbf{r_1} \times \mathbf{r_2}|^2} (\mathbf{r_1} - \mathbf{r_2}) \cdot \left(\frac{\mathbf{r_1}}{|\mathbf{r_1}|} - \frac{\mathbf{r_2}}{|\mathbf{r_2}|} \right) \tag{1.27}$$

Phillips and Snyder [145] noted that this expression is not practical for numerical simu-

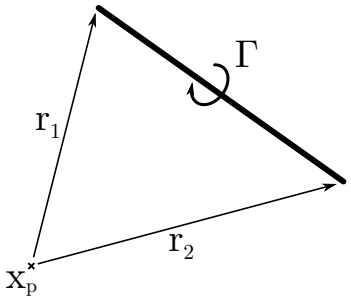

Figure 1.8: Notations used to compute the velocity induced by a single vortex segment with the Biot-Savart law. With $\mathbf{x_p}$ the position where the velocity is evaluated, $\mathbf{r_1}$ and $\mathbf{r_2}$ the vectors between the evaluation point and each end of the vortex line and Γ the circulation of the vortex line.

lations since the denominator of the leading term is zero when $\mathbf{r_1}$ and $\mathbf{r_2}$ are collinear, meaning that the evaluation point is on the axis of the vortex segment. They reworked this expressions using trigonometric relations to obtain an expression that is not singular when the evaluation point lies on the axis of the vortex segment, outside of the vortex segment itself [145]:

$$\mathbf{u_\Gamma}\left(\mathbf{x_p}\right) = \frac{\Gamma}{4\pi} \frac{\left(|\mathbf{r_1}| + |\mathbf{r_2}|\right)\left(\mathbf{r_1} \times \mathbf{r_2}\right)}{|\mathbf{r_1}||\mathbf{r_2}|\left(|\mathbf{r_1}||\mathbf{r_2}| + \mathbf{r_1} \cdot \mathbf{r_2}\right)} \tag{1.28}$$

This second expression is for example the one used by AWSM [205], the FVW code developed at Energy Research Centre of the Netherlands (ECN now Netherlands Organisation for Applied Scientific Research, or TNO).

The lift of the blade is converted into an equivalent bound circulation on the lifting-line using the Kutta-Joukowksi theorem linking the circulation around an airfoil to its lift:

$$\mathbf{L} = \rho(\mathbf{U} \times \mathbf{\Gamma}) \tag{1.29}$$

where $\mathbf{U}$ is the relative velocity vector of the fluid flow on the airfoil, $\mathbf{L}$ is the lift and $\mathbf{\Gamma}$ is the circulation around the airfoil. Then, following Kelvin's theorem, the global circulation does not change with time:

$$\frac{D\mathbf{\Gamma}}{Dt} = 0 \tag{1.30}$$

therefore every variation of the circulation of the airfoil has to be compensated by a vortex shed by the blade with the opposite circulation. This gives the strength of the vortices shed by the blade elements. In contrast, trailing vortices account for the spanwise variation of the circulation of the blade. The vortex line system of a blade discretized with three elements along the lifting line can be seen on Figure 1.9 with both shed and trailing

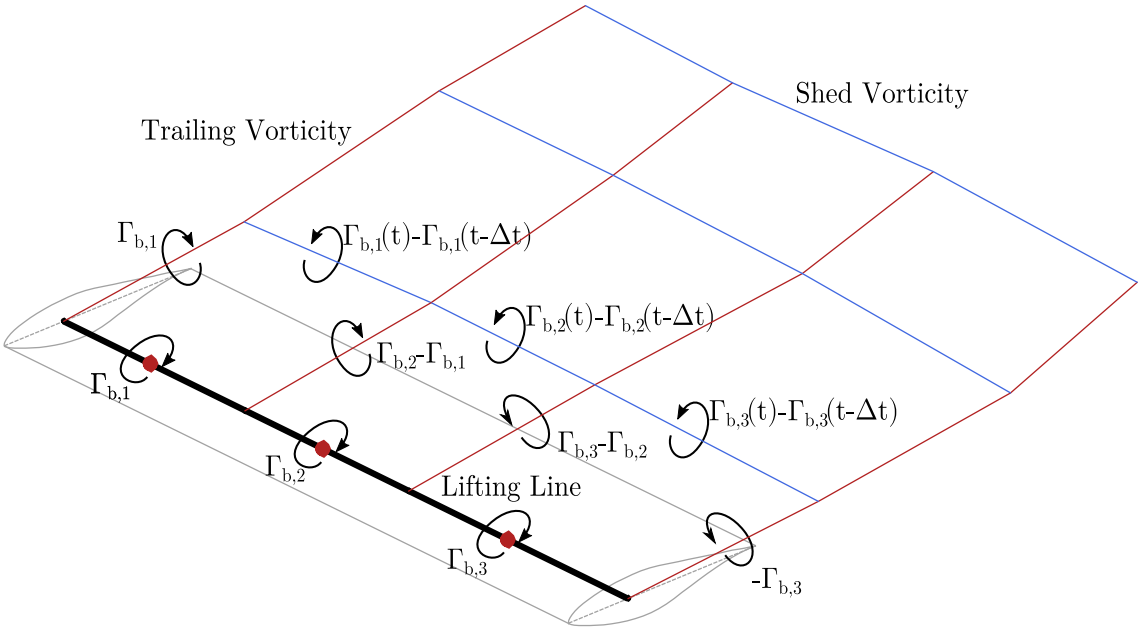

Figure 1.9: Lifting Line Free Vortex Wake method vortex emission. The lifting-line is the thick black line with the control points shown in red. The outline of the blade is shown. Trailing vorticity refers to vorticity related to the difference in circulation between two adjacent blade element (in red). Shed vorticity refers to circulation related to the temporal variation of the circulation of a blade element (in blue).

vortices.

As shown in Fig. 1.9, the circulation of the first emitted row of both shed and trailing vorticity depends on the vorticity bound to the lifting-line. Therefore, there is a mutual coupling between the first emitted elements and the lift over the blade. Indeed, the first emitted elements induce a velocity at the blade element control points. It changes the bound circulation by modifying the relative velocity and the lift at the blade control point which in turn changes the vorticity of the first emitted elements.

An iterative procedure is generally used to obtain the bound circulation at the blade and thus the lift distribution. A first guess of the bound circulation is made, either by using the bound circulation of the last time step or by evaluating it with only potential flow for the first time step. The circulation of the first emitted shed and trailing element is updated and the change in induced velocity is taken into account to update the lift and the bound circulation. The procedure is carried out until a convergence condition is met. Apart from the first row of shed and trailing vorticity which is currently being emitted, the circulation of the other vortex elements in the wake does not change once emitted.

Similar to the BEM, the lifting line FVW relies on airfoil polars and a dynamic stall model (see section 1.2.1.5) to compute the lift of blade elements from the local flow. However, since the FVW is inherently 3D and unsteady, all the temporal variation in the load and

the evolution of the wake are taken into account. There is no need to use additional empirical models to take into account dynamic inflow or a yaw misalignment such as for the BEM. This comes at the price of an increased computational cost. While the BEM computes the flow velocity only at the blade element control points, the FVW requires the flow velocity at every vortex segment end for the Lagrangian wake convection step.

Computing the wake self-induced velocity is commonly called an *n-body* problem: the influence of every vortex element has to be computed at every vortex element end point. The computational cost of such a problem grows with the square of the number of elements. Many reduce this cost by either neglecting some vorticity elements in the wake [30] or using a fixed convection velocity for part of the wake [104]. This reduces the quality of the model of the wake and might affect the loads on the wind turbine.

To obtain a steady state result, the wake behind the wind turbine has to be fully developed which means that the elements that were first emitted from the wake must have been convected sufficiently far away that the wake has reached a steady state. The simulation has to be done for a physical time that allows the full development of the wake to obtain this steady result. This physical time can be rather long and result in a large computational time. Here, the BEM shines as it can provide the result for steady operating conditions in a single computation step. The FVW strength is in simulating unsteady and dynamic conditions, for example blade pitch changes, an inflow misalignment with the rotor, or moving floating wind turbines.

1.2.3 Actuator disc and actuator line

The actuator disc and actuator line method are similar. They both use the Navier-Stokes equations that are numerically solved, typically over a mesh. The actual geometry of the blade is not meshed and the influence of the rotor on the flow is taken into account through source terms. They differ in the way this source term is applied in the flow.

1.2.3.1 Actuator disc

The actuator disc (AD) method uses the Navier-Stokes equations to compute the velocity field. The presence of the rotor is modeled by adding body forces in the Navier-Stokes equations at the position of the rotor disc. The body forces are obtained using either radially changing blade forces or a global rotor thrust. The radially varying forces are computed with airfoil polars giving the lift and drag coefficients from the angle of attack which is computed at control points over the rotor disc in the mesh, while a global thrust force can be obtained from a tabulated power curve giving the thrust as a function of the operating conditions: inflow, rotational speed of the rotor, and blade pitch. Either way, the body forces are smeared on the mesh with a Gaussian kernel to avoid numerical

instabilities.

In comparison to the BEM method, the actuator disc method includes some wake effects through the consideration of the velocity field upstream and downstream of the wind turbine. The actuator disc method can thus be used to study unsteady effects and wake effects such as what was done by Sørensen and Kock [182] or Sørensen et al. [181]. The AD method is often used with Large Eddy Simulation (LES) ([86],[87]) for wake simulations up to the wind farm scale ([218],[187]). However, the forces are applied on the whole rotor disc without taking into account the current position of the blades. The actuator line method presented in Section 1.2.3.2 refines this approach by actually considering the position of the blades to locally apply the body forces.

The actuator disc method can also be used in experiments to represent a wind turbine in a flow. They use porous discs that match the thrust of the modeled wind turbine. Aubrun et al. [13] compared the wake behind a porous disc and a wind turbine to assess if the porous disc is able to reproduce the wake of a similarly sized wind turbine. They found that at a stream-wise distance of three rotor diameters (i.e., $3D$), the wake of the tested porous disc is similar to the one of the wind turbine model with blades. The results match better for an atmospheric boundary layer with a 13% turbulence intensity at hub height than for a decaying isotropic turbulence inflow with 4% turbulence intensity. At a stream-wise distance of half a rotor diameter, the wakes of the porous disc and the wind turbine have different axial velocities, vertical velocities, and turbulence intensity. The pressure coefficient in the wakes are also different in the near wake: the pressure coefficient is lower for the wind turbine. For both the wind turbine and the porous disc, the pressure coefficient is near 0 after a distance $x = 1.5D$. This shows that porous discs are suitable to reproduce the far wake of wind turbines in both atmospheric boundary layer and decaying isotropic turbulence, but not the near wake behavior. Lignarolo et al. [107] had similar conclusions when comparing the wakes of a 2-bladed wind turbine and a porous disc. The velocities and the turbulence intensities are different close to the rotor and match better in the far wake at $x = 2.2D$. Porous discs for wind turbine experiments are used in [13], [107], [221], [222]. A comparison between measurements done on identical actuator discs was done by Aubrun et al. [14].

Actuator disc methods are valuable to study the wake of wind turbines and wind farm scale wake interactions thanks to the ability of CFD solvers to account for atmospheric turbulence and the turbulence generated by the rotor. They are not adapted to study the loads on the blade of wind turbines, since the rotor forces are distributed over the rotor disc, meaning that the local flow over the rotor is not solved in detail. These shortcomings are addressed by the actuator line method which takes into account the individual position of the blades.

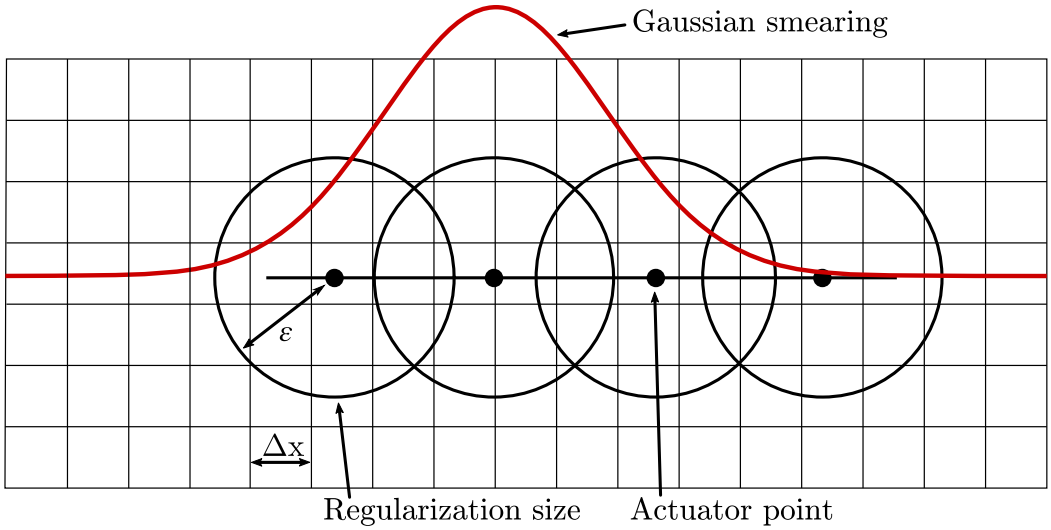

Figure 1.10: Typical spread of forces in Actuator Line method.

1.2.3.2 Actuator Line

In the actuator line method (AL) described by Sørensen and Shen in [183], the velocity field is computed with the Navier-Stokes equations. The actual position of the blade is taken into account as opposed to the actuator disc method for which the forces are spread over a disc. The aerodynamic forces are obtained with airfoil polars and then applied as body forces on the mesh at the position of the blades. The principle of the method is shown in Fig. 1.10. A Gaussian kernel is used to avoid singularities at the position of the blades:

$$g(d) = \frac{1}{\epsilon^3 \pi^{3/2}} \exp\left[-\left(\frac{d}{\epsilon}\right)^2\right] \tag{1.31}$$

where d is the distance to the actuator line and ϵ is a regularization parameter.

The actuator line is well suited for wind turbine wake computations and can capture details of the behavior of the wake. This is for example done in the work of Benard et al. [23] which shows that high-order spatial discretization with low dissipation and dispersion are better suited than first and second order schemes for wind turbine wake simulations. In both the AL and AD method, the presence of the nacelle and the tower can either be modeled by additional body forces or by a body-fitted mesh.

Two important modeling choices are made when using the actuator line method: the sampling method of the velocity field to compute the relative velocity at the blade and the smearing of the body forces. Those two aspects of the actuator line method are adressed next.

Body Force Smearing

A choice has to be made on the number of actuator points per blade. Usually, between 40 and 60 actuator points are used ([42]). The number of actuator points is related to the mesh size: if Δb is the distance between two actuator points and Δx is the grid size in the spanwise direction, according to Jha and Schmitz [85] the distribution of the actuator points should be so that $\Delta b/\Delta x \geq 1.5$.

Martínez-Tossas et al. [119] expressed optimal regularization parameters for the actuator line model in 2D cases. They found that by adjusting the regularization parameter ϵ (Eq. 1.31) and the position of the actuator line in the chordwise direction, a better reproduction of the fluid flow around a 2D airfoil profile can be obtained. They also explored the use of different regularization parameters along the chordwise and thickness directions, which gave improved results.

While Martínez-Tossas et al. [119] studied the regularization parameter in the airfoil plane, Mittal et al. [129] recommended a different regularization parameter in the spanwise direction than in the airfoil plane. They state that the spanwise regularization should be based on the length of the blade element while the regularization in the airfoil plane should be based on the chord length.

Meyer Forsting et al. [125] showed that the Gaussian smoothing of the force is equivalent to the viscous vortex core of a Lamb-Oseen vortex of core radius r_c equal to the AL regularization size ϵ. The effect of the smoothing leads to tip vortex core sizes that are often larger than what is experimentally measured because the regularization size chosen based on the mesh size leads to a vortex with a large core radius. When choosing large regularization sizes, the overly smoothed flow field near the tip of the blade affects the velocity sampling done to compute the aerodynamic force on the blade element. They proposed to use a vortex near-wake model to account for the missing induction when doing the velocity sampling step.

The lack of a tip correction can lead to higher than expected flow velocities at the tip of the blades which results in overly high blade loads near the tip. This was corrected by Shen et al. [173] by using a simple tip correction model of the same form as the one used for BEM (see section 1.2.1.2).

Velocity Sampling

The computation of the aerodynamic forces that need to be inserted as source terms in the Navier-Stokes equations require the knowledge of the flow velocity at the actuator point on the lifting-line. The velocity sampling method is not always well-described by authors using the actuator line method in the literature, but is a critical point.

As pointed out by Merabet and Laurendeau [124], different methods can be used to obtain

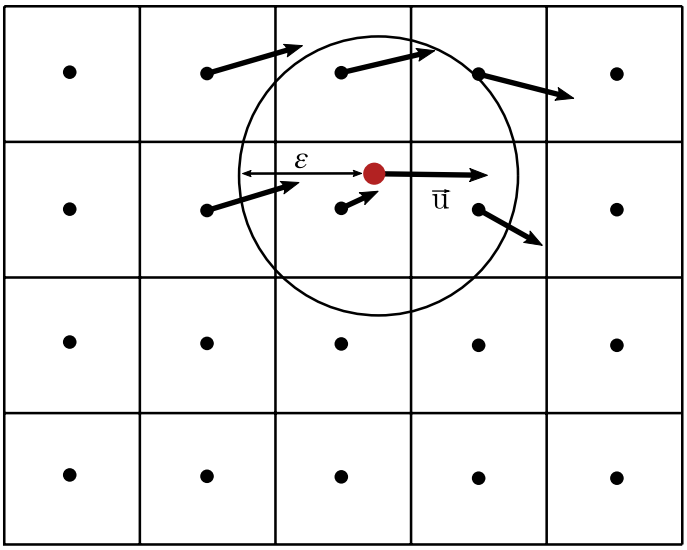

Figure 1.11: Schematic of velocity sampling at red point.

the flow velocity at the actuator point. Fig. 1.11 shows an actuator point within a mesh and the velocity vectors at the centers of the neighboring cells. Following Merabet and Laurendeau [124], the velocity at the actuator point can be either taken equal to the one at the closest cell center, computed as the average over neighboring cells, obtained from an interpolation over neighboring cells, or obtained by the Integral Velocity Sampling method presented by Churchfield et al. [42] and proposed by Spalard.

The Integral Velocity method consists in computing the value of the velocity at the actuator point as a weighted average where the weights are computed with the Gaussian smoothing function Eq. 1.31:

$$\mathbf{u}_i = \sum_{n=1}^{N_{cells}} \Omega_n g\left(d_n\right) \mathbf{u}_n \tag{1.32}$$

where Ω_n is the volume of the cell of index n, $\mathbf{u}_n$ the flow velocity at the center of this cell and d_n the distance between its center and the actuator point.

To better represent the effect of the blade on the flow, some efforts are made to take into account the shape of the blade when applying the source terms such as the work of Churchfield et al. [42] or Jha and Schmitz [85]. This is fundamentally done by using blade-resolved computation fluid dynamics, as will be presented next.

1.2.4 Blade-resolved computational fluid dynamics

Blade-resolved CFD uses a body-fitted mesh around the blades to capture the flow around the blade geometry. Reynolds-average Navier Stokes equations (RANS) or Large Eddy Simulation (LES) can be used to model turbulence. The necessary refinement of the mesh

in the boundary layer to properly model the flow generates meshes with a high number of cells, and can be computationally intensive.

The separation of the flow from the blade is difficult to capture even on a single pitching blade, as shown in the work of Barnaud et al. [18].

In the framework of the AVATAR project, some CFD code comparisons were done on a 2D airfoil at high Reynolds number (3×10^6 and 15×10^6)[184]. It was found that the dependency of the results to the grids is linked to the angle of attack. The results obtained with different grid sizes have higher discrepancies for higher absolute angles of attack. Good agreement between the codes was found with the finest mesh with a normal cell spacing of $1.5 \times 10^{-6} \Delta x/c$ with an hyperbolic tangent stretching and 384 cells in the chord-wise direction.

To properly capture the size of the tip vortex using blade-resolved CFD, Cormier et al. [44] used a mesh with 120 million cells, which leads to very high computational costs. Blade-resolved CFD has been used for the study of floating wind turbines [41, 106, 109, 111], but the computational cost of the method related to the large number of cells required to properly model the boundary layer on the blades limit the number of operating conditions that can be tested using this method.

Now that the main models used for the aerodynamic of wind turbines were presented, we next review the existing knowledge on the aerodynamics of floating wind turbines and more generally the dynamic behavior of floating wind turbines.

1.3 Dynamics of floating wind turbines

Traditionally, the study of floating wind turbine aerodynamics started by determining the motions that the rotor will likely experience due to the hydrodynamic effects of the sea state on the floater. Then the aerodynamics of wind turbines with imposed motions are considered. More recently, some studies were done in coupled wind and waves cases for which both the hydrodynamics and the aerodynamics are accounted for.

1.3.1 Floater motions and related aerodynamic unsteadiness

The BEM aerodynamic model has often been used in conjunction with hydrodynamic models to obtain the response of a floating wind turbine to a sea state [167]. This was done to have a first estimate of floater motions as it was not known whether the BEM with its empirical corrections is able to properly model wind turbine rotors in motion.

The motions of a floating wind turbine change the relative velocity at the blades and therefore modify the angle of attack and the lift produced by each blade. Even bottom-fixed wind turbines have a varying lift over a rotation, mainly due to the tilt angle,

typically non-zero for large wind turbines, and the shear of incoming wind due to the atmospheric boundary layer. The study of aerodynamic unsteadiness for wind turbine rotors is inspired by research in the rotorcraft field. The unsteady character of the flow over a blade is determined by studying its reduced frequency, k (Eq. 1.20).

Leishman [102] linked the reduced frequency of the perturbation to different regimes of the unsteadiness of the flow. It is considered unsteady if $0.05 < k \leq 0.2$ and highly unsteady if $k > 0.2$. The inboard side of the blade (near its root) has a higher reduced frequency than the tip of the blade, since the relative velocity due to the rotation of the wind turbine is lower, so it is more prone to flow separation. Following the work of Sebastian and Lackner [167], the reduced frequency along the blade is shown in Fig. 1.12 for the NREL 5MW wind turbine for its cut-in, rated, and cut-out conditions based on the blade chord and taking into account the rotation speed of the rotor, ω_r, as the source of unsteadiness. The cut-in conditions correspond to the minimal inflow wind speed for which the wind turbine operates, while the cut-out conditions correspond to the maximal inflow wind speed for which the wind turbine operates. It shows that the inboard half of the blades are subject to an unsteady flow for all conditions. In the cut-in conditions, the part of the blade closest to the hub is experiencing a highly unsteady flow. Similarly to the tilt of a wind turbine rotor, the motions of a floater generate some angle of attack variations over the blades that could lead to an unsteady behavior if their frequency is large. Sebastian and Lackner [167] studied with this method the respective effects of the six degrees of freedom added by the floater on the variation of the angle of attack in the absence of shear. For three tested floater designs, the respective floater motions were obtained from prior hydrodynamic computation and imposed in the FVW computations. The degrees of freedom introducing the most unsteady aerodynamic loads for the tested floaters are: the pitch for a barge, the pitch and yaw for a spar and the pitch and surge for a TLP. In addition to aerodynamic unsteadiness, Jonkman and Matha [89] found that the floater motions lead to increased ultimate loads compared to a fixed bottom wind turbine. Surge and pitch were identified as the motions leading to the highest effect on the aerodynamics of floating wind turbines. Indeed, these motions are the ones changing the relative inflow velocity of the rotor due to an upwind or downwind motion of the blades. This also explains the lower influence of the yaw motions The three other floater motions, heave, sway, and roll, have less aerodynamic importance.

Due to the high computational cost of detailed aerodynamic models and their relative complexity, it limits their use for exploring a large range of operating conditions and floater motions. Therefore, they are often used to study wind turbines in forced harmonic motions.

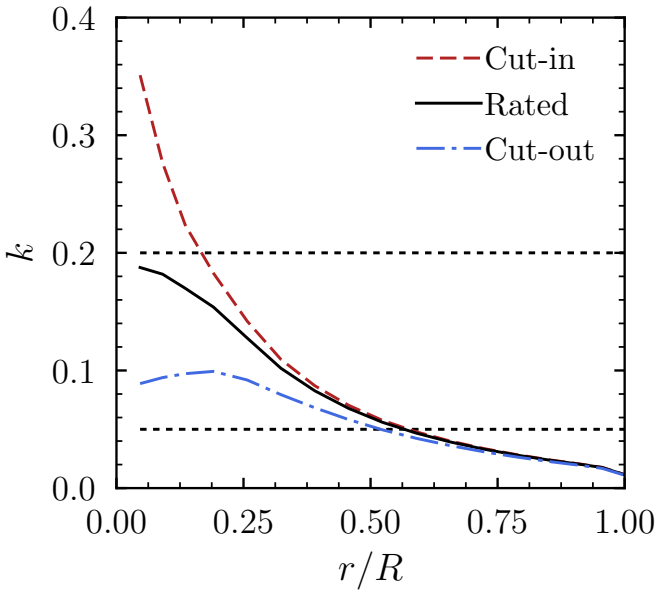

Figure 1.12: Reduced frequency along the blade for the NREL 5MW wind turbine

1.3.2 Imposed motions aerodynamics

A number of detailed aerodynamic models have been used to study floating wind turbines in imposed motions, ranging from 2D actuator disc [48] to blade-resolved CFD [43, 106]. The works have mainly focused on the more aerodynamically relevant surge and pitch motions.

For the surge motion, de Vaal et al. [48] found limited effects on the integrated load obtained with AD for a slow surge motion. For faster surge motions, various authors have found an increase of the average power and a decrease of the mean thrust. This was found with FVW [56, 174, 209], AL [11] and blade-resolved CFD [106]. Mancini et al. [115] compared BEM, FVW and AL to the measurements obtained in the UNAFLOW experiment on a rigid wind turbine in imposed surge motion. All the tested numerical models correctly predicted the variation of the thrust force measured in the experiment.

The imposed pitch motion increases the misalignment between the rotor and the inflow, which makes it a more challenging case for the BEM since the method assumes an axial inflow, and relies on a correction model for misaligned inflows. Wu and Nguyen [216] found good agreement between the open-source BEM simulation tool FAST and RANS blade-resolved CFD for a small amplitude imposed pitch motion ($\Delta\theta_p = 0.85°$ and $T_p = 10s$) with the NREL 5MW reference wind turbine. Similar results were found by Tran et al. [199, 201] for pitch amplitudes smaller than 1° and a period of $10s$. However, Tran and Kim [199] found larger differences between results from BEM and blade-resolved CFD for a 4° amplitude imposed pitch motion with a period $T_p = 5s$.

Similarly to the imposed surge case, an increase of the mean power was found with FVW [210] and with blade-resolved CFD [41, 106]. The effect of the pitch motion was modeled by Wen et al. [211] as an additional variable wind shear. Additionally, Arabgolarcheh et al. [11] showed with the AL method that the power generated by each blades is different in imposed pitch motion. They stated that it could affect the fatigue of the blades.

Limited experimental data is available for wind turbines in imposed motions representative of floating platforms. Within the LIFES50+ project [20, 143], a model wind turbine in imposed surge motion was investigated. However, due to the interaction between the natural frequency of the tower and the surge motion, the force measurements were perturbed by structural oscillations. The aerodynamic forces could not be separated from the inertial forces in the experimental data. A stiffer tower was used in the UNAFLOW project [22, 58] which made it possible to extract the aerodynamic forces from the measured forces [115]. Fontanella et al. [57] showed that up to a reduced frequency of $f_r = f_s D/U_\infty = 0.5$ with f_s the surge frequency, the aerodynamic thrust has a quasi-steady behavior. Fontanella et al. [57] stated that no conclusions could be made for higher reduced frequencies due to the influence of the tower elasticity. Wen et al. [212] presented an experiment consisting of a model wind turbine on an hexapod in front of an array of fan that they plan to use to study the aerodynamics of a wind turbine in imposed motions.

Purely sinusoidal motions might not be representative of actual floating wind turbine motions. To improve upon sinusoidal motions, some authors choose to pre-compute the coupled wind-wave dynamic of the floating wind turbine with BEM to then use higher fidelity aerodynamic models. Using the actuator disc method together with combined surge and pitch motions pre-computed for a barge and spar-type floater, Kopperstad et al. [97] found that the mean power was not significantly affected by the dominant period of the sea states for the spar motions, while the mean power computed for the barge was reduced for sea states with a large dominant period ($T_p = 22s$). Xu et al. [217] applied imposed motions precomputed with FAST for a TLP to a wind turbine simulated with the FVW method. Such a method does not allow for interactions between the aerodynamic and hydrodynamic forces.

1.3.3 Coupled wind-wave dynamics

Experiments

In order to take into account the coupled effect of the wind and waves on a floating wind turbines, floating wind turbine models have been studied in wave tanks equipped with wind generators. The scaling generally used for the experiments is the Froude scaling law as is done for other offshore structure such as ships. The Froude number is:

$$Fr = \frac{u}{\sqrt{gL}} \tag{1.33}$$

where g is the acceleration of gravity, u is a representative velocity and L a representative length of the system. The Froude scaling law implies that the Froude number at model scale is equal to the Froude number at full scale. The aerodynamic forces are also a function of the Reynolds number $Re = uL/\nu$ where ν is the kinematic viscosity of air. To properly model the aerodynamic forces, the Reynolds number should be equal between model scale and full scale. However, because of the Froude scaling, the relation between the velocity and the length is already set. Therefore, the only way to match the Reynolds number between the model scale and the full scale would be to change the viscosity of the fluids used in the experiment, which is impractical. Generally, Froude scaling is imposed and the Reynolds number at model scale is lower than the Reynolds number at full scale in coupled wind-waves experiments. One of the main effects of the difference in Reynolds number between model scale and full scale is that the airfoil profiles do not generate the same lift at a lower Reynolds number, which results in a lower thrust force than required.

Various methods have been proposed in the literature to generate the appropriate aerodynamic thrust force. One of them is to adapt the design of the blade as is done by Kimball et al. [95] who detailed the design process of the performance-matched wind turbine model used in a combined wind and waves experiment. The chord size of the blade is increased compared to a full size wind turbine to match the thrust coefficient while ensuring the blade operates far-enough from stall conditions. The pitch angle of the blade is then adapted to match the thrust coefficient corresponding to a specific rotational speed of the wind turbine in order to correctly represent the gyroscopic effect experienced by full scale wind turbines. Adapted blades were also used by Bredmose et al. [33]. Chen et al. [40] experimentally compared the dynamics of floating wind turbines using performance-matched blades and geometrically-scaled blades. The performance-matched blades have an enlarged chord to match the scaled thrust force, and therefore have a different geometry tan the full scale blades. This leads to a larger relative weight of the rotor that changes the center of mass of the floating wind turbine. The geometrically scaled blades are used with a much higher inflow wind speed to be able to match the scaled thrust. However, the increase of inflow wind speed means that the geometrically scaled wind turbine operates at a different tip speed ratio that the full scale wind turbine for a similar thrust coefficient, and the ratio between the inflow wind speed and the velocity of the floating wind turbine motions is not conserved.

Hall and Goupee [70] proposed a software-in-the-loop method to solve the problem of the scaling of the aerodynamic forces at model scale. In their method, aerodynamic forces are imposed at the tower top by using cables and forces computed with a numerical model. Using their method, they found similar results as coupled wind-waves experiments when

using Froude model-scaled aerodynamic loads while they found a significantly different behavior when using aerodynamic forces scaled to represent full-scale aerodynamic forces. It showed the importance of the scaling for aerodynamic forces. More aerodynamic damping of the pitch motion was found when using the correctly scaled aerodynamic forces compared to the Froude scaled aerodynamic forces. This was attributed to the comparatively larger ratio between the pitch motion related velocity and the wind speed for the Froude scaled rotor.

In their experiment, Koch et al. [96] added ballast mass to the floater to adapt the position of the center of mass, because the effective nacelle mass was larger than the target scaled nacelle mass due to the presence of the actuators used for the rotor and blade rotation.

Farrugia et al. [55] showed experimentally that the power coefficient of a 2-bladed wind turbine on a TLP subject to a surge motion is more affected by the waves at higher tip-speed-ratios. At low tip-speed-ratios, the power coefficient C_P of the floating Wind turbine is similar to the power coefficient of the equivalent fixed bottom wind turbine. Sant et al. [161] showed that the aerodynamic behavior of a 2-bladed floating wind turbine can induce a negative damping of the surge motion of a wind turbine at a particular wave condition. They stated that the higher sensitivity of the loads to the surge motion at high tip speed ratio are due to the fact that the tip vortices are closer to one another when the tip speed ratio is high.

An experimental campaign was carried on a DTU 10MW scaled wind turbine model on a triple spar floater in the DHI Denmark wave tank. A comparison between different controllers is presented by Bredmose et al. [33]. The experiment shows that a controller designed for onshore wind turbines leads to unstable oscillations of the wind turbine with wind only and no waves. The response of the structure to a focused wave group with and without wind shows that the wind provides a significant aerodynamic damping. A larger pitch and surge response was found when using a controller compared to a fixed blade pitch situation.

Goupee et al. [64] experimentally compared the response of a spar, a TLP and a semi-submersible floater. They operated the rotor at a fixed blade pitch and rotational speed. They found that for the semi-submersible floater they used, the coupling between the surge and pitch motion lead to little surge motion at the nacelle. Large differences were found between the responses of the three tested floater designs. It shows that specific floater designs lead to different responses of the global floating wind turbine system. The influence of different controllers on the response of floating wind turbines was experimentally investigated by Goupee et al. [65]. The variable speed controller they used reduced the platform surge and pitch compared to the case with a constant blade pitch and rotation speed of the rotor. They showed that with a variable speed controller, some of the wind kinetic energy induces an increase of the rotation speed instead of generating surge and

pitch motions. However, they expressed that their results might not be directly transferable to full-scale floating wind turbines due to the difference in aerodynamic loading between the scaled model wind turbine and full-scale wind turbines. Madsen et al. [112] also experimentally studied the influence of controllers on the dynamics of floating wind turbine on a TLP. They found that a controller tuned for onshore use leads to a larger response of the floater to the incoming waves compared to a controller tuned for floating use.

Overall, coupled wind-wave experiments have shown that the controller has a significant effect on the behavior of floating wind turbine and have allowed to test various floater designs. However, model scale wave tank experiments with wind generators cannot match the Reynolds number of full scale rotors, which generates differences in the aerodynamics. Numerical models do not face this limitation, since they allow to simulate floating wind turbines at full scale.

Numerical models

Coupled wind-wave simulations of floating wind turbines can use either engineering models or high fidelity models for the simulation of the effect of the waves and wind. During the OC5 project [157], several BEM aero-hydrodynamic engineering tools were compared to experimental data from a model floating wind turbine tested in a wind-wave tank. It was found that the simulation tools were underestimating the loads compared to the experimental data. This was attributed to the difficulty of reproduced the experimental conditions. For example, it was supposed that the instrumentation cable bundle was providing an additional stiffness to the model that was not reproduced in the numerical models.

The high fidelity models can be used for the wind, the waves, or both. The coupled effect of wind and waves for a free floating wind turbine was studied by Leroy [104] with the FVW method while Netzband et al. [135] used a panel method integrating both the effect of wind and waves in the same formulation. Leroy et al. [105] found significant differences for coupled wind-waves simulation between a BEM and a FVW aerodynamic model at high tip speed ratio ($\lambda = 7$). They also pointed out that when a controller is used, the variable blade pitch can reduce the difference in aerodynamic loading observed between different aerodynamic models.

Only limited results are available with both high fidelity models for both the wind and waves due to the high computational cost of these models. Quallen et al. [150] used a two-phase CFD tool to study the NREL 5MW at a fixed rotation speed on a spar floater. The full geometry of the wind turbine and floater was taken into account when building the mesh. The effect of both the wind on the turbine and the wave on the floater was taken into account by the two-phase CFD solver. Differences were found between the results

obtained with the two-phase CFD tool and FAST which were mainly attributed to the modeling of the hydrodynamic forces on the floater. Quallen and Xing [149] showed with both BEM and blade-resolved CFD that the tower shadow effect has a lower impact on the torque when the rotational degree of freedom of the rotor is taken into account with a controller compared to a fixed rotational speed. Tran and Kim [200] considered a steady wind with regular waves and studied a floating wind turbine on a semi-submersible floater with two-phase blade-resolved CFD for a fixed rotation speed. The surge motion predicted by the CFD simulation was 19% smaller than the one predicted by the BEM model of FAST. The CFD model predicted a lower amplitude for the thrust oscillations than the BEM and a larger amplitude of the power oscillations. Leble and Barakos [98] presented a coupling between a rigid multi-body dynamic solver, a blade-resolved CFD solver and a Smoothed Particle Hydrodynamics solver to simulated floating wind turbines. The presented coupling requires several hours of real time to simulated one second of physical time. Liu et al. [110] presented two-phase blade-resolved CFD simulations of a rigid wind turbine on a semi-submersible floater.

Full-scale floating wind turbines

Open-access data on full-scale floating wind turbines is rare due to the combination of the low number of floating wind turbines currently at sea and the fact that they are privately owned by utilities. However, Skaare et al. [177] compared numerical simulation to measurements done on the Hywind Demo floating wind turbine. Overall, good agreement between the experimental data and the simulations with the BEM aerodynamic model was found. The largest discrepancies were found for the mooring line tension in below rated wind speed. This was attributed to possible vortex induced vibrations on the mooring line due to the current and to the modeling of the wind loads because the below rated conditions correspond to a high thrust with small waves.

1.3.4 Aero-elastic dynamics

Due to the difficulty of building elastic blades for wind turbine models, stiff blades are often used in experiments. However, modern multi-megawatt rotors have elastic blades which are deformed by the aerodynamic forces. Only numerical models and full-scale intrumented wind turbines can be used to study the effect of elastic deformations on the dynamics of wind turbines. Most aero-elastic wind turbine simulation tool use the BEM aerodynamic model [94] and only a limited number of tools use more detailed aerodynamic models.

The aero-elastic behavior of wind turbines in prescribed surge motion has been studied by Liu et al. [111] for a rotor at a fixed rotation speed. They found that BEM was over-

estimating the amplitude of the thrust and power oscillation compared to their blade-resolved CFD results. This tool was later extended [109] to include hydrodynamic effects for floating wind turbine making it a coupled aero-hydro-elastic simulation tool using blade-resolved CFD aerodynamics.

The Free Vortex Wake method has been used in aero-elastic [159, 160] coupling due to its good trade-off between the computational cost and representation of the flow. It has been recently included in aero-servo-hydro-elastic simulation tools to simulate floating wind turbine such as in the hGAST [116] and MIRAS-HAWC2 [152]. Since the inclusion of FVW in these tools is recent, few results have been obtained on the dynamic of floating wind turbine.

1.3.5 Open questions

The aerodynamics of floating wind turbines need to be better understood to enable the large scale development of reliable and cost effective floating wind farms. Experiments are limited by the impossibility of obtaining at the same time Reynolds scaling for the aerodynamics and Froude scaling for the hydrodynamics. Generally, Froude scaling is chosen to properly model the hydrodynamics and the rotor geometry and operating conditions is adapted to provide the correct thrust force. However, this leads to different blade geometries, operating conditions, or mass distributions. The elastic properties of wind turbines are also difficult to reproduce at model scale, therefore experiments use stiffer models.

Numerical models can be used to study the aerodynamics of rotors in motions to better understand the modified air flow over the wind turbine. Since the BEM is initially intended for bottom-fixed wind turbines, experimental data or results from a higher fidelity model is required to validate the results obtained for floating wind turbines in motion and improve the confidence in the results obtained with the BEM method. For this, more insight in the aerodynamics of a wind turbine rotor in motion is needed. The hydrodynamics, elastic behavior and control algorithm also affect the dynamics of floating wind turbine. High-fidelity aerodynamic models are often used without a controller, at a fixed blade pitch and rotor speed, and therefore the rotational degree of freedom of the rotor is often not taken into account. It has been experimentally shown that the controller influences the interaction between aerodynamic and hydrodynamic forces. Therefore, it is of interest to perform aero-hydro-elastic simulations of floating wind turbines with higher-fidelity aerodynamic models including the behavior of the controller to study representative operating conditions. Similarly, the elasticity of the blade is rarely taken into account with higher-fidelity aerodynamic models while it becomes significant for the large turbine blades of the current and future wind turbine rotor designs.

To improve the knowledge on the aerodynamics of floating wind turbines, an increasing complexity approach is used. The response of a wind turbine to imposed motions will be

studied in the next chapter. A focus is made on three different changes of the operating conditions that might occur for a floating wind turbine: a change of blade pitch, a change of rotation speed and a translational velocity due to floater motion. A Free Vortex Wake model is then coupled to a hydro-servo-elastic tool for the simulation of floating wind turbines in Chapter 3. The computational cost of the FVW model is reduced with a wake simplification method to be able to simulate long one hour physical time cases relevant for floating wind turbines applications. It is thoroughly validated on reference test cases. This Free Vortex Wake aero-servo-hydro-elastic tool is then used to study the structural fatigue of floating wind turbines.

Chapter 2

Imposed motion dynamics

Le code open-source CACTUS de méthode vortex à lignes portantes est modifié pour simuler une éolienne en mouvements harmoniques imposés. Le code est parallélisé sur GPU pour réduire le temps de calcul. La méthode Actuator Line est implémenté dans le solveur Code_Saturne qui résout les équations de Navier-Stokes par la méthode des volumes finis. Les deux méthodes sont comparées dans le cas d'une éolienne en mouvement de cavalement harmonique imposé. Une augmentation de la puissance moyenne est prédite par les deux modèles, similaire à celle obtenue par une approche quasi-statique. Le profil de vitesse axiale en aval de l'éolienne obtenue avec les deux méthodes est proche, mis à part dans la région où se situe le vortex émit par l'extrémité de la pâle. Le phénomène de Dynamic Inflow est étudié avec la méthode Free Vortex Wake ainsi qu'un modèle hélicoïdale basé sur le modèle de rotor de Joukowsky. Trois perturbations différentes sont étudiées : un changement de l'angle d'orientation des pâles, un changement de la vitesse de rotation et un changement de la vitesse de translation du rotor. Le phénomène de Dynamic Inflow intervient pour le changement d'orientation des pâles et de vitesse de rotation tandis qu'aucun effet significatif n'apparaît dans le cas de la mise en translation du rotor.

2.1 Numerical tools for the study of wind turbines in imposed motions

High fidelity tools such as blade-resolved CFD are very computationally demanding, thus they can only be used for a small number of cases. This is not ideal for the simulation of floating wind turbines since they operate in a wide range of sea-states and wind conditions and therefore require to investigate a significant number of load cases.

A review of wind turbine aerodynamics models lead to the choice of the Free Vortex Wake and Actuator line method to study wind turbines in imposed surge motion. The main feature that is expected from these models is that they intrinsically account for phenomena for which the BEM method uses empirical correction models. The FVW and AL method include the effect of yaw misalignment, dynamic inflow, and turbulent wake state for which the BEM method requires corrections. Only the local airfoil aerodynamics are not properly captured by these lifting-line based models as they rely on airfoil polars.

The open source FVW code CACTUS was used and modified to be able to apply prescribed motions to the rotor. The AL method was implemented in the open source CFD solver *Code_Saturne*. Both tools are compared on the case of a floating wind turbine in imposed surge motion. The following section is a conference paper published at the TORQUE 2020 conference [45] that describes the numerical tools as well as their comparison on the case of a wind turbine in imposed surge.

2.2 Comparison between actuator line and free vortex wake for an imposed surge motion

The following is an article published at the TORQUE 2020 conference [45]:

Rémi Corniglion, Jeffrey Harris, Christophe Peyrard, and Matteo Capaldo. Comparison of the free vortex wake and actuator line methods to study the loads of a wind turbine in imposed surge motion. *Journal of Physics: Conference Series*, 1618:052045, September 2020. doi: 10.1088/1742-6596/1618/5/052045.

Abstract

To enable the development of floating offshore wind farms, it is important to have a clear understanding of the aerodyamic forces applied on a floating offshore wind turbine. The paper presents comparisons between a lifting line free vortex wake method and an actuator line method in the case of a wind turbine in surge with blade-resolved CFD data as a reference. Each model is compared to a quasi-steady estimation of the loads to understand the variations due to the surge movement. The near-wake flow field is investigated in order to give an insight into the flow features leading to the observed behavior. Both methods predict a higher axial velocity at the position of the rotor and one radius downstream of the rotor in surge conditions compared to the fixed case.

2.2.1 Introduction

As wind turbine development moves offshore to harness available wind resources, floating offshore wind turbines (FOWT) are a solution for deep-water sites where fixed bottom foundations are not economically feasible. Various floater designs exist, and are subject to different motions of their structure as discussed by Sebastian & Lackner [167]. From this, it is clear that the understanding of the unsteady aerodynamic loads of a floating offshore wind turbine in surge motion is an important topic for the energy production estimation of floating wind farms.

Several aerodynamic models exist for studying floating wind turbines, each with their strengths and weaknesses. The blade element momentum (BEM) method (see Burton et al. [35]) models the induction of the rotor while wake and dynamic effects are reproduced through the use of empirical or physics-based correction models. Those models have difficulties to reproduce the loads of a moving rotor, as reported by the LIFES50+ project [143] and by Bayati et al. ([21],[22]) because the correction models were initially developed for fixed bottom wind turbines. On the opposite side of the complexity scale, blade-resolved CFD simulations (*e.g.*, Lienard et al. [106]) represent the geometry of the wind turbine directly and model the flow turbulence. These models are computationally costly.

Thus, only a limited number of operating conditions can be explored with them. Lifting line models are a family of intermediate fidelity models that represent the blades as lifting lines and reproduce the efforts through the use of airfoil polars and dynamic stall models. The lifting line free vortex wake model (FVW) uses a Lagrangian vortex formulation to model the flow around the wind turbine while the actuator line (AL) method solves the Navier-Stokes equations with turbulence models. Actuator line models are superior than FVW to compute wind turbine wakes as they include turbulence and viscosity effects. However, the actuator line formulation does not reproduce well the loading at the tip of the blades when a correction model is not used, as explained by Martínez-Tossas & Meneveau [120].

The loads on floating wind turbines have been investigated with the FVW method by Wen et al. ([209, 210]). They studied the NREL 5MW reference wind turbine [90] which is the wind turbine which will be used in this paper. They have shown that the mean power level is increased with higher reduced frequency of the imposed movement for a fixed tip speed ratio. This was found both with a FVW [209] and a CFD code [106] for high tip speed ratios. For a fixed reduced frequency of the surge motion, Wen et al. [209] have shown with FVW simulations that the mean power level is increased when the tip speed ratio increases. In both cases, the NREL 5MW was studied with a fixed rotational speed and a fixed zero blade pitch angle. The wake of a floating wind turbine is not yet well understood. Sebastian & Lackner [168] have shown that most of the influence of the wake on the rotor is due to the near-wake. Some insights on the near-wake flow field were given by Lienard et al. [106] with blade-resolved CFD computations.

This paper aims at assessing the ability of a lifting line free vortex wake model and an actuator line model to evaluate the loads and near-wake flow field of a surging wind turbine. The relative variations of the thrust and power obtained with the FVW, AL, blade-resolved CFD and a quasi-steady estimation are studied. Comparisons of the near-wake flow field for different turbine positions during a surge period are done in order to explain the observed load behavior.

2.2.2 Numerical Methods

2.2.2.1 Free vortex wake method: CACTUS

To study the effects of imposed motions on the loads of a floating wind turbine, the FVW code CACTUS [132] from the Sandia National Laboratory was used. It has already been used for similar purposes by Leroy et al. [105]. The blades are represented as lifting lines located at the quarter chord of the airfoils. The lifting line is divided into several elements for which the local angle of attack and relative velocity is evaluated at half the spanwise length. Vortex line elements are shed into the wake to account for temporal and spanwise

variation of the lift force along the blades. The code has been improved by implementing functions to impose harmonic translations and rotations to the rotor. For efficiency, the computation of the self induced velocity of the wake has been parallelized on Nvidia GPUs using the CUDA language. The wake self-induced velocity is computed at every time step through equations 2.1 and 3.26.

$$\frac{d\mathbf{x_p}(t)}{dt} = \mathbf{u}(\mathbf{x_p}, t) = \sum_n \mathbf{u_{\Gamma,n}}(\mathbf{x_p}, t) + \mathbf{U}_\infty(\mathbf{x_p}, t) \tag{2.1}$$

$$\mathbf{u_{\Gamma,n}}\left(\mathbf{x_p}\right) = \frac{\Gamma_n}{4\pi} \frac{\left(|\mathbf{r_1}| + |\mathbf{r_2}|\right)\left(\mathbf{r_1} \times \mathbf{r_2}\right)}{|\mathbf{r_1}||\mathbf{r_2}|\left(|\mathbf{r_1}||\mathbf{r_2}| + \mathbf{r_1} \cdot \mathbf{r_2}\right) + \epsilon^2} \tag{2.2}$$

where $\mathbf{r_1}$ and $\mathbf{r_2}$ are vectors pointing to both ends of a vortex line element from a point at position $\mathbf{x_p}$ and ϵ is a desingularisation core radius taken equal to 0.2 times the local chord of the blade when the vortex element is shed into the wake. $\mathbf{U}_\infty$ is the undisturbed inflow velocity and $\mathbf{u_{\Gamma,n}}$ is the velocity induced by the n^{th} vortex line element of circulation Γ_n.

To enable comparisons between the flow field of the FVW and actuator line methods, the velocity field around the wind turbine is computed from the vortex wake of the FVW computation on a Cartesian 3D mesh using the Biot-Savard law. The same desingularisation core sizes as the one used during the computation of the free vortex wake are used. This operation which is run as a postprocessing was also parallelized on a GPU.

2.2.2.2 Actuator line method: Code_Saturne

The actuator line method of Sørensen and Shen [183] has been implemented in the finite volume Navier-Stokes solver *Code_Saturne* [12]. The Reynolds stress SSG [186] turbulence model is used, as second-order closure models are more suitable than first-order closure models to solve rotating flows [47] such as tip vortices, which are the main flow features of wind turbine flows. A Gaussian smearing g is applied with a Gaussian radius $\epsilon = 2\Delta_{grid}$ as recommanded by Troldborg [202]. The velocity sampling of the flow field to compute the sectional efforts along the blade with a lifting line approach is done with the integral velocity sampling method described both by Merabet & Laurendreau [124] and Churchfield et al. [42]. The Gaussian smearing g_i for the ith actuator point is:

$$g_i(x, y, z) = \frac{1}{\epsilon^3 \pi^{3/2}} exp\left(-\frac{(x - x_i)^2 + (x - y_i)^2 + (z - z_i)^2}{\epsilon^2}\right) \tag{2.3}$$

where (x_i, y_i, z_i) are the coordinates of the coordinates of the ith actuator point. The integral average velocity at this actuator point can then be computed as :

$$\mathbf{u_i} = \sum_{n=1}^{N_{cells}} \Omega_n g_i(x_n, y_n, z_n)\mathbf{u_n} \tag{2.4}$$

where $\mathbf{u_n}$ is the velocity at the center of cell n, (x_n, y_n, z_n) are its coordinates, Ω_n is its volume and N_{cells} is the total number of cells in the domain. The tip loss model of Prandtl modified by Glauert is used [62] to prevent an unphysical tip behavior due to the Gaussian smearing, which is reducing the velocity induction and therefore increasing the local effective angle of attack near the tip of the blade [120].

Two meshes were used for the actuator line computations. The first one has 23 million cells. A finer mesh of 44 million cells was used to check if the results were independent of the mesh while keeping the smoothing size constant. Minimal differences were found between the results obtained with the two meshes. Therefore, results obtained with the 23 million cells mesh are presented in the following. The topology of this mesh can be seen on Fig. 2.1. It has size $20R$ in the axial direction and $16R$ in both the horizontal and vertical directions with R the radius of the wind turbine. The mesh cell size is of $R/50$ at the position of the rotor and in the near-wake until the axial position $x = 10R$. The mesh has larger cells away from the rotor. The AL uses a time step of a duration that corresponds to a 1° rotor motion while the FVW uses larger time steps equivalent to a 6° rotor motion.

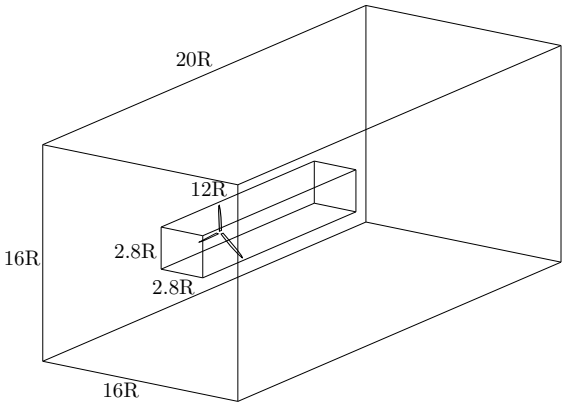

Figure 2.1: 23 million cell mesh used for the actuator line simulations, with an inner refined wake region comprising 840 × 140 × 140 cells.

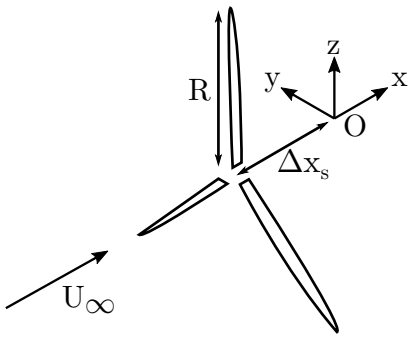

Figure 2.2: Definitions of the axes used to study the wind turbine in surge

2.2.2.3 Test conditions

The same polars and geometry definitions of the wind turbines are used in both the FVW and the actuator line simulations. Thus, the differences between the two models are due to the underlying physical models and not the simulation inputs. The tower, hub and nacelle are not modelled in either model. No dynamic stall model were used in both the FVW and AL models to focus on wake dynamic effects rather than local airfoil aerodynamics. For 16

rotations of the NREL 5 MW wind turbine at rated conditions, the computational times are reported in Table 2.1. The actuator line simulations have a much higher computational cost than the FVW simulations.

Table 2.1: Computational time for 16 rotations of the NREL 5 MW wind turbine. The GPU used is a NVidia V100 GPU and the processors used are Intel Xeon Gold 6140 (total of 630 cores).

Free Vortex Wake	Actuator Line
30 min GPU time	7979 CPU hours

The studied case is the surging wind turbine used by Lienard et al. [106]. It is the NREL 5MW reference wind turbine with included cone and tilt angle running at rated conditions: $U_\infty = 11.4$ m/s, tip speed ratio $\lambda = \omega R/U_\infty = 7$ with ω the rotation speed, for 16 rotations. The surge frequency is half the rotational frequency of the rotor. One of the blades is at the top position at the beginning of a surge period. The amplitudes of the surge movements tested are $\Delta x_s = 8$m and $\Delta x_s = 16$m. The inflow wind is not turbulent. The axes used for the study are defined of Fig. 2.2.

2.2.3 Results

2.2.3.1 Power and thrust variations

When the FVW approach is used, a surge movement of the wind turbine is equivalent to a fixed turbine in an oscillating wind field in the reference frame of the wind turbine. If the oscillation of the wind speed is considered quasi-steady, the thrust and power of the wind turbine for surge induced wind can be estimated from the static loads around the conditions of interest. The surge induced wind is expressed $u_{dyn}(t) = \omega_s \Delta x_s \cos(\omega_s t)$ for an harmonic surge motion of amplitude Δx_s, circular frequency ω_s and reduced frequency $k_s = \omega_s \Delta x_s / U_\infty$.

The power and thrust corresponding to the harmonic total velocity can be interpolated from a thrust and power curve computed around the current operational point at a constant rotation speed. The mean value of the thrust and power in quasi-steady behavior is then computed as the integral over a period of surge motion of the interpolated quantities. The results is the quasi-steady behavior *i.e.* the behavior that would happen if no dynamic or viscous effects are present in the blades or wake aerodynamics. This can be taken as a first approximation of the expected behavior.

Figure 2.3 shows the static power and thrust computed with CACTUS at constant rotation speed $\Omega = 12.1$ rpm around the rated conditions for the NREL 5MW wind turbine. P^* and T^* are the power and thrust normalized by the available power and thrust in the wind

at the rated conditions. Figure 2.4 shows an example of the temporal relative variations of the power and thrust over a period of the surge motion extrapolated from the static power and thrust curve around the rated conditions. For this quasi-steady estimation, Figure 2.4 shows that the mean thrust will be lower than the static case while the mean power will be higher. This is because the static power curve for constant rotation speed shown in Figure 2.3 is slightly convex around the rated condition $U_\infty = 11.4$ m/s, while the thrust curve is concave.

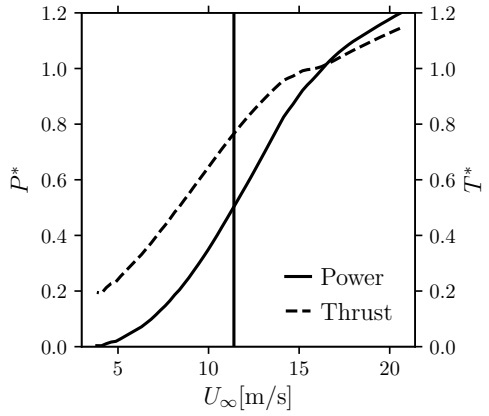

Figure 2.3: Static power and thrust curve for the NREL 5MW wind turbine at constant rated rotation speed normalized by the rated conditions. The vertical line shows the rated conditions.

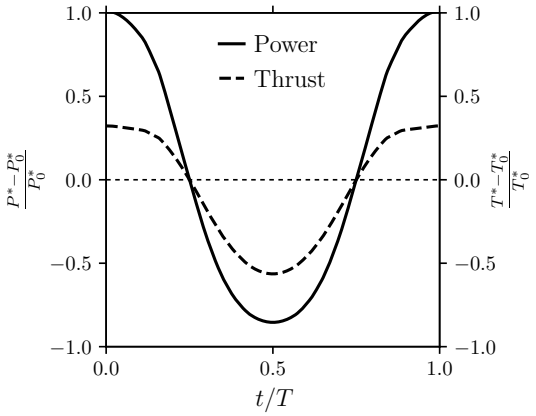

Figure 2.4: Quasi-steady variations over a period of surge of the power and thrust compared to the rated conditions for $\lambda = 7.0$ and $k_s = 0.44$. The index 0 stands for the rated conditions.

Figures 2.5 and 2.6 show the quasi-steady behavior computed with the method presented above as well as dynamic results from FVW (CACTUS) and AL (*Code_Saturne*) compared to blade resolved CFD from Lienard et al. [106] (*elsA*). The relative variation of the mean thrust and power in surging cases compared to the fixed bottom thrust and power are represented for each code. This is done to highlight specifically the changes induced by the surge movement.

The quasi-steady behavior does not cover the full range of surge reduced frequency because for low wind speeds, lower than 3.8 m/s, the FVW simulations used to compute the static power and thrust curves are unable to converge because the tip speed ratio is too high and the rotor blocks the incoming flow. This is not a problem in the dynamic case because the low total wind speed is only experienced by the rotor for a fraction of the surge motion.

The quasi-steady behavior is predicting an increase of the mean power and a decrease of the mean thrust when the reduced frequency is increased. This quasi-steady behavior is related to the local shape of the static power and thrust curve around the rated conditions, respectfully convex and concave. The dynamic FVW results, taking into account the temporal movements of the rotor, show variations close the quasi-steady estimation with

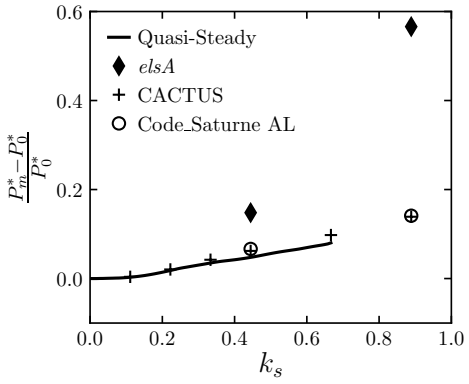

Figure 2.5: Relative variation of the mean power compared to the steady case in rated conditions. *elsA* data from Lienard et al. [106].

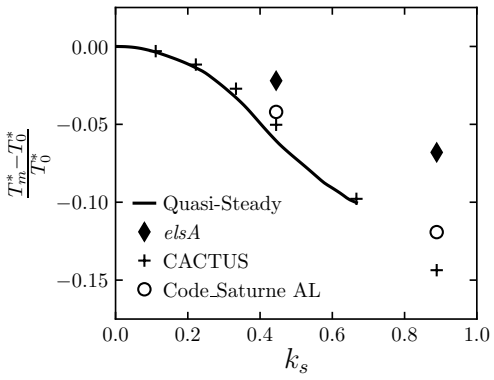

Figure 2.6: Relative variation of the mean thrust compared to the steady case in rated conditions. *elsA* data from Lienard et al. [106].

a difference growing with the reduced frequency for both the power and thrust. The mean power variation of the AL is similar to the FVW, while it predicts a smaller decrease of the mean thrust than the FVW. The blade resolved CFD results of Lienard et al. [106] show a bigger increase of the mean power and a smaller decrease of the mean thrust than the three other models. The difference between the blade resolved CFD and the other models grows with the reduced frequency.

The larger difference between the FVW and AL to the CFD results at high surge reduced frequency could be explained by the fact that the angle of attack is reaching higher values in the stall region and therefore the local loads on the blade become more difficult to predict with the lifting line approach that both the FVW and AL use. Here, no dynamic stall model is used, for both methods to focus on the wake induced dynamic effects. However, Barnaud et al. [18] have shown that even with a high fidelity WMLES, the behavior of an airfoil near stall is difficult to predict.

For reduced frequencies lower than $k_s = 0.22$, the FVW results are in good agreement with the quasi-steady estimation of the relative variations of the mean power and thrust. For small reduced frequencies, unsteady effects appear to be minimal.

2.2.3.2 Near Wake Flow Field

The induced velocity field of an actuator disc in surge motion has been investigated by de Vaal et al. [48]. They have shown that for larger values of the reduced frequency $k_s = \omega_s \Delta x / U_\infty$, the mean value of the induced velocity at the rotor plane is reduced compared to the static case. This is an interesting effect and it might be related to a faster wake breakdown due to tip vortex interactions, so when analyzing the thrust

and power of a surging turbine one has to take into account the combined effect of the oscillating apparent wind speed due to the surge motion as well as the additional wind speed at the rotor plane due to the lower induction of the rotor. The reduced induced velocity at the rotor plane means a higher axial velocity at the rotor disc and thus could increase the thrust. This could explain the higher mean thrust computed in the dynamic case by the FVW and the AL, compared to the quasi-steady estimation. Both methods take into account the wake and therefore any faster wake breakdown associated to the surge motion.

To verify this, the axial velocity along a line has been extracted from both the FVW and actuator line results, for the fixed case and for the surging case, with an amplitude of $\Delta x_s = 8$m to avoid any influence of dynamic stall on the comparisons. These velocity profiles are plotted in Fig. 2.7 for four different positions of the turbine during the last simulated surge period. Recall that the surge frequency is half the rotational frequency of the rotor and therefore the rotor is always at the same position during a surge period. The velocity profiles are extracted along the axial line for $y/R = 0.0$ and $z/R = 0.8$. The blade is therefore passing over the extraction line in Fig. 2.7a and 2.7c.

The axial velocity profiles of FVW and AL are very similar for axial positions between $x/R = -0.5$ and $x/R = 0.5$. The AL results predict consistently slightly higher values of the axial velocity than the FVW results. Further into the wake, stronger differences between the FVW and AL results can be seen, which can be related to the absence turbulence modeling in the FVW.

The axial velocity at the position of the blade is lower in the surging case than in the fixed case when the rotor is moving downwind (Fig. 2.7a). The opposite behavior is observed when the rotor is moving upwind (Fig. 2.7c). Figures 2.7b and 2.7d show the axial velocity in the rotor plane away from the blade. They show the deceleration of the incoming flow due to the blockage effect of the wind turbine. The axial velocity in the rotor plane away from the blade is higher in the surging case than in the fixed case. This velocity difference can be seen most clearly at the position of the rotor (noted as the vertical line in the figure). This behavior is observed both for the AL and FVW methods. It confirms the results of de Vaal et al. [48] which were obtained with an actuator disk method. It explains why the FVW, the AL and the blade resolved CFD predict a higher mean thrust than the quasi-steady estimation: the axial velocity in the rotor plane is higher than in the fixed case and is not taken into account in the quasi-steady estimation.

Figure 2.8 shows further comparisons of the near-wake axial velocity obtained with both models at position $x/R = 1$ in the wake. In Fig. 2.8a and 2.8c, the FVW results show a more rapid velocity change between the inner part of the wake ($|z/R| < 1$) and the outer part of the wake ($|z/R| > 1$). It is a sign of the difficulty to properly model tip vortices with the actuator line method which has been reported by several authors ([120],[85]).

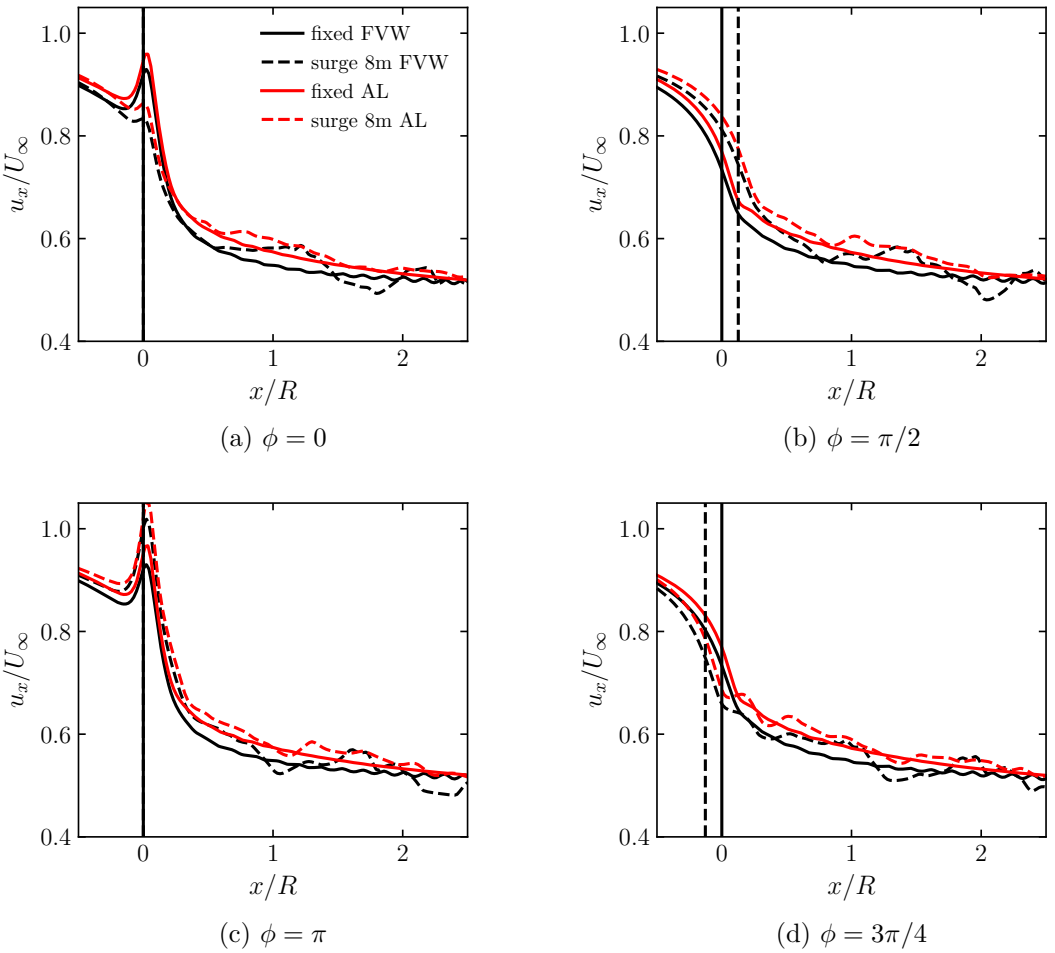

(a) $\phi = 0$ (b) $\phi = \pi/2$

(c) $\phi = \pi$ (d) $\phi = 3\pi/4$

Figure 2.7: Axial velocity profiles for different positions during a surge period. ϕ is the phase of the surge movement. The vertical lines represent the position of the wind turbine in the fixed (solid) and surging (dashed) cases. The extraction line coordinates are $x/R \in [-0.5, 2.5], y/R = 0, z/R = 0.8$ where the origin is at the center of the rotor hub in the fixed case.

Figure 2.8 shows that both the FVW and AL predict a higher axial velocity in the near-wake when the rotor is surging. This means that a surging rotor has a lower velocity deficit than a fixed rotor in the near-wake. If this behavior is also verified in the far wake, it would be valuable for the power production of other turbine in the same wind farm. Thus, studies of the velocities in the far wake should follow the present work in order to know the velocity deficit in the far wake of a surging wind turbine.

Comparisons of the axial velocity flow fields in Fig. 2.9 show that FVW and AL results are similar for positions near the rotor (x/R close to 0). Further downwind in the wake, the differences are larger while some similarities can still be found. The axial velocity is stronger in the hub region with the actuator line.

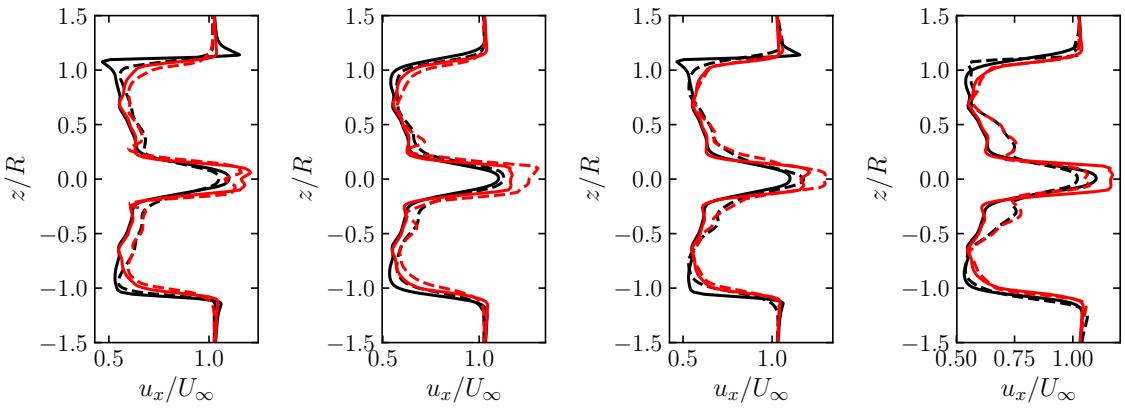

(a) $\phi = 0, x = R$ (b) $\phi = \pi/2, x = R$ (c) $\phi = \pi, x = R$ (d) $\phi = 3\pi/4, x = R$

Figure 2.8: Axial velocity profiles along a vertical line at $x/R = 1$ and $y/R = 0$

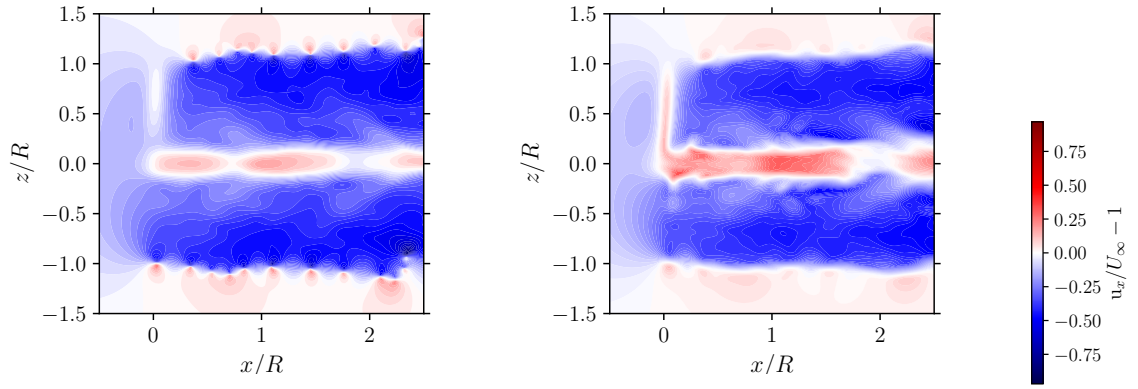

(a) Free Vortex Wake (b) Actuator Line

Figure 2.9: Axial velocity fields when the wind turbine is surging upwind ($\phi = \pi$) in the plane $y/R = 0$.

2.2.4 Conclusion

For surge movements with a high reduced frequency, the quasi-steady estimation predicts a lower mean thrust than the actuator line, free vortex wake and blade resolved CFD results. For the mean power, the opposite behavior is observed. The lifting line FVW and actuator line approaches have a limited ability to predict the aerodynamic loads of a floating wind turbine in large surge movements with dynamic stall, because the local flow around the blade profile is not resolved. Analyses of the near-wake velocity field have shown that the axial velocity at the position of the rotor is higher when the wind turbine is surging. This explains the higher mean thrust obtained with the FVW and AL compared to the quasi-steady estimation. A strong agreement between the axial velocities at the position of the rotor is found between the FVW and AL. At one radius behind the

rotor, both the free vortex wake and actuator line results show that the surge movement is increasing the axial velocity in the wake. This could be of great interest for the wind farm layout of floating offshore wind turbines.

2.3 The aerodynamics of a blade pitch, rotor speed, and surge step for a wind turbine regarding dynamic inflow

The following is an article published in Wind Energy journal [46]:

Rémi Corniglion, Jeffrey C. Harris, and Christophe Peyrard. The aerodynamics of a blade pitch, rotor speed, and surge step for a wind turbine regarding dynamic inflow. *Wind Energy*, 2022. doi: 10.1002/we.2702.

Abstract

Floater motions introduce unsteadiness in the aerodynamics of floating offshore wind turbines. The aerodynamics of a wind turbine after three perturbations are studied: a blade pitch step; a rotor speed step for which dynamic inflow is expected; and a surge velocity step. The Free Vortex Wake method and an analytical helical vortex model based on the Joukowsky rotor model are used to study the dynamic behavior of the induced velocity at the blades. As expected, the dynamic inflow effect is clear for the blade pitch and rotor speed changes, but for a surge velocity step, the models show that very little dynamic inflow effect takes place because the velocity induced by the vortex helix is not significantly modified: the tip vortex helix circulation change is partially compensated by the geometry change of the helix. For the rate of change, the velocities induced on the rotor by the vortex helix for the pitch and rotor speed changes show a rapid adjustment at the blade tip, with a slower change throughout the rest of the blade and at the center of the rotor. The convection velocity of the tip vortices is shown to be the main variable of the temporal evolution of the dynamic inflow effect.

2.3.1 Introduction

The development of floating offshore wind turbines (FOWTs) raises questions on how a wind turbine reacts to floater motions that make it operate in unsteady conditions [167]. For instance, surge motion changes the inflow of the wind turbine by changing the relative wind speed of the flow affecting the airfoil along the blade. The motions of the floater interact with the wind turbine controller [177] and affect the blade pitch and rotor speed. Knowledge of the dynamic response of a wind turbine to changes of blade pitch, rotor speed, and in surge movement is therefore important for the proper design of floating wind turbine structures and their controllers.

The dynamic change of rotor thrust in response to a blade pitch event is a phenomenon called the dynamic inflow effect that was first studied for helicopter rotors. Carpenter and Fridovich [38] measured this phenomenon for a helicopter rotor and modeled it with an apparent mass model. Another model was proposed by Pitt and Peters [147] to better

represent helicopters in forward flight. More recently, the dynamic inflow effect for wind turbines was studied in the JOULE 1 project [180]. Engineering models were compared to measurements done on the Tjæreborg wind turbine [142], such as the rotor torque and blade bending moment. This provides a validation database for the dynamic inflow effect, but the behavior for each radial station along the blade is unavailable as only global loads were measured, so only the integrated effect of the dynamic inflow on the rotor loads can be validated with this database. In the scope of the JOULE 1 project, the response of a model rotor to an inflow wind step was also investigated. Little to no dynamic effect was found, but the wind speed change was slower than the expected time scale of the dynamic inflow phenomenon. More recently, a surging oscillating wind turbine was tested in a wind tunnel[115], and no significant delay between the loads and the surge movement velocity was found both experimentally and numerically for small reduced frequency of the surge movement.

The Blade Element Momentum Theory (BEMT) is often used for wind turbine design, combining blade element theory, which divides a turbine into many blade segments with lift and drag coefficients under a 2D assumption for each section, and momentum theory, which computes the global changes in flow due to a presence of a turbine. BEMT is a quasi-steady model which needs an additional correction to take into account the dynamic inflow effect. A recent summary was given by Branlard [32]. Some models were created during the JOULE 1 project [180]. Newer dynamic inflow models have been recently developed such as the two dynamic inflow model of Yu et al. [224] and validated against a Computational Fluid Dynamics (CFD) actuator disc model or the model presented by Madsen et al. [113].

A more complex approach is the use of a Free Vortex Wake (FVW) model, which also divides each blade into segments, but actually solves for the three-dimensional flow of the wake due to a turbine, under the assumptions of incompressible and inviscid flow, with vorticity introduced along the length of the blades, and advected with the flow. Numerous open source tools have been developed, such as QBlade [118] and CACTUS [132]. In any case, Pirrung and Madsen [146] pinpointed the difficulty of extracting time constants from force measurements obtained with experiments or CFD, as the force overshoot hides the initial variation of the induction factors. They however noted the advantages of using FVW models to study dynamic inflow as it provides access to the induced velocities along the blade, as opposed to blade resolved CFD where these values are more complicated to obtain. The surge motion of a wind turbine on a floater as an oscillating motion has been previously studied with an actuator disk method by de Vaal et al. [48] and with the FVW method by Leroy et al. [105].

An experimental analysis of the dynamic inflow effect was done in the NREL Phase VI project [72, 176]. Measurements were done at five different radial positions along the blade, giving some insight into the radial behavior of the dynamic inflow. These results were

analyzed and compared to numerical and analytical models by Schepers [164], who found that the time constants of the dynamic inflow extracted both from the experiment and a FVW model do not experience strong variation over the blade span, while an analytical model, a semi-infinite cylindrical vortex sheet, showed a strong reduction of the time constant toward the tip of the blade. The time constants were based on force measurements which hide the initial transient of the induction factor and its radial variation as pinpointed by Pirrung and Madsen [146]. Another experimental approach is to study porous disks instead of bladed turbines. Yu et al. [222] studied the wake of a porous disc subject to dynamic changes of its porosity. They found that the transient time between the two steady states depends on the convection velocity of the wake and the turbulence intensity in the wake. Further study in the experiments done by Berger and Kühn [24] in a wind tunnel on a model wind turbine showed that there is a weak dependence of the axial induction dynamics on the radial position. The velocity variations are slightly faster closer to the tip of the blade. More insight into the radial behavior of the dynamic inflow effect was given by Berger et al. [25], who measured the axial induced velocity between two blades in the rotor plane. Similar temporal dynamics were found for a position near the edge of the rotor disc and around half the blade span.

One of the few large experimental campaigns to study rotor rotation speed steps was the MEXICO tests [165] (and the follow-up work), whereas most other experimental data for dynamic inflow for wind turbines is related to load variations with blade pitch instead. A dynamic behavior was observed only for the smallest wind tunnel wind speed, thus the largest tip speed ratio tested, suggesting that the dynamic inflow effect may not be particularly important for rotor speed changes. Understanding the importance of the dynamic inflow effect under different conditions is therefore of interest, particularly for ensuring that engineering models are able to capture the relevant physics, which by necessity use simplified semi-empirical relations. All the dynamic inflow models to date are based on azimuthally invariant approaches, be it vortex rings [141, 223, 224], vortex cylinders [179, 224] or an actuator disk [113]. Here, the dynamic inflow phenomenon will be studied, taking into account each blade and thus without the hypothesis of azimuthal invariance.

In the present paper, we describe the aerodynamic behavior of a rotor subject to three different changes of its operating conditions: a blade pitch change, a rotor speed change, and a surge movement. The surge motion is simplified to enable to study its effects. Starting from a fixed position, the rotor is assumed to translate axially, reaching a constant translation velocity. The translation is either in the same direction as the inflow wind or opposite to it, leading to a reduced or increased inflow velocity at the rotor due to the additional velocity related to the surge movement. The lifting line free vortex wake (FVW) code CACTUS from Sandia Lab [132] is used as it captures the wake dynamics and gives access to the axial induced velocity of the rotor. In addition, an analytical helical vortex

model based on the Joukowsky [91] rotor model is proposed to give more insight into the radial and global behavior of each of the three cases.

2.3.2 Dynamics study with Free Vortex Wake model

2.3.2.1 FVW setup and validation

The FVW code CACTUS was used to compute the time-varying loads and wake dynamics of the horiziontal wind turbines considered in this section. A lattice of vortex line elements is used to represent the turbine wake, where vorticity is given by the airfoil cross-section and the local flow conditions. For simplicity, no dynamic stall model is applied in this paper. Full details of the code can be found in Murray et al. [132]. For computational efficiency, the GPU-parallelization of CACTUS of Corniglion et al. [45] is used. For all of the cases presented here, the FVW uses a desingularization core radius of 10% of the local chord. Each blade is discretized in 30 elements with a cosine distribution, with more elements near the root and the tip of the blades. The time step is such that the blades rotate 10° per time step.

First, to evaluate the ability of the FVW to predict the near wake flow, and in particular the tip vortex position, the method is compared to the phase-locked PIV measurements of the MEXICO experiment [29]. The tip vortex positions are extracted by locating the local maxima out-of-plane vorticity on a rotating mesh after 30 rotations. The positions of the tip vortices predicted by the FVW for a range of tip speed ratios are shown in Fig. 2.10. The FVW shows a good agreement with the experiment for the position of the first vortex in the near wake in all cases. The FVW with vortex lines is unable to correctly predict the vortex breakdown after $x/R = 0.6$ at $\lambda = 10$, but the FVW predicts well the tip vortex positions for $\lambda = 6.7$ and $\lambda = 4.2$. In considering the range of tip speed ratio simulated with the FVW, we also see that the pitch of the tip vortex helix is reduced when the tip speed ratio increases. This is in agreement with the measurements of Haans [69] for various tip speed ratios and the comparison of measurements and FVW simulations of Whale et al. [213].

2.3.2.2 Thrust coefficient increase

To study thrust coefficient increases and decreases, an NREL 5MW reference wind turbine [90] geometry is used. The airfoil data provided in the definition document[90] of the wind turbine is used. The initial operating conditions are the rated conditions of the rotor of diameter 126 m, rotor speed $\omega_r = 1.267\ rad.s^{-1}$ ($\Omega = 12.1$ rpm), inflow wind $U_\infty = 11.4\ m.s^{-1}$, and therefore with a tip speed ratio of $\lambda = \omega_r R/U_\infty = 7.0$. The thrust coefficient is redefined to take into account the additional inflow wind speed at the rotor

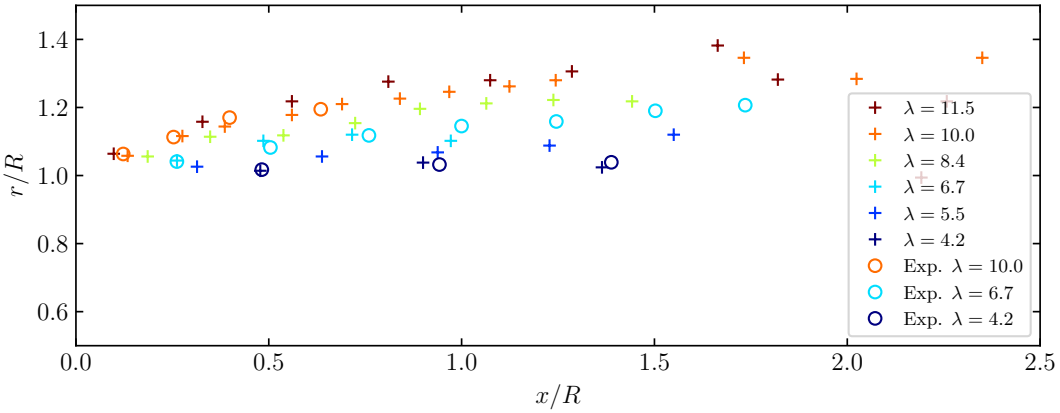

Figure 2.10: Comparison of tip vortex axial and radial positions for different tip speed ratios for the MEXICO wind turbine for experimental results[29] and FVW results of CACTUS.

Table 2.2: Thrust coefficient increase conditions starting from rated conditions, $\omega_r = 1.267$ $rad.s^{-1}$, $U_\infty = 11.4$ $m.s^{-1}$, $\beta = 0$ used to produce similar thrust coefficient variations for an NREL 5MW reference wind turbine.

	Blade pitch	Rotor Speed	Surge
Perturbation	$\Delta\beta = -1.75°$	$\Delta\omega_r = 0.181$ $rad.s^{-1}$	$U_s = -1.42$ $m.s^{-1}$

due to possible surge motion. We write this redefined thrust coefficient C_T^*:

$$C_T^*(t) = \frac{T(t)}{\frac{1}{2}\rho\pi R^2[U_\infty + U_s(t)]^2} \tag{2.5}$$

where T is the thrust force acting on the rotor, ρ is the air density, R is the radius of the rotor, U_∞ is the inflow wind speed and U_s is the additional inflow velocity due to the surge motion in the surge step case. The perturbations are applied after 20 rotor revolutions to ensure a converged result. After 20 rotations, the wake has reached $x/R = 17$. The time step is such that the blades rotate 6° per time step.

To enable a comparison of the aerodynamics due to the three perturbations, the amplitude of each perturbation is chosen such that it leads to the same final change of the thrust coefficient. The surge motion and rotor speed step are chosen such that the tip speed ratio becomes $\lambda = (\omega_r + \Delta\omega_r)R/(U_\infty + U_s) = 8.0$ after the ramp. The blade pitch step amplitude $\Delta\beta$ is interpolated from preliminary fixed blade pitch calculations to produce the same thrust coefficient variation. In the blade pitch case, the tip speed ratio is not modified by the perturbation. The three different case setups are summarized in Table 2.2.

The perturbation, either a blade pitch change, a rotor speed change, or a surge movement, is applied as a short-duration ramp to avoid airfoil-scale dynamic effects, or interaction

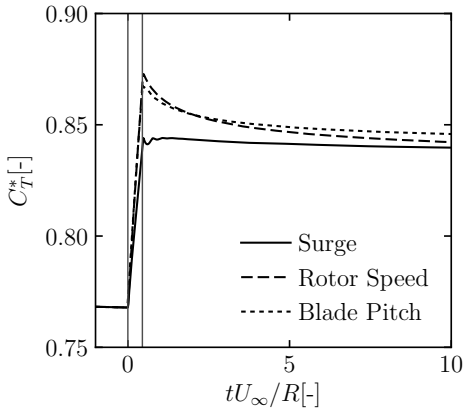

Figure 2.11: Thrust coefficient after a blade pitch, surge, and rotor speed ramp under the conditions listed in Table 2.2 as computed by the FVW model CACTUS for an NREL 5MW reference turbine. The vertical lines delimit the start and end of the applied ramps of duration $0.47R/U_\infty$.

between unsteady airfoil dynamics and wake dynamics. This is possible by the fact that the two phenomenon have different time scales: the local aerodynamics one is proportional to the local airfoil chord divided by the local relative velocity while the wake dynamics one is proportional to the rotor radius divided by the free wind speed. The duration of the ramp is $0.47R/U_\infty$ similar to the pitch duration in the experiment by Berger et al.[25].

Fig. 2.11 shows the variation of the thrust coefficient after the three perturbations leading to the same final thrust coefficient. Both the rotor speed and blade pitch change induce a dynamic behavior of the thrust coefficient. The ramp increases the thrust coefficient and it then decays towards its static value once the ramp is finished, but no significant dynamic effects can be seen in the surge case—the thrust coefficient changes during the ramp and is then stable at its static value. The presence of the dynamic inflow phenomenon for the blade pitch and rotor speed cases is expected from prior experiments [165], but to the authors' knowledge, the surging case with a fast ramp has never been studied experimentally. Only slow gusts were done in the JOULE 1 project [180] due to the experimental difficulty of producing a rapid change of inflow wind speed or a fast movement of the wind turbine model. The FVW method also shows more insight about the dynamic inflow by studying the flow around the wind turbine.

The tip vortices are the dominant features of the wind turbine flow. Fig. 2.12 shows the evolution in time of the tip vortex positions in the plane defined by the blade and the axial direction. Their positions are extracted from the FVW simulation by extracting the flow on a Cartesian rotating mesh and locating each local maximum of the out-of-plane vorticity. The tip vortices get closer to the rotor for the surge and rotor speed changes while their position is not significantly modified by the blade pitch change (Fig. 2.12b).

Table 2.3: Thrust coefficient decrease conditions starting from $\lambda = 9$, $\omega_r = 1.267\ rad.s^{-1}$, $U_\infty = 8.87\ m.s^{-1}$, $\beta = 0$.

	Blade pitch	Rotor Speed	Surge
Perturbation	$\Delta\beta = 1.73°$	$\Delta\omega_r = -0.281\ rad.s^{-1}$	$U_s = 2.53\ m.s^{-1}$

The radial positions of the vortices are also modified (Fig. 2.12c) but to a lesser extent than in the axial direction.

2.3.2.3 Thrust coefficient decrease

The three perturbations were also compared for a step-down of the redefined thrust coefficient C_T^*. The amplitude of the thrust coefficient step is chosen larger than for the step up. The starting condition is a rotor speed of $\Omega = 12.1$ rpm and an inflow wind of $U_\infty = 8.87\ m.s^{-1}$, resulting in a tip speed ratio of $\lambda = 9.0$. The surge motion and rotor speed step are chosen such that the tip speed ratio becomes $\lambda = 7.0$ after the ramp. The blade pitch step was chosen accordingly to produce the same thrust coefficient change from prior steady simulations for various blade pitches. The three perturbations applied are summarized in Table 2.3. The numerical parameters of the FVW model are the same than for the previous case except that the ramps are applied after 35 revolutions of the rotor for which the wake has reached $x/R = 24$ in order to ensure convergence of the wake at $\lambda = 9.0$.

The variation of the redefined thrust coefficient C_T^* after the ramp events is shown in Fig. 2.13. Similar to the step up of C_T^*, the rotor speed and blade pitch ramps lead to a dynamic change of C_T^*. In both cases, the ramp decreases the thrust coefficient to a lower value than the static level corresponding to the new operating conditions. Once the ramp is over, the flow adapts to the new operating conditions and the thrust coefficient increases to reach the static level corresponding to the new operating conditions. The redefined thrust coefficient shows no clear dynamic behavior in the imposed surge case once the ramp is over, as for the step-up of the thrust coefficient. The redefined thrust coefficient has reached the static value corresponding to the new operating conditions at the end of the ramp.

The axial and radial positions of tip vortices in the plane defined by a blade and the rotor axis is extracted in the same way as for the step-up of thrust coefficient. These positions are shown in Fig. 2.14. The surge and rotational speed ramps lead to a significant increase of the axial positions of the tip vortices. The blade pitch ramp exhibits very little change of the axial positions of the tip vortices in the near wake. The three cases show a reduction of the radial positions of the tip vortices as expected for a reduction of the thrust coefficient. For the blade pitch and rotor speed cases, some of the vortices move outwards before

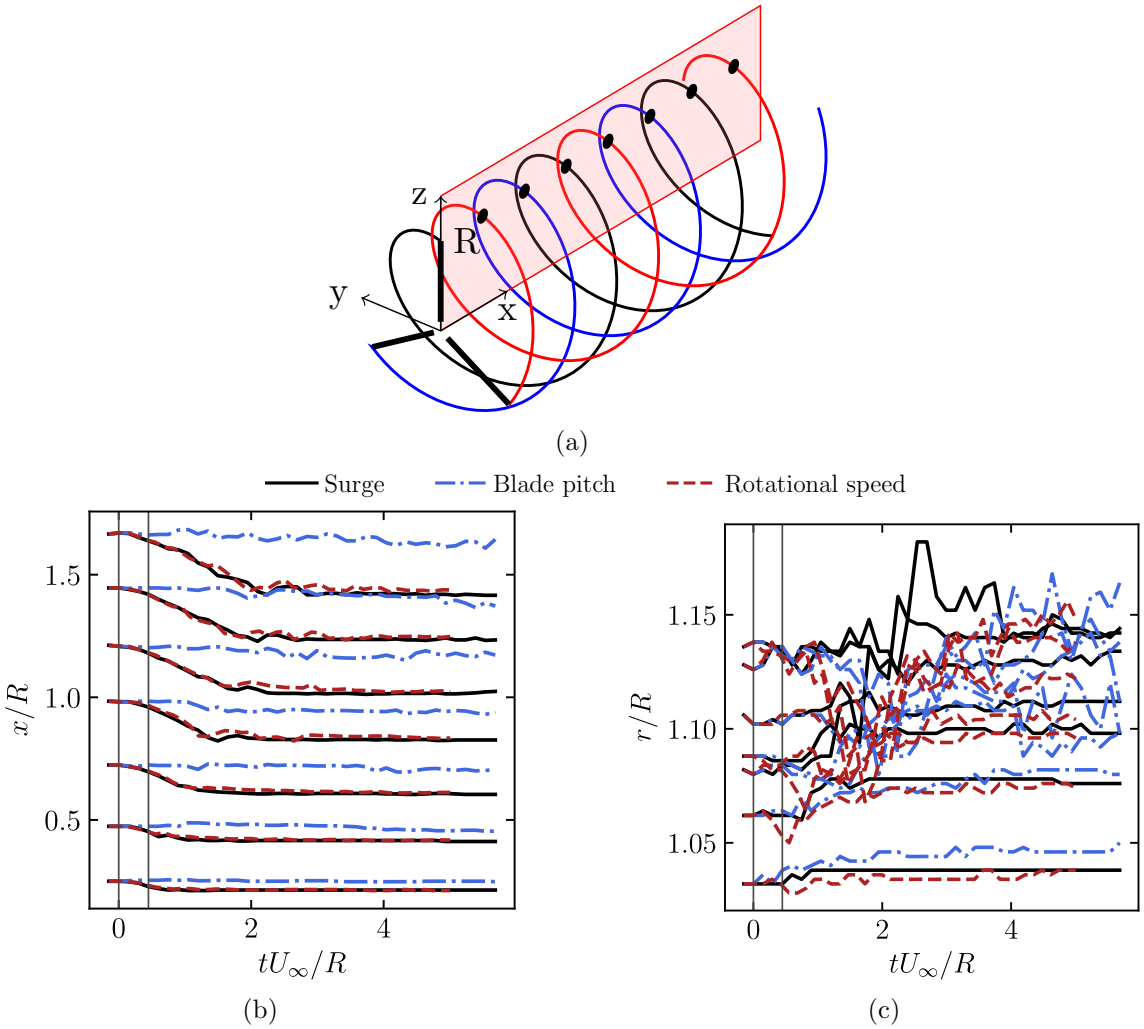

Figure 2.12: Tip vortex positions in the rotating plane defined by the blade and the axial direction for the thrust coefficient increase, after a blade pitch, surge, and rotor speed ramp (see Table 2.2): (a) scheme of the extracted tip vortex positions; (b) axial positions; and (c) radial positions. The first 7 intersections between tip vortices and the rotating blade plane are show in (b) and (c).

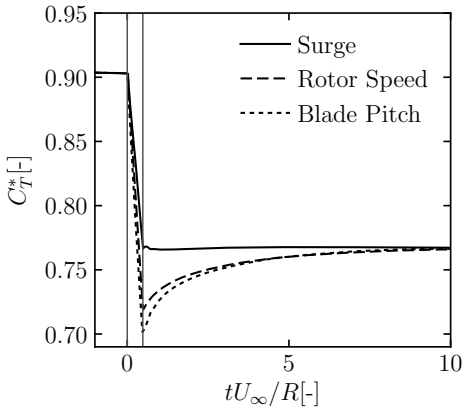

Figure 2.13: Thrust coefficient decrease after a blade pitch, surge and rotor speed ramp. The vertical lines delimit the applied ramps.

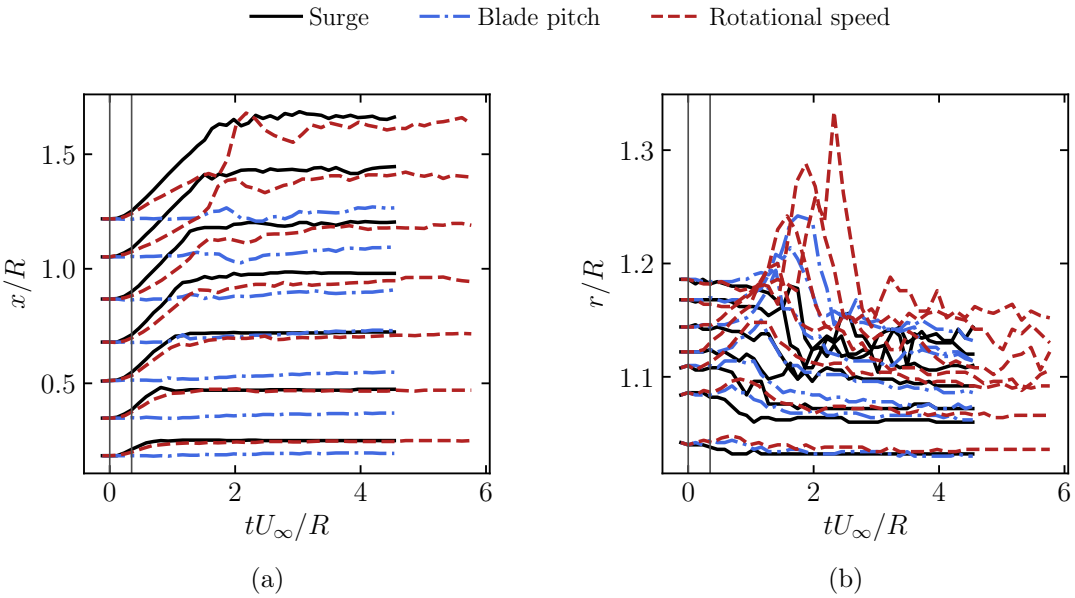

Figure 2.14: Tip vortex positions in the rotating plane defined by the blade and the axial direction for the thrust coefficient decrease, after a blade pitch, surge, and rotor speed ramp (see Table 2.3): (a) axial positions; (b) radial positions.

getting closer to the rotor axis as shown by the large increase of their radial position around $tU_\infty/R = 2$, which could be due to the occurrence of vortex pairing.

These numerical results are in agreement with the published literature: both the blade pitch and rotor speed steps exhibit dynamic inflow[165, 180]. To identify the physical processes leading to the different dynamic behaviors observed for the three studied perturbations and explore the radial behavior of the dynamic inflow, an analytical vortex model based on the Joukowsky rotor model will be considered next.

2.3.3 Analytical model of the aerodynamics

2.3.3.1 Rotor model

The rotor model of Joukowsky (see [91], [138] and [139]) is adopted: each blade has a constant circulation and only emits a tip vortex and root vortex. The objective is to express the change of the velocity induced by the vortex system on the rotor due to the three studied events: a blade pitch, a surge, and a rotor speed step. The root vortices are assumed to be merged and to lie on the axis of the rotor so they do not contribute to the axial velocity and will not be considered in the following analysis. The focus here will be on the tip vortices which are responsible for the axial induction of the rotor.

The wake of the wind turbine is taken as a system of n_b helices of radius R where n_b is the number of blades and R the radius of the wind turbine rotor. The system of helix is assumed to rotate at the same rotational velocity as the rotor at the instant of its emission in the flow. As stated by Wood and Boersma [215], this is a hypothesis made when doing phase-locked measurements in wind turbine wakes that seems to be well verified. We therefore consider below the rotating reference frame linked to one of the blades.

2.3.3.2 Blade pitch step

We will express the axial velocity induced by this helix of circulation Γ at point $\mathbf{x}$, shown in Fig. 2.15 . The equation of the helices are:

$$\begin{cases} x_s = U_{cv} t \\ y_s = R \sin(\omega_r t + \frac{2k\pi}{n_b}) \\ z_s = R \cos(\omega_r t + \frac{2k\pi}{n_b}) \end{cases} \tag{2.6}$$

for $k \in [0, n_b - 1]$, where U_{cv} is the convection velocity of the tip vortex helix, ω_r is the rotation speed of the rotor, and $\mathbf{x_s} = (x_s, y_s, z_s)$ denotes a point over the helix. The

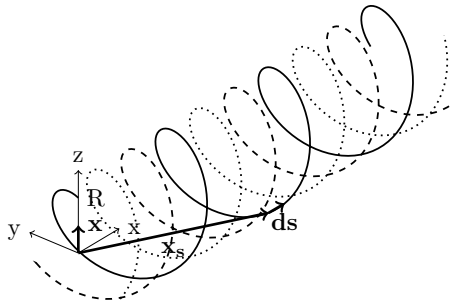

Figure 2.15: Sketch of the vortex helices emitted from a three-bladed rotor, where $\mathbf{x_s}$ is a point on a helix, $\mathbf{ds}$ is an infinitesimal section of a helix, and $\mathbf{x}$ is an arbitrary point of interest.

velocity induced by the helix at a point $\mathbf{x}$ is:

$$\mathbf{u_i}(\mathbf{x},t) = -\frac{1}{4\pi}\sum_{k=0}^{n_b-1}\int \Gamma(s)\frac{\mathbf{x}-\mathbf{x_s}}{\|\mathbf{x}-\mathbf{x_s}\|^3}\times\mathbf{ds} \tag{2.7}$$

where Γ is the local circulation of the vortex. The velocity field induced by an infinite helical vortex of constant circulation has been expressed by Hardin [74]. Here, the circulation varies over the helical vortex as the lift at the tip of the blade changes because of the blade pitch step, and the helix is semi-infinite. As a result, the expression given by Hardin cannot readily be reused. The factors of the vectorial product of the Biot-Savart law can be explicitly written as:

$$\mathbf{x}-\mathbf{x_s} = \begin{pmatrix} -U_{cv}t \\ -R\sin(\omega_r t + \frac{2k\pi}{n_b}) \\ r - R\cos(\omega_r t + \frac{2k\pi}{n_b}) \end{pmatrix} \text{ and } \mathbf{ds} = \begin{pmatrix} U_{cv}dt \\ \omega_r R\cos(\omega_r t + \frac{2k\pi}{n_b})dt \\ -\omega_r R\sin(\omega_r t + \frac{2k\pi}{n_b})dt \end{pmatrix} \tag{2.8}$$

where r denotes the radial position of point $\mathbf{x}$ and t is the time since the vortex at the point $\mathbf{x_s}$ was emitted on blade k.

The circulation along the helix, $\Gamma(s)$, is directly linked to the lift at the tip of the blade. The instant of the blade pitch event is written t_0. The circulation of the tip vortex emitted before and after can be approximated as constants Γ_0 and Γ_1. It is assumed that there is no dynamic effect for the lift of the tip because the flow at the tip of the blade is dominated by the tip vortex which corresponds to the new flow conditions, which leads to a stepwise distribution of the circulation along the helix:

$$\Gamma(s) = \begin{cases} \Gamma_0, \text{ if } t > t_0 \\ \Gamma_1 = (1+\epsilon)\Gamma_0, \text{ if } t \leq t_0 \end{cases} \tag{2.9}$$

where ϵ quantifies the relative change of the tip circulation.

Our objective is to study the axial component $u_{i,x}(\mathbf{x},t) = \mathbf{u_i}(\mathbf{x},t).\mathbf{e_x}$. From Eqs. 2.7, 2.8 and 2.9, the axial component of the velocity induced by the tip vortex helix of a wind turbine with n_b blades at radius r on one of the blades can be written:

$$u_{i,x}(r,t) = -\frac{\lambda\Gamma_0}{4\pi R}\sum_{k=0}^{n_b-1}\left[(1+\epsilon)\int_0^{\frac{U_\infty t}{R}} \frac{\left(1-\frac{r}{R}\cos(\lambda s+\frac{2k\pi}{n_b})\right)}{\left(e_{cv}^2 s^2+1+\frac{r^2}{R^2}-2\frac{r}{R}\cos(\lambda s+\frac{2k\pi}{n_b})\right)^{3/2}}ds + \int_{\frac{U_\infty t}{R}}^{+\infty} \frac{\left(1-\frac{r}{R}\cos(\lambda s+\frac{2k\pi}{n_b})\right)}{\left(e_{cv}^2 s^2+1+\frac{r^2}{R^2}-2\frac{r}{R}\cos(\lambda s+\frac{2k\pi}{n_b})\right)^{3/2}}ds\right] \tag{2.10}$$

where $e_{cv} = U_{cv}/U_\infty$ and without loss of generality, we take $t = 0$ as the instant of the blade pitch step. This integral has no closed form to the authors knowledge except at the center of the rotor where $r/R = 0$. This solution will be studied in Section 2.3.3.8.

2.3.3.3 Surge velocity step

The same process as the blade pitch case is applied for the surge step, but now there is a change of the convection velocity of the tip vortex helix U_{cv} which is related only to the change in relative inflow velocity due to the surge motion. The importance of changes to the convection velocity of tip vortices will be discussed in detail in Section 2.3.3.5.

A surge velocity step changes the pitch of the emitted tip vortex helix. When the inflow wind speed is reduced, the pitch of the tip vortex helix is also reduced. However, the pitch of the tip vortex helix emitted before the surge event is not modified. As a result, the position vector and the tangential vector to the helix can be written as:

$$\mathbf{x}-\mathbf{x_s} = \begin{cases} \begin{pmatrix} -\left(U_{cv}^{cur}t_0 + U_{cv}^{emi}(t-t_0)\right) \\ -R\sin(\omega_r t+\frac{2k\pi}{n_b}) \\ r-R\cos(\omega_r t+\frac{2k\pi}{n_b}) \end{pmatrix}, \text{ if } t > t_0 \\ \begin{pmatrix} -U_{cv}^{cur}t \\ -R\sin(\omega_r t+\frac{2k\pi}{n_b}) \\ r-R\cos(\omega_r t+\frac{2k\pi}{n_b}) \end{pmatrix}, \text{ otherwise} \end{cases}$$

$$\text{and } \mathbf{ds} = \begin{cases} \begin{pmatrix} U_{cv}^{emi}dt \\ \omega_r R\cos(\omega_r t+\frac{2k\pi}{n_b})dt \\ -\omega_r R\sin(\omega_r t+\frac{2k\pi}{n_b})dt \end{pmatrix}, \text{ if } t > t_0 \\ \begin{pmatrix} U_{cv}^{cur}dt \\ \omega_r R\cos(\omega_r t+\frac{2k\pi}{n_b})dt \\ -\omega_r R\sin(\omega_r t+\frac{2k\pi}{n_b})dt \end{pmatrix}, \text{ otherwise} \end{cases} \tag{2.11}$$

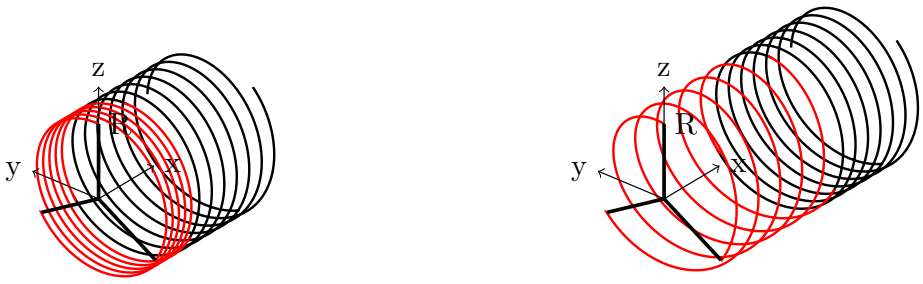

(a) $\Delta_u = -0.5$ (b) $\Delta_u = 0.75$

Figure 2.16: Deformation of the helix for $e_{cv} = 0.75$ and $\lambda = 7$, the red vortices are the newly emitted tip vortices after the surge velocity step. The vortex helix is truncated only for the visual representation. (a) Downwind surge, (b) Upwind surge.

where t_0 is the time of the surge step event, U_{cv}^{cur} is the current convection velocity of the tip vortex helix taking into account the surge motion and U_{cv}^{emi} is the convection velocity of the tip vortex helix prior to the surge step. The geometry of the helix modified by a surge in the upwind and downwind directions is shown in Fig 2.16. When the wind turbine moves downwind, the distance between the tip vortices is reduced, while for the upwind surge the distance between the tip vortices is increased.

This formulation can readily be used in the integral formulation of the induced velocity, as this integral has been divided into the contribution of the tip vortices emitted before and after the surge event. The expression of the velocity induced by the tip vortices of each blades in the surge case is:

$$u_{i,x}(r,t) = -\frac{\lambda\Gamma_0}{4\pi R}\sum_{k=0}^{n_b-1}\left[(1+\epsilon)\int_0^{\frac{U_\infty t}{R}} \frac{\left(1-\frac{r}{R}\cos(\lambda s+\frac{2k\pi}{n_b})\right)}{\left((1+\Delta_u)^2 e_{cv}^2 s^2+1+\frac{r^2}{R^2}-2\frac{r}{R}\cos(\lambda s+\frac{2k\pi}{n_b})\right)^{3/2}}ds \right.$$
$$\left. + \int_{\frac{U_\infty t}{R}}^{+\infty} \frac{\left(1-\frac{r}{R}\cos(\lambda s+\frac{2k\pi}{n_b})\right)}{\left(e_{cv}^2\left(\Delta_u\frac{tU_\infty}{R}+s\right)^2+1+\frac{r^2}{R^2}-2\frac{r}{R}\cos(\lambda s+\frac{2k\pi}{n_b})\right)^{3/2}}ds\right] \tag{2.12}$$

where Δ_u is the relative change of convection velocity of the tip vortices due to the additional surge velocity, such that $U_{cv}^{cur} = U_{cv}^{emi}(1+\Delta_u)$, $e_{cv} = U_{cv}^{emi}/U_\infty$ and $t = 0$ is the instant of the surge step. Once again, these integrals have no known closed form solution except at the center of the rotor (see Section 2.3.3.8).

2.3.3.4 Rotor speed step

For the rotor speed step case, the position vector and the vector tangential to the helix can be written as:

$$\mathbf{x}-\mathbf{x_s}=\begin{cases}\begin{pmatrix}-U_{cv}t\\ -R\sin(\omega_{r,1}t_0+\omega_{r,0}(t-t_0)+\frac{2k\pi}{n_b})\\ r-R\cos(\omega_{r,1}t_0+\omega_{r,0}(t-t_0)+\frac{2k\pi}{n_b})\end{pmatrix}, \text{ if } t>t_0\\ \begin{pmatrix}-U_{cv}t\\ -R\sin(\omega_{r,1}t+\frac{2k\pi}{n_b})\\ r-R\cos(\omega_{r,1}t+\frac{2k\pi}{n_b})\end{pmatrix}, \text{ otherwise}\end{cases} \tag{2.13}$$

and

$$\mathbf{ds}=\begin{cases}\begin{pmatrix}U_{cv}dt\\ \omega_{r,0}R\cos(\omega_{r,1}t_0+\omega_{r,0}(t-t_0)+\frac{2k\pi}{n_b})dt\\ -\omega_{r,0}R\sin(\omega_{r,1}t_0+\omega_{r,0}(t-t_0)+\frac{2k\pi}{n_b})dt\end{pmatrix}, \text{ if } s>s_0\\ \begin{pmatrix}U_{cv}dt\\ \omega_{r,1}R\cos(\omega_{r,1}t+\frac{2k\pi}{n_b})dt\\ -\omega_{r,1}R\sin(\omega_{r,1}t+\frac{2k\pi}{n_b})dt\end{pmatrix}, \text{ otherwise}\end{cases} \tag{2.14}$$

with $\omega_{r,0}$ the initial rotor speed and $\omega_{r,1}$ the rotor speed after the steps. The relative change of rotor speed Δ_ω is introduced such that $\omega_{r,1}=(1+\Delta_\omega)\omega_{r,0}$.

The expression of the axial velocity induced by the tip vortex helix after a rotor speed step at $t=0$ at a position $\mathbf{x}$ on a blade is:

$$u_{i,x}(r,t)=-\frac{\Gamma_0\lambda}{4\pi R}\sum_{k=0}^{n_b-1}\left[(1+\epsilon)(1+\Delta_\omega)\int_0^{\frac{tU_\infty}{R}}\frac{\left(1-\frac{r}{R}\cos((1+\Delta_\omega)\lambda s+\frac{2k\pi}{n_b})\right)}{\left(e_{cv}^2s^2+1+\frac{r^2}{R^2}-2\frac{r}{R}\cos((1+\Delta_\omega)\lambda s+\frac{2k\pi}{n_b})\right)^{3/2}}ds\right.$$
$$\left.+\int_{\frac{tU_\infty}{R}}^{+\infty}\frac{\left(1-\frac{r}{R}\cos(\lambda s+\frac{2k\pi}{n_b})\right)}{\left(e_{cv}^2s^2+1+\frac{r^2}{R^2}-2\frac{r}{R}\cos(\lambda(s-\Delta_\omega\frac{tU_\infty}{R})+\frac{2k\pi}{n_b})\right)^{3/2}}ds\right] \tag{2.15}$$

The rate of change of the tip vortex helix properties is related to how fast the vortices emitted by the blade are convected downstream. The tip vortex convection velocity is thus the driver of the dynamic inflow effect. The prediction of the axial tip vortex convection velocity from the operating conditions will be studied next.

2.3.3.5 Convection velocity of the tip vortices

For practical purposes, the convection velocity of the tip vortices is very often approximated to be the mean velocity between outside and inside the far-wake and assumed to be the same both in the near- and far-wake regions. This approximation of $U_{cv} = (1-a)U_\infty$ is done for example by Okulov et al. [138, 139], stating that it is the behavior when the pitch of the helix goes to zero. Others like Pirrung and Madsen [146] approximate the convection velocity of the tip vortices as $U_{cv} = (1-1.5a)U_\infty$. Seeing that this velocity appears in Eq. 2.10, 2.12, and 2.15 as the variable ruling the temporal behavior of the induced velocity, and noting that there is substantial experimental data available, we look at this in more detail in this section.

Wood and Boersma [215] devised an approximation of the self-induced convection velocity of an infinite vortex helix with n_b vortices for a small pitch of the helix which allows us to improve upon the approximation $e_{cv} = (1-a)$, which is the limiting behavior when the pitch goes to zero and is also based on an infinite helix. It is interesting for the dynamic inflow effect, as this phenomenon often occurs for highly loaded rotors and thus small helix pitch. With the current notation, the approximation for the self-induced convection velocity of an infinite vortex helix is:

$$U_{cv,self} = -\frac{\Gamma_0 n_b}{4\pi R p}\left(1 - \frac{p}{n_b}\frac{\log(n_b/p)}{(p^2+1)^{1/2}} + \frac{3}{4}\frac{p}{n_b} - p^2 + \frac{1}{n_b}\left(\frac{3}{8}\frac{\zeta(3)}{n_b^2} - \frac{7}{8}\right)p^3 + O(p^5)\right) \tag{2.16}$$

for small helix pitch p, where ζ is the Riemann zeta function and $2\pi pR$ is the axial distance traveled by the helix during one rotation, thus $p = e_{cv}/\lambda$. The total axial induction factor, a, of the rotor is defined as the ratio of the induced velocity divided by the free-stream velocity, which can be related to the circulation of the tip vortices as shown by Wood and Boersma [215]. With the current notation:

$$aU_\infty = \frac{n_b \Gamma \lambda}{4\pi R e_{cv}}. \tag{2.17}$$

The demonstration is found in Appendix 2.3.6. This relation lets us introduce the axial induction factor instead of the tip vortex circulation in Eq. 2.16. The total convection velocity of the tip vortex helix is the sum of the self-induced velocity $U_{cv,self}$ and the inflow U_∞. Once reworked using the relation $p = e_{cv}/\lambda$, this gives an expression of the helix pitch p as a function the tip speed ratio, the axial induction factor, and the number of blades:

$$p = \frac{1}{\lambda}\left[1 - a\left(1 - \frac{p}{n_b}\frac{\log(n_b/p)}{(p^2+1)^{1/2}} + \frac{3}{4}\frac{p}{n_b} - p^2 + \frac{1}{n_b}\left(\frac{3}{8}\frac{\zeta(3)}{n_b^2} - \frac{7}{8}\right)p^3 + O(p^5)\right)\right]. \tag{2.18}$$

This equation cannot analytically be solved, but numerical values can be obtained easily

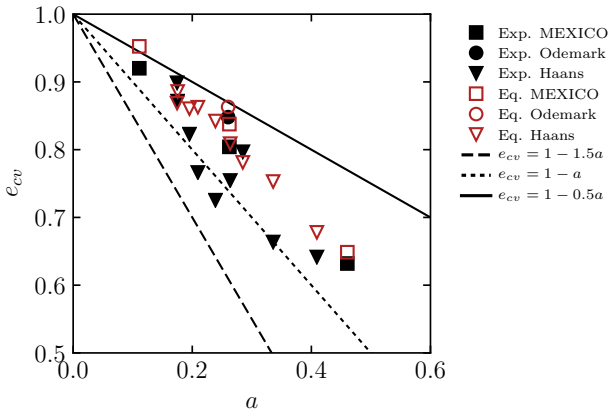

Figure 2.17: Experimental data for tip vortex convection velocity close to the rotor and calculated data with Eq. 2.18. MEXICO and Odemark cases are 3-bladed turbines, while the Haans case is a 2-bladed turbine.

with a fixed point iteration. The ratio between the convection velocity of the tip vortices and the inflow velocity is then obtained as $e_{cv} = \lambda p$. The values of e_{cv} computed this way depend both on the tip speed ratio and the axial induction factor.

Note that the approximation of small pitch in Eq. 2.16 is not valid for small induction factors. For example, if $\lambda = 4.0$ and $a = 0.1$ for a three bladed wind turbine, Eq. 2.18 gives $p = 0.24$, but the quality of the approximation increases as the axial induction factor increases and the helix pitch decreases. It is therefore appropriate for dynamic inflow prediction, as the effect is more pronounced for low inflow wind speeds, high tip speed ratios, and therefore high induction factors and dense wakes.

To study the accuracy of the above approximations, the axial convection velocity of tip vortices can be computed from experimental phase-locked PIV measurements in the near wake. Haans [69], for example, estimated the convection velocity from the position of the tip vortex after one rotation of the rotor. Measurements are also available for the 3-bladed MEXICO wind turbine [29] as well the 2-bladed wind turbine used by Haans [69]. Another approach was taken by Odemark and Fransson [137], who used a hot-wire probe to measure the time taken by the tip vortex to reach two different axial positions ($x/R = 0.8$ and $x/R = 1$). In these experiments, the rotor thrust is either measured with strain gauges [69, 137] or from extrapolated airfoil pressure measurements [29]. The corresponding axial induction factors were computed with the empirical relation of Buhl [34] using the experimentally measured thrust force. The estimation done with approximations for the convection velocity, as well as the experimental results, are shown in Fig. 2.17.

It can be seen that the experimental results lie in between $e_{cv} = 1-0.5a$ and $e_{cv} = 1-1.5a$. The use of the approximation $e_{cv} = 1 - a$ gives results with a good agreement with the experimental data for the 2-bladed turbines, but it seems to underestimate the axial

convection velocity of the tip vortices for the two 3-bladed turbines. For these 3-bladed turbines, Eq. 2.18 appears to provide a better estimate. Nonetheless, there are a number of clear limitations, as Eq. 2.18 does not take into account the radial expansion of the wake, and is based on an infinite vortex helix, whereas near the rotor the vortex helix is finite. The knowledge of the tip vortex convection velocity seems particularly important for the modeling of dynamic inflow, as it appears in the equation derived here as the main driver of this effect. This is not developed further here, but in future work, Eq. 2.18 could be used in dynamic inflow models.

2.3.3.6 Induced velocity radial profile and root vortex

The Joukowsky rotor model does not include root vortices, therefore it cannot describe the flow in detail near the root of the blade. Fig. 2.18 shows the radial induced velocity profiles for the NREL 5MW wind turbine at $\lambda = 9.0$ from FVW and from the Joukowsky model. The velocity induced by a set of helical vortices including a helical root vortex emitted at $r/R = 0.19$, instead of root vortices lying on the axis of the rotor, is included. The equation used to compute the velocity induced by this set of helical vortices including helical root vortices is provided in Appendix 2.3.5, Eq. 2.29. The convection velocity of the root vortices is taken equal to the convection velocity of the tip vortices. The attached circulation is computed using Eq. 2.17 with $a = 0.34$ and $e_{cv} = 0.75$. A desingularization core radius of $r_c/R = 0.007$, or half of the tip element chord, is used for the case including the helical root vortex, while no desingularization is used for the Joukowsky model to reduce the complexity of the equations when using the dynamic model, which is justified by the fact that the induced velocity variation is studied at positions far enough from the tip of the blade.

It can be seen in Fig. 2.18 that the large variation of the induced velocity near the root is due to the presence of helical root vortices. Both helical models are unable to capture the variation of the induced velocity along the blade due to the lack of trailing vorticity emitted along the span of the blade. Except for the root position and near the tip of the blade (due to the desingularization), the induced velocity computed with the Joukowsky model and the helical model, including helical root vortices, are qualitatively similar. Therefore, the Joukowsky model with axial root vortices is used in this work because the use of a helical root vortex would require too many additional hypotheses on its circulation and convection velocity variations in the dynamic cases that we are interested in. Here, the convection velocity of the root vortices was taken equal to the tip vortex one for simplicity, but it might be lower than the tip vortex one.

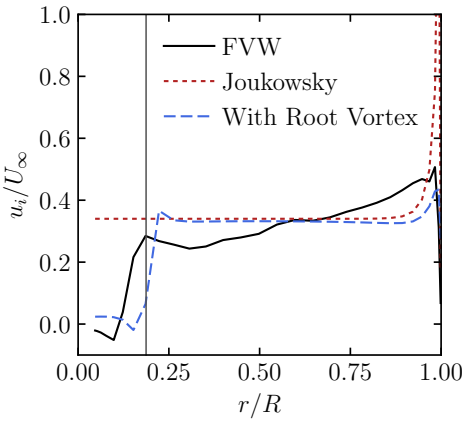

Figure 2.18: Induced velocity profile along the blade for the NREL 5MW wind turbine at $\lambda = 9.0$ from FVW and the Joukowsky rotor model compared with a helical wake including root vortices emitted at $r/R = 0.19$ and a vortex core size of $r_c/R = 0.007$. The vertical line shows the position of the root vortex.

2.3.3.7 Validation of the helix geometry change

The axial position of the tip vortices in the plane defined by the blade and the rotor axis (see Fig. 2.12a) can be expressed from equations 2.8, 2.11, and 2.13. The intersection of the helix with the plane does not change in time for the blade pitch step, given that the convection velocity of the tip vortex helix is assumed constant:

$$x = U_{cv}\frac{2\pi}{\omega_r}\left(m - \frac{k}{n_b}\right), \text{ for } m \in \mathbb{N}^*, k \in [0, n_b - 1]\,. \tag{2.19}$$

In the surge step case, the geometry of the helix is modified by the event. The position of the tip vortex helix in the blade plane is obtained from Eq. 2.11:

$$x(t) = \begin{cases} U_{cv}^{emi}\frac{2\pi}{\omega_r}\left(m - \frac{k}{n_b}\right), \text{ if } t < 0 \\ U_{cv}^{emi}\left(\frac{2\pi}{\omega_r}\left(m - \frac{k}{n_b}\right) - t\right) + U_{cv}^{cur}t, \text{ if } 0 \leq t \leq \frac{2\pi}{\omega_r}\left(m - \frac{k}{n_b}\right) \\ U_{cv}^{cur}\frac{2\pi}{\omega_r}\left(m - \frac{k}{n_b}\right), \text{ if } t > \frac{2\pi}{\omega_{r,1}}\left(m - \frac{k}{n_b}\right) \end{cases} \tag{2.20}$$

for $m \in \mathbb{N}^*, k \in [0, n_b - 1]$. Finally, a similar expression can be derived from Eq. 2.13 for the rotor speed step:

$$x(t) = \begin{cases} U_{cv}\frac{2\pi}{\omega_{r,0}}\left(m - \frac{k}{n_b}\right), \text{ if } t < 0 \\ \frac{U_{cv}}{R}\left(\frac{2\pi}{\omega_{r,0}}\left(m - \frac{k}{n_b}\right) - \Delta_\omega t\right), \text{ if } 0 \leq t \leq \frac{2\pi}{\omega_{r,1}}\left(m - \frac{k}{n_b}\right) \\ U_{cv}\frac{2\pi}{\omega_{r,1}}\left(m - \frac{k}{n_b}\right), \text{ if } t > \frac{2\pi}{\omega_r}\left(m - \frac{k}{n_b}\right) \end{cases} \tag{2.21}$$

for $m \in \mathbb{N}^*, k \in [0, n_b - 1]$.

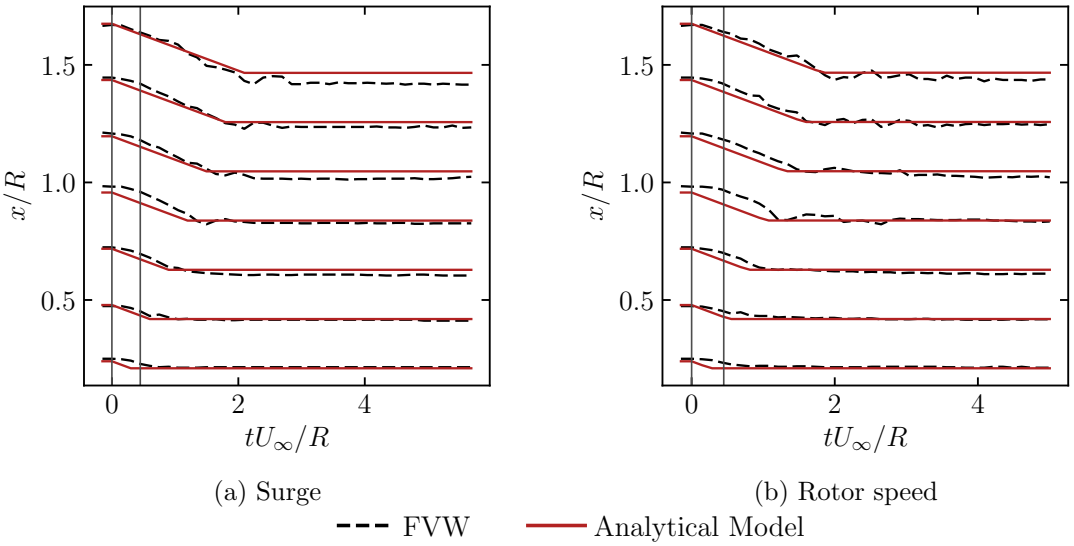

(a) Surge (b) Rotor speed

Figure 2.19: Tip vortex positions in the rotating plane defined by the blade and the axial direction from the FVW and analytical models in the thrust coefficient increase case of section 2.3.2.2: (a) surge velocity step; (b) rotor speed step. The vertical lines delimit the applied ramp for the FVW.

In each case, the convection velocity of the tip vortex helix needs to be known to use these equations. In order to improve on the estimation of the convection velocity from Section 2.3.3.5, the analytical model results are compared to the FVW results on the case of the thrust coefficient increase of Section 2.3.2.2 and the convection velocity of the tip vortex helix is estimated from the FVW results. The temporal dynamics of the position of the tip vortices in the blade plane can be expressed by the presented set of equations and is shown in Fig. 2.19 for the surge and rotor speed change.

Note that the analytical model predicts the temporal evolution of the geometry of the tip vortex helix with a good agreement to the FVW results even though the analytical model is built for a step event and not a ramp as used for the FVW cases. It validates that the chosen modeling method captures the change of the axial position of tip vortices.

2.3.3.8 Induced velocities at the center of the rotor

The axial induced velocity at the center of the rotor when no event occurs is:

$$u_{i,x}(r/R = 0, t) = -\frac{\lambda \Gamma_0 n_b}{4\pi R} \frac{1}{e_{cv}} \tag{2.22}$$

This can be compared to the helical model after different changes. While the analytical formulation at other radial locations is quite complicated, the expressions of the induced velocity in the three studied cases (Eq. 2.10, 2.12, and 2.15) have a closed-form solution

at the center of the rotor. These solutions give some information about the temporal evolution of the induced velocity as well as the amplitude of the induced velocity change along the blade due to the similarity of the predicted temporal behavior at the center of the rotor and for other radial positions along the blade which will be further studied in section 2.3.3.9. However, these solutions do not provide good estimates of the induced velocity and its variation at the center of the rotor because of the lack of helical root vortex helix (see Fig 2.18). They are:

- blade pitch step

$$u_{i,x}(r/R=0,t) = -\frac{\lambda\Gamma_0 n_b}{4\pi R}\left(\frac{1}{e_{cv}} + \frac{\epsilon\frac{tU_\infty}{R}}{\left(e_{cv}^2\frac{t^2U_\infty^2}{R^2}+1\right)^{1/2}}\right), \tag{2.23}$$

- surge step

$$u_{i,x}(r/R=0,t) = -\frac{\lambda\Gamma_0 n_b}{4\pi R}\left(\frac{1}{e_{cv}} + \frac{(\epsilon-\Delta_u)\frac{tU_\infty}{R}}{\left(e_{cv}^2(1+\Delta_u)^2\frac{t^2U_\infty^2}{R^2}+1\right)^{1/2}}\right) \tag{2.24}$$

- rotor speed step

$$u_{i,x}(r/R=0,t) = -\frac{\lambda\Gamma_0 n_b}{4\pi R}\left(\frac{1}{e_{cv}} + \frac{((1+\epsilon)(1+\Delta_\omega)-1)\frac{tU_\infty}{R}}{\left(e_{cv}^2\frac{t^2U_\infty^2}{R^2}+1\right)^{1/2}}\right) \tag{2.25}$$

where $t=0$ is the time of the step event for the three cases. In any case, note that the dynamic effect depends on the numerator of the second term. If it is zero, there is no dynamic effect.

For the blade pitch case, this is not possible: Eq. 2.17 shows that a change of the rotor loading changes the tip vortex circulation and ϵ cannot be equal to zero in this case. The induced velocity at the center of the rotor will always show a dynamic behavior if the blade pitch changes.

For the rotor speed step, it is possible to have no dynamic effect if $(1+\epsilon)(1+\Delta_\omega)=1$. Under the hypothesis that the convection velocity is constant, the variation of the tip circulation can be linked to the rotational speed change using Eq. 2.17: $(1+\epsilon)(1+\Delta_\omega) = a_1/a_0$, where we denote the axial induction factors a_0 and a_1 to correspond to the static conditions before and after the speed step. A rotor speed step changes the tip speed ratio and thus changes the loading and the axial induction factor a: a_1/a_0 will not be equal to 1 and dynamic effects for the induced velocity at the rotor center will always occur.

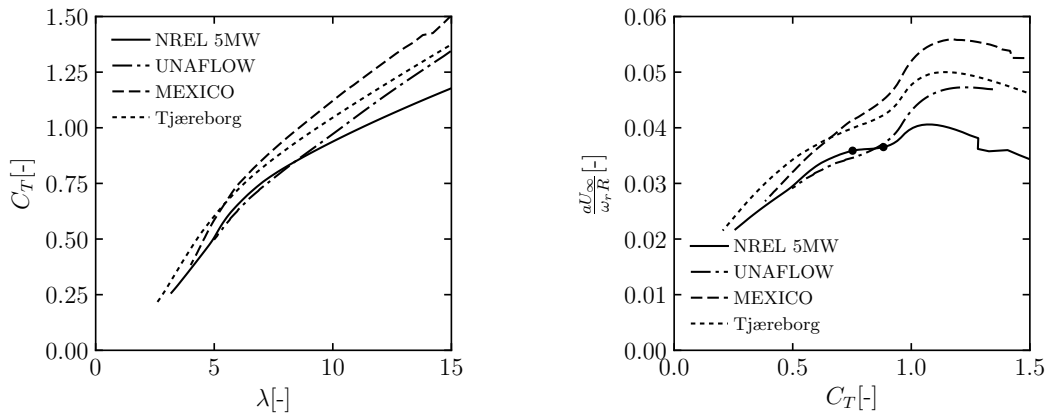

(a) (b)

Figure 2.20: (a) Thrust coefficient computed with BEMT for different wind turbine geometries. (b) Global axial induced velocity for different wind turbine geometries. The dots denote starting and final conditions (corresponding to tip speed ratios 9 and 7) of the thrust coefficient decrease of Section 2.3.2.3.

For the surge step, Eq. 2.17 can be used to express the tip vortex circulation variation ϵ as a function of the convection velocity variation Δ_u:

$$\epsilon = \frac{a_1 U_{\infty,1}}{a_0 U_{\infty,0}}(1 + \Delta_u) - 1 \tag{2.26}$$

where $U_{\infty,1}$ is equal to $U_{\infty,0}$ plus the additional velocity U_s due to the surge motion. The variation of aU_∞ for various loading conditions can be obtained with the blade element momentum theory for different rotor geometries (see Burton et al. [35]). Indeed, the relation between tip speed ratio and thrust coefficient is specific to a rotor geometry and in particular depends on the fixed blade pitch angle. The relation between the thrust coefficient and the tip speed ratio computed with the BEMT for different wind turbine geometries is shown in Fig. 2.20a. This can be used to evaluate whether dynamic effects might occur due to a surge step. The global axial induction factor can be computed from the thrust coefficient using momentum theory and Buhl's empirical relation[34] for high thrust cases. The evolution of the ratio a/λ for different thrust coefficients then indicates how much the global induced velocity of the rotor will change due to additional inflow due to a surge motion at a fixed rotor speed. This ratio is shown in Fig. 2.20b.

There is little change of aU_∞ between the starting and final conditions of the thrust coefficient decrease of Section 2.3.2.3 for the NREL 5MW wind turbine geometry. Other rotor geometries such as the MEXICO and Tjæreborg rotor would potentially experience more dynamic effects as the ratio $a_1 U_{\infty,1}/a_0 U_{\infty,0}$ would differ from 1. This shows that it is possible for the surge motion to induce a modification of the tip vortex helix geometry that compensates for the its change of circulation. The same was shown to be impossible

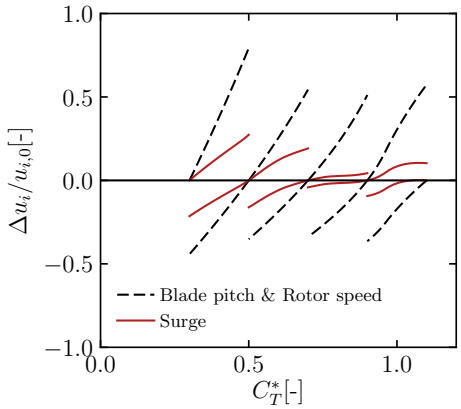

Figure 2.21: Amplitude of the axial induced velocity change at the rotor center for different starting thrust coefficients for the NREL 5 MW wind turbine. The surge case demonstrate much smaller variations of the axial induced velocity at the center of the rotor than the two other cases.

in the case of a rotational speed step. In the case of the blade pitch step, the helix geometry is supposedly unchanged and thus no geometry change can compensate the circulation change. The unchanged helix geometry due to the hypothesis of constant convection velocity of the tip vortices seems a reasonably good hypothesis based on the FVW results of Fig. 2.12 and 2.14, but for more radical thrust coefficient changes, the tip vortex convection velocity may no longer be assumed to be constant in the blade pitch and rotor speed step cases.

The magnitude of the axial induced velocity change at the rotor center, Δu_i, can be computed for the three cases from Eq. 2.23, 2.24, and 2.25, together with Eq. 2.17. The axial induced velocity in the starting operating conditions is written $u_{i,0}$. The magnitude is the same for the blade pitch and rotor speed steps due to Eq. 2.17:

$$\frac{\Delta u_i}{u_{i,0}} = \frac{a_1}{a_0} - 1 \tag{2.27}$$

The magnitude takes a different value for the surge step:

$$\frac{\Delta u_i}{u_{i,0}} = \frac{a_1 U_{\infty,1}}{a_0 U_{\infty,0}} - 1 \tag{2.28}$$

The empirical relation of Buhl [34] is used to extend momentum theory for high thrust coefficients to obtain the induction factor a as a function of the thrust coefficient C_T. From this, we can compute the amplitude of the axial induced velocity change for the blade pitch and the rotor speed step for different thrust coefficient changes. For the surge step, this amplitude is computed from aU_∞ depending on C_T, computed from BEMT, as shown on Fig. 2.20b. The magnitude of axial induced velocity variation obtained this way are shown

in Fig. 2.21. For any starting thrust coefficient, the variation of the axial induced velocity due to a blade pitch or rotor speed step is much larger than the one obtained with a surge step for the same C_T^* variation. It is specifically small for the surge case in the range $C_T^* = 0.7$ to $C_T^* = 0.9$, as aU_∞ is almost constant (see Fig. 2.20b). This shows that for the surge case, the velocity induced by the tip vortex helix at the center of the rotor is only marginally modified by the additional velocity due to the surge motion while the motion related velocity greatly changes the local velocity at the blade, so no dynamic inflow effect is to be expected at the center of the rotor because the motion related velocity variation dominates the induced velocity variation. The velocity induced by the tip vortex helix is only slightly modified, yet the air flow on the rotor is changed by the additional velocity due to the surge motion, and the loads variation will follow the dynamic of the surge step with no delay. For a thrust coefficient change due to a blade pitch or rotor speed step case, Fig. 2.21 shows that the velocity induced by the tip vortex helix on the rotor will be significantly modified. This change will take place with the temporal behavior predicted by Eq. 2.23 and 2.25 at the rotor center.

The temporal behavior discussed in this section is for the center of the rotor, but the complete helical model gives access to the induced velocities all along the span of the blade by numerically integrating Eq. 2.10, 2.12, and 2.15. This is studied next, to compare how the rest of the blade behaves with respect to the behavior at the center of the rotor.

2.3.3.9 Radial behavior

The induced velocities along the blade span can be extracted from the FVW results and compared to the induced velocities predicted by the modified Joukowsky model. The variation of the induced velocity along the blade span predicted by the FVW and the modified Joukowsky model after the three studied perturbations is shown in Fig. 2.22. Significant differences can be seen along the span of the blade between the FVW and modified Joukowsky model results. These can be related to the lack of a helical root vortex emitted near the bottom of the blade, the lack of spanwise trailing vorticity along the blade as well as the lack of shed vorticity. Yet, the helical vortex model predicts a similar temporal variation as the FVW, in particular in the blade pitch and rotor speed step cases. The radial behavior of the helical vortex model is studied in more detail below.

It would be useful to connect the results from the previous section to the dynamic behavior along the turbine blades. Until recently, the experimental knowledge on the radial behavior of the dynamic inflow effect was only from blade pressure taps measurements, such as the NREL Phase VI blade pitch measurements [176] and the MEXICO rotor speed steps [165]. Recently, Berger and Kühn [24] have made measurements of the velocity in the near wake as well as phase-locked flow measurements on a line between two blades in the rotor plane [25] for a rotor undergoing a blade pitch change. This gives a valuable insight into how

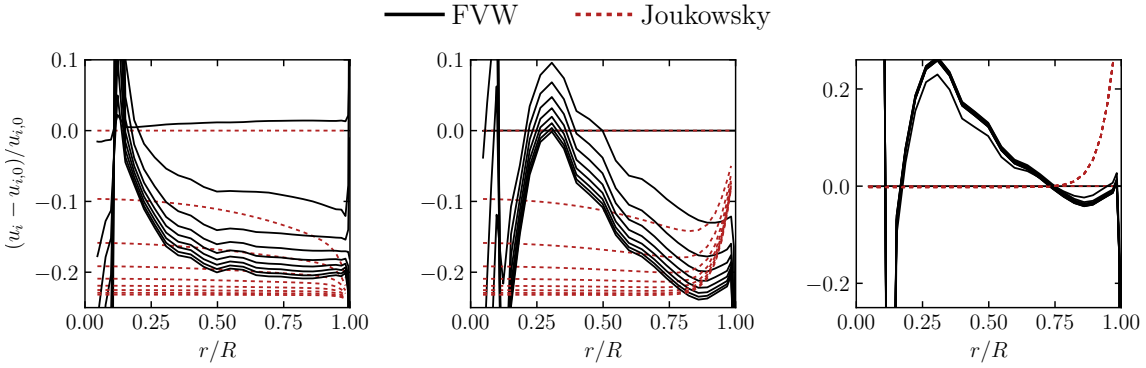

(a) Blade pitch (b) Rotor speed (c) Surge

Figure 2.22: Variation of the induced velocity at each radial station from FVW and the modified Joukowsky model represented for different time steps starting from the beginning of the perturbation at $t = 0$ with steps of $\Delta t U_\infty / R = 0.58$.

the dynamic inflow effect develops radially. They found a similar temporal behavior at $r/R = 0.6$ and $r/R = 0.9$.

First, let us consider the blade pitch step case. Most vortex models used to date to study dynamic inflow are azimuthally invariant, so they cannot differentiate the inter-blade position (halfway between two blades in the rotor plane) and the blade position, as the wake is either modeled by vortex rings or cylinders. The helical approach chosen here lets us study such a difference. The inter-blade position is rotated by π/n_b radians compared to the blade position. Taking this into account in the Biot-Savart law gives a similar integral than Eq. 2.10 with only π/n_b added to the factor of the cosine terms. It lets us compare the dynamic behavior at the inter-blade and blade positions using the helical vortex model.

Without a closed form solution to Eq. 2.10, the integrals are numerically computed with the *quad* routine from the Scipy library [207] for both the blade and inter-blade positions to study the temporal evolution of the inducted velocity after a blade pitch step. The integrals have a singularity at the tip position $r/R = 1$, but are straightforward to evaluate at all other points along the blade, as is done here. The blade and inter-blade positions are compared for $\lambda = 7.4$, $e_{cv} = 0.77$ and $\epsilon = -0.59$ in Fig. 2.23, with a focus on the initial transient.

The results for the blade and inter-blade positions essentially overlap for $r/R = 0.0$ and 0.3, meaning that close to the rotor center, the variation of the induced velocity has the same dynamic at the blade position and between two blades, with the hypothesis in this work that the vorticity shed from the blade span does not change for a change of pitch. Even at $r/R = 0.6$, only minimal differences can be seen, so measurements done at this radial station at the inter-blade position would give results close to the situation at the actual blade position. The largest difference between the blade and inter-blade position

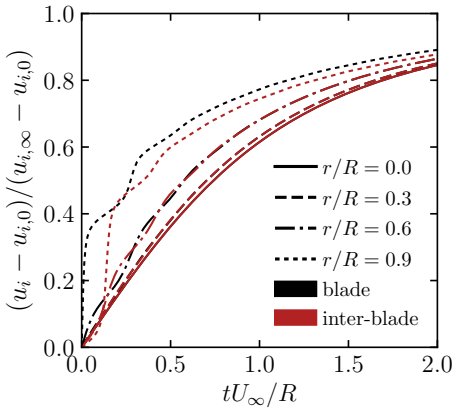

Figure 2.23: Induced velocity at the blade and inter-blade positions for various radial stations. The lines essentially overlap for $r/R = 0.0$ and 0.3. $u_{i,\infty}$ is the final converged induced velocity.

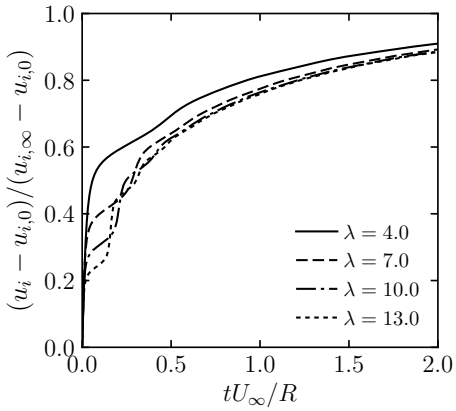

Figure 2.24: Influence of the tip speed ratio on the initial transient for $r/R = 0.9$.

is seen for $r/R = 0.9$. At this radial position, the inter-blade dynamic is close to the one observed at $r/R = 0.6$, in agreement with the experimental results of Berger et al. [25], while the induced velocity at the blade position shows a large initial transient followed by a slower dynamic. The amplitude of the transient is related to the tip speed ratio, as shown in Fig. 2.24, with the same ϵ and e_{cv} as before. The amplitude of the initial transient is diminished when the tip speed ratio increases, but for the largest tip speed ratio tested, $\lambda = 13$, the initial transient still accounts for more than 20% of the total induced velocity variation.

The staircase-like shape of the induced velocity variation for $r/R = 0.9$ (Fig.2.23, 2.24) is similar to the staircase-like variation of the thrust obtained for fast pitch steps for the AVATAR wind turbine within the MEXNEXT project (section 11.5 of the Final report of IEA Wind: Task 29 Mexnext (Phase 3)[29]). It was then linked to the blade passing in front of the wake of other blades. Here, the staircase effect might be reduced due to the lack of spanwise shed vorticity.

The fast adaptation of the flow near the tip to the new operating conditions can also be seen with the FVW method. Fig. 2.25 shows the induction factor and Fig. 2.26 the normal force coefficient in the thrust decrease case of Section 2.3.2.3 at different radial positions obtained with CACTUS. The blade pitch is applied as a ramp to avoid dynamic stall effects and reduce the effects of spanwise shed vorticity. As a result, the fast transient seen in the analytical model does not appear, but the outermost radial position still exhibits a faster variation of the induction factor than positions closer to the rotor center. Consequently, the flow is already more adapted to the new operating conditions when the ramp stops. There is therefore less variation of the induction factor after the ramp than for the other

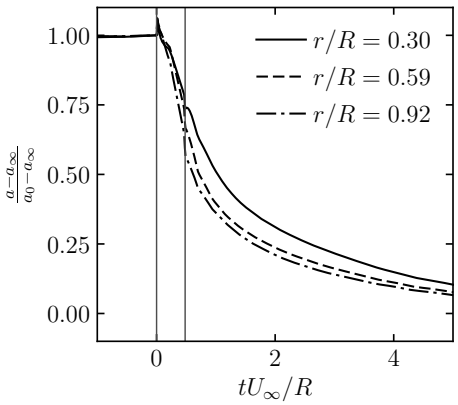

Figure 2.25: Dynamics of the induction factor from FVW for a thrust coefficient decrease due to a ramp of blade pitch. The vertical bars delimit the pitch ramp.

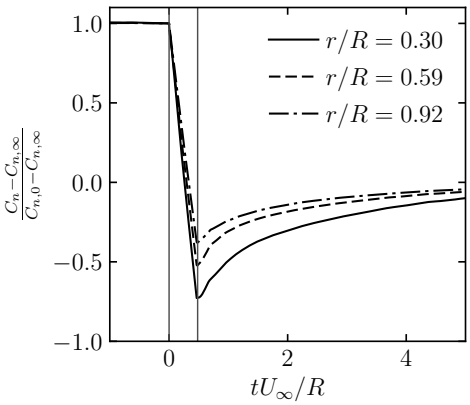

Figure 2.26: Normal force coefficient from FVW for a thrust coefficient decrease due to a ramp of blade pitch. The vertical bars delimit the pitch ramp.

positions. This leads to a reduced overshoot of the normal force coefficient (Fig. 2.26). Estimating time constants for dynamic inflow models from force measurements leads to a higher time constant near the tip than the middle of the blades as seen in Fig. 2.26, while the induction factors actually react faster to the perturbation near the tip of the blade.

The helical model presented can also be used to compute the radial dynamic behavior for the rotor speed step and surge case, showing the effect of the number of blades. The surge case is studied separately since it was shown in Section 2.3.3.8 that there is a smaller change of the induced velocity at the center of the rotor compared to the two other cases. The radial behavior is shown on Fig. 2.27 by numerically computing the integrals for the thrust coefficient decrease case of Section 2.3.2.3. Appropriate parameters corresponding to the simulated case are chosen: $\lambda = 9.0$ and $e_{cv} = 0.75$ for the three cases, with $\epsilon = -0.241$ for the blade pitch case, or $\epsilon = -0.027$ and $\Delta_\omega = -0.22$ for the rotor speed step. The variation of the circulation of the tip vortex ϵ is computed with the equations of Section 2.3.3.8 using the starting and final axial induction factors. To reach the same variation of the thrust coefficient, the tip vortex circulation has a larger variation in the blade pitch case than the rotor speed step case. The smaller change of the tip vortex circulation in the rotor speed step case leads to the same variation of the thrust coefficient due to the modification of the helix geometry with the rotor speed change: the helix pitch is increased (see Fig. 2.14) and this reduces the induced velocity at the rotor even though the tip vortex circulation is only slightly modified. The results are shown for a three-bladed turbine (Fig. 2.27a) similar to Section 2.3.2.3 as well as for a two-bladed turbine (Fig. 2.27b).

The contribution of the tip vortex emitted by the studied blade to the total dynamic is also shown in Fig. 2.27. This contribution is not accessible with azimuthally averaged

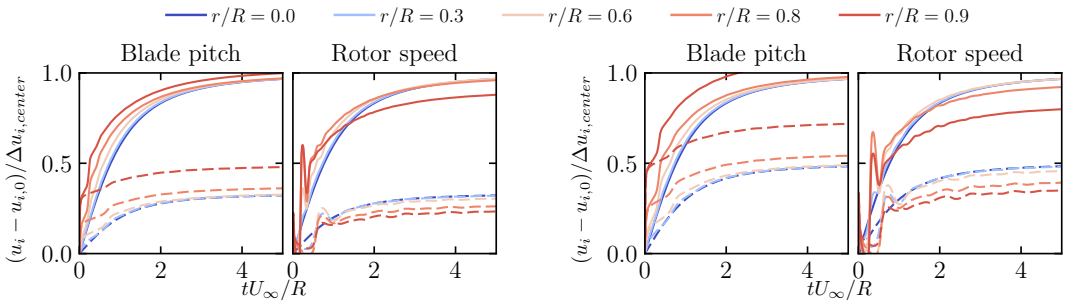

(a) $n_b = 3$ (b) $n_b = 2$

Figure 2.27: Radial dynamic behavior of the induced velocity from the helical model. The dashed lines represent the contribution from the tip vortex of the studied blade. The variation is scaled by the amplitude of the induced velocity change at the rotor center. Due to similar behavior for points at the rotor center, the lines for $r/R = 0.0$ and 0.3 are nearly overlapping.

models such as vortex cylinders or vortex rings. Near the tip of the blade, we see that the contribution of this vortex is responsible for a higher share of the total induction change. This contribution also reacts faster closer to the tip. Compared to the three-bladed case, the tip vortex emitted by the studied blade of a two-bladed rotor has a higher contribution to the total change for positions near the tip. This can be explained by the fact that the tip vortex emitted by the other blade is spatially further away from the tip of the studied blade than the two other tip vortices are in the three-bladed case. As a result, the dynamic inflow effect will affect less the tip of the blade in the two-bladed case than in the three-bladed case for identical flow parameters. For most of the blade, the two cases exhibit a temporal dynamic behavior that is close to the behavior at the center of the rotor. Only the outermost shown span has a substantially different behavior. This is particularly interesting as an analytical solution exists at the center of the rotor and was studied in Section 2.3.3.8, so the global behavior of the flow over the blade will be closely related to the one predicted by the analytical solution at $r/R = 0$.

For the blade pitch and rotor speed step cases, the effect of the vortex locally emitted by the blade at the tip is responsible for the initial transient for positions near the tip. In the rotor speed case, the small change of the tip vortex circulation for the selected conditions leads to the lack of the fast acting contribution near the tip, but the global contribution due to the helix pitch modification acts on the rotor and leads to the dynamic inflow effect. In the blade pitch case, the change in circulation of the vortex locally emitted at the tip of the blade accounts for the fast transient for positions near the tip, while the modifications of the vortex helix properties (mostly its circulation) is responsible for the slow variation of the induced velocity leading to dynamic inflow.

To return to the surge case, the radial behavior of the induced velocity for the redefined thrust coefficient decrease of Section 2.3.2.3 computed with the helical model is shown in

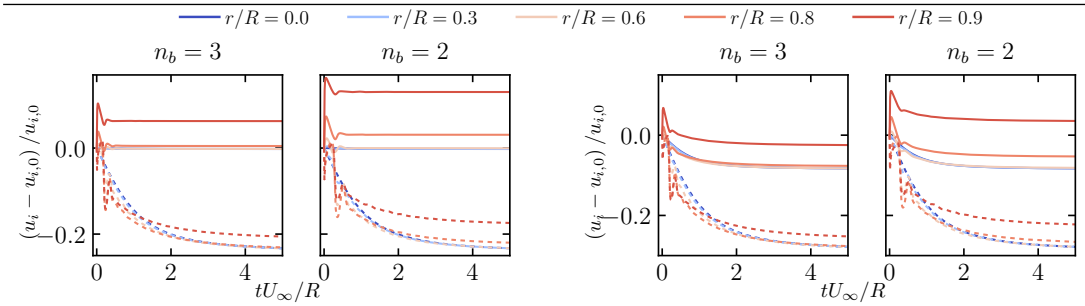

(a) NREL 5MW (b) UNAFLOW

Figure 2.28: Radial dynamic behavior of the induced velocity from the helical model in the surge case. The variation is scaled by the induced velocity at each radial station before the surge step. Due to similar behavior for points at the rotor center, the lines for $r/R = 0.0$ and 0.3 are nearly overlapping. The continous line represent the surge case while the dotted line shows the induced velocity variation for the corresponding rotor speed step. (a) NREL 5MW wind turbine. (b) UNAFLOW wind turbine.

Fig. 2.28 with $\lambda = 9.0$, $\epsilon = 0.4519$, $e_{cv} = 0.75$, and $\Delta_u = 0.4551$. The values of ϵ and Δ_u in the surge case are computed using the equations developed in Section 2.3.3.8. As showed previously, the induced velocity at the rotor center is not significantly modified by the surge step. As can be seen in Fig. 2.28, the inner portion of the blade has the same behavior as the rotor center, which is here no change of the induced velocity. For positions closer to the tip, the induced velocity does vary, and this variation is done through a short transient with no delay similar to what is seen for the dynamic inflow effect. For the same change of tip speed ratio from $\lambda = 9$ to $\lambda = 7$, the variation of the induced velocity in the surge case for the UNAFLOW wind turbine is shown in Fig. 2.28b. Since the value of aU_∞ with respect to the thrust coefficient is different depending on the geometry as seen in Fig. 2.20b, for this geometry, the parameters for the Joukowsky model are $\epsilon = 0.32$, $e_{cv} = 0.759$ and $\Delta_u = 0.43$. For the UNAFLOW wind turbine geometry, there is more variation of the induced velocity than for the NREL 5MW geometry, yet for both geometries, the induced velocity variation is small in the surge case compared to the rotor speed step case.

2.3.4 Conclusions

The unsteady aerodynamics of floating offshore wind turbines are often modeled with dynamic inflow models which were built for blade pitch changes, so they are being used for floater motions for which they might not be suitable. Here, a simplified condition, a surge velocity step, was compared to the two cases for which dynamic inflow was experimentally observed: blade pitch and rotor speed steps.

The variation of the thrust coefficient after a blade pitch, a rotor speed, and a surge step

computed with the FVW method were compared both with an increase and a decrease of the thrust coefficient. The rotor speed and blade pitch changes lead to an overshoot of the thrust coefficient with a delay to reach the steady value corresponding to the new operating conditions. This is the dynamic inflow effect. For the surge case, the thrust coefficient, which includes the additional velocity due to the motion in its normalization, does not exhibit a significant dynamic behavior which is compatible with the almost quasi-steady load variation recently found for a harmonically surging wind turbine by Mancini et al. [115].

The analytical helical vortex model presented showed that for the three perturbations, most of the blade has a temporal behavior very similar to the one at the rotor center for which a closed form solution exists. The helical vortex model can also be used to easily compute the induced velocity anywhere in the domain, notably at the inter-blade position. In the blade pitch case, while the temporal behavior at $r/R = 0.9$ and $r/R = 0.6$ are similar at the inter-blade position as found experimentally by Berger et al. [25], the position near the tip exhibits a faster temporal response at the blade position due to the fast-acting contribution of the tip vortex. This supports the use of smaller time constants near the very tip of the blade in dynamic inflow models for BEMT, with time constants otherwise similar for most of the span.

The study of the solutions at the center of the rotor for the blade pitch, rotor speed, and surge step showed that very little dynamic inflow effect occurs in the surge step case because the velocity induced by the vortex helix is only slightly modified while the surge motion velocities changes the local velocity at the blade with no delay. This happens even though the total flow over the rotor is changing due to the surge movement, because the change of the tip vortex helix circulation is partially compensated by its geometry change. As a result, the rotor loads change almost as fast as the additional inflow velocity due to the movement. In comparison, the blade pitch and rotor speed step cases were shown to have a significant variation of the velocity induced by the tip vortex helix which leads to the dynamic inflow effect. For the blade pitch and rotor speed step, the modification of the tip vortex circulation is not compensated by the modification of the helix geometry. This result might not hold for general surge motions of floaters due to vortex interactions in the wake and needs further investigation.

In any of the cases studied, the convection velocity of the tip vortices was shown to be the most important variable for the dynamic inflow effect. A computational method to obtain the convection velocity of the tip vortices for different tip speed ratio and axial induction factor was derived using existing work on the self-induced velocity of an infinite vortex helix with multiple vortices by Wood and Boersma [215]. This method gives a better estimation of the tip vortex convection velocity than simpler classic expressions when compared to experimental results. Dynamic inflow models for BEMT could benefit from explicitly taking into account the convection velocity of the tip vortices in their temporal

formulation since it physically drives the dynamic inflow effect.

In future work, the hypotheses on constant convection velocity of the tip vortices and constant radius of the tip vortex helix could be relaxed to improve the helical model. It could then be used to improve dynamic inflow models for the BEMT approach.

Acknowledgment

The work of R. Corniglion was funded by the ANRT (Association Nationale de la Recherche et de la Technologie), CIFRE agreement #2018/1790.

2.3.5 Appendix 1 Velocity induced by a set of helical vortices

The velocity induced by a set of helical vortices including a helical root vortex emitted at radius R_r shown in Fig. 2.18 with a desingularization core radius of r_c is computed with the following equation:

$$u_{i,x}(r,t) = -\frac{\lambda\Gamma_0}{4\pi R}\sum_{k=0}^{n_b-1}\left[\int_0^{+\infty}\frac{\left(1-\frac{r}{R}\cos(\lambda s+\frac{2k\pi}{n_b})\right)}{\left(\left(e_{cv}^2 s^2+1+\frac{r^2}{R^2}-2\frac{r}{R}\cos(\lambda s+\frac{2k\pi}{n_b})\right)^{1/2}+\frac{r_c}{R}\right)^3}ds + \int_0^{+\infty}\frac{\frac{R_r^2}{R^2}\left(1-\frac{r}{R}\cos(\lambda s+\frac{2k\pi}{n_b})\right)}{\left(\left(e_{cv}^2 s^2+\frac{R_r^2}{R^2}+\frac{r^2}{R^2}-2\frac{rR_r}{R^2}\cos(\lambda s+\frac{2k\pi}{n_b})\right)^{1/2}+\frac{r_c}{R}\right)^3}ds\right] \tag{2.29}$$

The velocity induced by the helical vortices with axial root vortices lying on the axis of the rotor is:

$$u_{i,x}(r,t) = -\frac{\lambda\Gamma_0}{4\pi R}\sum_{k=0}^{n_b-1}\int_0^{+\infty}\frac{\left(1-\frac{r}{R}\cos(\lambda s+\frac{2k\pi}{n_b})\right)}{\left(e_{cv}^2 s^2+1+\frac{r^2}{R^2}-2\frac{r}{R}\cos(\lambda s+\frac{2k\pi}{n_b})\right)^{3/2}}ds \tag{2.30}$$

using the notations introduced in section 2.3.3.

2.3.6 Appendix 2 Relation between axial induction factor and tip vortex helix properties

Wood and Boersma [215] presented a relation between the mean velocity in the far wake and the tip vortex helix circulation and pitch for a helix with multiple branches. Their

demonstration, based on different vortex and rotor radii, is here rewritten in the framework of the momentum theory to introduce the axial induction factor a and assuming that the radius of the helical system is equal to the radius of the rotor.

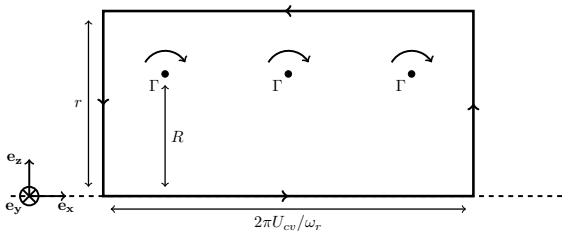

Figure 2.29: Closed contour used for Eq. 2.31 in the far wake.

The integral of the velocity around a closed contour, $\partial\Sigma$, shown in Fig. 2.29, a rectangular contour with one side $2\pi U_{cv}/\omega_r$ along the axis of rotation, and the other at a distance, r, from the axis, is equal to the enclosed circulation:

$$-n_b\Gamma = \int_{\partial\Sigma} \mathbf{u}.\mathbf{d}\sigma \tag{2.31}$$

The contribution of the two radial portions of the closed contour geometrically compensate each other in the integral of Eq. 2.31. As expressed by Wood and Boersma [215], if $r < R$ there is no enclosed circulation which means that the axial velocity at radius r is equal to the axial velocity on the rotor axis, therefore the axial velocity in the rotor far wake is constant for $r < R$. The momentum theory expresses the axial velocity inside the far wake as $(1-2a)U_\infty$ and the axial velocity outside the wake is U_∞. Thus Eq. 2.31 becomes:

$$-n_b\Gamma = \frac{2\pi U_{cv}}{\omega_r}(1-2a)U_\infty - \frac{2\pi U_{cv}}{\omega_r}U_\infty \tag{2.32}$$

and introducing the relation $U_{cv}/\omega_r = e_{cv}R/\lambda$,

$$aU_\infty = \frac{n_b\Gamma\lambda}{4\pi R e_{cv}} \tag{2.33}$$

This is compatible with the expression of the axial induced velocity on the rotor axis of Eq. 2.22 and extends it to the total axial induction factor.

2.4 Conclusion on the aerodynamics of wind turbines in imposed motions

The study of wind turbines in imposed surge motion has confirmed the mean thrust decrease and mean power increase for wind turbines operating at high tip speed ratio and fixed rotational speed found by Lienard et al. [106]. However, it can be expected that for a real floating wind turbine, the large thrust variation due to the surge motion would affect the dynamic of the floater and therefore modify the surge motion. Additionally, the floater could be subject to motions combining its 6 degrees of freedom: pitch, yaw, roll, surge, heave, and sway. The large variation of power at a fixed rotational speed are related to large torque variations. When the rotational degree of freedom of the rotor is taken into account together with the variable electrical torque of the generator due to the controller of the wind turbine, the rotational speed of the rotor is expected to change due to the large torque variation. The controller would also respond to the large torque variation by adjusting the pitch angle of the blades.

Here, we have showed that both a step of blade pitch or rotational speed induce the dynamic inflow phenomenon, while a step of surge velocity does not. However, the surge motion would cause both blade pitch and rotor speed variations for a real wind turbine due to the controller and rotational degree of freedom of the rotor, and dynamic inflow due to blade pitch and rotor speed variation would then occur. For the design of floating wind turbine, it is therefore important to properly model the interaction between the different physics influencing the behavior of the wind turbine. The DIEGO aero-hydro-servo-elastic simulation tool has been developed in-house at EDF R&D to simulation floater wind turbines in real-world operating conditions.

Regarding the numerous empirical correction models used with the BEM method, it is valuable to use the FVW method to provide a better insight into the aerodynamics of floating wind turbines, in particular for operating conditions which are challenging for the empirical correction models of the BEM method, which are encountered by floating wind turbines. Therefore, it was decided to add the FVW method to the in-house aero-hydro-servo-elastic simulation tool DIEGO.

The DIEGO tool will be presented next, with details on the implementation of the aerodynamic models, BEM and FVW. Within this work, the FVW model was added to the tool and the BEM model was overhauled. Both models are validated against a range of numerical and experimental datasets.

Chapter 3

DIEGO: An Aero-hydro-servo-elastic simulation tool with Free Vortex Wake

L'outil de simulation aéro-hydro-servo-élastique des éoliennes flottantes DIEGO est présenté. Il est couplé au module open-source OLAF pour utiliser la méthode Free Vortex Wake à lignes portantes pour l'aérodynamique des éoliennes flottantes. La librairie EXAFMM est couplée à OLAF pour paralléliser l'étape de calcul de la loi de Biot-Savart sur GPU. Une méthode de simplification du sillage est proposée pour réduire le coût de calcul et permettre d'effectuer des simulations d'une heure de temps physique, qui sont nécessaires pour l'étude des éoliennes flottantes. Le code DIEGO utilisant la méthode Free Vortex Wake est validé par rapport à des données experimentales et numériques. Les résultats obtenues avec la méthode Free Vortex Wake sont comparés à ceux obtenus avec la méthode Blade Element Momentum, qui est généralement utilisée pour la conception des éoliennes.

3.1 DIEGO: A coupled aero-hydro-servo-elastic tool for the study of floating wind turbines

3.1.1 What is DIEGO?

DIEGO is a numerical code aimed at simulating wind turbines. DIEGO stands for the French "*Dynamique Integrée des Eoliennes et Génératrices Offshore*". It has been developed mainly by Matteo Capaldo, Nicolas Relun, Christophe Peyrard and Yvan Bercovitz at EDF R&D. It can simulate onshore and offshore fixed or floating wind turbines. It models the aerodynamics, hydrodynamics, control and structural dynamics including elasticity of floating wind turbines.

The general structure of the code for the most general case of a floating wind turbine is shown in Fig. 3.1. The hydrodynamics module provides the kinematics of the tower base to the wind turbine module which models the aero-servo-elastic behavior of the wind turbine to return forces and torques to the hydrodynamics module. The floater kinematics is found by taking into account the loads due to the water, the moorings as well as those at the tower base.

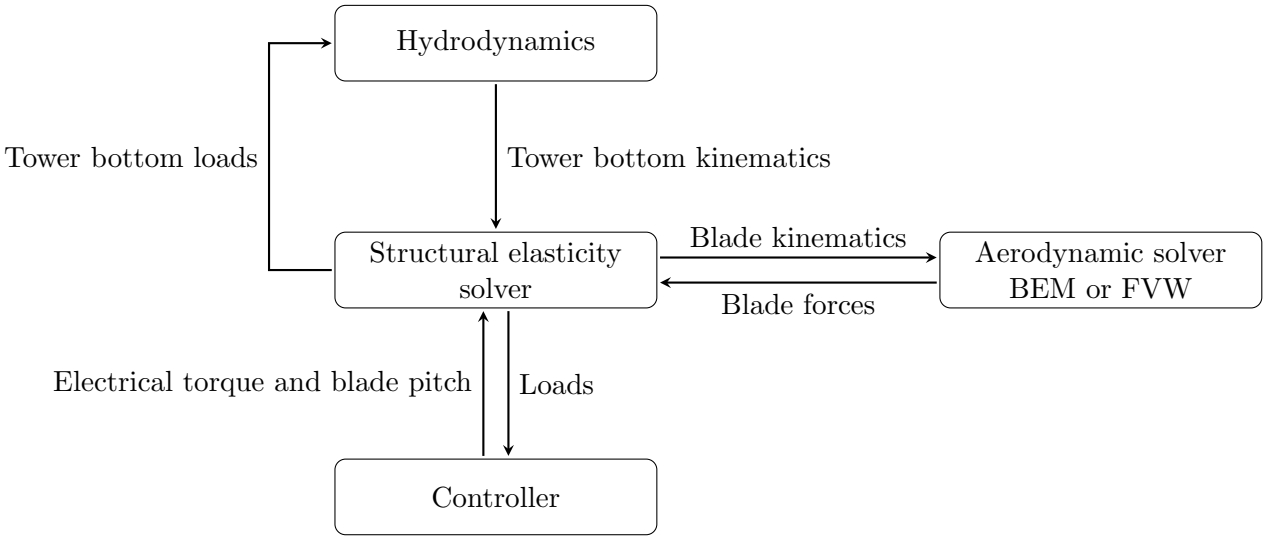

Figure 3.1: General architecture of DIEGO.

A typical visualisation of a DIEGO simulation of a floating wind turbine is shown in Fig. 3.2. The vorticity elements of the FVW are shown. Here, the blades are represented with volumes for graphical purposes but are discretized as aerodynamic lifting lines and structural Euler-Bernoulli beams [19] in the code.

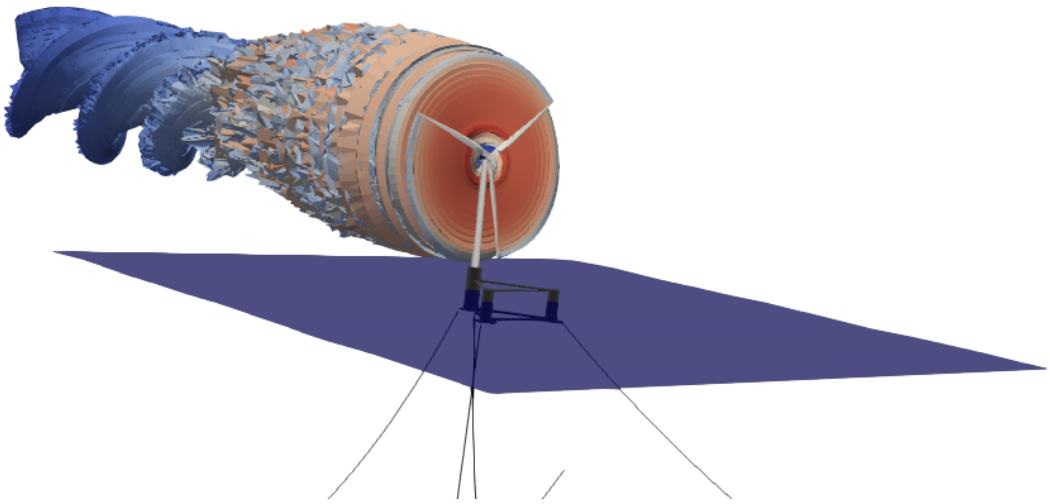

Figure 3.2: Typical visualization of a DIEGO simulation of a floating wind turbine using the FVW aerodynamics.

3.1.2 Hydrodynamics model

DIEGO uses the hydrodynamics simulation tool CALHYPSO developed in-house at EDF R&D. It uses potential flow theory to model the hydrodynamic forces on the floater. It is able to take into account first- and second-order effects [127].

The hydrodynamic forces on the floater are computed differently depending on the geometry of the different structural elements of the floater. For bodies with a characteristic size significantly smaller than the wavelength of the swell, the presence of the body does not affect the free-surface. It is generally considered that an object has no effect on the waves when $D/L < 0.2$ where D is the characteristic size of the object, its diameter for a cylinder, and L is the wavelength of the swell. When this conditions is true, the hydrodynamic forces on a cylinder can be computed with the Morison equation [131]:

$$\mathbf{F}_M = \rho C_M S \dot{\mathbf{u}}_T + \frac{1}{2}\rho C_D D \mathbf{u}_T \left|\mathbf{u}_T\right| \tag{3.1}$$

where C_M is an inertia coefficient, C_D is a drag coefficient, S is the cross-sectional area of the considered cylinder, $\mathbf{u}_T$ is the water velocity perpendicular to the axis of the cylinder. The dot represents a time-derivative.

For larger bodies, the presence of the body induces diffraction and radiation of waves that are respectively simplified or not taken into account by the Morison equation. Therefore, a pre-computed hydrodynamic database is used to take into account the radiation as well as diffraction due to the body. The Boundary Element Method code NEMOH [15] is used to compute the added mass and damping matrices due to radiation as well as the Froude-

Krylov forces. The radiation forces are then computed with the Free Surface Memory Effect using a convolution [130]. The different treatment of the hydrodynamic forces is shown in Fig. 3.3 for a generic floater. The hydrodynamic code CALHYPSO has been compared to experimental data and state-of-the-art hydrodynamic codes in the OC6 Phase I project [155] and seen to produce acceptable results.

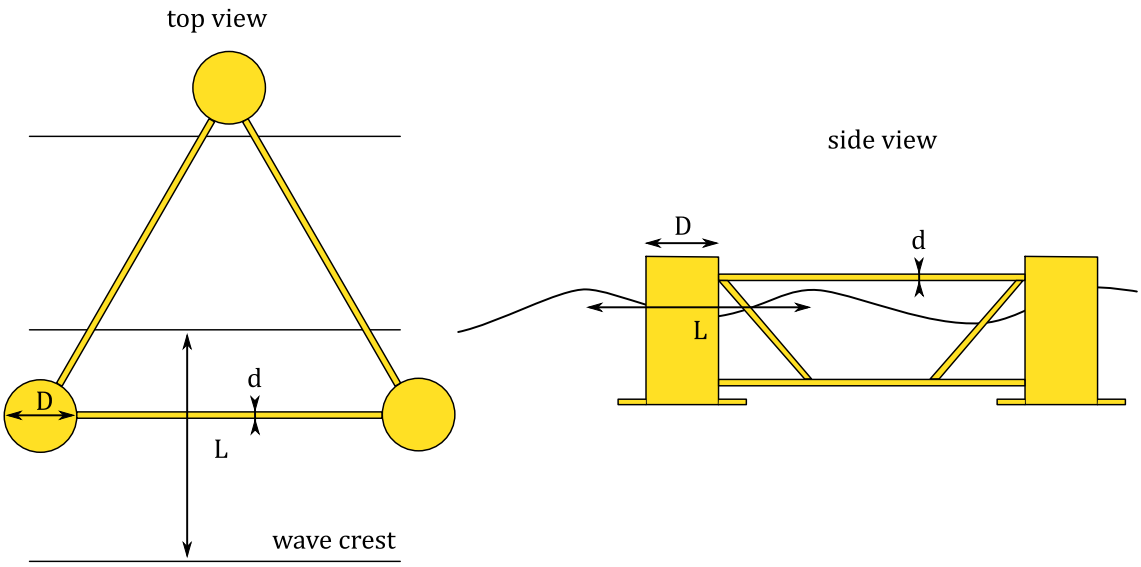

Figure 3.3: The structural struts of diameter d can be treated with the Morison equation because their size is small compared to the wave length L. The buoyancy cylinders of diameter D are too large to be treated with the Morison equation: a hydrodynamic database computed with NEMOH is used.

3.1.3 Moorings

DIEGO can model the mooring forces using either a quasi-steady method or a finite element method.

The tension at the attachment point between the mooring line and the floater, called the fairlead, is often studied. Simulation tools using quasi-steady mooring forces or a finite element method were compared in the OC4 project [156]. Differences in the evolution in time of the fairlead tension were found between the simulation tools using quasi-steady forces and finite elements. However, it did not generate large differences for the motion of the semi-submersible studied in the OC4 project.

3.1.4 Control

DIEGO is able to simulate the behavior of a wind turbine controller, which sets the pitch angle of the blade, the yaw of the turbine nacelle, and the electrical torque of the generator on the rotor axis as a function of the current operating conditions. For the purpose of

wind energy research, dedicated wind turbine controller algorithms are often released for a reference wind turbine design. For example, the NREL 5MW reference wind turbine design [90] includes the source code of its controller. More recently, Abbas et al. [6] introduced the ROSCO controller, which is an open-source toolbox to design and create wind turbine controller for both fixed-bottom and floating applications [136]. DIEGO can be connected to these external controllers and then apply the chosen blade pitch, yaw angle, and generator electric torque to the wind turbine. The rotational degree of freedom on the axis of the rotor is solved separately than the rest of the structural dynamics.

3.1.5 Aero-elasticity

The aero-elasticity algorithm uses a predictor-corrector approach. The algorithm is represented in Fig. 3.4. The structural motion is first computed using aerodynamic forces based on rigid body motions of the current time step with the elastic displacement, velocities and accelerations from the previous time step: this is the predictor step. The aerodynamic forces are then computed with the structural motion found by the predictor step, and the structural motion is solved again with the new aerodynamic forces: this is the corrector step.

The structural dynamics are solved using a multi-body method, where Lagrange multipliers are used to couple the different elastic bodies together. The blades are modeled as Euler-Bernoulli beams [19]. The tower is modeled as a Timoshenko beam [225]. The nacelle is a rigid body.

The Newmark Hilber-Hughes-Taylor (HHT) [75] algorithm is used for the time integration of the structural motion to obtain the elastic displacements X on any of the 6 degrees of freedom for each element. The algorithm is as follows for the blades and the tower:

First, the external forces, F_{ext}, for the new time step are computed taking into account the elastic displacement for the previous time step, X_n, with the rigid body motion obtained from the tower bottom kinematics given by the hydrodynamics model as well as blade rotation and blade pitch due to the controller. F_{ext} includes the inertial and gravity forces which are computed on the undeformed bodies. The external forces F_{ext} also include the aerodynamic forces which are computed using deformed body geometries since the elastic deformation of the blades can have a significant effect on the aerodynamic forces. The resolution is started by taking $X_{n+1} = X_n$, $\dot{X}_{n+1} = \dot{X}_n$ and $\ddot{X}_{n+1} = \ddot{X}_n$.

The elastic deformations X_{n+1}, velocities $\dot{X}_{n+1}$ and accelerations $\ddot{X}_{n+1}$ are iteratively updated to reach the values corresponding to the new aero-elastic equilibrium at time step $n+1$. This new equilibrium is considered found when a convergence criterion is met on the residual R_{n+1}. The equilibrium is computed as:

$$R_{n+1}^{i+1} = F_{ext} - KX_{n+1}^{i+1} - M\ddot{X}_{n+1} - C\dot{X}_{n+1} \tag{3.2}$$

where K is the rigidity matrix, M is the mass matrix, C is the damping matrix, i is the index of the iteration of the Newmark HHT algorithm, and n the index for the time step.The elastic displacement, velocities and accelerations are updated until the following convergence criterion is met:

$$min(\frac{\|R_{n+1}^{i+1} - R_{n+1}^{i}\|}{\|R_{n+1}^{i+1}\|}, \|R_{n+1}^{i+1}\|) < \epsilon \tag{3.3}$$

where ϵ is a tolerance taken equal to 10^{-6} in DIEGO. If the convergence criterion is not met, the elastic displacement is updated by solving the linear system:

$$\begin{gathered} AX_l = R_{n+1}, \text{ with } A = \alpha_{hht}K + \gamma_{hht}\frac{\alpha_{hht}}{\beta_{hht}h}C + \frac{1}{\beta_{hht}h^2}M \\ X_{n+1}^{i+1} = X_{n+1}^{i} + X_l. \end{gathered} \tag{3.4}$$

where α_{hht} is a user parameter between 0 and 1, $\gamma_{hht} = \frac{3}{2} - \alpha_{hht}$ and $\beta_{hht} = (2 - \alpha_{hht})^2/4$. The linear system is solved using the sparse LU method of the Eigen library[67]. The elastic velocities and accelerations are then updated according to the Newmark HHT algorithm:

$$\begin{gathered} \ddot{X}_{n+1} = \frac{1}{\beta_{hht}h^2}(X_{n+1} - X_n) - \frac{1}{\beta_{hht}h}\dot{X}_n - \left(\frac{1}{2\beta_{hht}} - 1\right)\ddot{X}_n \\ \dot{X}_{n+1} = \ddot{X}_n + h(1 - \gamma_{hht})\ddot{X}_n + h\gamma_{hht}\ddot{X}_{n+1} \end{gathered} \tag{3.5}$$

The damping matrix is computed as a combination of the mass matrix and the rigidity matrix:

$$C = \alpha_R K + \beta_R M \tag{3.6}$$

where α_R and β_R are Rayleigh coefficients. They are most often obtained from experimental free decay tests for a particular structure.

3.2 Aerodynamics model

3.2.1 Blade Element Momentum Theory

An implementation of the BEM method is already available in DIEGO. Since the BEM is corrected with different empirical models, it is important to detail how these models are implemented and how they interact with each other, as pointed out by Madsen et al.

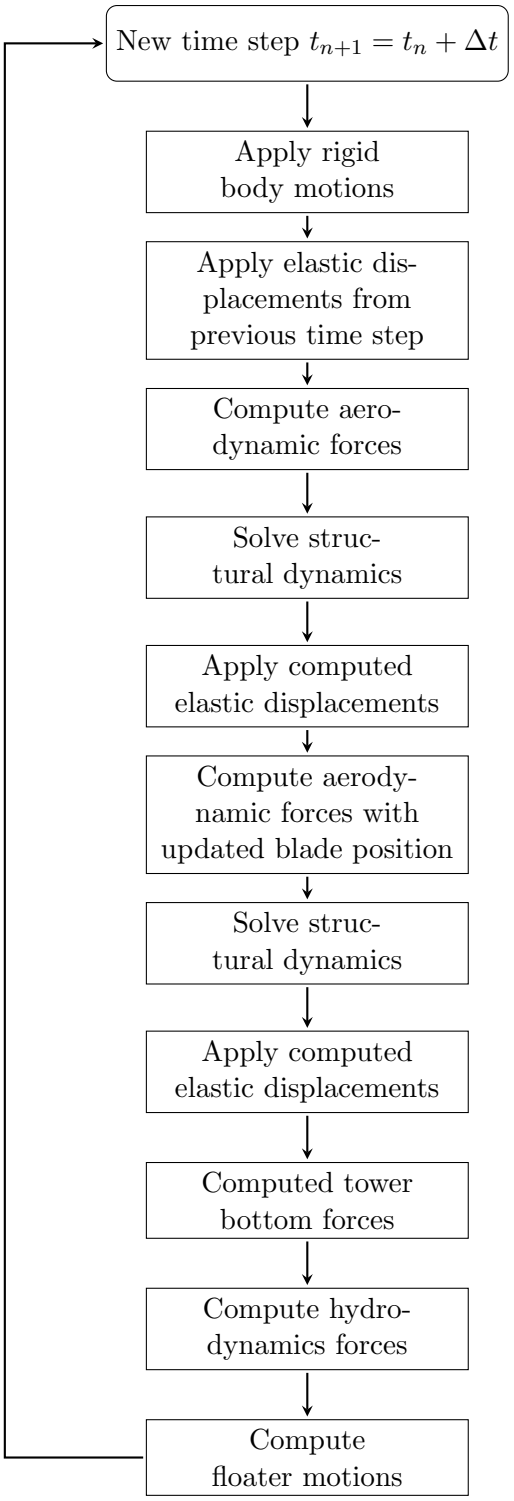

Figure 3.4: Schematic of aero-elasticity algorithm.

[113]. The details of BEM and correction models implemented in DIEGO are presented next.

DIEGO uses a local blade element formulation of the BEM. The equations are solved for each individual blade element rather than for an annulus on the rotor disc. This blade element formulation is for example also used in OpenFAST [5].

For non-lifting bodies, such as the tower or cylindrical root of the blades, the aerodynamic force is computed using a drag coefficient.

$$\mathbf{F}_a = \frac{1}{2}\rho c l C_d |\mathbf{u}_T| \mathbf{u}_T \tag{3.7}$$

where C_d is the drag coefficient of the element, c its largest width normal to the element axis, l its length and $\mathbf{u}_T$ is the relative wind velocity normal to the element axis which is along the spanwise direction.

For lifting elements, the algorithm starts by computing the axial and tangential induction factor a and a' with BEM using a turbulent wake state correction model for high induction factors. The computation of the induction factors is done iteratively until convergence is reached with the method explained next.

The inflow wind velocity $\mathbf{U}_w^d$ at the aerodynamic center of the element located at the quarter chord position is expressed in the blade rotor disc frame that is composed of the axis of the rotor for the axial direction, the vector aligned with the blade element axis normal to the rotor axis for the radial direction and the cross product of these two vectors for the tangential direction. The variables expressed in this frame will be expressed with the ^{d} exponent and the three components of the different velocities will be written (u, v, w) with indexes.

The structural velocity of the blade element $\mathbf{U}_s^d = \left(u_s^d, v_s^d, w_s^d\right)$ is computed from the rigid body motion (floater motion and rotation of the rotor) and the velocity due to the elastic deformations. It is expressed in the blade rotor disc frame.

The computation of the induction factors is an iterative procedure. The relative wind velocity on the blade element in the blade rotor disc frame $\mathbf{U}_r^d$ is computed as:

$$\mathbf{U}_r^d = \begin{pmatrix} u_r^d \\ v_r^d \\ w_r^d \end{pmatrix} = \begin{pmatrix} \left(u_w^d - u_s^d\right)(1-a) \\ v_w^d \\ \left(w_w^d - w_s^d\right)(1+a') \end{pmatrix} \tag{3.8}$$

The inflow angle is computed from the components of the relative wind velocity in the blade rotor disc frame:

$$\phi = \arctan\left(\frac{u_r^d}{-w_r^d}\right) \tag{3.9}$$

The angle of attack of the blade element, α, is computed from the relative wind velocity on the blade element. It is used to retrieve the lift and drag coefficients from the airfoil polars. If the dynamic stall model of Beddoes-Leishman [103] is used, it is applied at this step to express the lift and drag coefficients from the angle of attack taking into account unsteady airfoil aerodynamics.

The aerodynamic coefficients and inflow angle are used to compute the force coefficient normal and tangential to the rotor disc. C_n^d and C_n are the force coefficients normal to the rotor disc and normal to the airfoil chord, respectively. Similarly, C_t^d and C_t are the force coefficients tangential to the rotor disc and tangential to the airfoil chord, respectively:

$$C_n^d = C_l \cos\phi + C_d \sin\phi \tag{3.10}$$

$$C_t^d = C_l \sin\phi - C_d \cos\phi \tag{3.11}$$

The loss factor, F, is the product of the tip-loss factor, F_{tip}, and the hub-loss, F_{hub}:

$$F_{tip} = \frac{2}{\pi} \arccos\left(\exp\left(\frac{n_b\,(r-R)}{2r|\sin\phi|}\right)\right) \tag{3.12}$$

$$F_{hub} = \frac{2}{\pi} \arccos\left(\exp\left(\frac{n_b\,(R_{hub}-r)}{2R_{hub}|\sin\phi|}\right)\right) \tag{3.13}$$

where R_{hub} is the radius of the rotor hub.

When not in a turbulent wake state, the axial induction factor is:

$$a = \frac{\frac{\sigma C_n^d}{4F\sin^2\phi}}{1+\frac{\sigma C_n^d}{4F\sin^2\phi}} \tag{3.14}$$

where the local solidity at radius r is $\sigma = n_b c/(2\pi r)$.

To know whether the turbulent wake state correction has to be applied, the value of the induction factor at the last iteration of the convergence algorithm is used. The transition between the momentum theory and the turbulent wake state model is $a = 0.3539$. If the axial induction factor is larger than this threshold, the turbulent wake state model is used:

$$a = \frac{\frac{\sigma C_n^d}{4F\sin^2\phi}}{1+\frac{\sigma C_n^d}{4F\sin^2\phi}} \frac{4a\,(1-a)}{0.6+0.61a+0.79a^2} \tag{3.15}$$

where the value of a in the right hand side is the value from the last iteration of the convergence algorithm.

The tangential induction factor a' is:

$$a' = \frac{\frac{\sigma C_t^d}{4F \sin\phi \cos\phi}}{1 + \frac{\sigma C_t^d}{4F \sin\phi \cos\phi}} \tag{3.16}$$

and does not need to be corrected for a turbulent wake state.

The value of the induction factors obtained when the algorithm has converged is the quasi-steady value of the induction factors. The algorithm is considered converged when the relative change of both the axial and tangential induction factors over one iteration are lower than a set threshold.

If the user chooses to activate the dynamic inflow model, it is used once the quasi-steady value of the induction factors has been found. The dynamic inflow model of Øye [178] is implemented. The time constants of the model take into account the loading of the rotor through a global induction factor for the whole rotor disc that is written a_g.

$$\begin{aligned}
&\frac{du_{i,int}}{dt} + \frac{1}{\tau_1} u_{i,int} = k \frac{du_{i,qs}}{dt} + \frac{1}{\tau_1} u_{i,qs} \\
&\frac{du_i}{dt} + \frac{1}{\tau_2} u_i = \frac{1}{\tau_2} u_{i,int} \\
&\tau_1 = \frac{1.1}{1 - 1.3 a_g} \frac{R}{U_\infty} \\
&\tau_2 = \left(0.39 - 0.26 \left(\frac{r}{R}\right)^2\right) \tau_1 \\
&k = 0.6
\end{aligned} \tag{3.17}$$

where $u_{i,qs}$ is the quasi-steady axial induced velocity, $u_{i,int}$ is an intermediate induced velocity used in the model and u_i is the axial induced velocity taking into account the dynamic inflow. The model is numerically implemented using a first-order explicit finite difference scheme. The value of a_g in the expression of the time constant τ_1 is limited to a maximum of 0.7 to prevent the denominator from reaching 0.

The value of the quasi-steady induced velocity used as an input to the dynamic inflow model is computed from the quasi-steady induction factor:

$$u_{i,qs} = -a_{qs} \left(u_w^d - u_s^d\right) \tag{3.18}$$

The value of the local induction factor taking into account dynamic inflow is then computed as:

$$a = -\frac{u_i}{u_w^d - u_s^d} \tag{3.19}$$

and it is numerically limited to a lower value of 0 and an upper value of 1.

The global induction factor over the rotor disc, a_g, which represents the global loading of the rotor is computed from the global thrust coefficient computed at the last time step. In a wind turbine simulation with inflow turbulence, wind shear and time-varying wind velocity, the global thrust coefficient is computed using the average wind velocity over all the blade elements $\bar{\mathbf{U}}$:

$$C_T = \frac{T}{\frac{1}{2}\rho\pi R^2 |\bar{\mathbf{U}}|^2} \tag{3.20}$$

where $|\bar{\mathbf{U}}|$ is the magnitude of the average velocity over the blade elements at their current positions. The global induction factor is then computed from standard momentum theory if $C_T < 0.915$, which corresponds to the threshold between momentum theory and turbulent wake state in DIEGO as:

$$C_T = 4a_g\left(1 - a_g\right) \tag{3.21}$$

while for values $C_T > 0.915$, the turbulent wake state model is used. In this case, a_g is the positive solution of equation:

$$C_T = 0.6 + 0.61a_g + 0.79a_g^2 \tag{3.22}$$

Next, the variables related to the inflow misalignment correction model are computed. Since DIEGO is used to study floating wind turbines, the misalignment between the inflow and the rotor might not be only related to a nacelle yaw misalignment, the steady pitch of the floater due to the aerodynamic thrust on the rotor can also lead to a misalignment between the inflow and the rotor that adds to the geometrical tilt angle of the rotor. The yaw correction model is adapted to take this into account. The inflow angle of the wind, γ, is computed as the angle between the average inflow wind over the blade elements, $\bar{\mathbf{U}}$, and the axis of the rotor $\mathbf{e}_R$:

$$\gamma = \arccos\left(\frac{\mathbf{e}_R.\bar{\mathbf{U}}}{|\mathbf{e}_R||\bar{\mathbf{U}}|}\right). \tag{3.23}$$

The blade azimuth, ψ, used in the following inflow misalignment model has for reference the most downwind position of the rotor disc. It is equal to zero when the blade is at the most downwind position relative to the average inflow wind $\bar{\mathbf{U}}$.

The axial induction factor, a, which already includes the turbulent wake state, dynamic

stall and dynamic inflow models is corrected for inflow misalignment by multiplying it with the misalignment correction factor, L_m:

$$L_m = 1 + \frac{15}{64}\pi\frac{r}{R}\tan\left(\frac{\chi}{2}\right)\cos\psi \tag{3.24}$$

where χ is the wake skew angle, which is the angle between the axis of the rotor and the direction of the wake. The wake skew angle, χ, is different from the inflow angle γ as shown in Fig. 3.5. It is a function of the induction of the wind turbine. The approximated equation presented by Burton et al. [35] is used to compute the wake skew angle from the inflow angle:

$$\chi = (0.6a_g + 1)\,\gamma \tag{3.25}$$

This inflow misalignment deflects the wake of the wind turbine, and is being investigated [79, 134] to reduce the effect of the wake of wind turbines on the wind turbines located downwind.

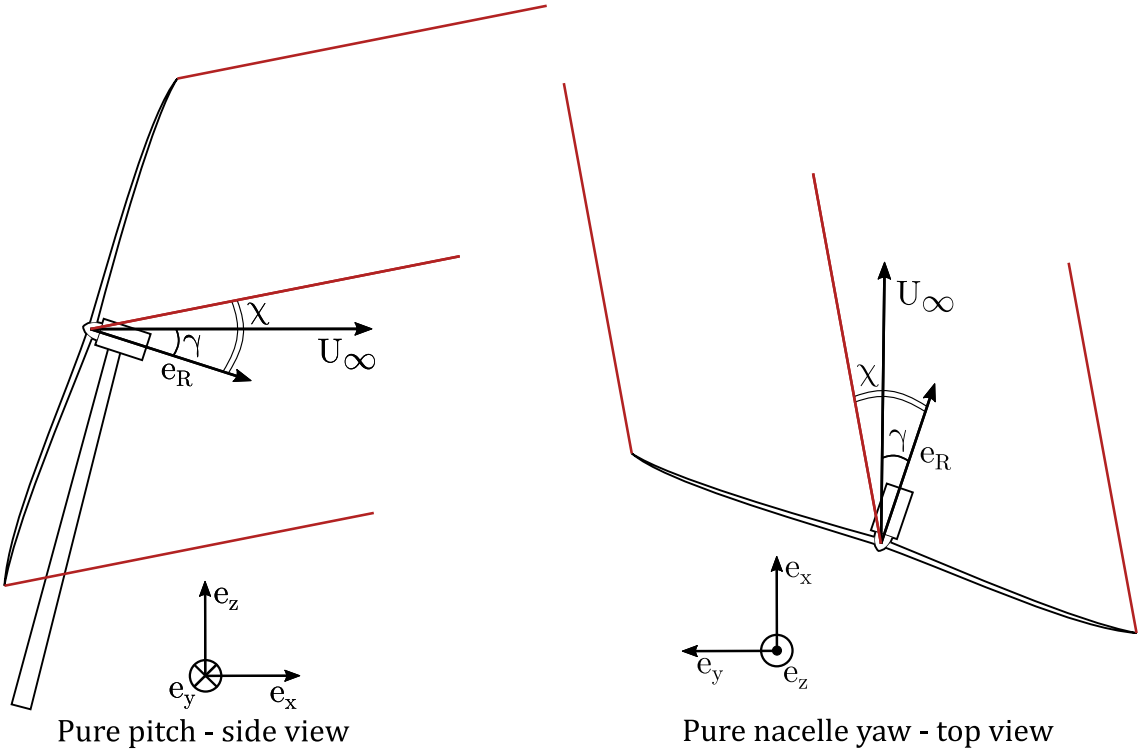

Figure 3.5: Inflow angle γ and wake skew angle χ for pure floater pitch and pure nacelle yaw. $\mathbf{e}_R$ is the unit vector along the axis of rotation of the rotor. The red lines show the direction of the wake.

Overall, the BEM uses a large number of empirical correction models: tip and hub losses, dynamic stall, turbulent wake state, dynamic inflow, and inflow misalignment models.

They are adapted for wind turbines operating in simple conditions but used in more complex conditions: for example, the dynamic inflow model and the inflow misalignment model were designed for a rotor operating in an uniform inflow, yet they are used for wind turbines operating with a sheared inflow wind. The turbulent wake state model is constructed for the global rotor induction, but used on the local blade element induction. The empirical corrections models for the BEM are therefore used in conditions for which they might not be well-suited, with possibly spurious interactions between the different correction models. However, their very low computational cost and the relative quality of the results obtained with them, when compared to experimental data, has made BEM theory one of the main numerical methods used for the design of wind turbines.

Alternatively, the Free Vortex Wake method is able to capture most of the aerodynamic behavior of wind turbines. It requires the use of airfoil polars and dynamic stall models when using the lifting line formulation, but is otherwise able to model turbulent wake state, dynamic inflow, and inflow misalignment directly. The FVW method used in DIEGO is presented next.

3.2.2 Free Vortex Wake

3.2.2.1 Lifting-line formulation

As part of this work, it was decided to add a FVW model for the aerodynamics of wind turbines in DIEGO. Indeed, the literature review and work on imposed motions (see Chapter 2) showed that the method was able to capture the aerodynamics of a wind turbine rotor in motion at a limited computational cost. FVW captures the effect of the rotor motion and misalignment with the inflow for a lower computational cost than other models such as the actuator line method and blade-resolved CFD. OLAF [170], the Free Vortex Wake (FVW) module of the open source wind turbine simulation tool OpenFAST was chosen to be coupled to DIEGO. This choice was made because OLAF is easier to use as a module than the previously used CACTUS: it is structured as a module coupled to the rest of the OpenFAST code which makes it particularly suitable to being coupled to DIEGO. During this work, it also benefited from ongoing open source development and discussions from the National Renewable Energy Laboratory (NREL) and the wind energy community.

OLAF offers two different options for vortex emission: the vorticity can be either shed directly from the lifting-line (Fig. 3.6c) or it can be shed from the trailing edge (Fig. 3.6b). OLAF stores the vorticity information as panel strengths, but it uses a vortex line formulation to evaluate the induced velocities. A panel is a quadrangle for which the edges are vortex lines. The circulation of a vortex line separating two panels is computed as the difference between the strength of the two panels of which this vortex line is an edge. The

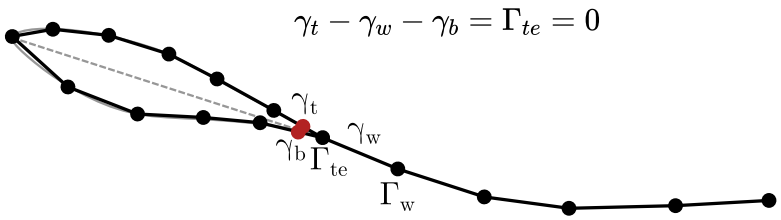

(a) Panel method

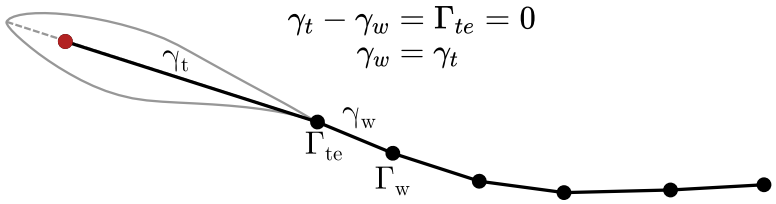

(b) OLAF trailing edge emission

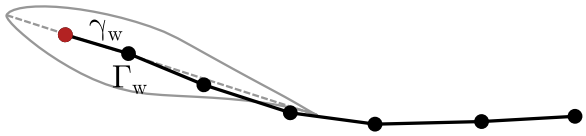

(c) OLAF direct emission

Figure 3.6: Wake emission: (a) for a panel vortex method, (b) OLAF trailing edge emission and (c) OLAF direct emission used in DIEGO. The red dot shows where the flow is solved to compute the circulation that is then emitted in the wake. For every case, Γ_w corresponds to the first freely convecting vortex. The outline of the airfoil is shown in grey.

two vorticity emission methods are shown in Fig. 3.6 together with the emission method for a panel vortex method modeling the shape of the airfoil.

When using the trailing edge emission formulation, the panel strength of the first wake panel is set to equal strength of the panel on the blade. This is done to respect the Kutta condition: the trailing edge should have no circulation. An example of this is given by Katz and Plotkin [93, p.435] for a panel-based vortex method. This means that when the emission of the wake at the trailing edge is used, a variation of the lift due to the flow conditions at the quarter-chord is changing the panel strength of the first wake panel due to the applied Kutta condition, which means that it changes the value of the first vortex line shed from the wing that has already convected at a distance $u\Delta t$, where u is the local flow speed and Δt the time step used, because its circulation is the difference between the panel strength of the first wake panel (set equal to the wind panel) and the second wake panel. To summarize: the flow conditions at the quarter chord are directly influencing the vortex placed approximately 3/4 chord and $u\Delta t$ further into the wake. This could lead to

an improper temporal behavior of the induction at the lifting line position.

In the case of the panel-based vortex method with panels around the airfoil profile (Fig. 3.6a), the value of the first wake panel is chosen so that the trailing edge circulation is zero, in order to meet the Kutta condition. The strength of the first wake panel is equal to the difference between the strength of the panel place next to the trailing edge on the upper and lower part of the airfoil. For the panel approach, the surface of the airfoil is fully discretized and the strength of the panels on the airfoil is computed at each time step to respect the no-flow condition. The panels placed next to the trailing edge and which change the value of the first wake panel are much more local than in OLAF's trailing edge wake emission.

OLAF's trailing edge wake emission is not adapted to temporal simulations since it induces instantaneous changes in the wake far from the source of those changes.

To show this, a good validation case is the pitching wing of Theodorsen [195]. One can validate both the added mass effect of the non-circulatory local airfoil unsteady aerodynamics and the circulatory contribution. For the BEMT, the dynamics of the circulatory contribution is accounted for using empirical models, here with the Beddoes-Leishman [103] dynamic stall model, while it is accounted for directly in the Free Vortex Wake method. The results for both vorticity emission methods for the pitching wing of Theodorsen are shown in section 3.3.3 (page 116). These results confirm the above arguments that the trailing edge wake emission (Fig. 3.6b) does not properly model the shed vorticity, and that the lifting-line wake emission (Fig. 3.6c) is a better model choice.

3.2.2.2 Desingularization model

The Biot-Savart law for a vortex segment with the nomenclature of Fig. 3.7 is written:

$$\mathbf{u_\Gamma}\left(\mathbf{x_p}\right) = \frac{\Gamma}{4\pi} \frac{\left(|\mathbf{r_1}| + |\mathbf{r_2}|\right)\left(\mathbf{r_1} \times \mathbf{r_2}\right)}{|\mathbf{r_1}||\mathbf{r_2}|\left(|\mathbf{r_1}||\mathbf{r_2}| + \mathbf{r_1} \cdot \mathbf{r_2}\right)}. \tag{3.26}$$

A desingularization model is applied to the Biot-Savart law. It serves both numerical and physical purposes. Its main point is to remove the singular behavior of the Biot-Savart equation: it prevents the value of the induced velocity to blow-up when the evaluation distance goes to zero. It also models the physical behavior of real vortices, as a real vortex does not have an infinite velocity. The vortex has a so-called "core" in which viscous effects dominate the flow. The "core size" or "core radius" is the common name of the distance between the center of the vortex and the maximum of tangential velocity.

In OLAF, there are four already available desingularization models: the Offset, Rankine, Lamb-Oseen and Vatistas models. Writing r_c the desingularization parameter used to represent the core radius and l the length of the vortex segment, the Offset model is:

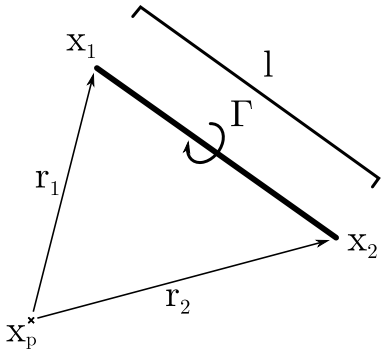

Figure 3.7: Variables used to compute the velocity induced by a vortex segment of circulation Γ at a point $\mathbf{x_p}$ in space. $\mathbf{r}_1 = \mathbf{x}_1 - \mathbf{x}_p$, $\mathbf{r}_2 = \mathbf{x}_2 - \mathbf{x}_p$, $l = |\mathbf{x}_2 - \mathbf{x}_1|$.

$$\mathbf{u_\Gamma}\left(\mathbf{x_p}\right) = \frac{\Gamma}{4\pi} \frac{\left(|\mathbf{r_1}| + |\mathbf{r_2}|\right)\left(\mathbf{r_1} \times \mathbf{r_2}\right)}{|\mathbf{r_1}||\mathbf{r_2}|\left(|\mathbf{r_1}||\mathbf{r_2}| + \mathbf{r_1} \cdot \mathbf{r_2}\right) + r_c^2 l^2}. \tag{3.27}$$

The three other models are based on a normalization factor, K_v, which is a function of the normalized radial distance to the vortex line $\rho = |\mathbf{r_1} \times \mathbf{r_2}| / l$ such that:

$$\mathbf{u_\Gamma}\left(\mathbf{x_p}\right) = K_v(\rho)\frac{\Gamma}{4\pi} \frac{\left(|\mathbf{r_1}| + |\mathbf{r_2}|\right)\left(\mathbf{r_1} \times \mathbf{r_2}\right)}{|\mathbf{r_1}||\mathbf{r_2}|\left(|\mathbf{r_1}||\mathbf{r_2}| + \mathbf{r_1} \cdot \mathbf{r_2}\right)}. \tag{3.28}$$

The Rankine model is:

$$K_v = \begin{cases} \frac{\rho^2}{r_c^2} \text{ , if } \frac{\rho^2}{r_c^2} < 1 \\ 1 \text{ , otherwise.} \end{cases} \tag{3.29}$$

whereas the Lamb-Oseen model is:

$$K_v = 1 - \exp\left(-\alpha \frac{\rho^2}{r_c^2}\right) \text{ , where } \alpha = 1.25643 \tag{3.30}$$

and the second-order Vatistas model is such that:

$$K_v = \frac{\frac{\rho^2}{r_c^2}}{\sqrt{1 + \frac{\rho^4}{r_c^4}}}. \tag{3.31}$$

based on the general model of Vatistas et al. [206].

The quality of these different desingularization core models for segment based lifting line free vortex wake is assessed in order to choose one of the options available in OLAF and to keep this desingularization model for all cases thereafter. The tangential velocity induced by a vortex segments of length l placed symmetrically around the origin is shown in Fig. 3.8. Multiple slenderness ratios r_c/l are shown because it influences the desingularization. The

Rankine model has a sharp transition between the vortex core and the outer part of the vortex due to the threshold effect in its formulation (see Eq. 3.29). It seems therefore less suitable to model real vortices than the other models since real vortices do not have this sharp transition. The Offset model shows a much lower maximum induced velocity than the other models. The Lamb-Oseen and the second-order Vatistas model have very similar results.

In the framework of the free vortex wake method, it is important that the different segments combine themselves together to form a longer vortex in order to properly model the tip vortices emitted by the blades of a wind turbine. To verify that the vortices correctly assemble with the different desingularization models, the velocity induced by two consecutive vortex segments of length l place respectively between $z/l = -1/2$ and $z/l = 1/2$ for the first one and $z/l = 1/2$ and $z/l = 3/2$ for the second one. The results are shown in Fig. 3.9 for $r_c/l = 0.2$. The Offset desingularization model shows an increase of the induced velocity at the transition between the two vortex segments at $z/l = 1/2$. This is not a desirable behavior for a desingularization model. One would expect that the velocity field induced by two consecutive vortex segments of length l would be equivalent to a single segment of length $2l$. The three models based on the ortho-radial distance to the vortex segment (Rankine, Lamb-Oseen and Vatistas) have this expected behavior. Similar results are found for other slenderness ratio r_c/l.

Given that the Rankine desingularization has a sharp transition between the inner core and the outer part of the vortex and that the Offset desingularization model does not assemble properly for consecutive vortices, the Lamb-Oseen and Vatistas model seem to be preferable over the other two models, and they show a similar distribution of the induced velocity. In the following, the Vatistas model is used if not specified otherwise. OLAF includes a numerical safeguard to avoid any division by 0 since the use of the K_v factor does not prevent this to happen. It sets the induced velocity to 0 if the denominator in the Biot-Savart equation is equal to 0, which would happen if the evaluation point is placed on the vortex segment.

3.2.2.3 Desingularization parameter: vortex core size

The vorticity emitted by a wind turbine blade is a vortex sheet that quickly rolls-up to form strong tip and root vortices. Advances in measurement techniques have recently enabled measurements of the core radius of vortices emitted by wind turbines. In particular, Mauz et al. [122] measured the core size of the tip vortex behind a full-scale wind turbine with an unmanned aerial vehicle. The available data on tip vortex core size of wind turbines is reported in Table 3.1. The data is separated between phase-averaged measurements and instantaneous measurements. The phase-averaging process increases the measured core size because of its smoothing effect.

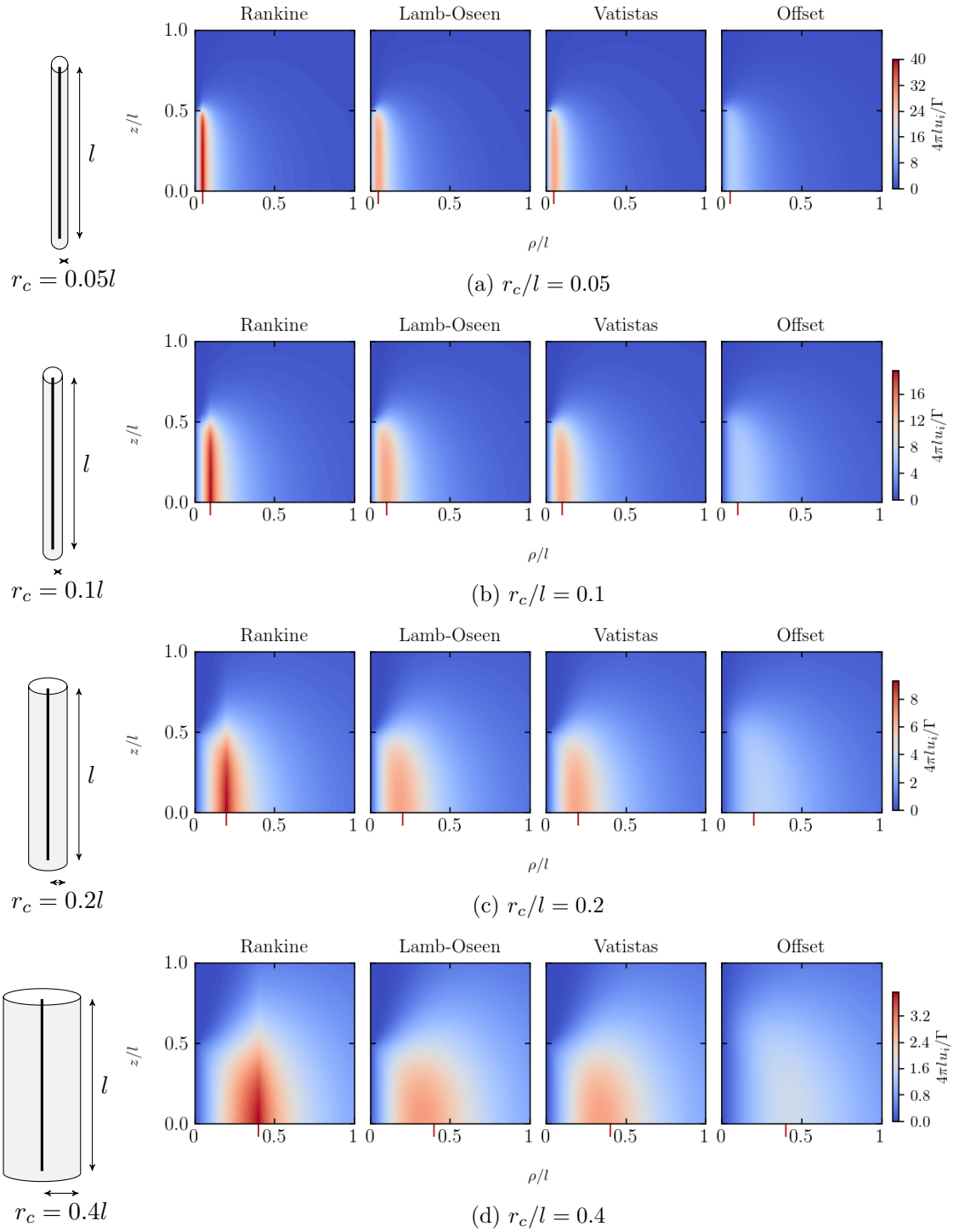

Figure 3.8: Non-dimensional tangential velocity induced by a vortex filament of length l placed symmetrically around the origin shown for various vortex core size r_c and the different desingularization models available in OLAF. The red tick shows the core radius.

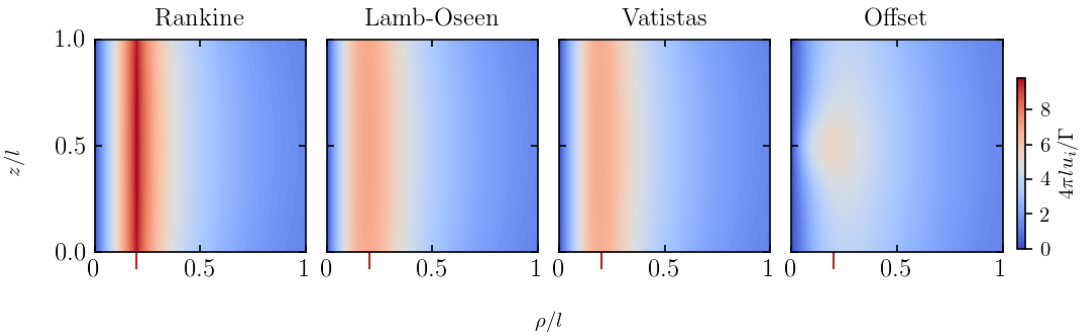

Figure 3.9: Non-dimensional tangential velocity induced by two consecutive vortex filaments of length l placed between $z/l = -1/2$ and $z/l = 1/2$ for the first one and $z/l = 1/2$ and $z/l = 3/2$ for the second one, shown for $r_c/l = 0.2$, and the different desingularization models available in OLAF. The red tick shows the core radius.

Table 3.1: Experimentally measured core radius size of wind turbine tip vortices

Wind turbine	r_c/R		R $[m]$
	Instantaneous	Phase-averaged	
Enercon E-112 [122]	0.011	-	57
MEXICO [29]	-	0.0067 - 0.018	2.25
BeRT [185]	0.008	0.011	1.5
Sherry et al. [175]	0.004 - 0.006	0.006 - 0.011	0.115
Ostovan et al. [140]	-	0.017	0.47
1:25 GROWIAN [49]	-	0.0048 - 0.0098	2

The vortex core radius has a value of about 1% of the rotor radius, but is often expressed as a fraction of the tip chord. For example, Devenport et al. [50] measured the core radius of a vortex behind a rectangular wing and found the core radii to be between $0.019c$ and $0.045c$. However, wind turbine blades are often tapered toward the tip making their tip chord quite small. This means that using a chord-based desingularization core radius would lead to a small core radius for the tip vortex which accounts for most of the circulation. Thus, the tip vortex would have a smaller core radius than tip vortices of real wind turbines. Choosing a fixed core radius of $0.01R$ allows for a tip vortex that has a core radius similar to experimentally measured ones.

It is important to verify that this core radius does not affect the shed vorticity. The shed vortices accounting for the temporal variation of the lift of the blade should not be at a distance smaller than the core radius from the blade, or other shed vortices, because it would give a nonphysical temporal variation of the lift of the blade.

We will consider a hypothetical wind turbine rotating at a fixed speed with no inflow represented in Fig. 3.10. This is purely a hypothetical case since a real wind turbine would not be rotating with no inflow, but it represents a limit case for the evaluation of the distance between shed vortices, since an inflow would convect the vortices further away from the blade.

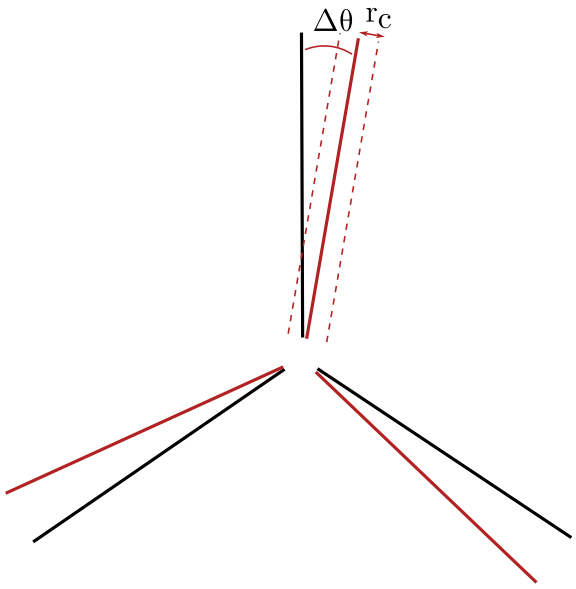

Figure 3.10: Hypothetical rotor with no inflow. Shed vorticity is represented in red and is emitted in the rotor plane. The dashed red lines represent the edge of the vortex core. Here the part of the blade closest to the root is inside the core of the shed vortex, which should be avoided to ensure a proper temporal resolution. A condition on $\Delta\theta$ can be expressed so that the lifting part of the blade is not inside the core of the shed vortex (see Fig. 3.11). The trailing vorticity is not shown.

The distance between the shed vortex and the blade at a spanwise position r for a rotational

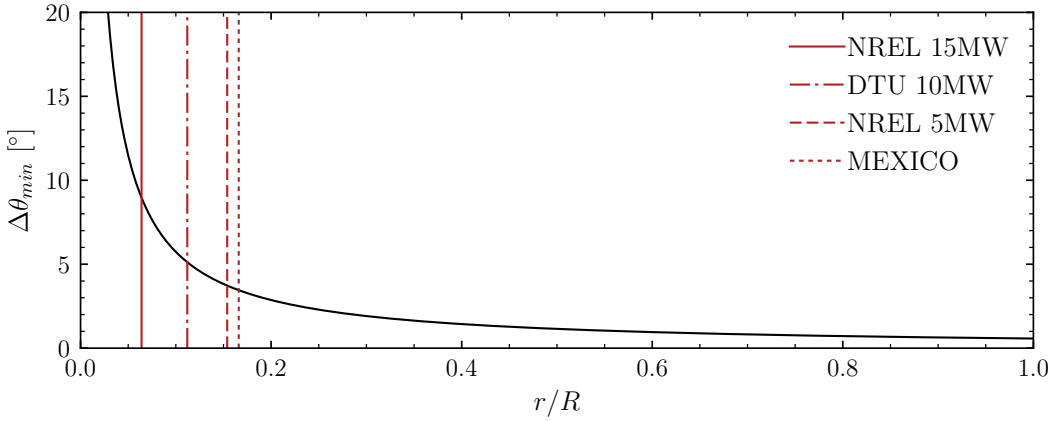

Figure 3.11: Limit angle of rotation between two steps that leads to a distance of $r_c = 0.01R$ between the blade and the shed vortex: $\Delta\theta_{min} = 2\arcsin(r_c/(2r))$. The vertical lines show the position of the first lifting element for different wind turbine geometries.

step of $\Delta\theta$ is $2r\sin(\Delta\theta/2)$. This distance needs to be greater than the core radius taken equal to $r_c = 0.01R$ so that the desingularization model does not modify the temporal behavior of the lift along the blade. This lets us express a lower bound $\Delta\theta_{min}$ for the rotational step that leads to a distance between the shed vortex and the blade to be equal to r_c. This minimal angle step depends on the radial station because of the rotation. For position towards the tip of the blade, the blade would travel a longer distance than for stations close to the root of the blade between two steps due to the rotation.

This limiting angle step is shown in Fig. 3.11. The position of the first lifting section closest to the root of the blade is shown for different wind turbine geometries. Indeed, the criterion on the shed vorticity is only of interest for lifting elements that shed some vorticity into the wake. In the free vortex wake method, the circular elements at the root of the blade do not emit vorticity. Fig. 3.11 shows that for the NREL 15MW wind turbine geometry, the angle step has to be of a minimum of 9° in order to avoid that the first lifting section of the blade is in the core region of its past shed vortex. This means a maximum of 40 shed elements by rotation. For the DTU 10MW, since the first lifting element is further away from the axis of the rotor, the condition leads to up to 70 shed vortices per rotation.

Since the inflow wind convects the vortices further away from the blade, this condition might be relaxed even further. Fig. 3.11 shows that for the large majority of the blade span, the blade will not be in the core region of past shed vortices for classical operating conditions when $r_c = 0.01R$.

3.2.2.4 Far-wake simplification

Floating wind turbines are typically studied for cases of 1 hour in order to properly account for given sea-state conditions. For a multi-MW sized wind turbine, the first vorticity elements emitted by the blades would have been convected several kilometers away from the rotor after an hour of operation. Their influence on the blades would be negligible due to their distance to the rotor. The wake of a wind turbines also recovers due to turbulence. The turbulent recovery of the wind turbine wake is not accounted for with the segment-based lifting line free vortex wake method of OLAF. Other vortex methods such as particle-based vortex methods can model turbulence and properly capture the wake recovery [26]. The actuator line method is also particularly suitable to model wake recovery because turbulence is well modeled by LES solvers. The focus of this work is floating wind turbines loads, therefore the fact that segment based vortex methods cannot capture wake recovery is not critical, since the far-wake is not the main point of interest here.

The far-wake simplification within the segment-based free vortex wake method serves a dual purpose: to limit the number of elements in the wake to limit the computational cost, and to remove the vorticity from the wake because no recovery from turbulence is present. Here the focus will be on limiting the computational cost for long floating wind turbine simulations. Indeed, to account for sea states, simulation cases need to be longer than for fixed-bottom wind turbines. Far wake simplifications enable to limit total number of elements into the wake and thus limit the growth of the computational time. OLAF already provides some far wake simplification features relevant for floating wind simulations.

The far wake simplification method of OLAF has 3 parameters:

- the number of the near wake elements taking into account all the emitted vorticity
- the number of free wake elements taking into account the local wake self-induced velocity. Elements outside the free wake are convected with a mean wind speed.
- the maximum number of wake elements. Elements are being removed at the end of the wake.

The portion of the wake which is not “free” and is convected by a mean wind speed prevents a deformation of the wake due to the removal of the vortex elements at the end of the wake.

The user and theory manual of OLAF [170] expresses the default value for two parameters: a total wake length of 8 rotor diameters ($16R$) and a free wake length of 6 rotor diameters ($12R$), but OLAF requires numbers of wake elements as inputs instead of wake lengths. The value of all three parameters will be explored next. The objective is to limit the

computational time by limiting the number of elements while keeping the same accuracy as a simulation with no far wake simplification. Here, the focus is on the wind turbine forces and not on the wake behavior.

It is useful to begin with the convergence of a simulation with no far wake simplification. Indeed, the wake takes some time to develop. By looking at the convergence of the thrust and power coefficients, the distance from the rotor when the wake stops having significant effects on the rotor can be determined, which can be called the convergence length of the wake. To obtain the same results with a wake simplification, it has to be applied at a distance further than the convergence length.

An estimation of this convergence length of the wake can be done using the helical vortex wake model used in Section 2.3. The goal is to have an a priori estimate of when it is possible to simplify the description of the wake and reduce the number of elements. The axial velocity induced by a semi-infinite helix is:

$$u_{i,0}^{helix} = -\frac{\lambda \Gamma_0 n_b}{4\pi R e_{cv}} \tag{3.32}$$

where λ is the tip speed ratio of the rotor, R the helix radius, Γ_0 the circulation of the tip vortex and e_{cv} is such that the convection velocity of the tip vortex is $U_{cv} = e_{cv} U_\infty$. The axial velocity induced by a finite helix of dimensionless length $e_{cv} U_\infty t/R$, meaning that it has convected during a time t at velocity $e_{cv} U_\infty$, is:

$$u_{i,0}^{short} = -\frac{\lambda \Gamma_0 n_b}{4\pi R} \frac{\frac{U_\infty t}{R}}{\left(\frac{e_{cv}^2 U_\infty^2 t^2}{R^2} + 1\right)^{1/2}}. \tag{3.33}$$

Therefore, the relative difference between the induced velocity at the center of the rotor by an helix of dimensionless length $e_{cv} U_\infty t/R$ and a semi-infinite helix is written:

$$\Delta_r u_{i,x}^{helix} = \left| \frac{u_{i,x}^{short} - u_{i,x}^{helix}}{u_{i,x}^{helix}} \right| = \left| \frac{\frac{e_{cv} U_\infty t}{R}}{\left(\frac{e_{cv}^2 U_\infty^2 t^2}{R^2} + 1\right)^{1/2}} - 1 \right|. \tag{3.34}$$

It is remarkable through rotational symmetry that this relative error does not depend on the shape of the helix as the relative error is the same if it is a dense helix linked to a high tip speed ratio or a loose helix due to a low tip speed ratio: only the helix length matters. This relative error is plotted in Fig. 3.12. The part of the helix contained in the first 7 radius length behind the rotor accounts for 99% of the axial velocity induced at the center of the rotor.

We have three wake simplification steps to perform: reducing the vortex sheet to tip and root vortices, using a simplified convection velocity, and eventually removing elements.

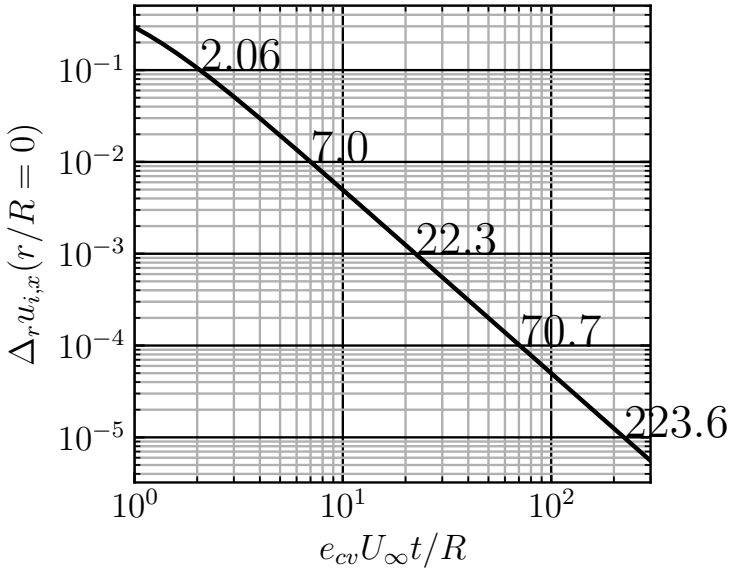

Figure 3.12: Relative error on the axial velocity induced at the center of the rotor between a helix of relative length $e_{cv}U_\infty t/R$ and a semi-infinite helix. The relative lengths to reach relative errors of 10^{-1}, 10^{-2}, 10^{-3}, 10^{-4} and 10^{-5} are shown.

We are going to use a scaled approach, reducing the error by one order of magnitude before applying each simplification. The wake simplification to tip and root vortices is going to be applied at a distance of $2.06R$ from the rotor, where the relative error between the velocity induced by a finite helix of length $2.06R$ and a semi-infinite helix is 10^{-1}. A simplified convection velocity instead of a local velocity induced by the wake is going to be used after $7R$ and the vortices are deleted once they reach an axial distance from the rotor greater than $22.3R$. The wind speed used to convect the wake elements between $7R$ and $22.3R$ is the sum of the local inflow wind and the wake-induced velocity averaged over the part of the wake simplified as tip and root vortices between $2.06R$ and $7R$. The distances are obtained from Eq. 3.34. The principle of the wake simplification method is shown in Fig 3.13.

Alternatively, Boorsma et al. [30] presented a method of wake simplification that relies on a specific number of rotations of the rotor before the transition, where one out of two or more elements are skipped. OLAF has a similar wake simplification method: the near-wake size can be set to a specific number of elements. This means that a set number of rotations of the wind turbine wake are going to be modeled with all spanwise elements (shed and trailing) before transitioning to tip and root vortices only.

The distance-based wake simplification method presented in Fig. 3.13 was implemented into OLAF to be available with DIEGO. Its performances on the MEXICO test case [29] are compared to a simulation with no wake simplification and the already available

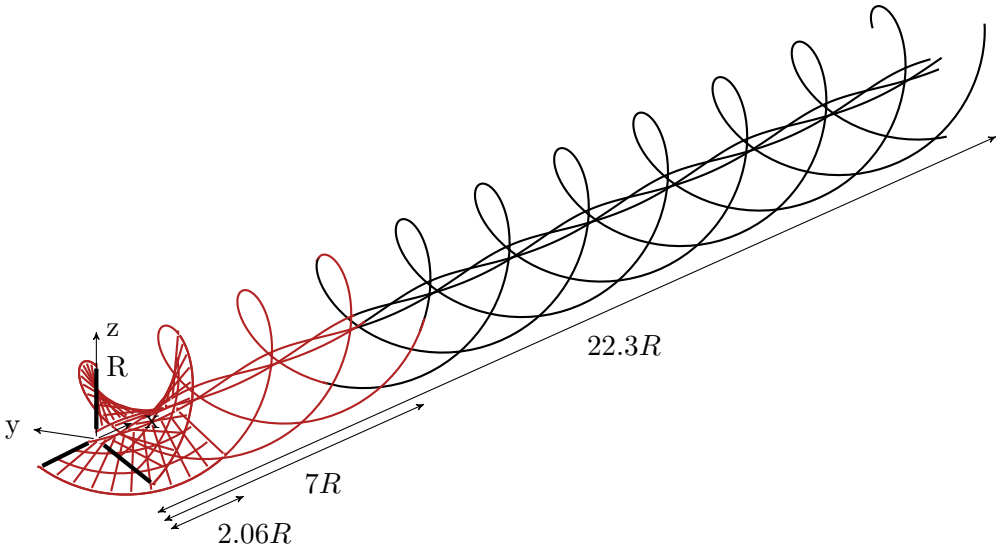

Figure 3.13: Wake simplification method: only the tip and root vortices are kept after $2.06R$. The wake self-induced velocity is computed for the first $7R$ behind the rotor shown in red. Vorticity elements are removed at a distance of the rotor greater than $22.3R$.

Table 3.2: Performances of the proposed distance-based wake simplification method (labeled "Distance") against a regular number of rotation-based (4 rotations) simplification (labeled "Rotation") for the MEXICO wind turbine, compared to a simulation with no wake simplification. All setups are run for 32 turbine rotations. The error is computed on the average over the last rotation. The speed-up is the ratio between the wall clock time of the full wake simulation, and the wake simplification simulation wall-clock time using the GPU implementation detailed in Section 3.2.2.5.

λ	ΔC_T		ΔC_P		Speed-up	
	Rotation	Distance	Rotation	Distance	Rotation	Distance
4.2	-0.012%	-0.0050%	-0.029%	-0.018%	4.8	8.0
6.7	0.53%	0.091%	1.2%	0.24%	4.8	5.7
10	1.5%	1.0%	5.3%	3.4%	4.8	3.0

rotation-based wake simplification method. The computational times, as well as the relative errors on the thrust and power coefficients, are reported in Table 3.2 for simulations of 32 rotations of the rotor. The rotation-based model transitions to tip and root vortices only after 4 rotations. For the two lowest tip speed ratios, $\lambda = 4.2$ and $\lambda = 6.7$, the two simplification methods have similarly low errors, and provide results close to the simulation with no wake simplification. The distance-based simplification method presented here provides an improved computational time compared to the regular method, in particular for $\lambda = 4.2$. For the highest tip speed ratio, $\lambda = 10$, the distance based method has significantly lower errors than the rotation-based method. This comes at the cost of a higher computational time: the speed-up is reduced because more elements are kept into the wake.

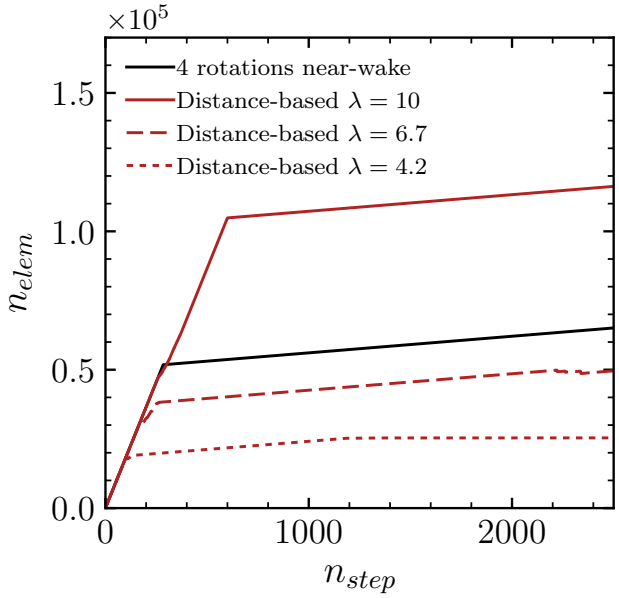

Figure 3.14: Total number of elements for the simulations of Table 3.2. Without any wake simplification, the total number of elements at the last step is 4.5×10^5. n_{step} is the number of time steps.

The number of elements in the wake at each time step for the two wake simplification methods and the three tip speed ratios is shown in Fig. 3.14. For the rotation based simplification, there is no variation in tip speed ratio. The better speed-ups obtained by the distance-based method for $\lambda = 4.2$ and $\lambda = 6.7$ are explained by the fact that the wake is transitioned to tip and root vortices earlier than with the rotation based method because the wake has reached $2.06R$. The wake can be approximated earlier without significant errors in thrust and power predictions as seen in Table 3.2. For $\lambda = 10$, the wake starts to be approximated later with the distance-based method because the wake takes more time to reach a distance of $2.06R$ behind the rotor. This explains the lower speed-up obtained, but gives a lower relative error than with the rotation-based method. Using a lower number of rotations before the transition to a simplified wake with the number of rotation-based method would improve the speed-up at low tip speed ratio without increasing much the error, but it would increase even more the error at higher tip speed ratio, meaning that this method requires specific inputs for specific tip speed ratios to work best. For example, Wen et al. [209] truncate the wake after a specific number of rotations depending on the tip speed ratio. To establish the number of rotations needed for each tip speed ratio, costly full wake preliminary simulations must be run.

Overall, the newly implemented distance-based method provides an optimized number of elements that enables a large speed-up of the simulations while limiting the error caused by the simplification for all tip speed ratios. Compared to the number of rotation-based

method already available in OLAF, it does not require specific inputs for specific tip speed ratios in order to provide good performance in term of speed and error. The proposed method also has the advantage of requiring no user inputs at all, meaning that it is easily usable by non-expert users.

It has been decided to not reduce the number of elements in the near-wake, where all the vortex elements are kept, but only increased. This was purposely done in order to not shorten the near-wake when a floating wind turbine is surging or pitching upwind since this near-wake shortening might have some detrimental effects when the wind turbine is moving downwind next, moving towards a less refined wake. This limitation could be removed by verifying that the wake shortening does not have detrimental effects.

For the following simulations, the proposed wake simplification method is used unless otherwise specified. Further data regarding the quality of this wake simplification model is provided in the validation process of DIEGO with vortex method (see Section 3.3).

3.2.2.5 Computational efficiency

Parallelizing the FVW kernel calls of CACTUS on GPU with CUDA provided a large performance improvement (see Chapter 2) over CPU processing. Therefore, the choice was made to also parallelize the Biot-Savart kernel of OLAF on GPU. The CUDA GPU routines for CACTUS were written from scratch. To improve upon this, it was decided to use the EXAFMM library [219] that implements the Fast Multipole Method (FMM) [66] on GPU for particles. It is able to handle very large numbers of particles. One of the reasons that led to the choice to use EXAFMM is the good memory handling that is done by the library. Indeed, the positions of the data in the memory are very important for GPU performance. The data that is going to be read in memory to perform a basic operation should be located consecutively in memory to provide best performance, as is done in EXAFMM. It can also use several GPUs at the same time, by distributing the computational loads between the available GPUs.

By default, EXAFMM is a particle solver while OLAF works with vortex lines. Therefore, modifications to EXAFMM needed to be done so that it could be used to compute the velocity induced by vortex lines. The Biot-Savart law for vortex lines with the desingularization model of Vatistas was implemented in the EXAFMM library following the proper memory management architecture of the library. To compute the velocity induced by a particle on a point, a set amount of data has to be transfered to the GPU: the position of the target point (3 real numbers), the position of the particle (3 real numbers), the strength of the particle (3 real numbers) and its core size (1), for a total of 10 double precision real numbers. For vortex lines, the target point (3), the positions of the two ends of the vortex line (6), its circulation (1) and its core size (1) for a total of 11 real numbers need to be transfered to the GPU. The use of vortex lines adds one more real

number to transfer to the GPU per vortex line.

It was decided not to implement the FMM for the vortex lines, since the expected total number of elements when using the wake simplification model of Section 3.2.2.4 would be in the range where the FMM is just becoming faster than the direct computation. Indeed, the Fast Multipole Method has an algorithmic overhead and is becoming faster than a direct computation only when the number of elements is large. Yokota and Barba [220] find that the FMM had better performances than a direct computation for a number of elements larger than 4×10^4. This threshold depends highly on the available GPU hardware.

Coupling routines were implemented so that every time OLAF needs to compute the Biot-Savart law for a large number of vortex lines, EXAFMM is called instead of the OLAF routines, in order to do the processing on the GPU. Fig. 3.15 shows how EXAFMM is integrated in DIEGO.

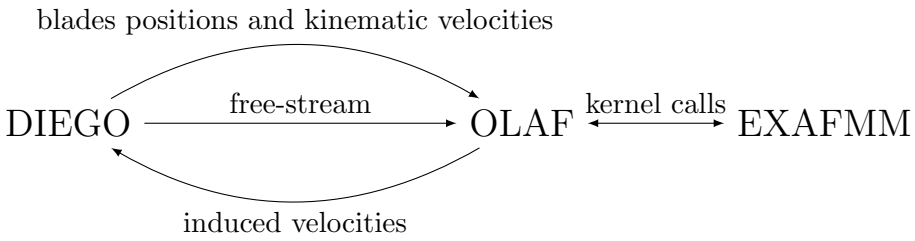

Figure 3.15: Coupling between DIEGO, OLAF and EXAFMM.

The NREL 5MW reference wind turbine is used to perform of benchmark of the different computational methods. The already available direct CPU and particle-based CPU treecode are compared to the EXAFMM direct GPU implementation and the newly implemented segment-based CPU treecode. The CPU algorithms are parallelized with OpenMP and run on 2 Intel Xeon Gold 5112 processors with 4 cores each for a total of 8 cores, while the GPU algorithm runs on 2 NVidia V100 PCI-E GPUs which corresponds to a higher computational power.

The simulation is run for 121 rotations with 30 elements per blade. No wake simplification method is used to intentionally reach high numbers of elements and assess the performances for these number of elements. The wall-clock time taken to compute a time step for increasing numbers of vortex elements is shown in Fig. 3.16. First and foremost, the direct CPU evaluation of the wake self-induced velocity results has a large computational time per timestep even though it is parallelized with OpenMP. The particle-based CPU treecode improves the computational time compared to the direct CPU evaluation. As expected from the treecode formulation, it also has a better scaling with the number of elements: the computational time grows less rapidly than for the direct CPU evaluation which has a $O(n_{elem}^2)$ complexity, where n_{elem} is the number of vortex elements.

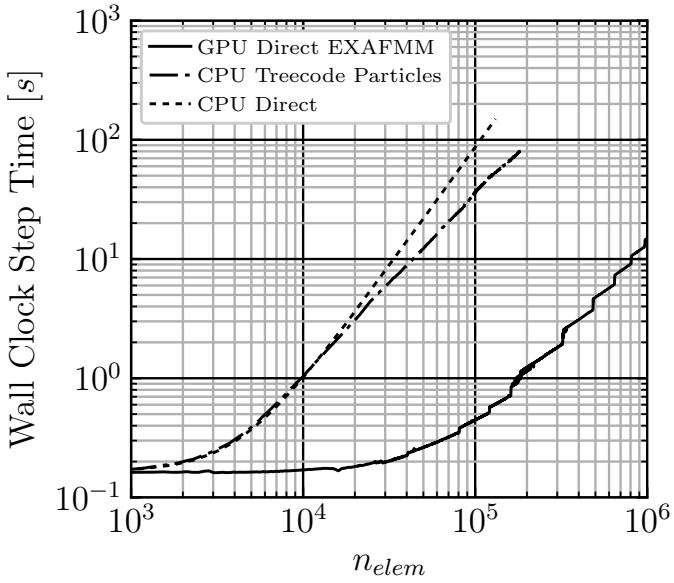

Figure 3.16: Wall clock duration of a time step for an increasing number of vortex elements for different computational methods. Data obtained with 30 elements per blade for the NREL 5MW wind turbine at rated conditions with an angle step of 7.2° per time step.

With the wake simplification algorithm presented in Section 3.2.2.4, the number of elements was found to be of the order of 10^5 after the simplification is applied. For this number of elements, Fig. 3.16 shows that the direct GPU evaluation using the modified EXAFMM library for segments is more than one order of magnitude faster than the CPU treecode of OLAF. Part of the performance difference is due to the available hardware. Moreover, the GPU architecture is particularly suitable to n-body problems such as a computing the wake self-induced velocity. The GPU direct evaluation is going to be used systematically because it provides much smaller computational time than the CPU algorithm for the range of elements of interest.

Since the segment kernel was implemented solely as a direct evaluation in EXAFMM, it is expected to have a computational cost that scales with n_{elem}^2 similar to the CPU direct evaluation. However, that is not the behavior that can be seen in Fig. 3.16. Between 10^4 and 10^5 vortex elements, the computational cost is not increasing as fast as the CPU direct evaluation. The fact that the computational time does not scale as $O(n_{elem}^2)$ is a sign that it is not dominated by the self-induced velocity computation step and that other parts of DIEGO or OLAF account for much of the computational time. This is likely due to the architecture of the GPU, which requires memory transfer between the CPU and the GPU. Once the data to be processed has been transfered to the GPU, it takes about as much time do to a small number of operations than a large number of operations, as long as that number of operation does not exceed the number of computational processes

available on the GPU. If the number of interactions to compute is higher than the number of processes available, the remaining operations wait for computing processes to be free. The steps seen in the increase of the GPU time step cost are possibly due to the fact that the number of vortex interactions to compute has reached the number of available computing processes on the GPU and that some interactions therefore need to wait for compute processes to finish. Between these steps, the increase of computational cost is likely due to the larger memory transfer that has to be done between the CPU and GPU.

For future developments, recall that EXAFMM is initially made for particles. Particle-based vortex methods are particularly appropriate to study the turbulent wake decay of wind turbines and wake interactions as done for example by Bex et al. [26]. The coupling between DIEGO, OLAF and EXAFMM opens the possibility for the future use of DIEGO to study the wakes of floating wind turbines and wake interactions. It would require modifications to DIEGO and OLAF to emit particles directly from the blades or to convert the emitted vortex lines into particles. This second operation requires care since particles and vortex lines have different induced velocity fields, and particle-based methods have core size requirements to ensure stability. The EXAFMM library is well suited to deal with a large number of small particles to properly simulated turbulence.

A vortex line-based treecode algorithm was implemented and submitted to the open source repository of OpenFAST to improve upon the existing particle-based treecode algorithm. It is presented in Appendix A. The direct GPU parallelization combined with the wake simplification model was preferred over the vortex line-based treecode algorithm due to the very good computational performances of the GPU parallelization. However, the vortex line-based treecode algorithm is useful when a GPU is not available for computation.

In the following, the GPU parallelization done with EXAFMM is always used.

3.3 Validation of aero-elastic modeling

3.3.1 Validation strategy

The validation of aero-hydro-servo-elastic simulation tools for wind turbines is a complicated process since there does not exist a perfect validation case for such a tool. This is related to the difficulty of setting up a model rotor with both aerodynamic and structural forces scaling corresponding to a real rotor. Most aerodynamic experiments concentrate on rigid rotors to provide a better understanding of the aerodynamics, without adding the complexity of elasticity.

Here, a step by step process is used to validate the aero-elastic implementation of DIEGO with the FVW aerodynamic model, by increasing the complexity of the simulated cases with added physical phenomena at each step. The aerodynamics of a rigid rotor in axial

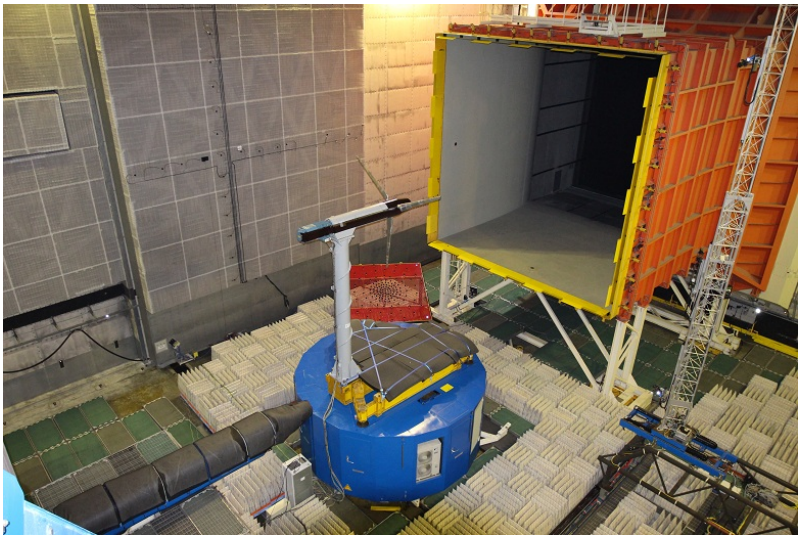

Figure 3.17: MEXICO wind turbine in the large German Dutch Wind Tunnel, DNW. Picture taken from [29].

conditions is validated in axial and then in yawed conditions, followed by the aerodynamics of a rigid surging rotor. It is followed by a validation of the aero-elastic coupling, first by studying single blade aero-elasticity before considering full rotor elasticity. The validation cases are summarized in Table 3.3.

Table 3.3: Validation strategy for the aero-elastic coupling

Physical phenomenon	Case	Page
Rigid rotor in axial flow	MEXICO [29]	page 112
Rigid rotor in yawed flow	MEXICO [29]	page 113
Pitching airfoil	Theodorsen [195]	page 116
Surging rigid rotor	UNAFLOW [57]	page 117
Single blade aero-elasticity	Tang and Dowell [194]	page 121
Full rotor aero-elasticity	Liu et al. [111]	page 124

3.3.2 MEXICO

The New MEXICO experiment [29] provides one of the few experimental data sets of radial force measurements on a wind turbine in a controlled environment. The MEXICO wind turbine can be seen in Fig. 3.17. Several models have been validated against the experimental data within the IEA Wind Task 29 project [29]. Experimental data is available for three different tip speed ratios: $\lambda = 4.2$, $\lambda = 6.7$, and $\lambda = 10.0$, in both axial and yawed conditions, with a yaw angle of 30°.

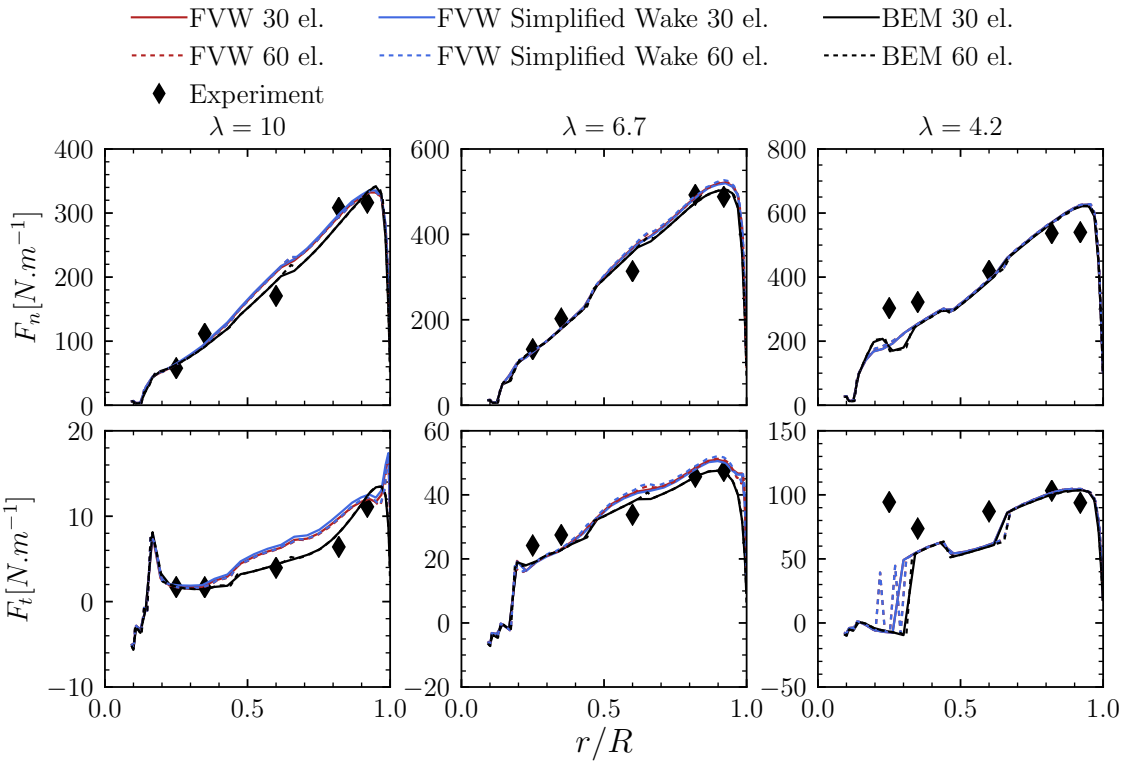

Figure 3.18: Forces on the MEXICO wind turbine blades. Experimental data from [29]. The results with solid lines use 30 elements per blade while 60 elements per blade results are shown with dashed lines. FVW results with and without the wake simplification model overlap.

3.3.2.1 Axial flow

The normal and tangential forces for five radial stations along the blades were reconstructed from pressures measurements around the blade section in the New MEXICO project. The results obtained with DIEGO for the BEM, the FVW and the FVW with the wake simplification method of Section 3.2.2.4 are shown in Fig. 3.18. Both the BEM and the FVW show blade forces close to the experimental results. The largest discrepancies are found near the root for $\lambda = 4.2$, both for normal and tangential forces. The large discrepancy is due to the fact that the flow is stalled near the root of the blade for $\lambda = 4.2$. The use of the wake simplification does not change significantly the distribution of the forces along the blade. Only small differences can be seen for $\lambda = 10$ which explains the higher error for that tip speed ratio on the thrust (see Section 3.2.2.4).

Using twice as many aerodynamic elements along the blade does not change significantly the results. The oscillations near the root of the blades seen when using 60 elements per blade are related to the stalled flow experienced by the blade at this position which induces large variation of the lift coefficient and angle of attack. Using more elements along the blades mean that more vortex elements are emitted from the blades, which

greatly increases the computational cost, while it barely changes the results. As a result, 30 elements per blade is used in the following, as it provides good results for a limited computational cost. It is in line with the number of elements used to mesh blades with FVW methods in the literature: Boorsma et al. [31] used both 20 and 31 elements with two different codes.

3.3.2.2 Yawed flow

Yawed conditions are a particularly important validation case for floating wind turbines since floaters often have a steady pitch angle when the wind turbine is producing electricity. This generates a misalignment between the inflow and the rotor, similar to what is experienced by the wind turbine for a yaw misalignment.

In the New MEXICO project, the forces along the blades were measured for a 30° yaw angle. The results obtained with DIEGO with BEM, FVW and FVW with the wake simplification method of Section 3.2.2.4 are shown in Fig. 3.19 and 3.20. The simulations are run for 32 rotations of the wind turbine and the results are extracted on the last rotation. Once again, the differences between the FVW with a full wake and with the wake simplification model are small. This justifies the use of this wake simplification model for misaligned inflow conditions.

The free vortex wake method is in good agreement with the variation of the forces during the rotation of the wind turbine. In particular, the results are very close to the experimental data near the tip of the blade ($r/R = 0.82$ and $r/R = 0.92$) for $\lambda = 10$ and $\lambda = 6.7$. This is expected from the FVW method, since it takes into account the evolution of the wake behind the rotor, and the fact that the wake leaves the rotor plane with an angle due to the yaw misalignment.

The case is more challenging for BEM theory since it relies on empirical models to correct the loading for misaligned inflows. The results are shown in Fig. 3.19 and Fig. 3.20, both with and without the empirical correction model for inflow misalignment (Eq. 3.24). Without the inflow misalignment model, the maximum of normal and tangential force coefficient occur at a different azimuth angle than the experimental data for positions toward the tip of the blade ($r/R > 0.6$) for the two largest tip speed ratios. The inflow misalignment model greatly improves the prediction of the forces along the blades. In particular, the prediction of the variation of the tangential force coefficient is greatly improved which is important for the prediction of the torque and power of the wind turbine.

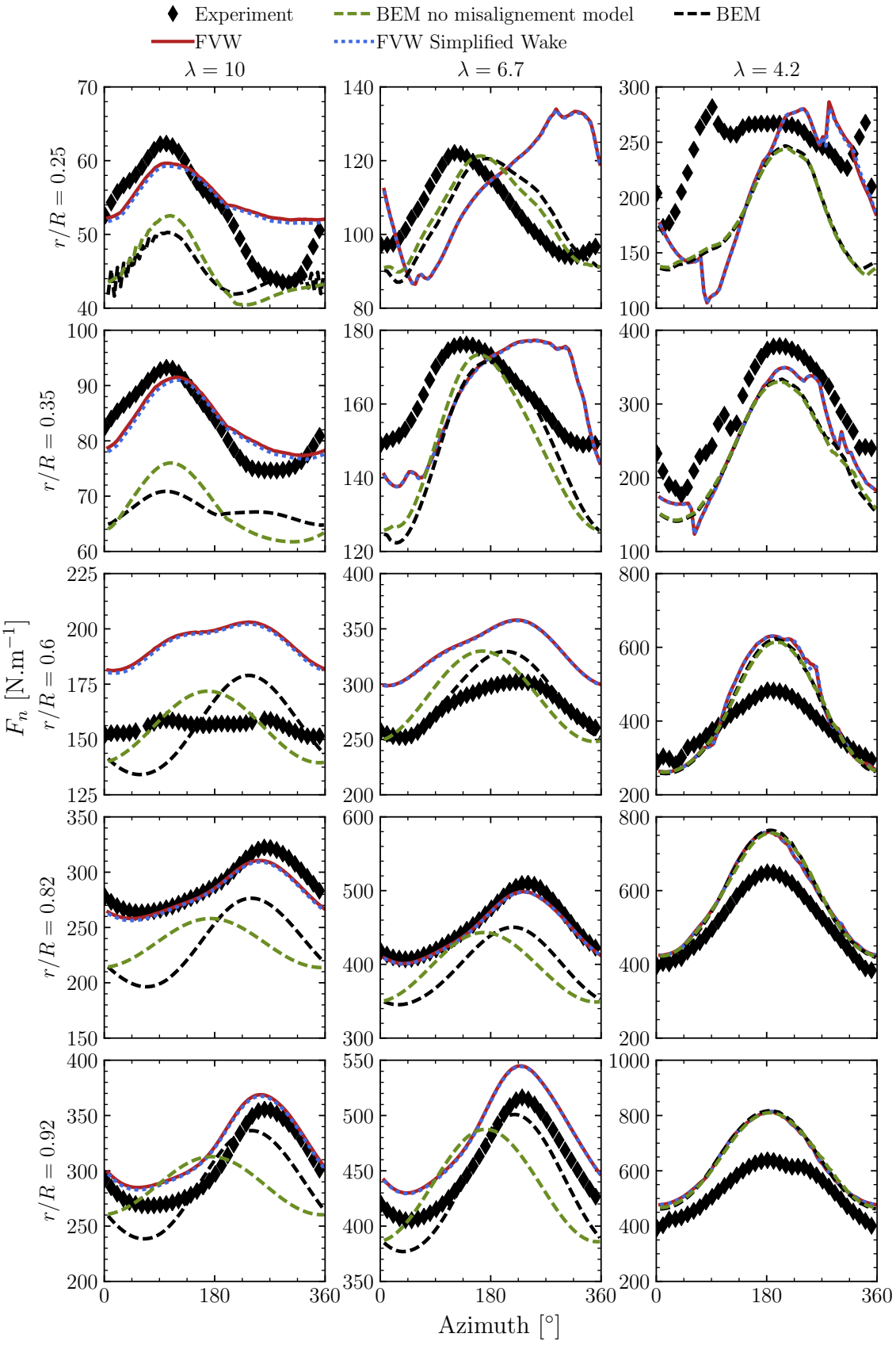

Figure 3.19: Normal force on the MEXICO wind turbine. Experimental data from [29]. The wake simplification algorithm for FVW predicts similar forces as the FVW with no wake simplification. The misalignment model for the BEM improves the results near the tip of the blade.

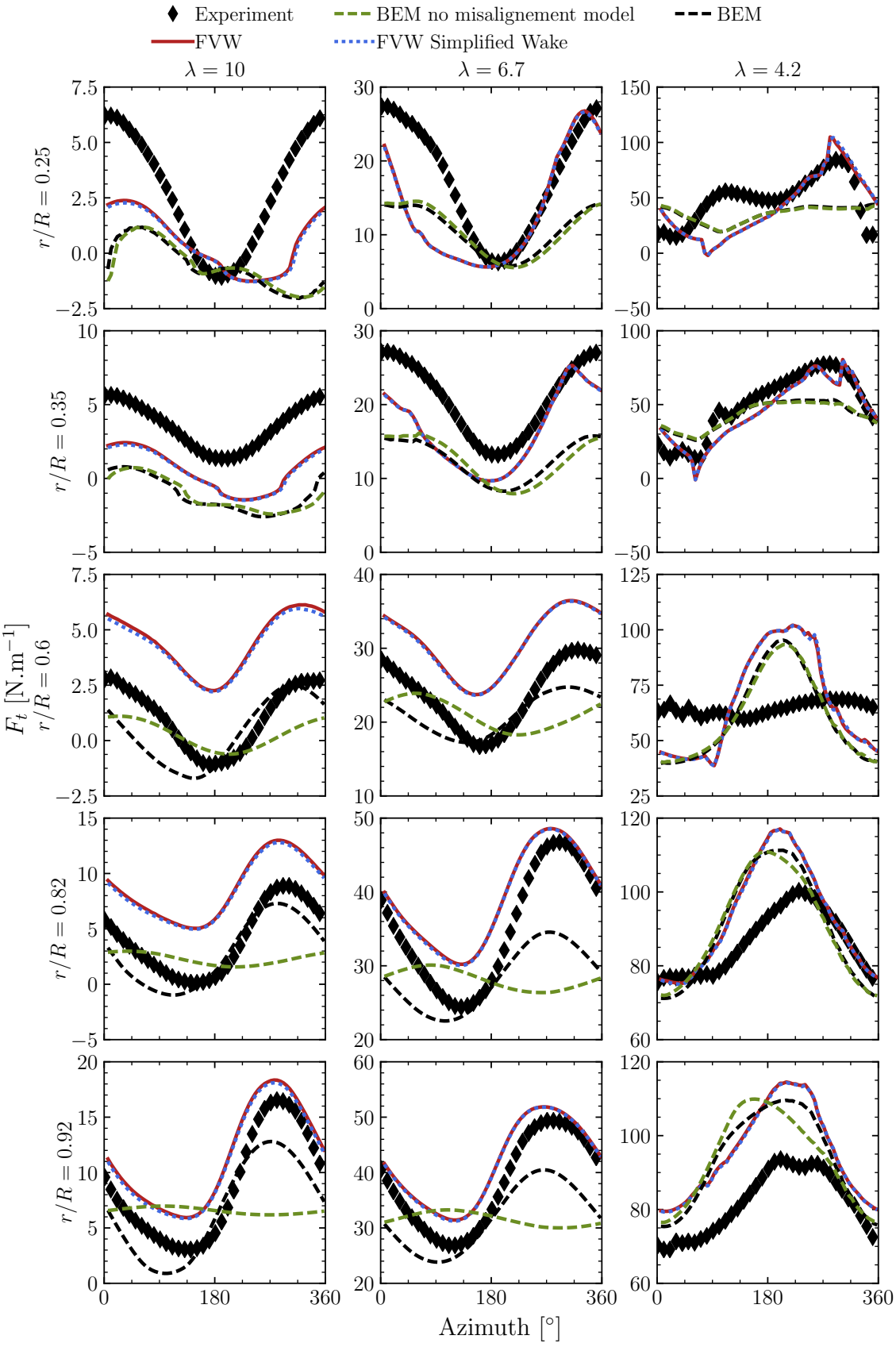

Figure 3.20: Tangential force on the MEXICO wind turbine. Experimental data from [29]. The wake simplification algorithm for FVW predicts similar forces as the FVW with no wake simplification. The misalignment model for the BEM improves the results near the tip of the blade.

3.3.3 Attached flow unsteady aerodynamics

Theodorsen [195] analytically expressed under the assumption of potential flow the lift of a 2D pitching flat plate undergoing a small amplitude pitch motion. The solution given by Theodorsen is a function of the reduced frequency $k = \omega c/(2U)$, where c is the chord and U the inflow wind. For a 2D pitching flat plate, the dynamic lift coefficient can be written [102, pg. 435]:

$$C_l = \Re(C(k)\alpha_a e^{i\omega t}). \tag{3.35}$$

The geometrically applied pitch angle of the wing is written α_g, and it is the real part of the complex pitch angle $\alpha_a e^{i\omega t}$ where ω is the pulsation of the applied pitch motion and $\Re(z)$ is the real part of the complex number z. Theodorsen's function $C(k)$ is written [54]:

$$C(k) = \frac{K_1(ik)}{K_1(ik) + K_0(ik)} \tag{3.36}$$

where K_n is the modified Bessel function of the second kind. The lift coefficient computed from Theodorsen's solution (Eq. 3.35) for a geometrical angle amplitude of 5° is shown in Fig. 3.21 for a range of reduced frequency. Increasing the reduced frequency reduces the amplitude of the lift coefficient oscillations. A phase lag between the geometrical angle of attack and the lift coefficient is also introduced. This has a damping aerodynamic effect because when the angle of attack is increasing, the lift coefficient is increasing slower than a quasi-steady lift coefficient computed from $C_l = 2\pi\alpha_g$.

To run a 2D case in DIEGO, a wing with a very large aspect ratio is used. The length of the wing is set to 1000 chord lengths. The wing is divided into three aerodynamic elements so that the middle element is unaffected by the tip vortices at each end of the wing because they are sufficiently far away. The time step is chosen so that every period of the geometrical pitch oscillation is divided into 100 time steps. The desingularization core size is $\epsilon = 5 \times 10^{-3} c$.

Both the BEM and FVW are compared to the analytical solution. Since the wing is not rotating, there is no induction and the BEM reduces to its unsteady local airfoil aerodynamic model, which in DIEGO is the model by Leishman and Beddoes [103]. This model accounts for the unsteady attached flow over the airfoil.

This model is also used with the FVW wake, but without the circulatory terms, since the shed vorticity that these terms represent is inherently accounted for in the FVW method. The circulatory terms are responsible for the phase-lag between the geometrical angle of attack and the dynamic lift coefficient. This test case can validate whether the Leishman and Beddoes [103] unsteady airfoil aerodynamic model and the FVW method properly exhibit this phase lag.

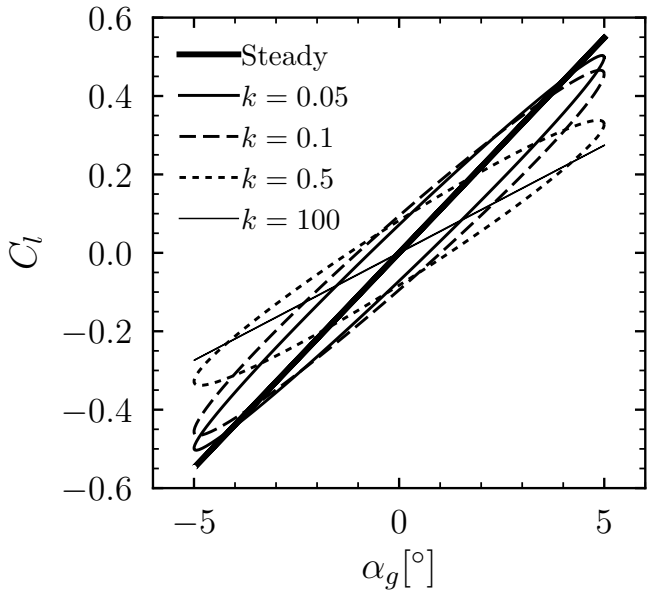

Figure 3.21: Lift coefficient from Theodorsen's solution (Eq. 3.35) for a pitching flat plate for various reduced frequency k. The hysteresis cycles are run through counter-clockwise.

The results obtained with DIEGO are compared to the theory in Fig. 3.22. The last cycle of a series of ten oscillations is shown. The phase-lag between the geometrical angle of attack and the dynamic lift coefficient is properly reproduced by both the local unsteady airfoil aerodynamic model with circulatory terms used in the BEM and by the FVW with wake emission at the lifting line. FVW with wake emission at the trailing edge underestimates the hysteresis effect due to the oscillations of the pitching flate plate. This confirms the arguments of Section 3.2.2.1 that the wake emission at the lifting line is a better formulation than wake emission at the trailing edge when the blade is modeled as a lifting line. The reduction of the amplitude of the lift variation due to the oscillatory motion is captured as well.

3.3.4 UNAFLOW - OC6 Phase III

Within the UNAFLOW project [22], force measurements were done on a rigid experimental wind turbine model in imposed surge motions of frequency f_s. Fontanella et al. [57] showed that the variation of the measured forces follows the quasi-steady behavior up to a reduced time scale of $f_s D/U_\infty = 0.5$ by analyzing the experiments. They stated that the uncertainties on the flexible response of the tower need to be improved to obtain reliable results at higher reduced frequencies. The experimental data has been openly shared by the experimental team [58].

The data from the UNAFLOW experiment was compared to several numerical models by

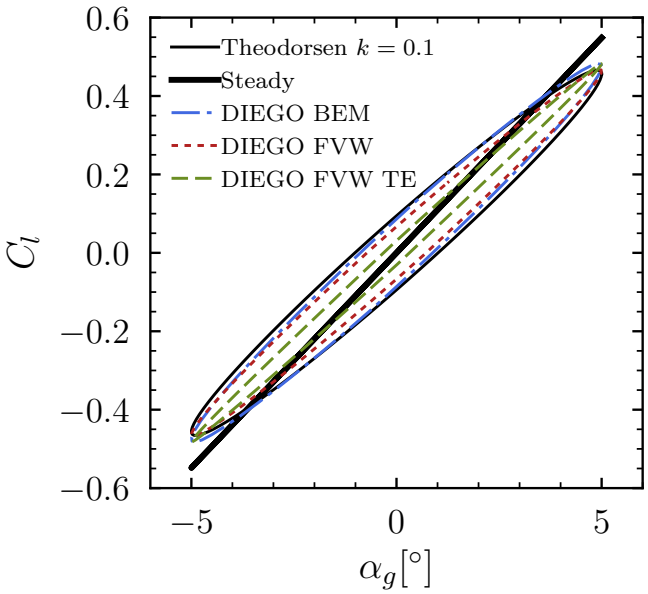

Figure 3.22: Lift coefficient from DIEGO and Theodorsen's solution (Eq. 3.35) for a pitching flat plate at a reduced frequency $k = 0.1$. FVW TE in green designates wake emission at the trailing edge (TE) and FVW in red is using the wake emission at the lifting line (see Section 3.2.2.1).

Mancini et al. [115]. Very good agreement was found between the measured and simulated thrust coefficient amplitudes for BEM, FVW, Actuator Line and blade-resolved CFD.

This dataset is used in the International Energy Agency (IEA) Task 30 OC6 Phase III project as a reference to which a range of numerical models for wind turbine simulations are compared.

The results obtained with DIEGO with the BEM and FVW models are compared to the experimental data from Fontanella et al. [58] and to the actuator line results provided by Mancini et al. [115] in Fig. 3.23.

The FVW simulations were done using the wake simplification model presented on page 102, using 60 time steps per rotation of the rotor, both with and without the dynamic stall model. The BEM results use the dynamic stall model both with and without the dynamic inflow model. This test case is used to validate that the FVW and the BEM with dynamic inflow are able to predict the forces on a wind turbine in imposed surge motion. In particular, the dynamic inflow model for the BEM should not introduce a delay between the thrust and surge velocity since the experimental data has no delay between the two.

The thrust and torque coefficients amplitude and mean are compared, with the thrust coefficient defined as:

$$C_\Gamma = \frac{\Gamma}{\frac{1}{2}\rho\pi R^3 U_\infty^2} \tag{3.37}$$

with Γ the rotor torque. The reduced frequency is $k = 2\pi\Delta x_s f_s / U_\infty$. DIEGO is also compared to the actuator line results of Mancini [114] for surge frequencies higher than the ones for which experimental data is available. Good agreement between the experimental and numerical data is found for the amplitude of the thrust coefficient variation, ΔC_T, for all tested models (Fig. 3.23). For reduced frequencies larger than the one tested in the experiment, DIEGO has larger thrust coefficient variations than the actuator line results. This difference could be due to differences in the airfoil polar used in DIEGO and the actuator line simulations from Mancini [114]. Indeed, the lift coefficient can be very different for large angles of attack depending on the Reynolds number as shown in Fig. 3.25. The maximum lift coefficient before stall influences the maximum thrust force. Thus, differences on the airfoil polar near stall can lead to differences in the amplitude of the thrust coefficient variation for large reduced frequency k. Larger discrepancies are found between the numerical results and the experimental data for the torque coefficient while the numerical models have similar results. The differences in torque coefficient amplitude, ΔC_Γ, could be due to possible elasticity of the rotor axis in the experiment that is not present in the numerical models. All the numerical models underestimate the average thrust coefficient, $\bar{C}_T$, of the wind turbine model, and DIEGO underestimates the average torque coefficient, $\bar{C}_\Gamma$, both with BEM and FVW.

The phase shift between the thrust and the surge motion, ϕ_{T-S}, is shown in Fig. 3.23e for different values of the ratio between the surge frequency f_s and the rotational frequency of the rotor $f_R = \omega_R/(2\pi)$. The amplitude of the thrust and torque coefficient variation are a function of the reduced frequency $k = 2\pi\Delta x_s f_s / U_\infty$ which is a ratio between the maximum surge velocity and the inflow velocity, but the phase shift between the thrust and surge position is a function of the surge frequency f_s. All of the models predict a phase shift close to $-90°$ for values of f_s/f_R lower than 0.5. The variation of the thrust are in phase with the surge velocity. For larger values of the surge frequency, the actuator line results show a delay between the thrust and surge velocity variation also present in the DIEGO FVW results when the dynamic stall model is not used (labelled "FVW no DS" with DS for Dynamic Stall) as is the case for the actuator line simulations. This shows that the wake simplification model is able to predict the dynamic on the forces on the blades for a moving rotor, as it gives results close to a higher fidelity model (actuator line).

The local unsteady airfoil aerodynamics are important to model for rapidly changing angle of attack. Therefore, simulations were done with DIEGO using the dynamic stall model. When it is activated, the phase shift is close to $-90°$ with slightly higher values for the FVW.

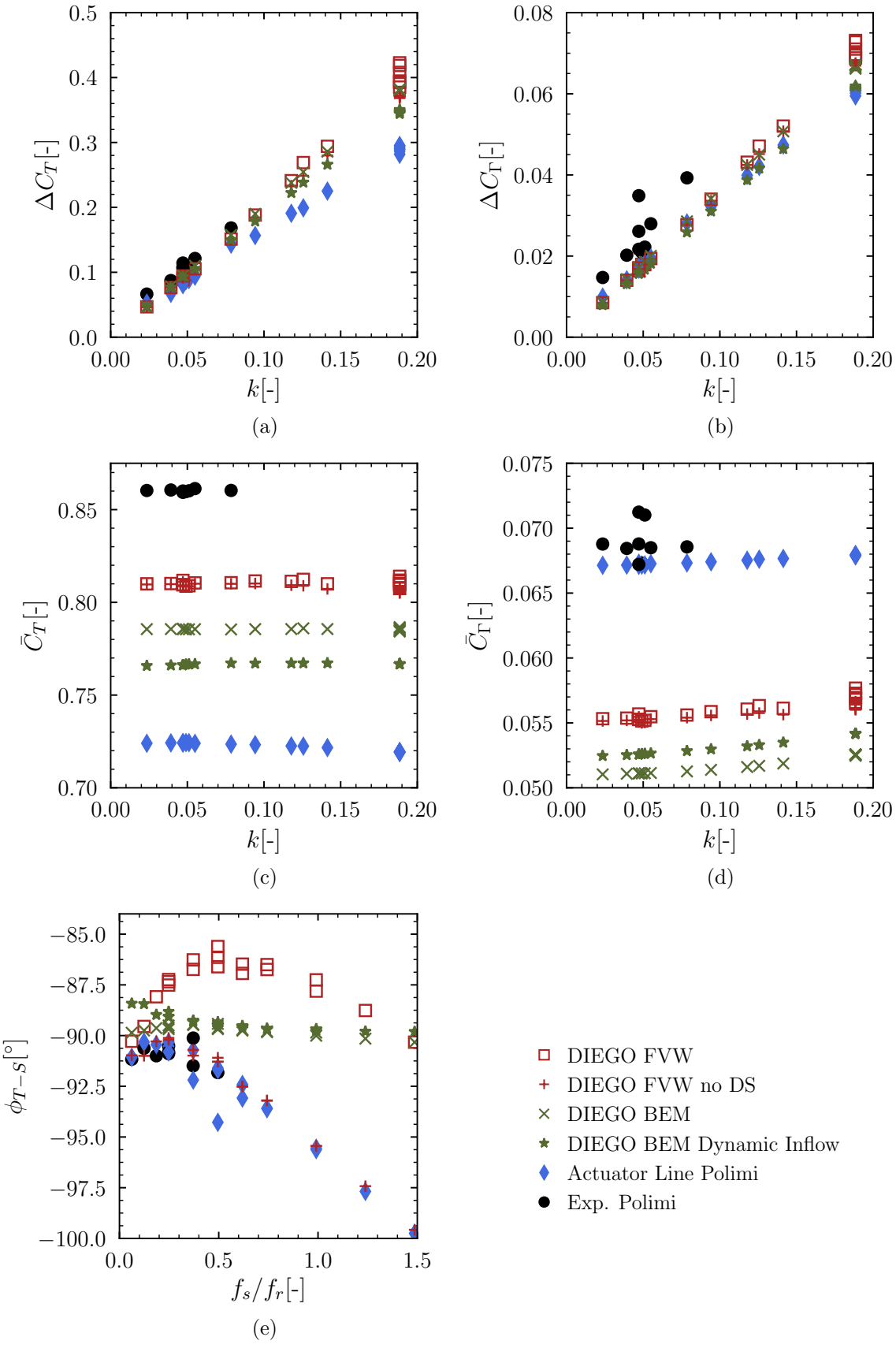

Figure 3.23: Comparison of the BEM and FVW aerodynamic models of DIEGO with experimental data [58] and Actuator Line results [115] on the UNAFLOW case in rated conditions. $\lambda = 7.5$. "no DS" stands for results without the dynamic stall model. ϕ_{T-S} is the phase shift between the thrust and the surge motion.

3.3.5 Aero-elasticity: wing case

The validation of aero-elastic models is a difficult process since very few experimental data sets are available. Moreover, most aero-elastic experiments were aimed at validating aero-elasticity for commercial and military planes and not wind turbines, such as the work of Dietz et al. [51] for transport aircraft wings, or the work of the collaborative research Center SFB 401 at RWTH Aachen [17].

Commercial and military aircraft wings have aspect ratios radically smaller than wind turbines. The aspect ratio of a wing is defined as the ratio between the square of the wing span b and the wing area S: $AR = b^2/S$. For a rectangular wing, it reduces to the ratio of the wing span over the chord length. For example, the experiment of Kämpchen et al. [92] on a commercial aircraft-type rectangular wing uses a wing of $AR = 4.5$.

As pointed out by Afonso et al. [8] in their review on the aero-elasticity of high aspect ratio wings, the works of Tang and Dowell [194] is one of the only experimental data set available. The wing they used has an aspect ratio of $AR = 8.87$ (Table 3.4). A slender body was attached to the tip of the wing to lower the twist motion natural frequency, and its properties are listed in Table 3.5.

Table 3.4: Experimental wing model properties from [194].

Property	Value
Span L	$0.4508\ m$
Chord c	$0.0508\ m$
Mass per unit length	$0.2351\ kg.m^{-1}$
Moment of inertia around mid-chord	$0.2351 \times 10^{-4}\ kg.m$
Position of spanwise elastic axis	50% chord
Position of center of gravity	49% chord
Flap bending rigidity	$0.4186\ N.m^2$
Chordwise bending rigidity	$0.1844 \times 10^2\ N.m^2$
Torsional rigidity	$0.9539\ N.m^2$
Flap structural modal damping ξ_w	0.02
Chordwise structural modal damping ξ_v	0.025
Torsional structural modal damping ξ_ϕ	0.031

Table 3.5: Slender body properties from [194].

Property	Value
Radius R	$0.4762 \times 10^{-2}\ m$
Chord length c_{sb}	$0.1406\ m$
Mass M	$0.0417\ kg$
Moment of inertia I_{xx}	$0.9753 \times 10^{-4}\ kg.m^2$
Moment of inertia I_{yy}	$0.3783 \times 10^{-5}\ kg.m^2$
Moment of inertia I_{zz}	$0.9753 \times 10^{-4}\ kg.m^2$

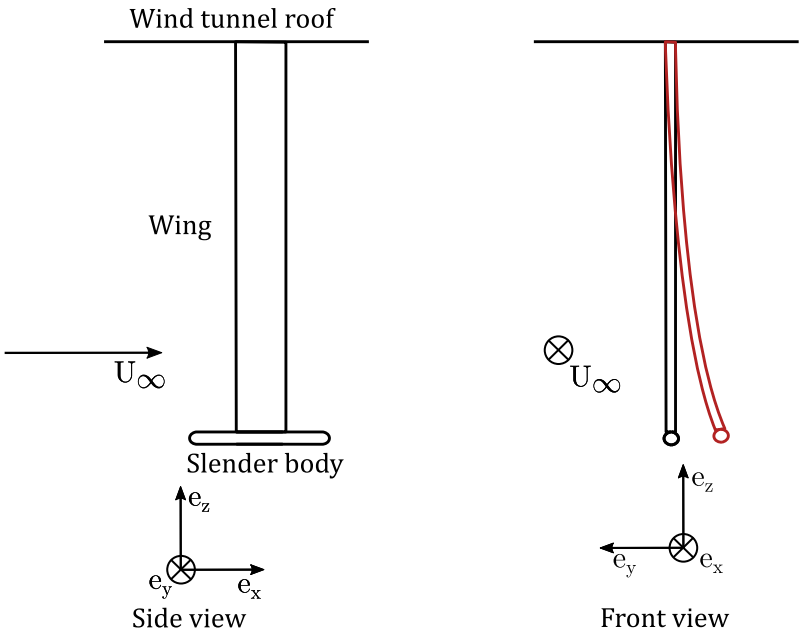

Figure 3.24: Roof mounted wing with tip slender body. The deformed wing in presence of an inflow wind is shown in red.

In order to reduce the influence of gravity on the experimental results, the wing model was attached to the top of the wind tunnel, and therefore gravity induces no static bending deformation of the wing. The experimental setup is shown on Fig. 3.24.

The Reynolds number based on the airfoil chord has a strong impact on the stall angle of the airfoil. Experimental data for the lift coefficient of the NACA0012 airfoil is shown in Fig. 3.25. For a Reynolds number of 6.0×10^6, the stall angle is around 16°, while for $Re = 3.6 \times 10^5$ the stall happens earlier, around 11°. It can be seen that in the attached-flow region, the lift coefficient is not affected by the Reynolds number. Thus, it is less important to use airfoils polars for a specific Reynolds number when the airfoil is operating in attached-flow conditions.

The experimental data from Sheldahl and Klimas [171] shown in Fig. 3.25 are going to be used due to the lack of available quality experimental data for lower Reynolds numbers. The maximum Reynolds number in the experimental data of Tang and Dowell [194] is $Re = 1.2 \times 10^5$.

Modal analysis

A structural modal analysis is done to check whether DIEGO is able to properly reproduce the structural characteristics of the wing model together with its tip slender body. DIEGO was modified to be able to include specific moments of inertia for the tip mass in order to represent the slender body placed at the tip. Before this work, it only allowed punctual

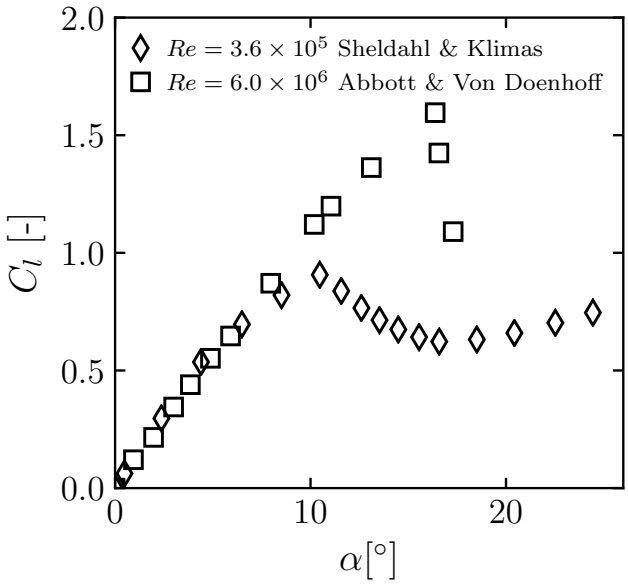

Figure 3.25: Lift coefficient for the NACA0012 airfoil. The stall angle is radically modified by the Reynolds number. Experimental data from Abbott and Doenhoff [7] and Sheldahl and Klimas [171].

masses without moment of inertia. The code was also modified to enable a single blade modal analysis instead of a full rotor modal analysis. In DIEGO, 30 structural nodes are used to mesh the wing with Euler-Bernoulli beam elements [19].

The results obtained with DIEGO for the first few modes are compared to the ones obtained experimentally, as well as the one obtained numerically by Suleman et al. [189] with a Euler-Bernoulli beam formulation in Table 3.6. Apart from the first flapwise bending mode which is underpredicted, DIEGO finds natural frequencies close to the experimental ones. It is interesting to note that DIEGO has similar relative errors as the numerical model of Suleman et al.. The results obtained with DIEGO are considered good enough to move to the time domain analysis.

Table 3.6: Modal analysis of the wing with slender body of Tang and Dowell [194] with numerical results from Suleman et al. [189]. Data retrieved from [189].

Mode	Exp.	DIEGO		Suleman et al. [189]	
	Freq. [Hz]	Freq. [Hz]	Rel. Error %	Freq. [Hz]	Rel. Error %
1st Flap	2.625	2.255	-14.1	2.270	-13.5
1st Chord	14.130	14.859	5.2	14.958	5.9
2nd Flap	17.880	17.567	-1.8	17.872	-0.04
1st Torsion	22.880	23.442	2.5	23.078	0.9

Static aero-elastic deflections

Tang and Dowell [194] measured the static deformation of the wing for different wind speeds with the geometrical angle of attack θ_0 (the one fixed at the root of the wing) set at $\theta_0 = 1°$. The flapwise and tip deflections at the tip were measured. These measurements can validate the aero-elastic coupling of DIEGO for static cases. Numerical results obtained by Tang and Dowell [194] with the system of equations devised by Hodges and Dowell [77] for a uniform untwisted elastic wing with the ONERA dynamic stall model [198] are also presented.

The same structural setup as for the modal analysis is used in DIEGO, meaning 30 structural nodes along the blades. To obtain static deflections for a range of wind speeds, a very slow wind ramp is applied as an inflow wind. The simulation is started with an inflow wind $U_\infty = 0.5\ m.s^{-1}$ which is kept constant until $t = 10\ s$ in order to reach the end of the initial transient. Then, the wind speed is increased linearly up to $U_\infty = 35\ m.s^{-1}$ over 990 s for a total simulation time of 1000 s. A time step of $\Delta t = 0.045\ s$ is chosen. The blade is modeled with 31 aerodynamic elements placed with a cosine distribution along the span. The FVW is used with no wake simplification models, since only a wing is simulated while the presented simplication model is designed for rotors.

The results obtained with DIEGO with both the BEM and FVW models are compared to the experimental results of Tang and Dowell [194] in Fig. 3.26. The BEM predicts larger flapwise and twist deflections than the FVW. Both models have satisfactory results compared to the experimental data.

3.3.6 Aero-elasticity: surging rotor

To the author's knowledge, the aerodynamic responses of an elastic wind turbine rotor has not yet been studied experimentally. For now, most experiments use a very rigid rotor in order to focus on pure aerodynamics rather than aero-elasticity: for example the MEXICO rotor [29] and the UNAFLOW rotor model [22, 57] are rigid models. Therefore, experimental validation data is lacking for aero-elastic numerical models. One possibility is to use higher fidelity models to validate simpler models. Here, we will be using the blade-resolved CFD data of Liu et al. [111] to validate the aero-elastic solver of DIEGO.

Liu et al. [111] coupled the multi-body dynamic code MBDyn to the CFD solver OpenFOAM. The structural model uses a beam formulation similar to the one used in DIEGO while the aerodynamics is modelled with RANS CFD. The k-ω SST turbulence model is used [123]. The deformations of the beam elements are used to move the boundary points of the mesh on the surface of the blade through interpolation before updating the internal cells of the mesh with a dynamic mesh motion solver.

They used a tight coupling between the fluid and structural solvers. The forces and

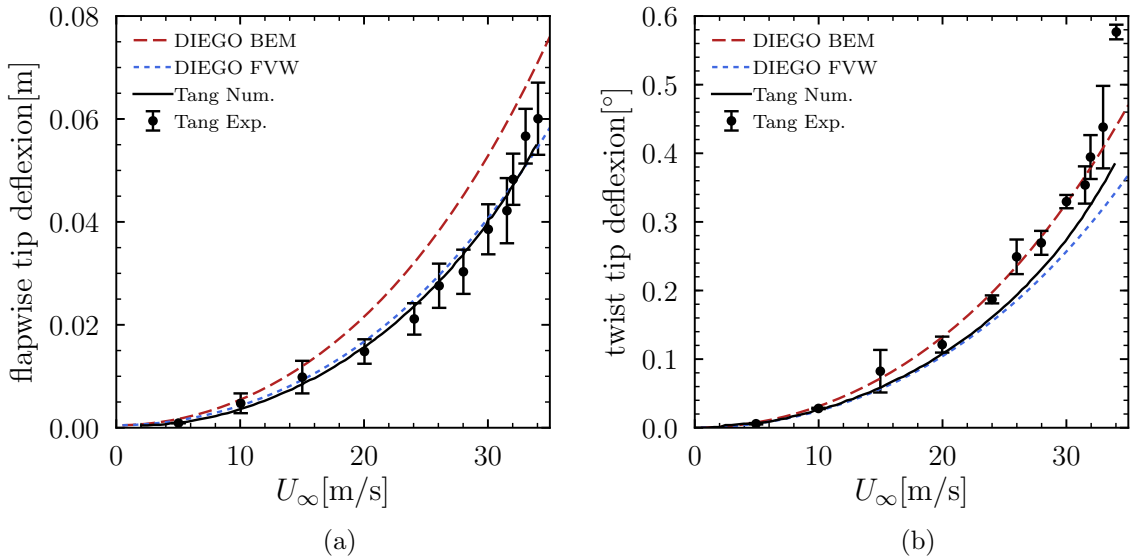

Figure 3.26: Elastic deformations at the tip of the wing of the NREL 5MW wind turbine at rated conditions computed with the BEM and FVW of DIEGO compared to experimental data and numerical model from Tang and Dowell [194]: (a) flapwise deflection and (b) twist deflection.

displacements are exchanged between the two solvers at every subiteration of the flow solver until the flow is sufficiently converged. After that, only structural subiterations are done until the structural dynamic is converged.

Liu et al. [111] kindly provided the results from coupled blade-resolved CFD and multi-body dynamics used in this comparison.

3.3.6.1 Steady axial case

The blade deflections obtained by Liu et al. [111] are compared to the results of DIEGO for both the BEM and FVW aerodynamic models in a steady case before studying a surging case. The studied wind turbine is the NREL 5MW reference wind turbine [90], with no tilt angle, in a uniform steady inflow, at rated conditions $U_\infty = 11.4\ m/s$ and $\Omega = 12.1\ rpm$. The definition document of the NREL 5MW reference wind turbine [90] includes the structural properties of the wind turbine. The blades are discretized in 30 aerodynamic elements and 50 structural Euler-Bernoulli beam elements. The results are extracted after $240s$ of simulation with a time step of $\Delta t = 0.1\ s$.

The results obtained with DIEGO are compared to the blade-resolved CFD results of Liu et al. [111] in Fig. 3.27. Both models have flapwise and edgewise deflections close to the one obtained with blade-resolved CFD by Liu et al. [111]. The BEM predicts results closer to the CFD results for the flapwise deflection while the FVW predicts closer results to the CFD for the edgewise deflection.

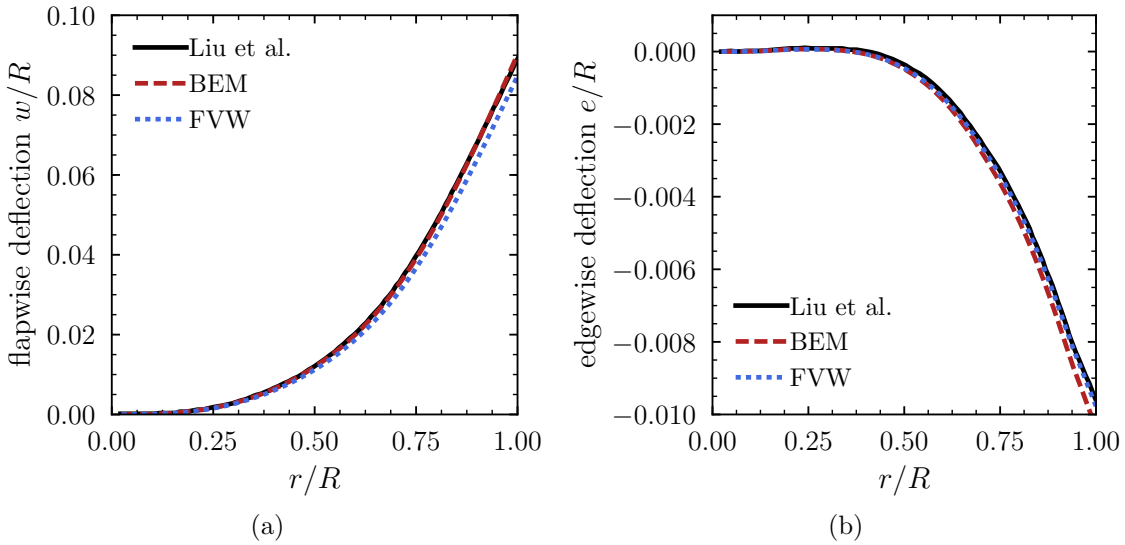

Figure 3.27: Elastic deformations of the blade of the NREL 5MW wind turbine at rated conditions computed with the BEM and FVW of DIEGO compared to numerical blade-resolved CFD data from Liu et al. [111]: (a) flapwise deflection and (b) edgewise deflection.

3.3.6.2 Imposed surge case

After having validated DIEGO in a steady axial case, DIEGO is compared to the results obtained by Liu et al. [111] for an imposed sinusoidal surge motion of amplitude $\Delta x_s = 2\ m$ and period $T_s = 12\ s$. The numerical setup is the same as for the steady case. The deformations at the tip of the blade are extracted on the last surge period of the $240s$ simulations and shown in Fig. 3.28.

The FVW and BEM have a dynamic variation of the flapwise tip deflections close to the blade-resolved CFD data from Liu et al. [111]. The FVW has a better agreement than the BEM with the CFD on the flapwise tip deflection. Compared to the other results, the BEM results show some small oscillations of the edgewise tip deflection in addition to the large amplitude oscillations.

These results show that DIEGO is able to properly predict the deformations of the blades of a wind turbine in imposed surge at a fixed rotation speed, which provides confidence for the use of DIEGO to study floating wind turbines in free motion with variable rotor speed and blade pitch, with elastic blades, for which no validation cases are available.

Conclusion

The aero-hydro-servo-elastic tool DIEGO has been presented with details on the implementations of the two aerodynamic models BEM and FVW. The computational performances of the FVW was improved with a GPU parallelization and a far wake simplification model

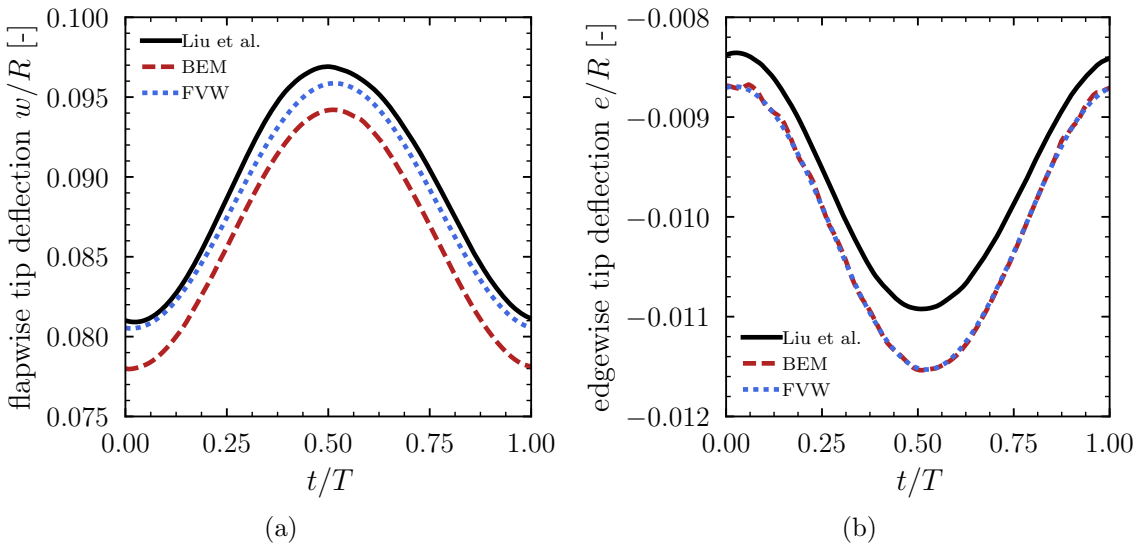

Figure 3.28: Elastic deformations at the tip of the blade of the NREL 5MW wind turbine at rated conditions computed with the BEM and FVW of DIEGO compared to numerical blade-resolved CFD data from Liu et al. [111] for an imposed surge motion of period $T_s = 12\ s$ and amplitude $\Delta x_s = 2\ m$: (a) flapwise deflection and (b) edgewise deflection.

was presented and implemented to optimize the computational cost. The aero-elastic coupling was presented and validated against blade-resolved CFD and experimental data.

In the following chapter, DIEGO is used to study the dynamics of an operating elastic floating wind turbines. The BEM and the FVW aerodynamic models are used to study the fatigue damage of the blades. The goal is to compare the fatigue predicted by both aerodynamic models and to identify the possible shortcomings of the BEM method.

Chapter 4

Effects of the aerodynamics on the fatigue of a floating wind turbine

Dans ce chapitre, les modèles aérodynamiques Blade Element Momentum et Free Vortex Wake sont comparés pour l'étude de la fatigue structurelle en pied de pâle lié au moment de battement d'une éolienne de taille industrielle. Les cas d'une éolienne fixe, d'une éolienne flottante sur un flotteur semi-submersible et d'une éolienne flottante sur une une plateforme à lignes tendues sont étudiés. La méthode Blade Element Momentum mène à une fatigue significativement plus élevée que la méthode Free Vortex Wake. Les deux flotteurs étudiés induisent une fatigue réduite par rapport à l'éolienne posée, en particulier pour les vitesses de vent générant le plus de poussée aérodynamique. Cette réduction de la fatigue est lié au mouvement de cavalement dans le cas de la plateforme à lignes tendues et au mouvement de tangage dans le cas du flotteur semi-submersible. Ces degrées de liberté apportent une souplesse au système et réduisent les efforts les plus extrêmes, ce qui mène à une fatigue réduite. Les variations du vent turbulent poussent l'éolienne au lieu de générer de fort moment de battement en pied de pâle.

4.1 Wind turbine fatigue

Structural fatigue is the damage related to the accumulation of load cycles that would not cause failure for a single cycle [166]. The prediction of the fatigue of wind turbine is a key point for the design of wind turbines and wind farms. It is done to estimate the operating lifetime of wind turbines. Underestimating the fatigue can cause structural failure of the wind turbine with for example rupture of the blades. An overestimation of the fatigue induces an underestimation of the operating lifetime. Wind turbines that could still safely operate for a long time would be decommissioned too early.

Marín et al. [117] analyzed the damage on a blade of a 300kW turbine and found that the cracks were related to fatigue damage. A full-scale fatigue testing of a 3MW rotor blade done by Lee et al. [99] lead to failure at the root of the blade. According to them, the deformation of the shell at the blade root increased the loads and lead to failure. It is therefore important to properly predict the fatigue at the root of the blade.

Turbulence has been identified [153, 154] as the main driver of fatigue on the blades. Higher levels of turbulence generate larger fatigue because of higher amplitude cyclic loadings. Thomsen and Sørensen [196] showed that the farm-generated turbulence can increase fatigue loads. However, other sources of fatigue have been identified. The importance of the atmospheric stability on fatigue damage has been shown by Sathe and Bierbooms [162]. Different inflow profiles lead to significantly different fatigue damage, however their study was done without turbulence. Frohboese and Anders [59] studied the effect of icing on wind turbine fatigue. The situation where two out of the three blades were iced was the worst for fatigue.

Different methods exist to evaluate the fatigue of structures. The rainflow counting method of Matsuishi and Endo [121], which is a method to extract equivalent load cycles from a temporal signal, has been standardized and is used most of the time. Sutherland and Veers [193] stressed the importance of the large stress cycles that have a low probability of occurrence on the predicted service lifetime of fiberglass blades. Sutherland and Mandell [192] found that the blade fatigue was overestimated when the mean stress is not accounted for using experimental load spectra from on-site wind turbines. Hammerum et al. [71] developed an alternative to rainflow counting to estimate the fatigue of a wind turbine and used this new method to optimize a controller to obtain the longest lifetime possible. Hu et al. [80] presented a dynamic wind load uncertainty model to account for annual wind load variations both on the mean wind speed and on the turbulence intensity. Sun and Jahangiri [190] analyzed on-site measurements of wind and waves to generate probabilistic distributions of the wind and wave environmental conditions, then used for fatigue damage estimations.

Horn and Leira [78] accounted for the downtime of wind turbines in their estimation of

wind turbine lifetime as they stated that fatigue damages accumulate much faster in non-operational conditions. They used a stochastic model for the downtime of wind turbine instead of a deterministic one.

Wang et al. [208] studied a 10MW wind turbine on a semi-submersible floater in combined wind and wave with OpenFAST together with SIMPACK for the drive-train dynamics. BEM was used for the aerodynamic module. They suggested that similar studies should be carried out for floaters with a different dynamic behavior as well as for individual blade pitch control. For the three studied wind speed cases, they used the most probable values for the significant wave height and the wave period. They found that the turbulence intensity increased the fatigue of the main bearings.

In their preprint work, Nanos et al. [134] use hGast to study the fatigue of a floating wind turbine pitched with a ballasted floater. They did not mention whether they used BEM or FVW aerodynamics model of hGast.

A comparison between the fatigue obtained with BEM and FVW was done by Boorsma et al. [31] for a bottom-fixed wind turbine. They found that FVW predicted lower fatigue levels than BEM. Perez-Becker et al. [144] also compared the fatigue predicted by BEM and FVW for the 10MW reference wind turbine [16] in fixed bottom conditions with a structural model based on a modal method, taking into account the first and second flapwise mode and the first edgewise mode, therefore not modeling the twist degree of freedom. They also found that using the FVW method results in lower fatigue damage than using the BEM method. They stated that using a structural model taking into account the torsional degree of freedom, in particular the twist that influences the angle of attack of the airfoil sections, might increase the difference seen between the two aerodynamic models.

In this Chapter, the fatigue predicted by DIEGO with BEM and FVW is compared for a bottom-fixed and floating wind turbine for a 15 MW wind turbine. Two different floaters are compared: a semi-submersible and a TLP. The differences between the FVW and the BEM are explored as well as the differences between the fixed and floating conditions. The focus is on the fatigue related to the flapwise root bending moment since it is mainly due to the aerodynamic forces and will therefore be affected by differences in the aerodynamic models.

4.2 Methodology

4.2.1 Floating wind turbine geometry

The studied floating wind turbine model is the IEA 15MW wind turbine presented by Gaertner et al. [61] along with the semi-submersible floater designed by University of

Maine [9]. This floating wind turbine is used in the HIPERWIND project [37]. The natural frequency of the original tower is close to the passing frequency of the blades, therefore the tower has been redesigned in the HIPERWIND project to move the natural frequency of the tower away from the blade passing frequency. Here, the HIPERWIND version of the floating wind turbine is adopted, with for example the modification of the moorings to accommodate for a water depth of 150 m and an increase of the mass of the rotor-nacelle assembly. The only modification that is done compared to the HIPERWIND definition is an artificial increase by a factor 100 of the tower stiffness to focus on the blades dynamics. The rated wind speed of the wind turbine is $U_\infty = 40.59\ m/s$, which is the smallest wind speed for which the turbine is able to produce its rated electrical power of 15MW.

In addition to the semi-submersible floater designed by University of Maine [9], a TLP floater designed specifically for the IEA 15MW wind turbine is used. It consists of two coaxial cylinders with three vertical mooring lines connected to the floater by horizontal tendons equally spaced at the bottom of the lower cylinder. The geometry is detailed in Fig. 4.1 and Table 4.1.

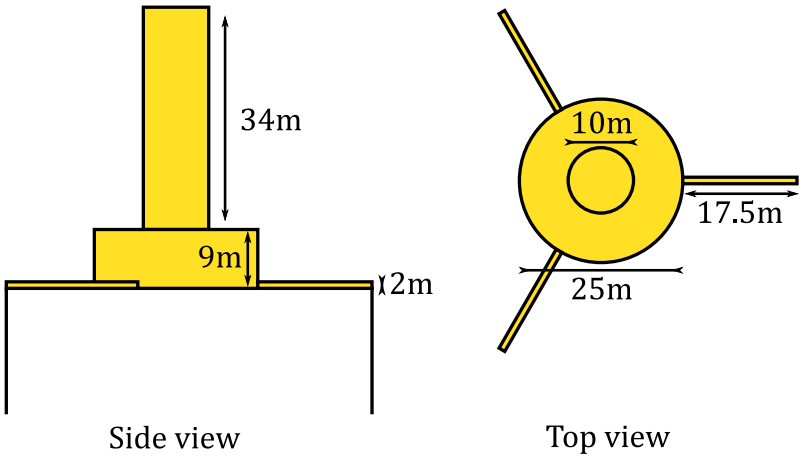

Figure 4.1: Schematic of the geometry of the TLP.

Table 4.1: Mooring line properties.

Unstretched length	ES (axial stiffness)	ρ
114.9 m	4509 MN	8000 kg/m^3

4.2.2 Fatigue estimation

The damage D is estimated using the linear damage hypothesis of Palmgren and Miner [128]:

$$D = \sum_{i=1}^{k} \frac{n_i}{N_i} \tag{4.1}$$

where k is the number of stress amplitudes, n_i is the number of cycles experienced by the structure at a given stress amplitude of index i while N_i is the number of cycles that would result in failure at this amplitude of stress cycle. Failure occurs when $D = 1$. The number of cycles leading to failure for different stress levels is most often obtained from experiments on a sample of the material. Measurements are done to link a stress cycle amplitude to a maximum number of cycles. These data are summarized on an S-N curve, where S stands for stress and N designates the number of cycles leading to failure. The composite materials used for wind turbine blades have been experimentally studied to obtain the relation between the stress cycle amplitude and failure cycle number [10, 191].

A curve fit of experimental data is used to conduct fatigue analysis. Sutherland [191] stated that for wind turbine blade composites, both a log-log and a log-linear relation can be used, but the choice of equation has a large impact on the predicted lifetime of the blade. Toft and Sørensen [197] chose to use a log-log law fitted on the experimental data from the OPTIMAT database, compiled for wind turbine blades composites:

$$\log N = \log K - m \log \Delta\sigma \tag{4.2}$$

where K is a material related parameter and m is the fatigue exponent. The value of these parameters depends on whether the material is in tension or compression. The focus is here on the flapwise bending moment for which the blade is in tension. When the fatigue exponent m is large, the fatigue is dominated by the largest stress cycles which generate the largest amount of damage. A fatigue exponent of $m = 9.51$ as taken by Toft and Sørensen [197] based on the OPTIMAT database is chosen. Composite materials have a high fatigue exponent, larger than the one recommended for steel $m = 3$ to 5 [2], meaning that the most extreme cycles will contribute more to the damage relatively to the repetition of smaller amplitude stress cycles. The S-N curve used for the fatigue analysis is shown in Fig. 4.2.

The rainflow counting algorithm by Matsuishi and Endo [121] is used to count the number of cycles at each stress range in the one-hour time series of the flapwise root bending stress of the blade. An open-source python implementation of the algorithm is used [83]. The residual cycles are accounted for as half-cycles.

4.2.3 Metocean conditions

The metocean conditions are chosen to be representative of conditions in South Brittany, France, taken from the ANEMOC database [4] at coordinates (46.80°, −4.59°), as used in

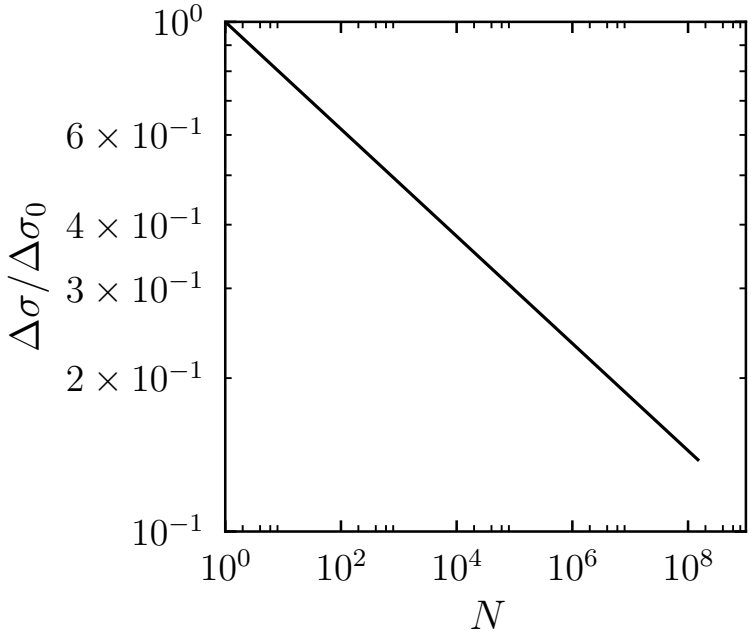

Figure 4.2: S-N curve of a wind turbine blade composite material used for the flapwise root bending moment fatigue analysis. $\Delta\sigma_0$ is the stress amplitude leading to failure for one cycle. The S-N curve has a fatigue exponent $m = 9.51$.

Table 4.2: Metocean conditions.

U_{ref} $[m/s]$	5	9	13	17	21	25
H_s $[m]$	1	1	2	2.5	5	7.5
T_p $[s]$	8	9	11	13	13.5	14

the Hiperwind project [37]. The probability distribution of the wind is shown in Fig 4.3. For each wind speed, the most likely set of significant wave height and period (Hs, T_p) is used with a JONSWAP spectrum. The wind and waves are assumed to be aligned. The metocean conditions are detailed in Table 4.2. A turbulent wind with a Kaimal spectrum and a turbulence intensity corresponding to the class C defined by the IEC 61400-1 standard [82] is generated with TurbSim [88]. The choice of turbulence intensity is arbitrary, since there is no field data available to support that choice, but it is still a realistic value. For each wind speed, 6 one-hour simulations are done using different seeds for the random generation of the wind and waves.

4.2.4 Free Vortex Wake Sub-iteration

Precursor aero-hydro-servo-elastic simulations done with the BEM aerodynamic model have shown that for the wind speeds above rated conditions (13 m/s to 25 m/s) a time step of $\Delta t = 0.05s$ is necessary for the structural solver to converge. For the below rated

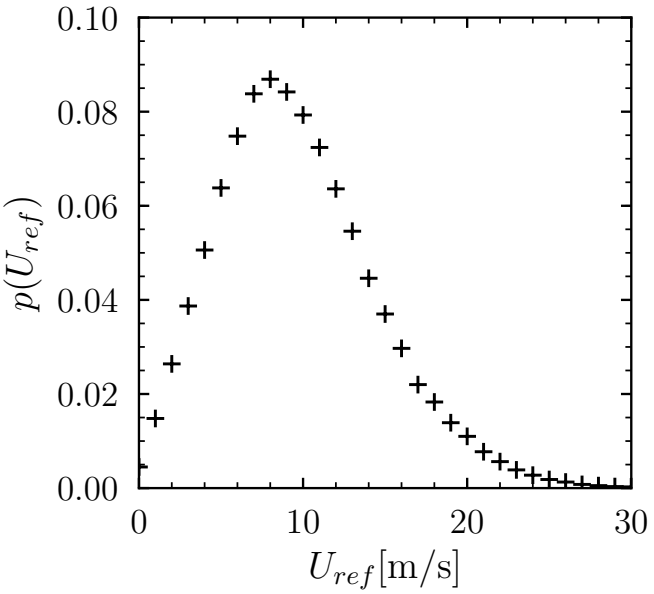

Figure 4.3: Wind speed probability distribution at the reference height for the chosen site taken from ANEMOC [4].

wind speeds (5 m/s and 9 m/s), a time step of $\Delta t = 0.1s$ is sufficient to obtain convergence in the structural solver.

When using the Free Vortex Wave method, increasing the number of time steps drastically increases the computational cost of the simulation due to the larger number of vortex elements in the wake that have to be accounted for when computing the velocity field. A time step of $\Delta t = 0.05s$ leads to more than 156 time steps per rotation at rated conditions. It induces the emission of a very large number of vortex elements into the wake that results in a very high computational cost of the simulations.

A sub-iteration procedure is set-up for the Free Vortex wake method, to lower the computational cost, while solving the aero-hydro-servo-elastic model every $\Delta t = 0.05s$. A threshold time interval Δt_{FVW} for the emission of new vortex elements is imposed. New vortex elements are emitted into the wake only if the time interval since the last vortex emission is higher than Δt_{FVW}. The velocity induced by the wake on the deformed blade shape is still computed twice per time step in the predictor-corrector algorithm as well as the wake self-induced velocity for the convection step of the wake. Only the wake emission differs.

This procedure also allows to reduce the number of elements emitted in the wake for case with a low rotation speed of the rotor. The threshold time interval chosen for the study is shown in Table 4.3.

The sub-iteration procedure is compared to the original algorithm with vortex emission

Table 4.3: Time steps used for the vortex wake emission Δt_{FVW} and for the aero-servo-hydro-elastic solver Δt for the different wind conditions.

U_{ref} $[m/s]$	5	9	13	17	21	25
Δt_{FVW} $[s]$	0.2	0.1	0.1	0.1	0.1	0.1
Δt $[s]$	0.1	0.1	0.05	0.05	0.05	0.05

Table 4.4: Relative fatigue damage difference between FVW with vortex emission at every time step and with a threshold $(D_{FVW,full} - D_{FVW,threshold})/D_{FVW,threshold}$.

U_{ref} $[m/s]$	5	9	13	17	21	25
Blade 1	5%	0%	−2%	−3%	−0%	−1%
Blade 2	−1%	0%	1%	1%	0%	2%
Blade 3	−2%	0%	1%	−1%	1%	1%

at every time step in Table 4.4. The fatigue obtained over half an hour of physical time after 5 minutes of initialization is compared between the FVW with a threshold on vortex emission specified in Table 4.3 and vortex emission at every time step. The comparison is done over one seed of the metocean condition for the wind turbine on the UMaine semi-submersible floater. The comparison is limited to half an hour due to the large computational time of the FVW with vortex emission at every time step. No differences are found for $U_{ref} = 9\ m/s$ since the vortex emission time step and the aero-servo-hydro-elastic solver time step are the same (see Table 4.3). The relative fatigue fatigue difference is limited for the other wind speeds. The number of cycles exceeding different stress levels are shown in Appendix B. Very good agreement is found between the FVW with a larger time step for vortex emission and FVW with vortex emission at every time step of the aero-servo-hydro-elastic solver. Therefore, time steps reported in Table 4.3 are used in the following for the FVW vortex emission to reduce the computational time of the FVW simulations.

4.2.5 Computational cost

For each of the 6 selected wind speeds, 6 different seeds are used to generated the turbulent wind and the irregular waves for a total of 36 one hour simulations per aerodynamic model and per floater. The simulations are done on 2 Intel Xeon Gold 5112 processor with 4 cores each, for a total of 8 cores, while the GPU algorithm runs on 2 NVidia V100 PCI-E GPUs. The BEM code is serial and only uses a single core while the FVW code is parallelized on the GPUs. The total computational cost of the 36 simulations are shown in Table 4.5. Since the simulations are independent, the cases can be distributed on several computational nodes and run in concurrently.

The total computational cost is slightly increased for the floating cases. This is likely due to the resolution of the floater motion as well as the increased complexity of the cases

Table 4.5: Total computational cost for the set of 36 one hour simulations.

	Fixed	Semi-submersible	TLP
BEM	20 h	26 h	23 h
FVW	521 h	531 h	520 h

which could require more iterations in the resolution of the elastic deformations. FVW has a significantly larger computational cost than BEM.

4.3 Results

4.3.1 Fatigue

Stress-cycles are compared for the selected metocean conditions (Table 4.2) between a bottom-fixed case, a TLP, and a semi-submersible, with BEM and FVW. For each wind conditions, the same 6 randomly generated turbulent inflow wind realizations are used for floating and fixed conditions, with BEM and FVW, so that the wind turbine operates in the same wind conditions. The same is done for the wave field, the TLP and semi-submersible operate in the same wave conditions. In the following, "floating conditions" will refer to the wind turbine on the semi-submersible and on the TLP as opposed to fixed conditions that refer to the bottom-fixed wind turbine. The differences between the rainflow counted stress cycles obtained with BEM and FVW is therefore due to the aerodynamic models while the differences between fixed and floating for a specific aerodynamic model is due to the difference between the dynamic of a fixed and a floating wind turbine.

The number of cycles exceeding a stress amplitude level in the rainflow-counted cycles for the simulated cases is shown in Fig. 4.4. Due to the large fatigue exponent of wind turbine blades composite, the largest stress cycles generate the largest part of the total damage.

For below rated conditions at $U_{ref} = 5\ m/s$, the stress cycles are similar between the fixed conditions and with the two floaters for both BEM and FVW. It means that the dynamic of the floating wind turbine does not significantly affect the flapwise root bending stress of the blades for this wind speed. However, the BEM predicts significantly larger stress cycles than the FVW for both fixed and floating conditions.

At $U_{ref} = 9\ m/s$, both aerodynamic models predict a significant reduction of the amplitude of the stress cycles for the wind turbine on a the semi-submersible or the TLP compared to the fixed one, with good agreement between the FVW and BEM.

Above rated conditions at $U_{ref} = 13\ m/s$, the differences in stress cycle amplitude are significant for the largest stress cycles. FVW predicts smaller amplitudes than the BEM for the largest stress cycles. Nevertheless, both aerodynamic models show a reduction of the amplitude of the largest stress cycles for the floating conditions compared to the fixed

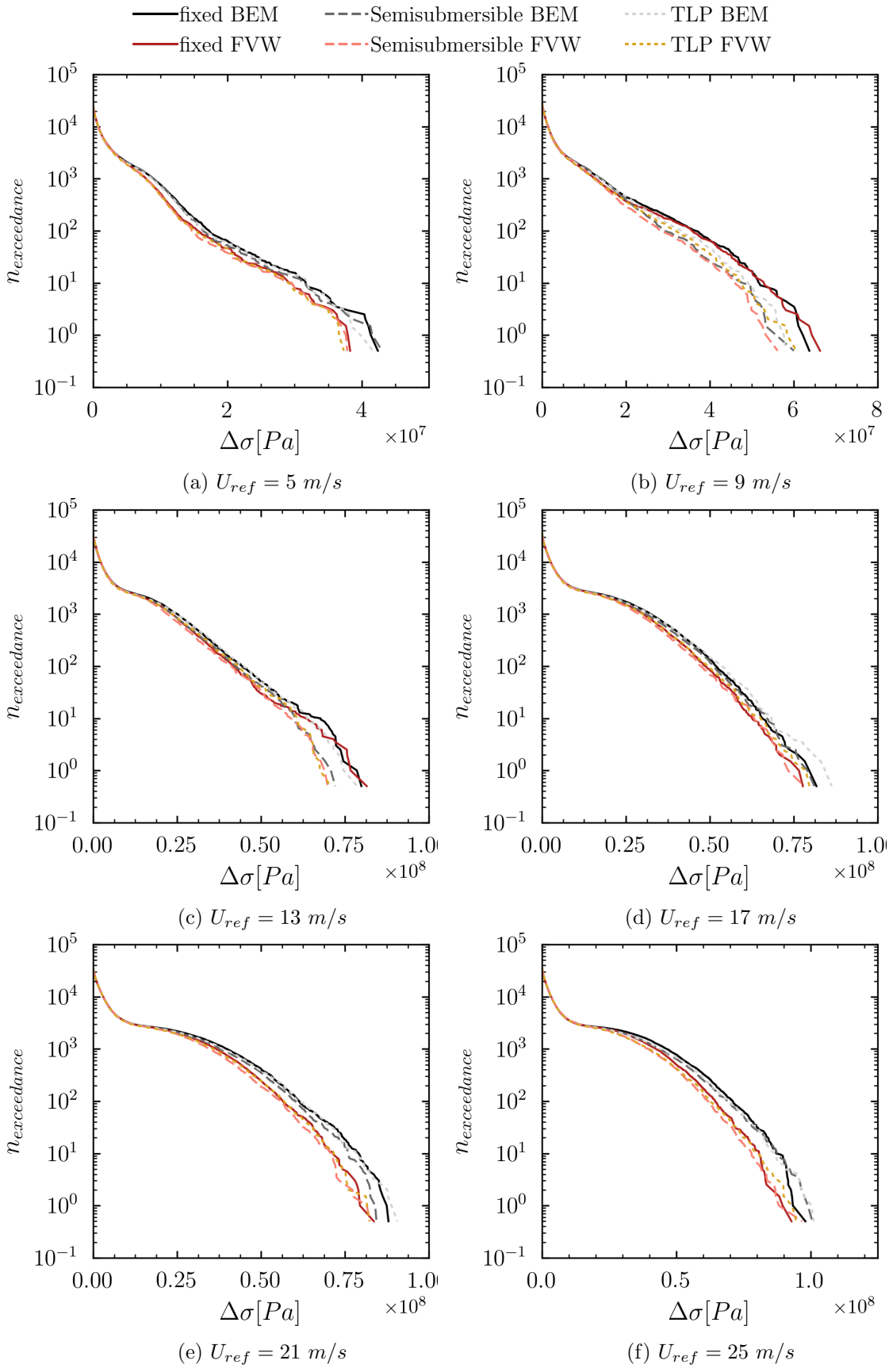

(a) $U_{ref} = 5\ m/s$ (b) $U_{ref} = 9\ m/s$

(c) $U_{ref} = 13\ m/s$ (d) $U_{ref} = 17\ m/s$

(e) $U_{ref} = 21\ m/s$ (f) $U_{ref} = 25\ m/s$

Figure 4.4: Number of exceedance of stress cycle amplitude of the rainflow counted stress cycles over the 3 wind seeds in fixed bottom conditions.

conditions.

For the three largest wind speeds $U_{ref} = 17\ m/s$, $U_{ref} = 21\ m/s$ and $U_{ref} = 25\ m/s$, limited differences are found by both aerodynamic models between the fixed and floating conditions for the largest stress cycles. The BEM method predicts constantly larger stress cycles than the FVW method.

The largest differences between the fixed wind turbine and the two floating wind turbines are found for the wind speed close to rated conditions $U_{ref} = 9\ m/s$ and $U_{ref} = 13\ m/s$. Less differences are found for other inflow winds. While the BEM and FVW agree on the difference between fixed and floating conditions, the BEM predicts constantly higher stress cycle amplitudes than the FVW.

The fatigue related to each wind speed affects the total fatigue of the wind turbine depending on how frequent the wind conditions are. Indeed, the wind speed varies and the probability distribution of the reference wind speed at hub height at the chosen site is shown in Fig. 4.3. Even though the fatigue generated by the operation of the wind turbine in an inflow of $U_{ref} = 25\ m/s$ is large due to the high amplitude of the stress cycles shown in Fig. 4.4f, these wind conditions occur less than 0.02% of the time during the lifetime of the wind turbine. Therefore, even though the amplitude of the stress cycles is lower for an inflow wind of $U_{ref} = 13\ m/s$, these conditions occur during 5.46% of the lifetime of the wind turbine, thus generating a similar amount of accumulated damage than larger less frequent wind speeds.

The amount of damage generated by each wind conditions taking into account the probability of occurrence of the wind conditions is shown in Fig. 4.5. It can be seen that the inflow wind of $U_{ref} = 5\ m/s$ generates a negligible amount of damage compared to other wind speeds. This is due to the low amplitude of the stress cycles (see Fig. 4.4a) that generates little damage even though this wind condition is common, occurring 6.38% of the lifetime of the wind turbine.

For $U_{ref} = 17\ m/s$, there are few differences between the damage computed for the fixed turbine and the semi-submersible case, while the damage is larger for the TLP case. However, the FVW predicts much less damage than the BEM due to the smaller amplitude of the largest stress cycles.

For the two largest wind speeds, $U_{ref} = 21\ m/s$ and $U_{ref} = 25\ m/s$, the fatigue damage is similar for the fixed and TLP cases, while it is lower for the semi-submersible. Even though the probability of occurrence of the largest inflow wind speed is small, it generates a comparatively similar amount of damage than smaller wind speed because of the large fatigue exponent m of blade composites.

The damage due to the flapwise root bending moment for the wind turbine on a TLP and a semi-submersible are compared to the damage obtained in fixed conditions with the BEM in Table 4.6 and with the FVW in Table 4.7.

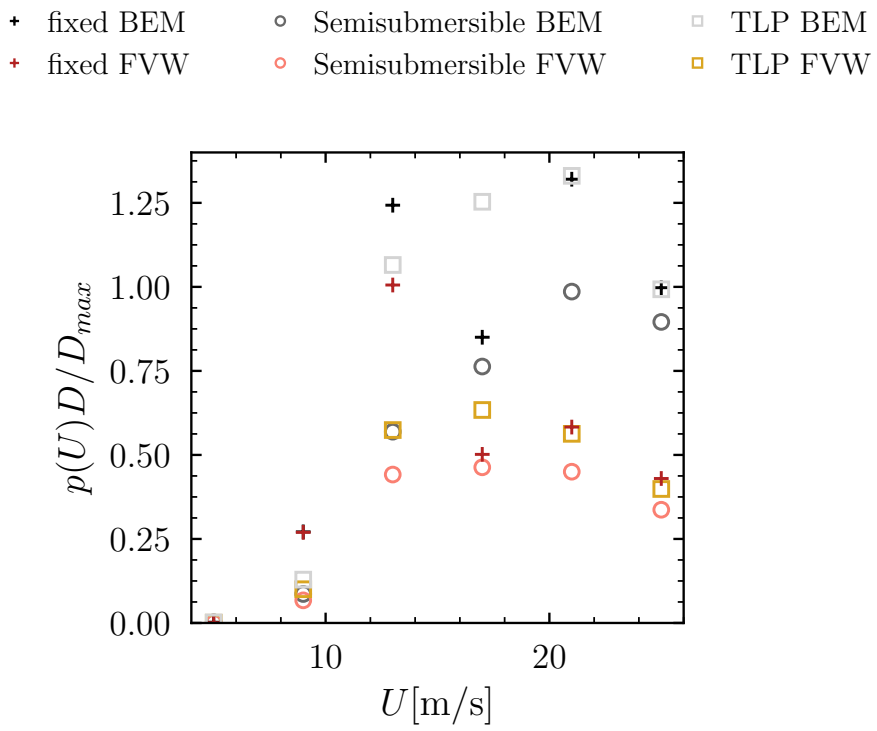

Figure 4.5: Accumulated damage over lifetime taking into account the probability of occurrence of the wind condition. The data is scaled by the maximum damage of one seed obtained with the BEM.

Table 4.6: Relative damage reduction between a floating wind turbine and a fixed wind turbine with BEM $(D_{floating} - D_{fixed})/D_{fixed}$.

U_{ref} $[m/s]$	5	9	13	17	21	25
Semi-submersible	−15%	−68%	−54%	−10%	−25%	−10%
TLP	−22%	−52%	−14%	+47%	+1%	0%

Table 4.7: Relative damage reduction between a floating wind turbine and a fixed wind turbine with FVW $(D_{floating} - D_{fixed})/D_{fixed}$.

U_{ref} $[m/s]$	5	9	13	17	21	25
Semi-submersible	−14%	−75%	−56%	−8%	−23%	−22%
TLP	−21%	−63%	−43%	+26%	−3%	−7%

Overall, there is a good agreement in the damage reduction predicted by both aerodynamic models. This shows that the dynamics of the floating wind turbines is equally captured by the BEM and the FVW. The semi-submersible shows a large damage reduction for inflow wind speeds of $U_{ref} = 9\ m/s$ and $U_{ref} = 13\ m/s$, with a lower reduction of the fatigue damage for other wind speeds. Since these two wind conditions generate damage comparable to other wind speed conditions when taking into account the probability of occurrence of the wind, a reduction of the overall flapwise root bending stress damage over the lifetime of the floating wind turbine can be expected.

The TLP shows reduced damage for $U_{ref} = 9\ m/s$ compared to the fixed bottom wind turbine. For $U_{ref} = 17\ m/s$, both aerodynamic models predict an increase of the fatigue damage for the TLP compared to the fixed turbine, with FVW predicting a smaller increase than the BEM.

The dynamics of both floating wind turbine are studied in the next section to explain the difference in damage between the fixed and floating conditions.

4.3.2 Floating wind turbine dynamic

To investigate the differences in fatigue between the fixed and floating conditions, the power spectral density of the flapwise root bending moment is shown in Fig. 4.6 for the bottom-fixed turbine and the two floating wind turbines computed with the FVW. A major difference between bottom-fixed and floating turbines dynamics is the low frequency motions experienced by these last ones. The natural pitch frequency of the floating wind turbine on the semi-submersible, including the floater and the mooring lines, is $f_p = 0.036\ Hz$, while the natural surge frequency of the floating wind turbine on a TLP is $f_s = 0.023\ Hz$. The natural frequencies were computed from free decay tests, in absence of wind. A clear reduction of the power spectral density of the blade root moment can be seen near the natural pitch frequency of the semi-submersible in Fig. 4.6, while a similar reduction can be seen near the natural surge frequency for the TLP. The power spectral density obtained with the BEM aerodynamic model is shown in Appendix C. It exhibits the same behavior as the FVW results. This reduction is large for $U_{ref} = 9\ m/s$ and $U_{ref} = 13\ m/s$. For the TLP, a larger response of the flapwise root bending moment can be observed compared to the fixed conditions near the frequency of the waves for the larger wind speeds for which the significant wave height is larger (see Table 4.2).

The pitch motion of the semi-submersible is alleviating some of the flapwise root bending moments loads. This explains the reduced fatigue damage observed for this floater compared to a bottom-fixed wind turbine. The wind is pushing the floating wind turbine downstream, which is able to move, instead of generating large bending moments. For the TLP, the surge motion acts similarly and alleviates some of the flapwise root bending moments loads. However, for the cases with large significant wave height, the TLP

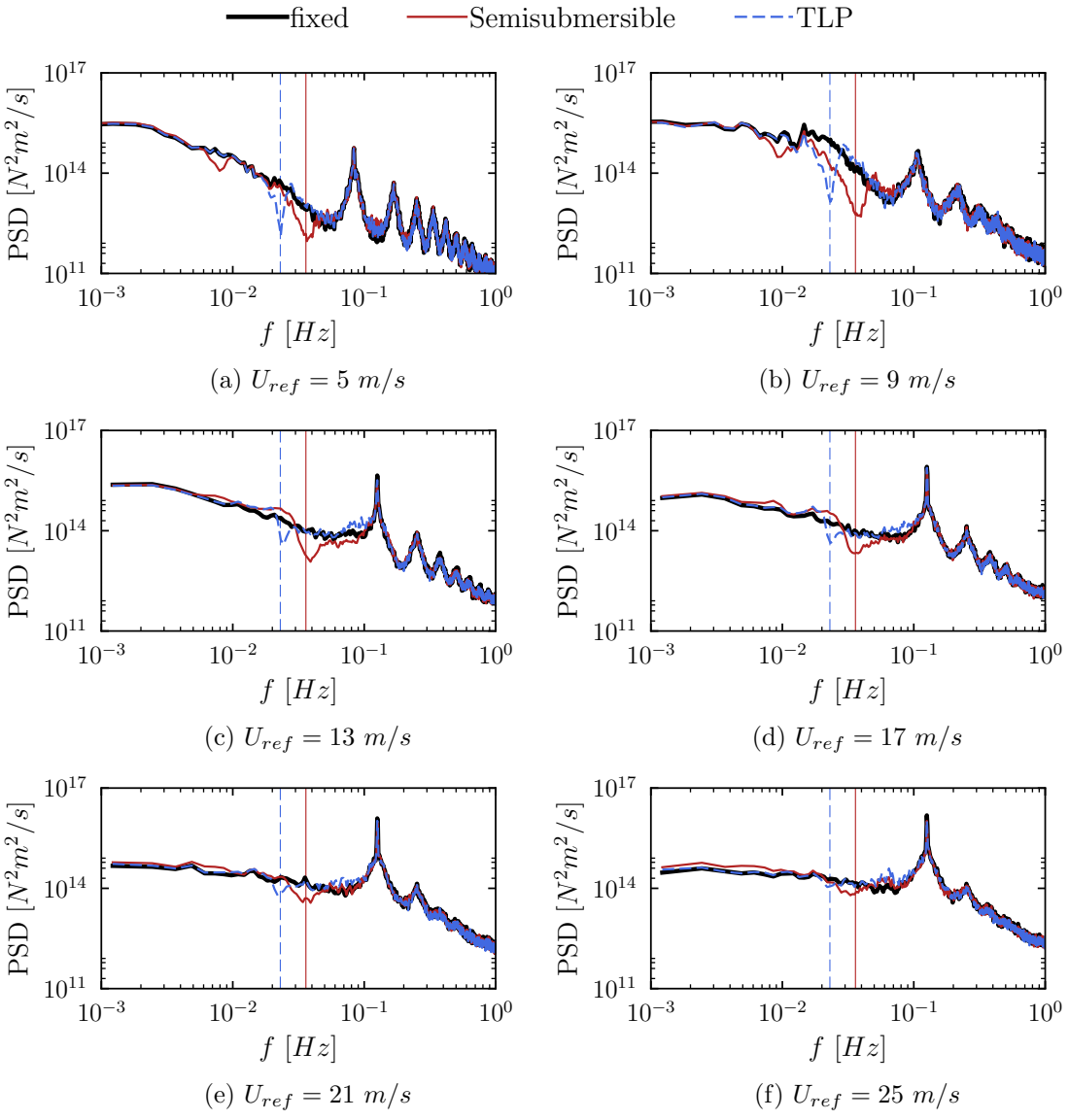

(a) $U_{ref} = 5\ m/s$ (b) $U_{ref} = 9\ m/s$

(c) $U_{ref} = 13\ m/s$ (d) $U_{ref} = 17\ m/s$

(e) $U_{ref} = 21\ m/s$ (f) $U_{ref} = 25\ m/s$

Figure 4.6: Power Spectral Density of the flapwise root bending moment for FVW. The red vertical line shows the natural pitch frequency of the floating wind turbine with the semi-submersible while the blue dashed line shows the natural surge frequency of the floating wind turbine on the TLP.

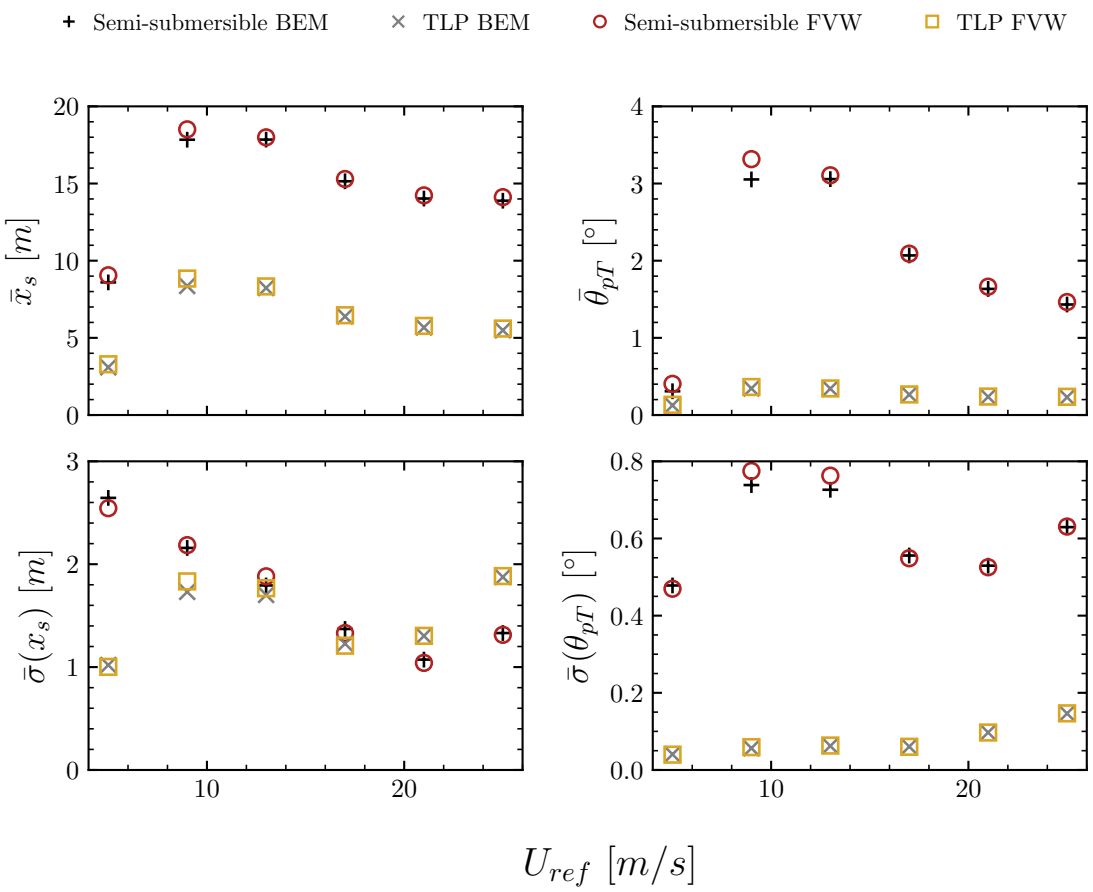

Figure 4.7: Average and standard deviation of the surge position and platform pitch.

is put in motion by the waves, which generates an overall increase of the fatigue damage for $U_{ref} = 17\ m/s$ and a level of damage similar to the bottom-fixed conditions for $U_{ref} = 21\ m/s$ and $U_{ref} = 25\ m/s$.

The average and standard deviation of the surge position, x_s, and platform pitch, θ_{pT}, are shown in Fig. 4.7. The standard deviation is averaged between the different seeds at each wind speed. There is a good agreement between the BEM and FVW on the average and standard deviation of the surge position and platform pitch. The two studied floaters have a different behavior. The TLP shows very little platform pitch, which is expected for a TLP with vertical mooring lines. A TLP with inclined mooring lines would experience more pitch as shown by Milano et al. [126]. For both floaters, the average surge is larger for the wind speeds for which the thrust is the largest ($U_{ref} = 9\ m/s$ and $U_{ref} = 13\ m/s$). The average platform pitch of the semi-submersible is also larger for these wind speeds due to the large thrust force. However, the effects of the low frequency motions on the fatigue is similar at the end, with a reduction due to some large aerodynamic forces being transfered to inertia instead of internal forces.

The average power predicted by the BEM is in good agreement with the one predicted by

Table 4.8: Relative difference in average power between a floating wind turbine and a fixed wind turbine $(\bar{P}_{floating} - \bar{P}_{fixed})/\bar{P}_{fixed}$.

	U_{ref} $[m/s]$	5	9	13	17	21	25
BEM	Semi-submersible	-1%	-3%	-1%	0%	0%	0%
	TLP	0%	-1%	0%	0%	0%	0%
FVW	Semi-submersible	-1%	-3%	-1%	0%	0%	0%
	TLP	0%	-2%	0%	0%	0%	0%

FVW for the three wind turbines. This shows the quality of the BEM as an engineering tool: it predicts similar average values than a higher fidelity model for a much lower computational cost. For above rated conditions ($U_{ref} > 10.59\ m/s$), the average power is the same for the three wind turbines and the two aerodynamic models because the controller is actively acting to maintain the power at 15MW. Very good agreement is found on the effect of the floater on the mean power between BEM and FVW as shown in Table 4.8.

To study further the dynamics of the two floating wind turbines, the power spectral density of the floater displacements are shown in Fig. 4.8. For each degree of freedom, the corresponding natural frequency obtained from a free decay test without wind is shown. While both floaters have similar standard deviations of the surge displacement as shown in Fig. 4.7, the surge motion has a different behavior for the two floater. For the semi-submersible, the wind generates low frequency surge motions, in particular for low inflow wind speeds. For the TLP, the wind generates a surge motion at a frequency slightly lower than the natural surge frequency for the two cases with the largest thrust, $U_{ref} = 9\ m/s$ and $U_{ref} = 13\ m/s$. The high wind speed cases have the largest waves, which generate surge motion at frequencies close to the frequencies of the incoming waves.

The semi-submersible experiences some wind-generated pitch motion for the two wind speeds for which the fatigue reduction is the largest ($U_{ref} = 9\ m/s$ and $U_{ref} = 13\ m/s$; see Table 4.7). The pitch motion occurs at frequencies smaller than the natural frequency of the pitch motion extracted from a windless free decay test (Fig. 4.8). Additional decay tests done in the presence of a laminar sheared inflow wind with the controller activated have shown the same behavior; the period of the oscillations are increased compared to a windless decay test. This is attributed to the combined effect of the wind and the controller.

Both floating wind turbines exhibit a low frequency surge response, however it does not significantly affect the low frequency response of the flapwise root bending moment as seen in Fig. 4.6. The low frequency surge motions do not induce a relative inflow velocity large enough to affect the aerodynamic forces on the rotor.

Overall, the compliance provided by the floaters and the mooring lines is reducing the fatigue damage, because the flapwise bending moment variation is reduced by the pitch

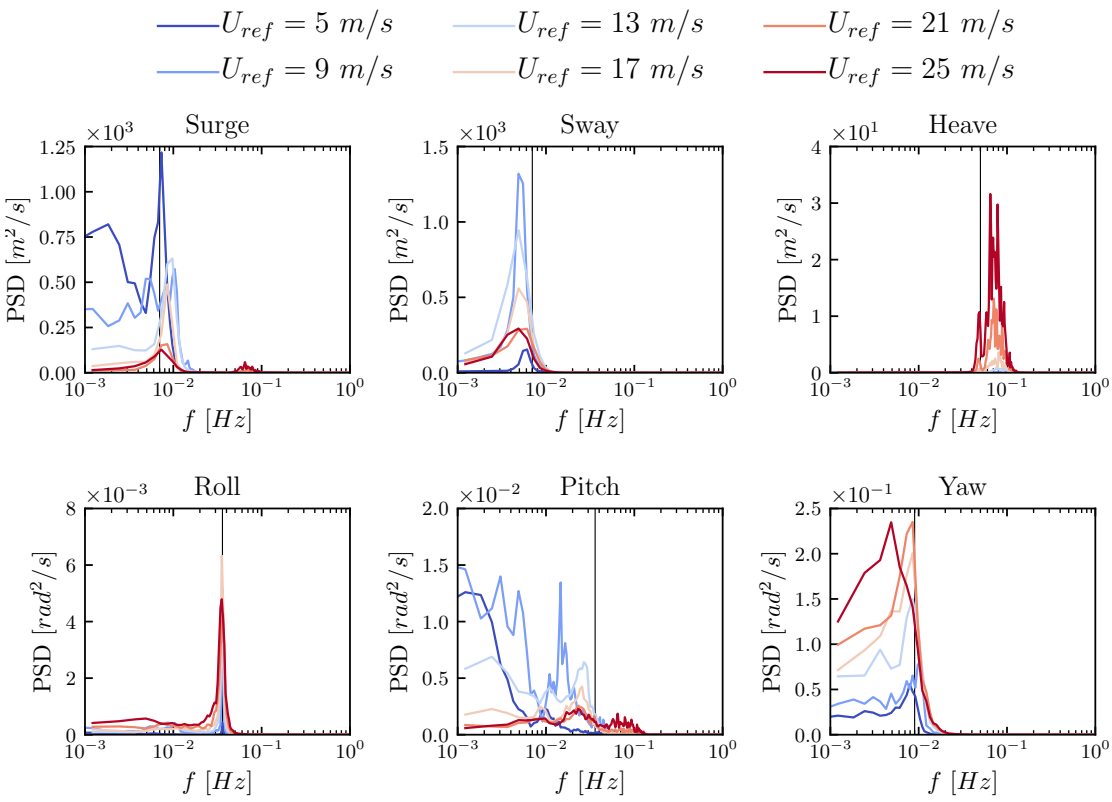

(a) Semi-submersible

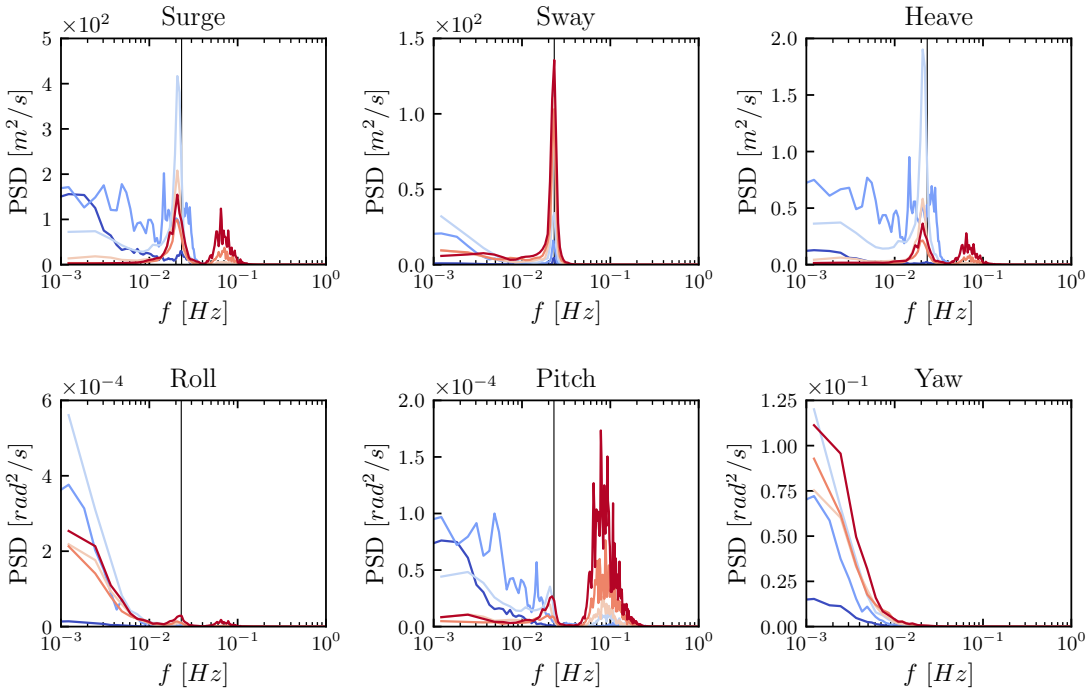

(b) TLP

Figure 4.8: Power Spectral Density of the floater motions with FVW: (a) semi-submersible, (b) TLP, . The vertical line shows the natural frequency of each degree of freedom of the floating wind turbine with the respective floater.

motion of the semi-submersible and the surge motion of the TLP. The results show that to decrease the fatigue of the blades, it is beneficial that the floating wind turbine system has one of its natural frequencies of the motions generating a relative inflow velocity, surge or pitch, smaller than the sea state frequencies to provide compliance in the range of the turbulent wind spectrum to alleviate some of the fatigue generated by the turbulent wind.

Conclusions and future work

Floating wind turbines are a way to harness previously inaccessible offshore wind resources to increase the production of renewable energy. The aerodynamics of floating wind turbine need to be specifically studied since floating foundations induce motions of the wind turbine due to the action wind and waves. The steady Blade Element Momentum theory is often used to study floating wind turbines, but it relies on empirical corrections to model unsteady aerodynamic effects. Higher fidelity models such as the Actuator Line and Free Vortex Wake methods give better results than BEM at lower computational cost than blade-resolved CFD.

The aerodynamics of floating wind turbines has been studied, first for imposed surge motions with the Actuator Line method and lifting line Free Vortex Wake method, to evaluate the two models. The Actuator Line method was implemented in the open-source CFD solver *Code_Saturne*. The open-source Free Vortex Wake code CACTUS was modified to apply imposed motions to the rotor and it was parallelized on GPU to improve the computational speed. The axial velocities predicted by both methods in the near wake of the wind turbine for a fixed rotor and a surging rotor were found to be similar. In agreement with the published literature, an increase of the average power and a decrease of the average thrust were found with both methods for a surging rotor at tip speed ratio 7, with a fixed rotational speed and blade pitch angle. The imposed surge motions generate a large variation of the power that could, for an operating wind turbine, lead to variations of the rotational speed and changes of the blade pitch angle by the controller.

The dynamic inflow phenomenon is known to occur after a blade pitch variation and was experimentally observed for a rotor speed change. The BEM theory relies on empirical dynamic inflow corrections. Their use for floating wind turbines motivates to further study dynamic inflow as wind turbine motions might generate more blade pitch and rotor speed variations than the ones experienced by bottom-fixed wind turbines. Dynamic inflow was investigated using Free Vortex Wake and an analytical helical vortex model for a blade pitch step, a rotor speed step and a surge step. Very little dynamic inflow effect was found in the case of the surge step because the tip vortex circulation change is partially compensated by the tip vortex helix geometry change. The dynamic inflow effect occurs for the blade pitch and rotor speed step, and it was shown that the variation of the velocity

induced by the tip vortex helix at the blades position is similar, except near the tip of the blade, for blade pitch steps and rotor speed steps leading to the same thrust coefficient variation.

Floating wind turbines operate in an unsteady environment, with interactions between the hydrodynamics, structural dynamic, controller behavior and aerodynamics. These interactions are modeled in aero-hydro-servo-elastic tools for the simulation of floating wind turbine. Most of these tools, including the EDF R&D in-house tool DIEGO, use BEM for the aerodynamics, which relies on a set of empirical models to model aerodynamic effects. In this work, the open-source lifting line FVW code OLAF was coupled to DIEGO, to study the aerodynamics of floating wind turbines. The FVW code OLAF was accelerated by implementing the vortex line kernel in the EXAFMM open-source library to parallelize the Biot-Savart law on GPU. A wake simplification method was proposed and implemented to reduce the computational cost of the FVW method for the study of floating wind turbines which require long simulations to account for the sea state. DIEGO with FVW aerodynamics was validated using experimental data and numerical data from higher fidelity models, and compared with results using the BEM aerodynamics model.

The aero-hydro-servo-elastic tool DIEGO was used to study the structural fatigue of the blades root of the IEA 15 MW wind turbine in fixed-bottom and floating conditions. Two different floaters were tested: the UMaine reference semi-submersible and a TLP. It was found that the BEM overestimates the fatigue due to the flapwise bending moment at the blade root compared to FVW, for both fixed and floating conditions. Both aerodynamic models show a reduction of the fatigue damage for the floating wind turbines compared to the fixed-bottom wind turbine, at the wind speeds corresponding to the highest thrust force. This fatigue reduction is due to the compliance provided by the degrees of freedom of the floater in the along wind direction, either pitch or surge. For the studied semi-submersible, the pitch degree of freedom is alleviating some of the loads, while it is the surge degree of freedom for the studied TLP.

For future works, the computational efficiency of the FVW can still be improved to lower the computational time. At the moment, the velocity induced by the vortex elements already emitted by the blades is computed when solving the circulation along the lifting line, and it is computed once again when computing the velocity at the blade taking into account the newly computed circulation along the lifting line. This velocity field could be stored between these two operations, and only the contribution due to the new circulation along the lifting line would need to be computed. In addition, the vortex wake convection step is independent from the computation of the hydrodynamic forces, therefore it could be done concurrently.

A particle formulation could be adopted for the FVW to better take into account turbulence. It would allow simulation of wake decay and wake interactions for floating wind

turbines. This could be done efficiently since EXAFMM is initially made to simulate vortex particles with the Fast Multipole Method which reduces the computational cost for high number of particles compared to a direct computation of the Biot-Savart law.

The differences observed between the FVW and BEM could be further investigated. In particular, the polar-grid implementation of the BEM of Madsen et al. [113] seems promising to address some of the shortcomings of the BEM method.

The coupling between the aerodynamic and hydrodynamic domains could be improved in DIEGO, by solving the mooring line structural dynamic together with the floater and wind turbine structural motion, instead of imposing the motion at the bottom of the tower, as is currently done.

Regarding the study of floating wind turbines, GPU parallelization and wake simplification make FVW a computationally efficient method that can replace BEM to study wind turbines in conditions for which it provides more reliable results than BEM.

Appendix A

Segment-based treecode in OLAF

A.1 OLAF's Treecode Algorithm

In the OLAF model, treecode methods are applied to vortex particles. Below is the description of the algorithm implemented in OLAF.

The vortex segments are converted to particles. The user chooses the number of particles used to represent one vortex segment. The chosen number of particles are equally spaced along the vortex segment. Their strength is $\alpha = \Gamma l/n_p$ where Γ is the circulation of the vortex segment, l its length and n_p the number of particles chosen for the approximation. The desingularization size of each particle is taken equal to the desingularization size of the vortex line.

An octree is then constructed from the set of particles. The space holding the particles is divided in 8 equally sized volumes. The initial set of all the particles is the root of the tree. Each one of the 8 subsets is a branch of the tree. Then recursively, each subset is divided into 8 equally sized volumes which are branches attached to the current branch, a level deeper.

For each branch, a vorticity-weighted barycenter of all the vortex particles in this branch is computed. The moments of order 0, 1 and 2 of the subset of particles about this barycenter are then computed for the approximation of the velocity field induced by this set of particles.

To evaluate the velocity field at a control point, the process is also recursive. The distance between the control point and the root is compared to the direct evaluation distance. If the control point is far enough from the vorticity barycenter (user set parameter), then the quadrupole approximation is used to computed the induced velocity at this control point. If the control point is too close from the vorticity barycenter then the same process is applied to the sub-branches of the current branch. The distance between the control point and the sub-branches barycenter is evaluated and compared to the criterion. Some

might be far enough to use the quadrupole approximation (one step) while other might require to go deeper into the tree (several steps).

The approximation of the velocity field induced by a vortex line, by one or more vortex particle is the starting point of the treecode method used in OLAF. The number of particles used for each vortex line is set by the user, and the same number is used for every vortex line. In the next section, the quality of this approximation as well as guidelines for the conversion from segment to particles will be explored.

A.2 Quality of the segment to particle approximation

The approximation of a vortex segment by vortex particles induces an error. Here, the error done by approximating a vortex segment of unit length by a set of equally spaced vortex particles is studied. A cylindrical coordinate system with its origin at the center of the vortex segment is chosen for simplicity.

The Lamb-Oseen desingularization core model is chosen for the vortex line, while an exponential kernel is used for the vortex particles. They are written respectively:

$$K_v^{LO} = 1 - \exp\left(-\alpha \frac{\rho^2}{r_c^2}\right) \tag{A.1}$$

$$K_v^{p} = 1 - \exp\left(-\frac{r^3}{r_c^3}\right) \tag{A.2}$$

where $\alpha = 1.25643$, $r^2 = \rho^2 + z^2$ and r_c is the core size.

The norm of the velocity induced by the vortex line of length l at a point of coordinate (ρ, θ, z) is:

$$u_s = \frac{\Gamma}{4\pi}\left(1 - \exp\left(-\alpha \frac{\rho^2}{r_c^2}\right)\right) \frac{l\rho(r_1 + r_2)}{r_1 r_2 (r_1 r_2 + \boldsymbol{r_1}.\boldsymbol{r_2})} \tag{A.3}$$

with the vectors $\boldsymbol{r_1}$ and $\boldsymbol{r_2}$ pointing from the bottom and top of the vortex segment to the studied point respectively. They distances are:

$$r_1 = \left(\rho^2 + \left(z + \frac{l}{2}\right)^2\right)^{1/2}, \tag{A.4}$$

$$r_2 = \left(\rho^2 + \left(z - \frac{l}{2}\right)^2\right)^{1/2}, \tag{A.5}$$

$$\boldsymbol{r_1}.\boldsymbol{r_2} = \rho^2 + z^2 - \frac{l^2}{2^2} \tag{A.6}$$

The norm of the velocity induced by the set of n vortex particles is :

$$u_p = \sum_{i=0}^{n-1} \frac{\Gamma}{4\pi} \left(1 - \exp\left(-\frac{r_i^3}{r_c^3}\right)\right) \frac{l\rho}{nr_i^3} \tag{A.7}$$

with

$$r_i = \left(\rho^2 + (z - z_i)^2\right)^{1/2}, \text{ and } z_i = -\frac{l}{2} + \frac{l}{n}\left(\frac{1}{2} + i\right) \tag{A.8}$$

where z_i is the axial position of the equally spaced particles in the cylindrical coordinate system. The dimensionless difference $4\pi l|u_s - u_p|/\Gamma$ can be computed numerically for various number of particles and vortex core sizes. The error made by approximating a filament of unit length l and core size r_c by n particles is shown in Fig. A.1. The error made is much higher for slender vortex filaments, with low r_c/l ratio. It can be explained by the fact that the geometry of wider vortex filaments resembles more to particles than the one of slender filaments. It can be seen that the error reduces with the distance to the filament. This is visible for any number of approximating particles. Seen from a sufficiently far distance, a filament behaves like a group of particles which justifies the quadrupole approximation in the treecode algorithm.

Closer to the vortex filament center, the error grows and has its maximum at a radial distance close to the core radius, r_c. For the more slender filaments with $r_c/l = 0.05$ and $r_c/l = 0.1$, the distribution of the error is modified and reduced when the number of particles is increased (Fig. A.1a, A.1b). For $r_c/l = 0.2$ (Fig. A.1c), the error does not change when increasing the number of particles from 5 to 6, while for $r_c/l = 0.4$ (Fig. A.1d), the error does not change when using more than 3 particles.

This shows that for specific conditions, there is an ideal number of particles to use to approximate a vortex filament. Using more particles than this ideal number of particles will not improve the approximation of the induced velocity field. For example, in the case of Fig. A.1d with $r_c/l = 0.4$, using more than 3 particles is not improving the results and is a waste of computational power.

To refine this first impression, we use the root mean square error to compare the fields of the norm of the velocity induced by a filament and sets of particles. We define:

$$RMSE(n) = \frac{4\pi l}{\Gamma} \left(\sum_{k=1}^{N} \frac{\left(u_s(\boldsymbol{x_k}) - u_p(\boldsymbol{x_k})\right)^2}{N}\right)^{1/2} \tag{A.9}$$

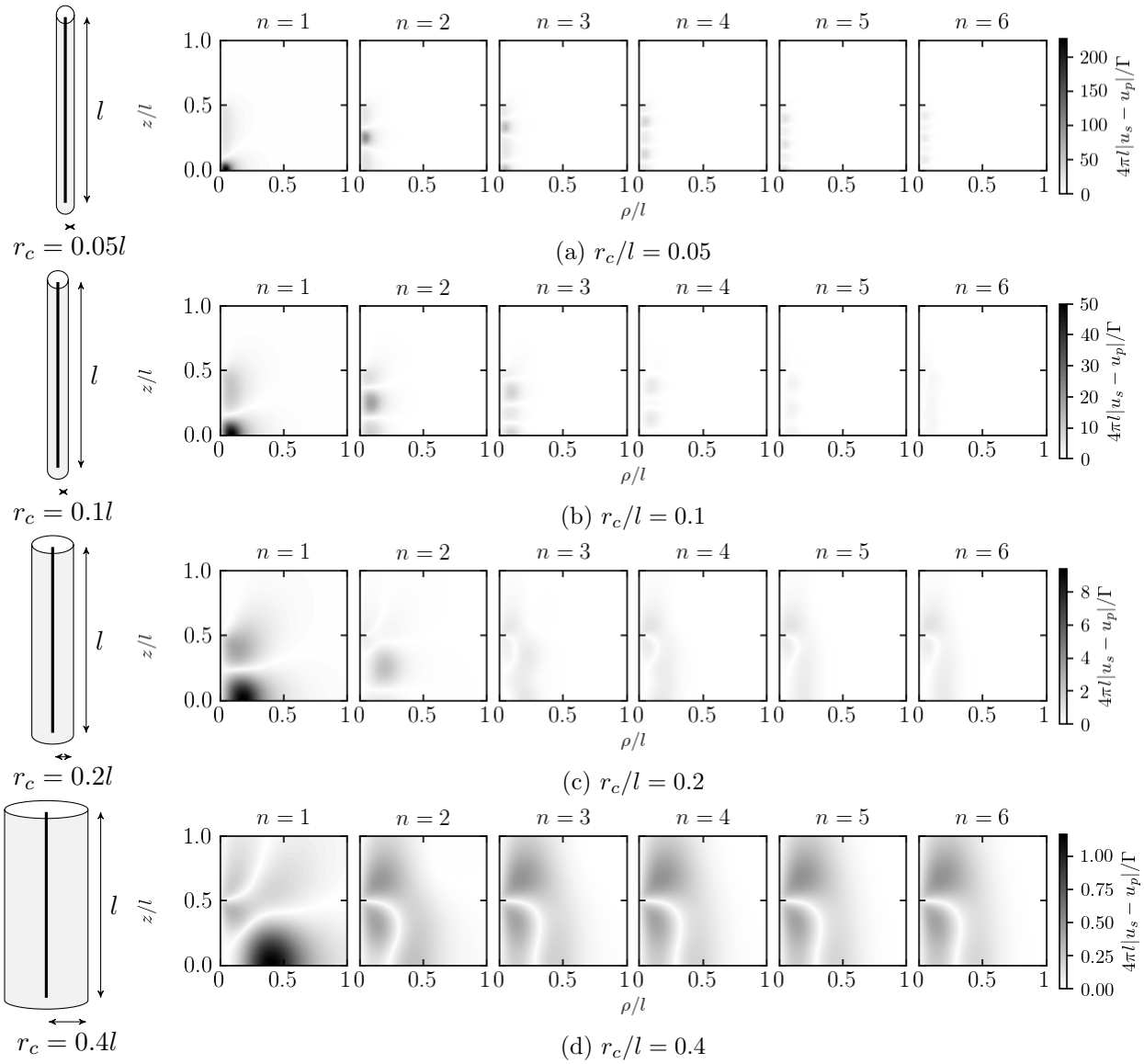

Figure A.1: Absolute error between the norm of the velocity induced by a vortex filament and sets of vortex particles. The error is shown for various vortex core size r_c and number of approximating particles n. The error is higher for the more slender vortices while it is lower for wide filaments, resembling the approximating particles. A different scale is used for each slenderness.

where the N points, $\boldsymbol{x_k}$, are evaluation points in the studied domain. Here, the domain is chosen to be $\rho \in \left[10^{-4}, 1\right]$ and $z \in [0, 1]$. The domain for ρ does not start at 0 because even though the desingularization of Eq. A.1 removes the physical singularity, it does not get rid of the numerical singularity: Eq. A.3 can not be evaluated at $\rho = 0$.

The root mean square error computed on a Cartesian grid of the defined domain with 1000 points in each direction for a total of $N = 10^6$ evaluation points is shown on Fig. A.2. When using only one approximating particle, the root mean square error is higher for slender filaments than for wide filaments confirming the visual observation of Fig. A.1. When the number of particle increases, the root mean square error reaches a threshold value. This threshold error is higher for slender vortices than for wide ones, confirming the difficulty to approximate the velocity field of slender vortices by sets of vortex particles.

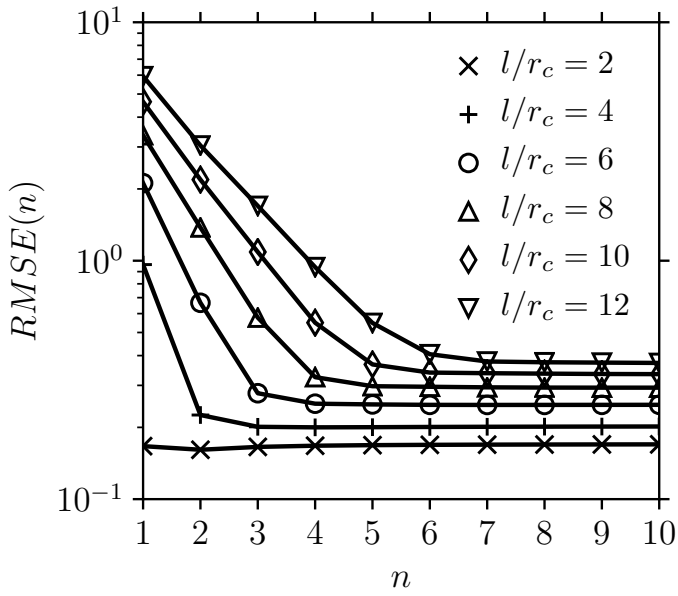

Figure A.2: Root mean square error as defined in Eq. A.9 computed for $N = 10^6$ evaluation points in the domain $\rho \in \left[10^{-4}, 1\right]$ and $z \in [0, 1]$ for various core sizes and number of particles. Slender vortex filaments require more approximating particles than wide filaments.

The number of particles for which the threshold value seems to be reached for each core size is summarized in Table A.1.

Table A.1: Number of particules to reach threshold root mean square error.

l/r_c	2	4	6	8	10	12
n	3	3	4	5	6	7

These results suggest the following rule to chose the ideal number of particle to approximate vortex filaments:

$$n_{ideal} = floor\left(\frac{l}{2r_c}\right) + 1 \tag{A.10}$$

where the function $floor$ takes the integer part of a real number. Using this rule provides a suitable number of particle for each vortex filaments. Slender filaments are approximated by a large number of particles while wide ones are approximated by only a few particles. It also removes any parameter that can be set by the user. There is no need to decide whether one, two or more particles will be used to approximate filaments (which is currently a fixed value for every vortex in OLAF). The choice can be automatically done with the rule of Eq. A.10.

Vortex lines have a tendency to stretch when they are convected downstream of a wind turbine, which increases the ratio l/r_c and thus the number of particles needed for the approximation from lines to particles. The number of particles to approximate the vortex line wake of a wind turbine can be evaluated using the values of l/r_c extracted from a FVW simulation using vortex lines with the code CACTUS.

The simulation setup is the following: NREL 5MW reference wind turbine [90] at rated conditions ($\lambda = 7$, $U_\infty = 11.4m/s$) with 60 steps per rotation and 30 elements per blade. The required number of particles is evaluated after 16 rotations for all 1.7×10^5 vortex lines in the wake. The initial core size of the vortices is taken to be $r_c = 0.2c$ where c is the local chord.

The core size is evaluated both with and without the following viscous diffusion core growth model [27]:

$$r_c = \sqrt{4\alpha\delta\nu t_0 + r_0^2} \tag{A.11}$$

where $\alpha = 1.256429$, δ is a parameter usually between 1 and 1000, $\nu = 1.47 \times 10^{-5}\ m^2.s^{-1}$ is the kinematic viscosity of air, t_0 is the age of the vortex and r_0 is its initial size, here based on the local chord.

Using the rule of Eq. A.10 for a wake from CACTUS, the statistics of number of approximating particles are shown in Table A.2.

Table A.2: Number of particles needed to approximate $N_{seg} = 1.7 \times 10^5$ vortex lines in the wake of the NREL 5MW wind turbine, computed with the rule of Eq. A.10. $\bar{n}$ is the mean number of particles per segment which is also equal to the ratio of total number of particles N_{part} over the total number of segments N_{seg}; $n_{1/2}$ is the median.

δ	N_{part}	$\bar{n} = N_{part}/N_{seg}$	$n_{1/2}$
0	4.9×10^6	28.5	9
100	2.7×10^6	15.2	7
1000	1.2×10^6	6.8	3

The fact that the mean number of particles is larger than the median number of particles shows that very slender filaments exist in the wake and increase the number of required particles. The viscous diffusion core growth model reduces the number of particles needed since the core size of the vortices increases with their age and they are therefore wider than without the core growth model.

In the most favorable and diffuse case ($\delta = 1000$), 6.8 times more particles than segments are needed. This increases significantly the computational load which is a problem for the efficiency of the computation (the aim of the treecode algorithm is efficiency). An additional problem is the residual error by approximating a slender vortex segment by vortex particles.

Overall, converting vortex line into particles generates an error. This error is reduced by increasing the number of approximating particles, but this increases the computational cost. Instead of converting the vortex lines into particles to apply the treecode algorithm, the treecode algorithm can be adapted and directly applied to vortex lines, which would remove the error of approximating a vortex line with vortex particles. In the following section, the multipole expansion of vortex particles is presented. Then the same process is applied to vortex lines to derive the multipole expansion to be used inside a vortex-line based treecode algorithm.

A.3 Treecode expansion with vortex particles

The velocity induced at $\boldsymbol{y}$ by a vortex particle at $\boldsymbol{x_j}$ can be written:

$$\boldsymbol{u_j}(\boldsymbol{y}) = \boldsymbol{K_p}(\boldsymbol{y}, \boldsymbol{x_j}) \times \boldsymbol{\omega_j} \tag{A.12}$$

with $\boldsymbol{\omega_j}$ the particle vorticity and the kernel:

$$\boldsymbol{K_p}(\boldsymbol{y}, \boldsymbol{x_j}) = \boldsymbol{K}(\boldsymbol{y}, \boldsymbol{x_j}) = -\frac{1}{4\pi} \frac{\boldsymbol{y} - \boldsymbol{x_j}}{|\boldsymbol{y} - \boldsymbol{x_j}|^3} \tag{A.13}$$

The total induced velocity at point $\boldsymbol{y}$ of a cluster of particles is the sum of the contribution of the N particles in the cluster. Here, we perform a Taylor series expansion of this contribution around the center of the cluster of particles $\boldsymbol{x_c}$ following the method of Lindsay and Krasny [108] where $\boldsymbol{k} = (k_x, k_y, k_z)$ is an integer multi-index:

$$\boldsymbol{u}(\boldsymbol{y}) = \sum_{j=1}^{N} \boldsymbol{K_p}(\boldsymbol{y}, \boldsymbol{x_j}) \times \boldsymbol{\omega_j} = \sum_{j=1}^{N} \sum_{\boldsymbol{k}} \frac{1}{\boldsymbol{k}!} D_{\boldsymbol{y}}^{\boldsymbol{k}} \boldsymbol{K_p}(\boldsymbol{y}, \boldsymbol{x_c}) \left(\boldsymbol{x_j} - \boldsymbol{x_c}\right)^{\boldsymbol{k}} \times \boldsymbol{\omega_j}. \tag{A.14}$$

which can be separated between the part depending on evaluation point position $\boldsymbol{y}$ and the part depending on particle position $\boldsymbol{x_j}$:

$$\boldsymbol{u}(\boldsymbol{y}) = \sum_{\boldsymbol{k}} \frac{1}{\boldsymbol{k}!} D_{\boldsymbol{y}}^{\boldsymbol{k}} \boldsymbol{K}_{\boldsymbol{p}}(\boldsymbol{y}, \boldsymbol{x_c}) \times \sum_{j=1}^{N} (\boldsymbol{x_j} - \boldsymbol{x_c})^{\boldsymbol{k}} \, \boldsymbol{\omega_j}. \tag{A.15}$$

It can be rewritten:

$$\boldsymbol{u}(\boldsymbol{y}) = \sum_{\boldsymbol{k}} \boldsymbol{a_k}(\boldsymbol{y}, \boldsymbol{x_c}) \times \boldsymbol{m_k}(\boldsymbol{x_c}) \tag{A.16}$$

with:

$$\boldsymbol{a_k}(\boldsymbol{y}, \boldsymbol{x_c}) = \frac{1}{\boldsymbol{k}!} D_{\boldsymbol{y}}^{\boldsymbol{k}} \boldsymbol{K}_{\boldsymbol{p}}(\boldsymbol{y}, \boldsymbol{x_c}) \tag{A.17}$$

and

$$\boldsymbol{m_k}(\boldsymbol{x_c}) = \sum_{j=1}^{N} (\boldsymbol{x_j} - \boldsymbol{x_c})^{\boldsymbol{k}} \, \boldsymbol{\omega_j}. \tag{A.18}$$

Here, no desingularization model was chosen so the kernel for the elementary vortex line element and the vortex particle are the same, thus $\boldsymbol{a_k}(\boldsymbol{y}, \boldsymbol{x_c}) = \boldsymbol{c_k}(\boldsymbol{y}, \boldsymbol{x_c})$. However, the center of a cluster of particles might be different than the center of a cluster of vortex lines so the expansion might not be done around the same point. In the following, the expansion for a set of vortex lines will be made around the same point $\boldsymbol{x_c}$.

A.4 Treecode expansion with vortex line

The velocity induced by an elementary element of a vortex line of index j at a point $\boldsymbol{y}$ can be expressed:

$$\boldsymbol{u_j} = -\frac{1}{4\pi} \frac{\boldsymbol{y} - \boldsymbol{x_j}}{\|\boldsymbol{y} - \boldsymbol{x_j}\|^3} \times \Gamma_j \boldsymbol{dl}. \tag{A.19}$$

Let us rewrite the kernel and the associated strengths:

$$\boldsymbol{K}(\boldsymbol{y}, \boldsymbol{x_j}) = -\frac{1}{4\pi} \frac{\boldsymbol{y} - \boldsymbol{x_j}}{\|\boldsymbol{y} - \boldsymbol{x_j}\|^3} \tag{A.20}$$

and

$$\boldsymbol{w_j} = \Gamma_j \boldsymbol{dl}. \tag{A.21}$$

The total induced velocity is the sum of the contribution of N vortex line L integrated between their extremities $\boldsymbol{x_{j1}}$ and $\boldsymbol{x_{j2}}$:

$$\boldsymbol{u} = \sum_{j=1}^{N} \int_{\boldsymbol{x_{j1}}}^{\boldsymbol{x_{j2}}} (\boldsymbol{K}(\boldsymbol{y}, \boldsymbol{x_j}) \times \boldsymbol{w_j}) = \sum_{j=1}^{N} \int_{L} (\boldsymbol{K}(\boldsymbol{y}, \boldsymbol{x_j}) \times \boldsymbol{w_j}) \,. \tag{A.22}$$

Again, following the method of Lindsay and Krasny [108]:

$$\boldsymbol{u}(\boldsymbol{y}) = \sum_{j=1}^{N} \int_{L} \left(\sum_{\boldsymbol{k}} \frac{1}{\boldsymbol{k}!} D_{\boldsymbol{y}}^{\boldsymbol{k}} \boldsymbol{K}(\boldsymbol{y}, \boldsymbol{x_c}) \, (\boldsymbol{x_j} - \boldsymbol{x_c})^{\boldsymbol{k}} \times \boldsymbol{w_j} \right) . \tag{A.23}$$

The derivatives can be taken out of the integral:

$$\boldsymbol{u}(\boldsymbol{y}) = \sum_{j=1}^{N} \sum_{\boldsymbol{k}} \frac{1}{\boldsymbol{k}!} D_{\boldsymbol{y}}^{\boldsymbol{k}} \boldsymbol{K}(\boldsymbol{y}, \boldsymbol{x_c}) \times \int_{L} \left((\boldsymbol{x_j} - \boldsymbol{x_c})^{\boldsymbol{k}} \, \boldsymbol{w_j} \right) . \tag{A.24}$$

and the derivative term is now independent of the properties (position and strength) of each vortex line:

$$\boldsymbol{u}(\boldsymbol{y}) = \sum_{\boldsymbol{k}} \frac{1}{\boldsymbol{k}!} D_{\boldsymbol{y}}^{\boldsymbol{k}} \boldsymbol{K}(\boldsymbol{y}, \boldsymbol{x_c}) \times \sum_{j=1}^{N} \int_{L} \left((\boldsymbol{x_j} - \boldsymbol{x_c})^{\boldsymbol{k}} \, \boldsymbol{w_j} \right) . \tag{A.25}$$

Writing the summation over the multi-index $\boldsymbol{k} = (k_x, k_y, k_z)$ for a Taylor approximation of order p, and writing $\boldsymbol{x_{j1}} = (x_{j1}, y_{j1}, z_{j1})$, $\boldsymbol{x_{j2}} = (x_{j2}, y_{j2}, z_{j2})$, $\boldsymbol{x_c} = (x_c, y_c, z_c)$ and $\boldsymbol{x_j} = (x_j, y_j, z_j) = (1-s)\boldsymbol{x_{j1}} + s\boldsymbol{x_{j2}}$ with s the curvilinear abscissa along the vortex line L:

$$\begin{aligned} \boldsymbol{u}(\boldsymbol{y}) = & \sum_{k_x=0}^{p-1} \sum_{k_y=0}^{p-k_x-1} \sum_{k_z=0}^{p-k_x-k_y-1} \frac{\partial_x^{(k_x)} \partial_y^{(k_y)} \partial_z^{(k_z)} \boldsymbol{K}(\boldsymbol{y}, \boldsymbol{x_c})}{k_x! k_y! k_z!} \\ & \times \sum_{j=1}^{N} \Gamma_j l_j \left(\int_0^1 ((1-s)x_{j1} + s x_{j2} - x_c)^{k_x} ((1-s)y_{j1} + s y_{j2} - y_c)^{k_y} ((1-s)z_{j1} + s z_{j2} - z_c)^{k_z} ds \boldsymbol{e_j} \right) \end{aligned} \tag{A.26}$$

where $\boldsymbol{e_j}$ is the normalized direction vector and $l_j = \|\boldsymbol{x_{j2}} - \boldsymbol{x_{j1}}\|$ is the length of the j^{th} vortex line, which can be rewritten:

$$\boldsymbol{u}(\boldsymbol{y}) = \sum_{k_x=0}^{p-1} \sum_{k_y=0}^{p-k_x-1} \sum_{k_z=0}^{p-k_x-k_y-1} \boldsymbol{c_{k_x,k_y,k_z}}(\boldsymbol{y}, \boldsymbol{x_c}) \times \boldsymbol{b_{k_x,k_y,k_z}}(\boldsymbol{x_c}) \tag{A.27}$$

where

$$\boldsymbol{c_{k_x,k_y,k_z}}(\boldsymbol{y},\boldsymbol{x_c}) = \frac{\partial_x^{(k_x)}\partial_y^{(k_y)}\partial_z^{(k_z)}\boldsymbol{K}(\boldsymbol{y},\boldsymbol{x_c})}{k_x!k_y!k_z!} \tag{A.28}$$

depends on the evaluation point $\boldsymbol{y}$, while the following term $\boldsymbol{b_{k_x,k_y,k_z}}$ does not depend on the evaluation term but depends on each vortex line properties:

$$\boldsymbol{b_{k_x,k_y,k_z}}(\boldsymbol{x_c}) = \sum_{j=1}^{N} \Gamma_j l_j \left(\int_0^1 ((1-s)x_{j1} + sx_{j2} - x_c)^{k_x} ((1-s)y_{j1} + sy_{j2} - y_c)^{k_y} ((1-s)z_{j1} + sz_{j2} - z_c)^{k_z} ds \boldsymbol{e_j} \right). \tag{A.29}$$

In this case, the Taylor expansion for vortex particles and vortex lines differs only because the $\boldsymbol{m_k}$ and $\boldsymbol{b_k}$ terms are different. Their difference and how it affects the Taylor expansions will be assessed next.

A.5 Difference between the lines and particles Taylor expansions for a single vortex line

The vortex line and particle expansion of section A.4 and A.3 are compared for the evaluation of the induced velocity field of a single vortex line of length l such that $\boldsymbol{x_{j1}} = (0, 0, -l/2)$ and $\boldsymbol{x_{j2}} = (0, 0, l/2)$. The barycenter of the vortex line is the origin: $\boldsymbol{x_c} = (0, 0, 0)$.

The method used in OLAF to approximate a vortex line with particles is chosen, *i.e.*, equally spaced particles with equally distributed strength. As an example, when one particle per vortex line is used, the position of the particle $\boldsymbol{x_j}$ is the center of the vortex line $(\boldsymbol{x_{j1}} + \boldsymbol{x_{j2}})/2$ and its strength is $\boldsymbol{\omega_j} = \Gamma_j(\boldsymbol{x_{j2}} - \boldsymbol{x_{j1}})$.

For n approximating particles:

$$\boldsymbol{x_i} = \boldsymbol{x_{j1}} + \frac{1}{n}\left(i - \frac{1}{2}\right)(\boldsymbol{x_{j2}} - \boldsymbol{x_{j1}}) \text{ and } \boldsymbol{\omega_j} = \Gamma_j(\boldsymbol{x_{j2}} - \boldsymbol{x_{j1}})/n \text{ , for } i \in [1, n]\,. \tag{A.30}$$

Therefore, focusing on a single vortex line of circulation Γ_j and extremities $\boldsymbol{x_{j1}}$ and $\boldsymbol{x_{j2}}$, for n approximating particles per vortex line, the coefficients $\boldsymbol{m_k}$ can be expressed from the properties of the initial vortex lines the particles approximate:

$$\begin{aligned}\boldsymbol{m_k}(\boldsymbol{x_c}) =& \sum_{i=1}^{n} \left(\boldsymbol{x_{j1}} + \frac{1}{n}\left(i-\frac{1}{2}\right)(\boldsymbol{x_{j2}}-\boldsymbol{x_{j1}}) - \boldsymbol{x_c} \right)^{\boldsymbol{k}} \Gamma_j(\boldsymbol{x_{j2}}-\boldsymbol{x_{j1}})/n \\ =& \sum_{i=1}^{n} \left(x_{j1} + \frac{1}{n}\left(i-\frac{1}{2}\right)(x_{j2}-x_{j1}) - x_c \right)^{k_x} \\ & \left(y_{j1} + \frac{1}{n}\left(i-\frac{1}{2}\right)(y_{j2}-y_{j1}) - y_c \right)^{k_y} \\ & \left(z_{j1} + \frac{1}{n}\left(i-\frac{1}{2}\right)(z_{j2}-z_{j1}) - z_c \right)^{k_z} \boldsymbol{\omega_j}/n \end{aligned} \tag{A.31}$$

In the studied case, the coefficients $\boldsymbol{m_k}$ are written:

$$\begin{aligned}\boldsymbol{m_k}(\boldsymbol{x_c}) =& \sum_{i=1}^{n} 0^{k_x}0^{k_y} \left(-\frac{l}{2}\left(1+\frac{\frac{1}{2}-i}{n}\right) + \frac{1-\frac{1}{2}}{n}\frac{l}{2} \right)^{k_z} \Gamma_j l/n \boldsymbol{e_z} \\ =& \sum_{i=1}^{n} 0^{k_x}0^{k_y} \left(\frac{l(2i-n-1)}{2n} \right)^{k_z} \Gamma_j l/n \boldsymbol{e_z} \end{aligned} \tag{A.32}$$

while for the vortex line, the coefficients $\boldsymbol{b_k}$ are:

$$\begin{aligned}\boldsymbol{b_k}(\boldsymbol{x_c}) &= \Gamma_j l_j \left(\int_0^1 ((1-s)x_{j1} + s x_{j2} - x_c)^{k_x} ((1-s)y_{j1} + s y_{j2} - y_c)^{k_y} ((1-s)z_{j1} + s z_{j2} - z_c)^{k_z} ds \right) \boldsymbol{e_j} \\ &= \Gamma_j l \left(\int_0^1 (-x_c)^{k_x} (-y_c)^{k_y} ((s-1)\frac{l}{2} + s\frac{l}{2} - z_c)^{k_z} ds \right) \boldsymbol{e_j} \end{aligned} \tag{A.33}$$

where $\boldsymbol{e_j}$ is the direction vector of $\boldsymbol{dl}$.

Taking $\boldsymbol{x_c}$ at the center of the vortex line: $\boldsymbol{x_c} = (0,0,0)$, the coefficients $\boldsymbol{b_k}$ can be written:

$$\begin{aligned}\boldsymbol{b_k}(\boldsymbol{x_c}) &= \Gamma_j l \left(\int_0^1 0^{k_x}0^{k_y} \left((s-1)\frac{l}{2} + s\frac{l}{2} \right)^{k_z} ds \right) \boldsymbol{e_l} \\ &= \Gamma_j l 0^{k_x}0^{k_y} l^{k_z} \frac{2^{-k_z-1}((-1)^{k_z}+1)}{k_z+1} \boldsymbol{e_z}. \end{aligned} \tag{A.34}$$

which means that if k_x or k_y are non-zero, then $\boldsymbol{b_k} = \boldsymbol{0}$.

To compare both methods, we compare the root mean square error between the fields computed with each method and the field computed with the Biot-Savart equation for vortex lines:

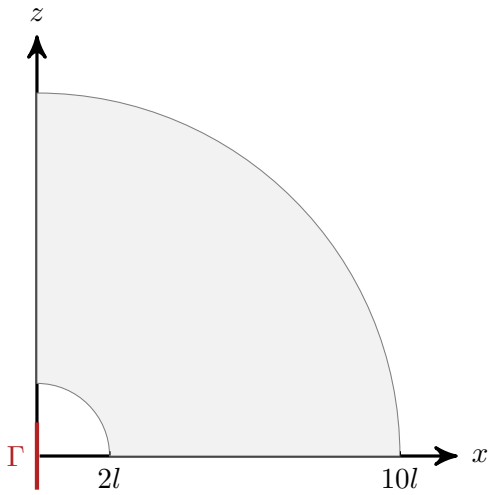

Figure A.3: Vortex line and domain for the root mean square error evaluation: $\rho \in [2l, 10l]$ and $\theta \in [0, \pi/2]$.

$$RMSE = \frac{4\pi l}{\Gamma} \left(\sum_{k=1}^{N} \frac{\left(u_{Biot}(\boldsymbol{x_k}) - u_{Tree}(\boldsymbol{x_k})\right)^2}{N} \right)^{1/2} \tag{A.35}$$

where the N points $\boldsymbol{x_k}$ are evaluation points in the studied domain. Here, the domain is chosen to be $\rho \in [2l, 10l]$ and $\theta \in [0, \pi/2]$ to compute $x_k = \rho \cos\theta$ and $z_k = \rho \sin\theta$. The domain and vortex line are shown in Fig. A.3. The radial and azimuthal dimensions are each discretized with 200 elements for a total of $N = 4 \times 10^4$ evaluation points.

The root mean square error of the vortex line and vortex particle treecode expansion to the Biot-Savart law are shown on Fig. A.4. To evaluate the opportunity to use more than one particle to model the vortex line, the treecode expansion is tested for 1 to 6 vortex particles. This shows that for one approximating particle, increasing the order of the polynomial approximation does not improve the approximation. This can be seen in Eq. A.32. When using only one particle, the only non-zero moment is $\boldsymbol{m_{0,0,0}}$. Using more than one particle improves the quality of the expansion. The vortex line expansion has a lower root mean square error than the particle expansion when $p \geq 3$. The vortex line expansion has a root mean square error about one order of magnitude lower than the single particle expansion for a similar computational load. This tends to justify the use of a vortex line based treecode rather than a particle based treecode algorithm.

For the vortex line expansion, only even orders provide an improvement of the expansion. Each additional order of the expansion requires additional derivative evaluations and moment computations but permits the use of the expansion on sets of vortices closer to the evaluation point. There might therefore be a trade-off.

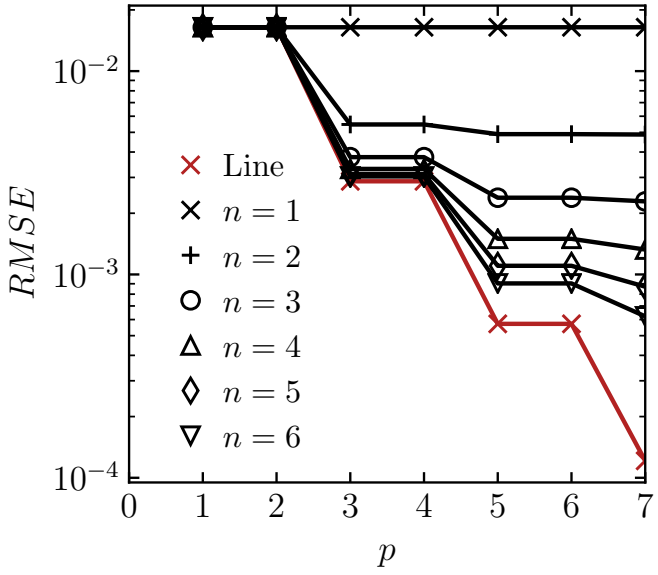

Figure A.4: Root mean square error as defined in Eq. A.35 computed for $N = 4 \times 10^4$ evaluation points for vortex line and particle treecode expansions computed on the domain defined in Fig. A.3. $\rho \in [2l, 10l]$ and $\theta \in [0, \pi/2]$.

A.6 Implementation of a vortex line-based treecode in OLAF

A vortex line-based treecode algorithm has been implemented in OLAF, taking as a base the existing particle-based treecode algorithm. Similarly to the particle-based treecode already available in OLAF, the order of the expansion was set to $p = 3$ for the computation of the multipole expansions (Eq. A.26).

A.7 Validation of the vortex line-based treecode for a finite helix of constant circulation

The test case of a finite helix with constant circulation has the interest of having an analytical solution which can be integrated on the axis of the helix.

The chosen vortex helix has a unit radius with a pitch $p = 0.107$ and is comprised of 20 rotations. It is discretized with 1200 vortex lines. For this helix, the particle approximation with one particle per vortex line, the corresponding treecode with one particle per vortex line and the vortex line-based treecode are compared to the direct vortex line Biot-Savart evaluation for the self-induced velocity field. The comparison of the normalized L2 norm of the error to the direct calculation is shown on Fig. A.5 for different Branch Factor. The Branch Factor in OLAF is a parameter to set how many radius from a tree element, the

quadrupole evaluation is used instead of smaller tree elements (other quadrupoles or direct evaluations). The radius of a tree element is taken as the largest distance between two of its elements. The numbers of quadrupole evaluation and direct evaluation are shown in Fig. A.6. It can be seen that while increasing the Branch Factor greatly increases the number of direct evaluation, it has a smaller effect on the number of quadrupole evaluations. For the line-based treecode, it can be seen in Fig. A.5 and Fig. A.6 that increasing the Branch Factor increases the number of direct evaluations and thus reduces the error of the treecode. For the particle-base method, the situation is different. Fig. A.5 shows that most of the error is from approximating the vortex line by a single vortex particle. Increasing the Branch Factor has almost no effect on the error since a large error is incurred when doing direct evaluations with vortex particles instead of vortex lines.

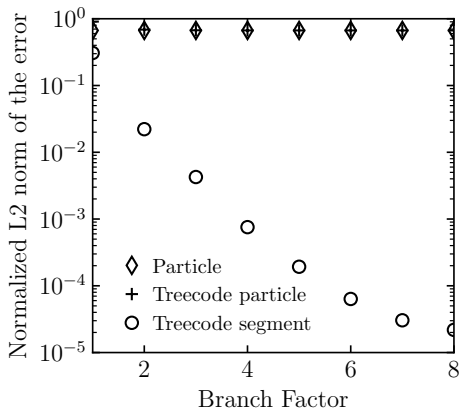

Figure A.5: Normalized L2 norm of the error to the direct calculation for the self-induced velocity.

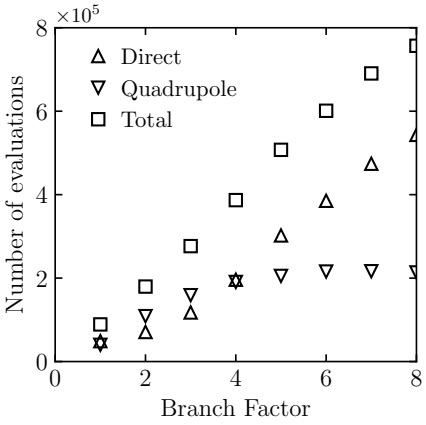

Figure A.6: Number of direct and quadrupole evaluation for the self-induced velocity with the vortex line-based treecode.

Choosing a smaller Branch Factor implies a reduced computational time because fewer evaluations need to be done, both direct and quadrupole, at the cost of a larger error. The choice of the Branch Factor is a trade-off between speed and accuracy.

Conclusion

The vortex line-based treecode algorithm implemented here in OLAF was submitted to the official open-source repository of OpenFAST [5]. It is now available option for OpenFAST users. It generates lower approximation errors than the particle based treecode and requires fewer user inputs which simplifies its use. It is CPU-parallelized using OpenMP.

Appendix B

Rainflow counted cycles for FVW with a specific time step for vortex emission.

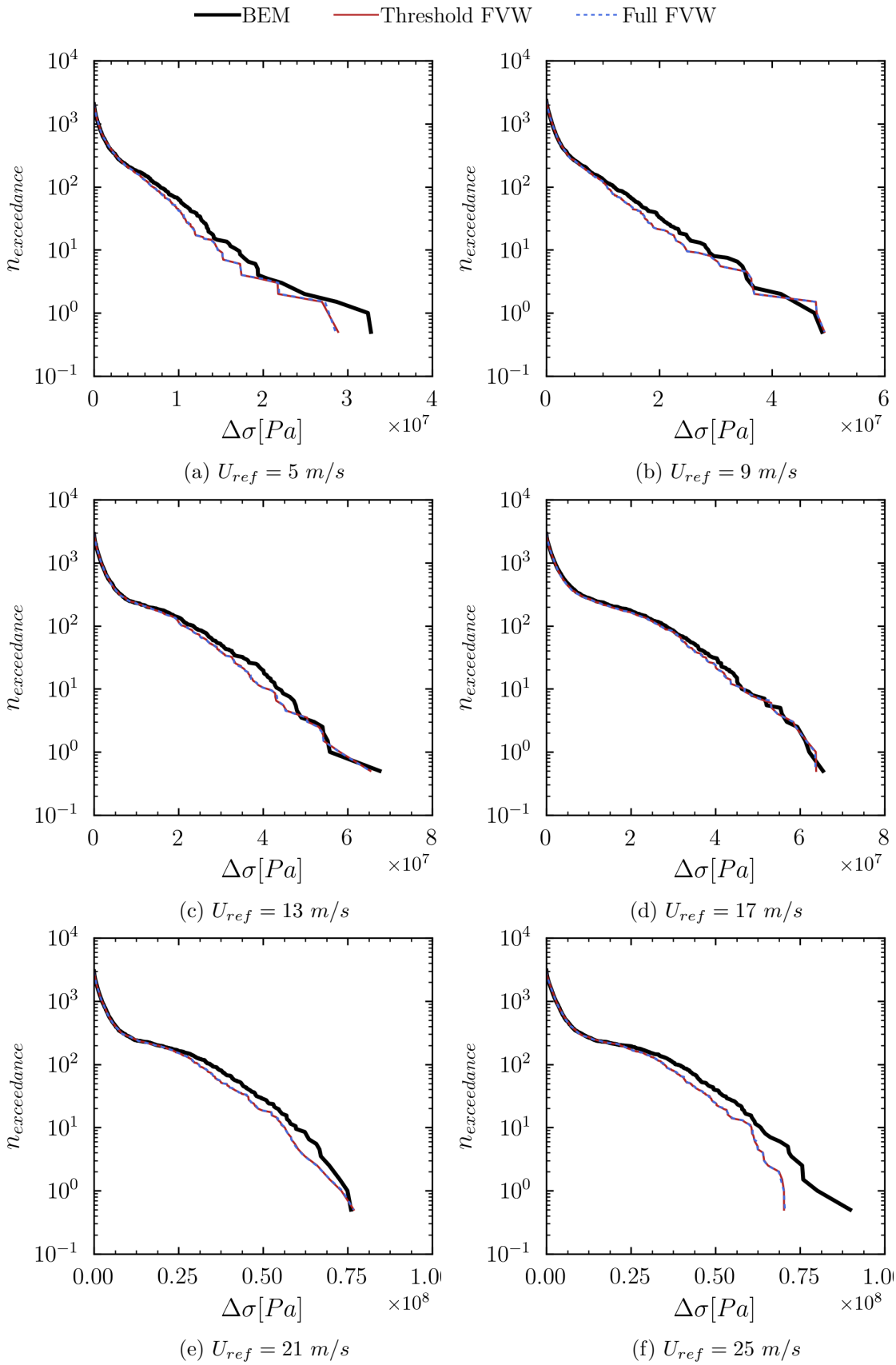

(a) $U_{ref} = 5\ m/s$ (b) $U_{ref} = 9\ m/s$

(c) $U_{ref} = 13\ m/s$ (d) $U_{ref} = 17\ m/s$

(e) $U_{ref} = 21\ m/s$ (f) $U_{ref} = 25\ m/s$

Figure B.1: Number of exceedance of stress cycle amplitude of the rainflow counted stress cycles for one metocean case for the wind turbine on the semi-submersible with vortex emission at every step and at larger time steps for a 30 minute case (see Table 4.3).

Appendix C

Flapwise root bending moment power spectral density with BEM

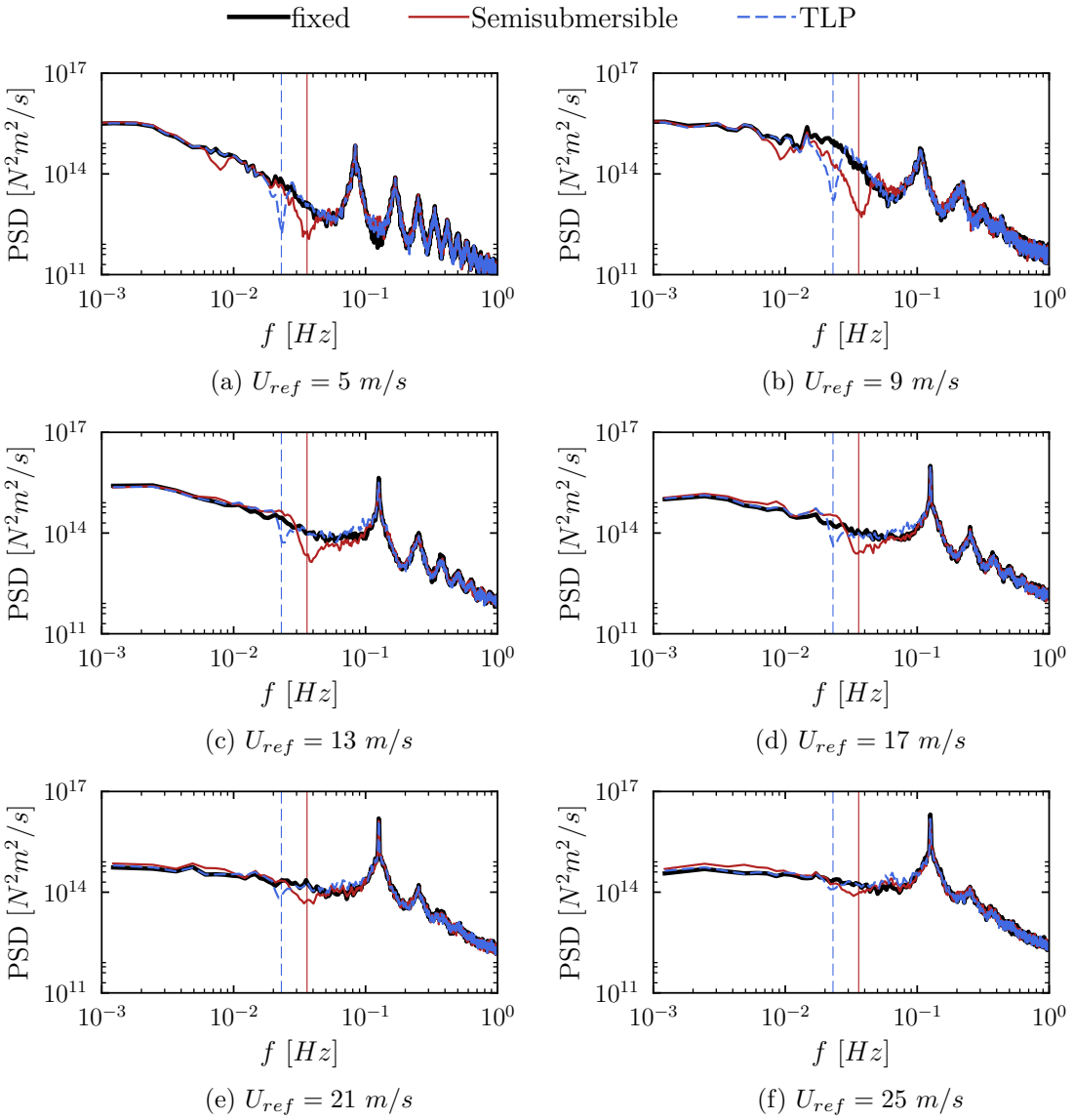

(a) $U_{ref} = 5\ m/s$ (b) $U_{ref} = 9\ m/s$

(c) $U_{ref} = 13\ m/s$ (d) $U_{ref} = 17\ m/s$

(e) $U_{ref} = 21\ m/s$ (f) $U_{ref} = 25\ m/s$

Figure C.1: Power Spectral Density of the flapwise root bending moment with BEM aerodynamic model. The vertical line shows the natural pitch frequency of the floating wind turbine including the floater and the mooring lines $f_p = 0.036\ Hz$ which alleviates some of the aerodynamic loads.

Bibliography

[1] URL https://www.eti.co.uk/programmes/offshore-wind/deep-water. Accessed : 2022-02-25.

[2] Recommended practice DNV-RP-C203: Fatigue design of offshore steel structures.

[3] Hywind Scotland remains the UK's best performing offshore wind farm. URL https://www.equinor.com/en/news/20210323-hywind-scotland-uk-best-performing-offshore-wind-farm.html. Accessed : 2022-02-25.

[4] Anemoc (digital atlas of ocean and coastal sea states). http://anemoc.cetmef.developpement-durable.gouv.fr/.

[5] OpenFAST. https://github.com/OpenFAST/openfast. URL https://github.com/OpenFAST/openfast.

[6] Nikhar J. Abbas, Daniel S. Zalkind, Lucy Pao, and Alan Wright. A reference open-source controller for fixed and floating offshore wind turbines. *Wind Energy Science*, 7(1):53–73, January 2022. doi: 10.5194/wes-7-53-2022. URL https://doi.org/10.5194/wes-7-53-2022.

[7] Ira H. Abbott and Albert E. Von Doenhoff. *Theory of Wing Sections including a summary of airfoil data*. Dover Publications, New York (USA), 1959.

[8] Frederico Afonso, José Vale, Éder Oliveira, Fernando Lau, and Afzal Suleman. A review on non-linear aeroelasticity of high aspect-ratio wings. *Progress in Aerospace Sciences*, 89:40–57, February 2017. doi: 10.1016/j.paerosci.2016.12.004. URL https://doi.org/10.1016/j.paerosci.2016.12.004.

[9] C. Allen, A. Viselli, H. Dagher, A. Goupee, E. Gaertner, N. Abbas, M. Hall, and G. Barter. Definition of the UMaine VolturnUS-S reference platform developed for the IEA wind 15-megawatt offshore reference wind turbine. Technical report, National Renewable Energy Laboratory, 2020.

[10] S.I. Andersen, P.W. Bach, W.J.A. Bonnee, C.W. Kensche, H. Lilholt, A. Lystrup, and W. Sys. Fatigue of materials and components for wind turbine rotor blades. Technical report, DLR, 1996.

[11] Alireza Arabgolarcheh, Sahar Jannesarahmadi, and Ernesto Benini. Modeling of near wake characteristics in floating offshore wind turbines using an actuator line method. *Renewable Energy*, 185:871–887, February 2022. doi: 10.1016/j.renene.2021.12.099. URL https://doi.org/10.1016/j.renene.2021.12.099.

[12] Frédéric Archambeau, Namane Méchitoua, and Marc Sakiz. Code Saturne: A finite volume code for the computation of turbulent incompressible flows-industrial applications. *International Journal on Finite Volumes*, 1, 2004.

[13] S. Aubrun, S. Loyer, P.E. Hancock, and P. Hayden. Wind turbine wake properties: Comparison between a non-rotating simplified wind turbine model and a rotating model. *Journal of Wind Engineering and Industrial Aerodynamics*, 120: 1–8, September 2013. doi: 10.1016/j.jweia.2013.06.007. URL https://doi.org/10.1016/j.jweia.2013.06.007.

[14] S. Aubrun, M. Bastankhah, R.B. Cal, B. Conan, R.J. Hearst, D. Hoek, M. Hölling, M. Huang, C Hur, B. Karlsen, I. Neunaber, M. Obligado, J. Peinke, M. Percin, L. Saetran, P Schito, B. Schliffke, D. Sims-Williams, O. Uzol, M.K. Vinnes, and A. Zasso. Round-robin tests of porous disc models. *Journal of Physics: Conference Series*, 1256:012004, July 2019. doi: 10.1088/1742-6596/1256/1/012004. URL https://doi.org/10.1088/1742-6596/1256/1/012004.

[15] Aurélien Babarit and Gérard Delhommeau. Theoretical and numerical aspects of the open source BEM solver NEMOH. In *11th European Wave and Tidal Energy Conference (EWTEC2015)*, Proceedings of the 11th European Wave and Tidal Energy Conference, Nantes, France, September 2015.

[16] C. Bak, F. Zahle, R. Bitsche, T. Kim, A. Yde, L. Henriksen, M.H. Hansen, J.P.A.A. Blaques, M. Gaunaa, and A. Natarajan. The DTU 10-MW reference wind turbine. Technical report, DTU, 2013.

[17] Josef Ballmann, editor. *Flow Modulation and Fluid—Structure Interaction at Airplane Wings*. Springer Berlin Heidelberg, 2003. doi: 10.1007/978-3-540-44866-2. URL https://doi.org/10.1007/978-3-540-44866-2.

[18] F. Barnaud, P. Bénard, G. Lartigue, V. Moureau, and P. Deglaire. Flow around thick airfoils at very high Reynolds number. stall and dynamic stall applications. In *Direct and Large-Eddy Simulation XI*, pages 359–365. Springer International Publishing, 2019. doi: 10.1007/978-3-030-04915-7_47. URL https://doi.org/10.1007/978-3-030-04915-7_47.

[19] O.A. Bauchau and J.I. Craig. *Structural Analysis*, chapter Euler-Bernoulli beam theory, pages 173–221. Springer Netherlands, 2009. doi: 10.1007/978-90-481-2516-6_5.

[20] I. Bayati, M. Belloli, and L. Bernini. Qualification of innovative floating substructures for 10MW wind turbines and water depths greater than 50m : LIFES50+ D3.1 AeroDyn validated model. Technical report, Politecnico di Milano, 2016.

[21] I. Bayati, M. Belloli, L. Bernini, and A Zasso. Wind tunnel validation of AeroDyn within LIFES50+ project: imposed surge and pitch tests. *Journal of Physics: Conference Series*, 753:092001, sep 2016. doi: 10.1088/1742-6596/753/9/092001. URL https://doi.org/10.1088/1742-6596/753/9/092001.

[22] I. Bayati, M. Belloli, L. Bernini, D.M. Boldrin, K. Boorsma, M. Caboni, M. Cormier, R. Mikkelsen, T. Lutz, and A. Zasso. UNAFLOW project: UNsteady aerodynamics of FLOating wind turbines. *Journal of Physics: Conference Series*, 1037:072037, 2018. doi: 10.1088/1742-6596/1037/7/072037. URL https://doi.org/10.1088/1742-6596/1037/7/072037.

[23] P Benard, A Viré, V Moureau, G Lartigue, L Beaudet, P Deglaire, and L Bricteux. Large-eddy simulation of wind turbines wakes including geometrical effects. *Computers & Fluids*, 173:133–139, 2018.

[24] Frederik Berger and Martin Kühn. Experimental investigation of dynamic inflow effects with a scaled wind turbine in a controlled wind tunnel environment. *Journal of Physics: Conference Series*, 1037:052017, June 2018. doi: 10.1088/1742-6596/1037/5/052017. URL https://doi.org/10.1088/1742-6596/1037/5/052017.

[25] Frederik Berger, Leo Höning, Iván Herráez, and Martin Kühn. Comparison of a radially resolved dynamic inflow pitch step experiment to mid-fidelity simulations and BEM. *Journal of Physics: Conference Series*, 1618:052055, September 2020. doi: 10.1088/1742-6596/1618/5/052055. URL https://doi.org/10.1088/1742-6596/1618/5/052055.

[26] Camille Choma Bex, Gregory Pinon, Myriam Slama, Benoist Gaston, Grégory Germainy, and Elie Rivoalen. Lagrangian vortex computations of turbine wakes: recent improvements using Poletto's synthetic eddy method (SEM) to account for ambient turbulence. *Journal of Physics: Conference Series*, 1618:062028, September 2020. doi: 10.1088/1742-6596/1618/6/062028. URL https://doi.org/10.1088/1742-6596/1618/6/062028.

[27] Mahendra J Bhagwat and J Gordon Leishman. Generalized viscous vortex model for application to free-vortex wake and aeroacoustic calculations. In *Annual forum*

proceedings-American helicopter society, volume 58, pages 2042–2057. American Helicopter Society, Inc, 2002.

[28] K Boorsma. *Power and Loads for Wind Turbines in Yawed Conditions: Analysis of Field Measurements and Aerodynamic Predictions*. ECN-E-12-047, 2012.

[29] K. Boorsma, J.G. Schepers, S. Gomeez-Iradi, I. Herraez, T. Lutz, P. Weihing, L. Oggiano, G. Pirrung, H.A. Madsen, W.Z. Shen, H. Rahimi, and P. Schaffarczyk. Final report of IEA wind: Task 29 mexnext (phase 3). Technical report, ECN, Petten, The Netherlands, 2018.

[30] Koen Boorsma, Luca Greco, and Gabriele Bedon. Rotor wake engineering models for aeroelastic applications. *Journal of Physics: Conference Series*, 1037:062013, June 2018. doi: 10.1088/1742-6596/1037/6/062013. URL https://doi.org/10.1088/1742-6596/1037/6/062013.

[31] Koen Boorsma, Florian Wenz, Koert Lindenburg, Mansoor Aman, and Menno Kloosterman. Validation and accommodation of vortex wake codes for wind turbine design load calculations. *Wind Energy Science*, 5(2):699–719, June 2020. doi: 10.5194/wes-5-699-2020. URL https://doi.org/10.5194/wes-5-699-2020.

[32] Emmanuel Branlard. *Wind Turbine Aerodynamics and Vorticity-Based Methods: Fundamentals and Recent Applications*. Springer, 2017.

[33] H. Bredmose, F. Lemmer, M. Borg, A. Pegalajar-Jurado, R.F. Mikkelsen, T. Stoklund Larsen, T. Fjelstrup, W. Yu, A.K. Lomholt, L. Boehm, and J. Azcona Armendariz. The triple spar campaign: Model tests of a 10mw floating wind turbine with waves, wind and pitch control. *Energy Procedia*, 137:58–76, oct 2017. doi: 10.1016/j.egypro.2017.10.334. URL https://doi.org/10.1016/j.egypro.2017.10.334.

[34] Jr. Buhl, M.L. New empirical relationship between thrust coefficient and induction factor for the turbulent windmill state. Technical report, NREL, 1617 Cole Boulevard, Golden, Colorado 80401-3393, 8 2005.

[35] Tony Burton, David Sharpe, Nick Jenkins, and Ervin Bossanyi. *Wind energy handbook*. John Wiley & Sons, 2001.

[36] S. Butterfield, W. Musial, J. Jonkman, and P. Sclavounos. Engineering challenges for floating offshore wind turbines. In *Proceedings of the 2005 Copenhagen Offshore Wind Conference*, 2005.

[37] M. Capaldo, M. Guiton, G. Huwart, E. Julan, N. Krasimirov Dimitrov, T. Kim, A. Lovera, and C. Peyrard. Design brief of HIPERWIND offshore wind turbine cases: bottom fixed 10MW and floating 15MW. Technical report, EDF IFDP-EN DTU, 2021.

[38] P.J. Carpenter and B. Fridovich. Effect of a rapid blade-pitch increase on the thrust and induced-velocity response of a full-scale helicopter rotor. Technical report, Langley Aeronautical Laboratory, Langley Aeronautical Laboratory Langley Field, Va., 1953.

[39] P. K. Chaviaropoulos and M. O. L. Hansen. Investigating three-dimensional and rotational effects on wind turbine blades by means of a quasi-3d Navier-Stokes solver. *Journal of Fluids Engineering*, 122(2):330, 2000. doi: 10.1115/1.483261. URL https://doi.org/10.1115/1.483261.

[40] Jiahao Chen, Zhiqiang Hu, Decheng Wan, and Qing Xiao. Comparisons of the dynamical characteristics of a semi-submersible floating offshore wind turbine based on two different blade concepts. *Ocean Engineering*, 153:305–318, April 2018. doi: 10.1016/j.oceaneng.2018.01.104. URL https://doi.org/10.1016/j.oceaneng.2018.01.104.

[41] Ziwen Chen, Xiaodong Wang, Yize Guo, and Shun Kang. Numerical analysis of unsteady aerodynamic performance of floating offshore wind turbine under platform surge and pitch motions. *Renewable Energy*, 163:1849–1870, January 2021. doi: 10.1016/j.renene.2020.10.096. URL https://doi.org/10.1016/j.renene.2020.10.096.

[42] Matthew J. Churchfield, Scott J. Schreck, Luis A. Martinez, Charles Meneveau, and Philippe R. Spalart. An advanced actuator line method for wind energy applications and beyond. In *35th Wind Energy Symposium*. American Institute of Aeronautics and Astronautics, jan 2017. doi: 10.2514/6.2017-1998. URL https://doi.org/10.2514/6.2017-1998.

[43] M. Cormier, M. Caboni, T. Lutz, K. Boorsma, and E. Krämer. Numerical analysis of unsteady aerodynamics of floating offshore wind turbines. *Journal of Physics: Conference Series*, 1037:072048, jun 2018. doi: 10.1088/1742-6596/1037/7/072048. URL https://doi.org/10.1088/1742-6596/1037/7/072048.

[44] Marion Cormier, Manuel Bühler, Moritz Mauz, Thorsten Lutz, Jens Bange, and Ewald Krämer. CFD prediction of tip vortex aging in the wake of a multi-MW wind turbine. *Journal of Physics: Conference Series*, 1618:062029, September 2020. doi: 10.1088/1742-6596/1618/6/062029. URL https://doi.org/10.1088/1742-6596/1618/6/062029.

[45] Rémi Corniglion, Jeffrey Harris, Christophe Peyrard, and Matteo Capaldo. Comparison of the free vortex wake and actuator line methods to study the loads of a wind turbine in imposed surge motion. *Journal of Physics: Conference Se-*

ries, 1618:052045, September 2020. doi: 10.1088/1742-6596/1618/5/052045. URL https://doi.org/10.1088/1742-6596/1618/5/052045.

[46] Rémi Corniglion, Jeffrey C. Harris, and Christophe Peyrard. The aerodynamics of a blade pitch, rotor speed, and surge step for a wind turbine regarding dynamic inflow. *Wind Energy*, n/a(n/a), 2022. doi: https://doi.org/10.1002/we.2702. URL https://onlinelibrary.wiley.com/doi/abs/10.1002/we.2702.

[47] Benoit de Laage De Meux. *Modélisation des écoulements turbulents en rotation et en présence de transferts thermiques par approche hybride RANS/LES zonale*. PhD thesis, ISAE-ENSMA Ecole Nationale Supérieure de Mécanique et d'Aérotechique, 2012.

[48] J.B. de Vaal, M.O. L. Hansen, and T. Moan. Effect of wind turbine surge motion on rotor thrust and induced velocity. *Wind Energy*, 17(1):105–121, oct 2012. doi: 10.1002/we.1562. URL https://doi.org/10.1002/we.1562.

[49] L. Deppe and W.J. Wagner. Experimental investigation of the periodical wake structure of a wind turbine model. In *Twelfth European Rotorcraft forum*, Garmisch-Partenkirchen, Federal Republic of Germany, 1986.

[50] William J. Devenport, Michael C. Rife, Stergios I. Liapis, and Gordon J. Follin. The structure and development of a wing-tip vortex. *Journal of Fluid Mechanics*, 312: 67–106, April 1996. doi: 10.1017/s0022112096001929. URL https://doi.org/10.1017/s0022112096001929.

[51] G Dietz, G Schewe, F Kießling, and M Sinapius. Limit-cycle-oscillation experiments at a transport aircraft wing model. In *Proceedings of the International Forum on Aeroelasticity and structural Dynamics IFASD*, 2003.

[52] Zhaohui Du and M.S Selig. The effect of rotation on the boundary layer of a wind turbine blade. *Renewable Energy*, 20(2):167–181, June 2000. doi: 10.1016/s0960-1481(99)00109-3. URL https://doi.org/10.1016/s0960-1481(99)00109-3.

[53] Horia Dumitrescu, Vladimir Cardoş, and Alexandru Dumitrache. Modelling of inboard stall delay due to rotation. *Journal of Physics: Conference Series*, 75:012022, July 2007. doi: 10.1088/1742-6596/75/1/012022. URL https://doi.org/10.1088/1742-6596/75/1/012022.

[54] Brenden P. Epps and Bernard T. Roesler. Vortex sheet strength in the Sears, Küssner, Theodorsen, and Wagner aerodynamics problems. *AIAA Journal*, 56(3): 889–904, March 2018. doi: 10.2514/1.j056399. URL https://doi.org/10.2514/1.j056399.

[55] R. Farrugia, T. Sant, and D. Micallef. Investigating the aerodynamic performance of a model offshore floating wind turbine. *Renewable Energy*, 70:24–30, oct 2014. doi: 10.1016/j.renene.2013.12.043. URL https://doi.org/10.1016/j.renene.2013.12.043.

[56] R. Farrugia, T. Sant, and D. Micallef. A study on the aerodynamics of a floating wind turbine rotor. *Renewable Energy*, 86:770–784, February 2016. doi: 10.1016/j.renene.2015.08.063. URL https://doi.org/10.1016/j.renene.2015.08.063.

[57] Alessandro Fontanella, Ilmas Bayati, Robert Mikkelsen, Marco Belloli, and Alberto Zasso. UNAFLOW: a holistic wind tunnel experiment about the aerodynamic response of floating wind turbines under imposed surge motion. *Wind Energy Science*, 6(5):1169–1190, September 2021. doi: 10.5194/wes-6-1169-2021. URL https://doi.org/10.5194/wes-6-1169-2021.

[58] Alessandro Fontanella, Ilmas Bayati, Robert Mikkelsen, Marco Belloli, and Alberto Zasso. UNAFLOW: UNsteady Aerodynamics of FLOating Wind turbines, May 2021. URL https://doi.org/10.5281/zenodo.4740006.

[59] Peter Frohboese and Andreas Anders. Effects of icing on wind turbine fatigue loads. *Journal of Physics: Conference Series*, 75:012061, July 2007. doi: 10.1088/1742-6596/75/1/012061. URL https://doi.org/10.1088/1742-6596/75/1/012061.

[60] Robert Edmund Froude. On the part played in propulsion by differences of fluid pressure. *Trans. Inst. Naval Architects*, 30:390, 1889.

[61] E. Gaertner, J. Rinker, L. Sethuraman, F. Zahle, B. Anderson, G. Barter, N. Abbas, F. Meng, P. Bortolotti, W. Skrzypinski, G. Scott, R. Feil, H. Bredmose, K. Dykes, M. SHields, C. Allen, and A. Viselli. Defintion of the iea 15-megawatt offshore reference wind turbine. Technical report, National Renewable Energy Laboratory, 2020.

[62] H. Glauert. Airplane propellers. In *Aerodynamic Theory*, pages 169–360. Springer Berlin Heidelberg, 1935. doi: 10.1007/978-3-642-91487-4_3. URL https://doi.org/10.1007/978-3-642-91487-4_3.

[63] Hermann Glauert. *A general theory of the autogyro*, volume 1111. HM Stationery Office, 1926.

[64] Andrew J. Goupee, Bonjun J. Koo, Richard W. Kimball, Kostas F. Lambrakos, and Habib J. Dagher. Experimental comparison of three floating wind turbine concepts. *Journal of Offshore Mechanics and Arctic Engineering*, 136(2), March 2014. doi: 10.1115/1.4025804. URL https://doi.org/10.1115/1.4025804.

[65] Andrew J. Goupee, Richard W. Kimball, and Habib J. Dagher. Experimental observations of active blade pitch and generator control influence on floating wind turbine response. *Renewable Energy*, 104:9–19, April 2017. doi: 10.1016/j.renene.2016.11.062. URL https://doi.org/10.1016/j.renene.2016.11.062.

[66] Leslie Greengard and Vladimir Rokhlin. A new version of the fast multipole method for the laplace equation in three dimensions. *Acta Numerica*, 6:229–269, January 1997. doi: 10.1017/s0962492900002725. URL https://doi.org/10.1017/s0962492900002725.

[67] Gaël Guennebaud, Benoît Jacob, et al. Eigen v3. http://eigen.tuxfamily.org, 2010.

[68] J. Bosschers H. Snel, R. Houwink. Sectional prediction of lift coefficitens on rotating wind turbine blades in stall. Technical report, Energy Research Centre of the Netherlands, 1994.

[69] Wouter Haans. *Wind turbine aerodynamic in yaw*. PhD thesis, TU Delft, Delft, 2011.

[70] Matthew Hall and Andrew J. Goupee. Validation of a hybrid modeling approach to floating wind turbine basin testing. *Wind Energy*, 21(6):391–408, feb 2018. doi: 10.1002/we.2168. URL https://doi.org/10.1002/we.2168.

[71] K Hammerum, P Brath, and N K Poulsen. A fatigue approach to wind turbine control. *Journal of Physics: Conference Series*, 75:012081, July 2007. doi: 10.1088/1742-6596/75/1/012081. URL https://doi.org/10.1088/1742-6596/75/1/012081.

[72] M.M. Hand, D.A. Simms, L.J. Fingersh, D.W. Jager, J.R. Cotrell, S. Schreck, and S.M. Larwood. Unsteady aerodynamics experiment phase VI: Wind tunnel test configurations and available data campaigns. Technical report, NREL, 1617 Cole Boulevard Golden, Colorado 80401-3393, 2001.

[73] M.H. Hansen, Mac Gaunaa, and Helge Aagaard Madsen. *A Beddoes-Leishman type dynamic stall model in state-space and indicial formulations*. 2004. ISBN 87-550-3090-4.

[74] Jay C. Hardin. The velocity field induced by a helical vortex filament. *Physics of Fluids*, 25(11):1949, 1982. doi: 10.1063/1.863684. URL https://doi.org/10.1063/1.863684.

[75] Hans M Hilber, Thomas JR Hughes, and Robert L Taylor. Improved numerical dissipation for time integration algorithms in structural dynamics. *Earthquake Engineering & Structural Dynamics*, 5(3):283–292, 1977.

[76] H Himmelskamp. *Profile investigations on a rotating airscrew*. Ministry of Aircraft Propulsion, Great Britain, 1947.

[77] D.H. Hodges and E.H. Dowell. Nonlinear equations of motion for the elastic bending and torsion of twisted nonuniform rotor blades. Technical Report NASA TN D-7818, NASA.

[78] Jan-Tore Horn and Bernt J. Leira. Fatigue reliability assessment of offshore wind turbines with stochastic availability. *Reliability Engineering & System Safety*, 191: 106550, November 2019. doi: 10.1016/j.ress.2019.106550. URL https://doi.org/10.1016/j.ress.2019.106550.

[79] Michael F. Howland, Sanjiva K. Lele, and John O. Dabiri. Wind farm power optimization through wake steering. *Proceedings of the National Academy of Sciences*, 116(29):14495–14500, 2019.

[80] Weifei Hu, K. K. Choi, and Hyunkyoo Cho. Reliability-based design optimization of wind turbine blades for fatigue life under dynamic wind load uncertainty. *Structural and Multidisciplinary Optimization*, 54(4):953–970, April 2016. doi: 10.1007/s00158-016-1462-x. URL https://doi.org/10.1007/s00158-016-1462-x.

[81] IEA. Offshore wind outlook 2019. Technical report, International Energy Agency, 2019.

[82] IEC61400-1. Wind turbines – part 1: Design requirements. Standard, International Electrotechnical Commission, Geneva, CH, 2005.

[83] Piotr Janiszewksi. Rainflow ASTM E1049-85 python implementation. https://github.com/iamlikeme/rainflow, 2018.

[84] Minu Jeon, Seungmin Lee, and Soogab Lee. Unsteady aerodynamics of offshore floating wind turbines in platform pitching motion using vortex lattice method. *Renewable Energy*, 65:207–212, 2014. doi: 10.1016/j.renene.2013.09.009. URL https://doi.org//10.1016/j.renene.2013.09.009.

[85] Pankaj K. Jha and Sven Schmitz. Actuator curve embedding - an advanced actuator line model. *Journal of Fluid Mechanics*, 834, nov 2018. doi: 10.1017/jfm.2017.793. URL https://doi.org/10.1017/jfm.2017.793.

[86] A Jimenez, A Crespo, E Migoya, and J Garcia. Advances in large-eddy simulation of a wind turbine wake. *Journal of Physics: Conference Series*, 75:012041, jul 2007. doi: 10.1088/1742-6596/75/1/012041. URL https://doi.org/10.1088/1742-6596/75/1/012041.

[87] A Jimenez, A Crespo, E Migoya, and J Garcia. Large-eddy simulation of spectral coherence in a wind turbine wake. *Environmental Research Letters*, 3(1):015004, jan 2008. doi: 10.1088/1748-9326/3/1/015004. URL https://doi.org/10.1088/1748-9326/3/1/015004.

[88] B.J. Jonkman. Turbsim user's guide: Version 1.50. Technical report, NREL, 2009.

[89] J. M. Jonkman and D. Matha. Dynamics of offshore floating wind turbines-analysis of three concepts. *Wind Energy*, 14(4):557–569, jan 2011. doi: 10.1002/we.442. URL https://doi.org/10.1002/we.442.

[90] Jason Jonkman, Sandy Butterfield, Walter Musial, and George Scott. Definition of a 5-MW reference wind turbine for offshore system development. Technical report, National Renewable Energy Lab.(NREL), Golden, CO (United States), 2009.

[91] N.E. Joukowsky. *Théorie tourbillonaire de l'hélice propulsive*. Travaux de l'Institut central aéro-hydrodynamique. Gauthier-Villars, Paris, 1929.

[92] M. Kämpchen, A. Dafnis, H.-G. Reimerdes, G. Britten, and J. Ballmann. Dynamic aero-structural response of an elastic wing model. *Journal of Fluids and Structures*, 18(1):63–77, August 2003. doi: 10.1016/s0889-9746(03)00090-2. URL https://doi.org/10.1016/s0889-9746(03)00090-2.

[93] Joseph Katz and Allen Plotkin. *Low-Speed Aerodynamics*. Cambridge Aerospace Series. Cambridge University Press, 2 edition, 2001. doi: 10.1017/CBO9780511810329.

[94] Y. Kim and O.J. Kwon. Effect of platform motion on aerodynamic performance and aeroelastic behavior of floating offshore wind turbine blades. *Energies*, 12 (13):2519, June 2019. doi: 10.3390/en12132519. URL https://doi.org/10.3390/en12132519.

[95] Richard Kimball, Andrew J. Goupee, Matthew J. Fowler, Erik-Jan de Ridder, and Joop Helder. Wind/wave basin verification of a performance-matched scale-model wind turbine on a floating offshore wind turbine platform. In *Volume 9B: Ocean Renewable Energy*. ASME, June 2014. doi: 10.1115/omae2014-24166. URL https://doi.org/10.1115/omae2014-24166.

[96] Christian Koch, Friedemann Borisade, Frank Lemmer, Po Wen Cheng, Filippo Campagnolo, and Denis Matha. Validation of INNWIND.EU scaled model tests of a semisubmersible floating wind turbine. *International Journal of Offshore and Polar Engineering*, 28(01):54–64, 2016.

[97] Karsten M. Kopperstad, Rajan Kumar, and Kourosh Shoele. Aerodynamic characterization of barge and spar type floating offshore wind turbines at different sea

states. *Wind Energy*, 23(11):2087–2112, July 2020. doi: 10.1002/we.2547. URL https://doi.org/10.1002/we.2547.

[98] Vladimir Leble and George Barakos. Demonstration of a coupled floating offshore wind turbine analysis with high-fidelity methods. *Journal of Fluids and Structures*, 62:272 – 293, 2016. ISSN 0889-9746. doi: https://doi.org/10.1016/j.jfluidstructs.2016.02.001. URL http://www.sciencedirect.com/science/article/pii/S088997461600027X.

[99] Hak Gu Lee, Min Gyu Kang, and Jisang Park. Fatigue failure of a composite wind turbine blade at its root end. *Composite Structures*, 133:878–885, December 2015. doi: 10.1016/j.compstruct.2015.08.010. URL https://doi.org/10.1016/j.compstruct.2015.08.010.

[100] Hakjin Lee and Duck-Joo Lee. Effects of platform motions on aerodynamic performance and unsteady wake evolution of a floating offshore wind turbine. *Renewable Energy*, 143:9–23, December 2019. doi: 10.1016/j.renene.2019.04.134. URL https://doi.org/10.1016/j.renene.2019.04.134.

[101] T. Lee and P. Gerontakos. Investigation of flow over an oscillating airfoil. *Journal of Fluid Mechanics*, 512:313–341, 2004. doi: 10.1017/S0022112004009851.

[102] Gordon J Leishman. *Principles of helicopter aerodynamics*. Cambridge University Press, 2006.

[103] JG Leishman and TS Beddoes. A generalised model for airfoil unsteady aerodynamic behaviour and dynamic stall using the indicial method. In *Proceedings of the 42nd Annual forum of the American Helicopter Society*, pages 243–265. Proceedings of the 42nd Annual forum of the American Helicopter Society, 1986.

[104] Vincent Leroy. *Unsteady aerodynamic modelling for seakeeping analysis of Floating Offshore Wind Turbines*. PhD thesis, L'École Centrale de Nantes, 2018.

[105] Vincent Leroy, Jean-Christophe Gilloteaux, Mattias Lynch, Aurélien Babarit, and Pierre Ferrant. Impact of aerodynamic modeling on seakeeping performance of a floating horizontal axis wind turbine. *Wind Energy*, 22(8):1019–1033, April 2019. doi: 10.1002/we.2337. URL https://doi.org/10.1002/we.2337.

[106] C. Lienard, R. Boisard, and C. Daudin. Aerodynamic behavior of a floating offshore wind turbine. *AIAA Journal*, pages 1–13, May 2019. doi: 10.2514/1.j059255. URL https://doi.org/10.2514/1.j059255.

[107] L E M Lignarolo, D Ragni, C J Simão Ferreira, and G J W van Bussel. Kinetic energy entrainment in wind turbine and actuator disc wakes: an experimental analysis. *Journal of Physics: Conference Series*, 524:012163, June 2014. doi:

10.1088/1742-6596/524/1/012163. URL https://doi.org/10.1088/1742-6596/524/1/012163.

[108] Keith Lindsay and Robert Krasny. A particle method and adaptive treecode for vortex sheet motion in three-dimensional flow. *Journal of Computational Physics*, 172(2):879–907, September 2001. doi: 10.1006/jcph.2001.6862. URL https://doi.org/10.1006/jcph.2001.6862.

[109] Yuanchuan Liu and Qing Xiao. Development of a fully coupled aero-hydro-mooring-elastic tool for floating offshore wind turbines. *Journal of Hydrodynamics*, 31(1): 21–33, January 2019. doi: 10.1007/s42241-019-0012-6. URL https://doi.org/10.1007/s42241-019-0012-6.

[110] Yuanchuan Liu, Qing Xiao, Atilla Incecik, Christophe Peyrard, and Decheng Wan. Establishing a fully coupled CFD analysis tool for floating offshore wind turbines. *Renewable Energy*, 112:280–301, 2017.

[111] Yuanchuan Liu, Qing Xiao, Atilla Incecik, and Christophe Peyrard. Aeroelastic analysis of a floating offshore wind turbine in platform-induced surge motion using a fully coupled CFD-MBD method. *Wind Energy*, 22(1):1–20, September 2018. doi: 10.1002/we.2265. URL https://doi.org/10.1002/we.2265.

[112] F.J. Madsen, T.R.L. Nielsen, T. Kim, H. Bredmose, A. Pegalajar-Jurado, R.F. Mikkelsen, A.K. Lomholt, M. Borg, M. Mirzaei, and P. Shin. Experimental analysis of the scaled DTU10mw TLP floating wind turbine with different control strategies. *Renewable Energy*, 155:330–346, August 2020. doi: 10.1016/j.renene.2020.03.145. URL https://doi.org/10.1016/j.renene.2020.03.145.

[113] Helge Aagaard Madsen, Torben Juul Larsen, Georg Raimund Pirrung, Ang Li, and Frederik Zahle. Implementation of the blade element momentum model on a polar grid and its aeroelastic load impact. *Wind Energy Science*, 5(1):1–27, January 2020. doi: 10.5194/wes-5-1-2020. URL https://doi.org/10.5194/wes-5-1-2020.

[114] Simone Mancini. An experimental, analytical and numerical study of FOWT's unsteady aerodynamics. Master's thesis, Politecnico Milano, 2020. URL https://www.politesi.polimi.it/handle/10589/153239.

[115] Simone Mancini, Koen Boorsma, Marco Caboni, Marion Cormier, Thorsten Lutz, Paolo Schito, and Alberto Zasso. Characterization of the unsteady aerodynamic response of a floating offshore wind turbine to surge motion. *Wind Energy Science*, 5(4):1713–1730, December 2020. doi: 10.5194/wes-5-1713-2020. URL https://doi.org/10.5194/wes-5-1713-2020.

[116] Dimitris I. Manolas, Vasilis A. Riziotis, George P. Papadakis, and Spyros G. Voutsinas. Hydro-servo-aero-elastic analysis of floating offshore wind turbines. *Fluids*, 5 (4):200, November 2020. doi: 10.3390/fluids5040200. URL https://doi.org/10.3390/fluids5040200.

[117] J.C. Marín, A. Barroso, F. París, and J. Cañas. Study of fatigue damage in wind turbine blades. *Engineering Failure Analysis*, 16(2):656–668, March 2009. doi: 10.1016/j.engfailanal.2008.02.005. URL https://doi.org/10.1016/j.engfailanal.2008.02.005.

[118] D. Marten, J. Wendler, G. Pechlivanoglou, C. N. Nayeri, and C. O. Paschereit. QBlade: an open source tool for design and simulation of horizontal and vertical axis wind turbines. *International Journal of Emerging Technology and Advanced Engineering*, 3:264–269, 2013.

[119] L. A. Martínez-Tossas, M. J. Churchfield, and C. Meneveau. Optimal smoothing length scale for actuator line models of wind turbine blades based on gaussian body force distribution. *Wind Energy*, 20(6):1083–1096, jan 2017. doi: 10.1002/we.2081. URL https://doi.org/10.1002/we.2081.

[120] Luis A. Martínez-Tossas and Charles Meneveau. Filtered lifting line theory and application to the actuator line model. *Journal of Fluid Mechanics*, 863:269–292, January 2018. doi: 10.1017/jfm.2018.994. URL https://doi.org/10.1017/jfm.2018.994.

[121] Masanori Matsuishi and Tatsuo Endo. Fatigue of metals subjected to varying stress. *Japan Society of Mechanical Engineers, Fukuoka, Japan*, 68(2):37–40, 1968.

[122] Moritz Mauz, Alexander Rautenberg, Andreas Platis, Marion Cormier, and Jens Bange. First identification and quantification of detached-tip vortices behind a wind energy converter using fixed-wing unmanned aircraft system. *Wind Energy Science*, 4(3):451–463, August 2019. doi: 10.5194/wes-4-451-2019. URL https://doi.org/10.5194/wes-4-451-2019.

[123] F.R. Menter. Two-equation eddy-viscosity turbulence models for engineering applications. *AIAA Journal*, 32(8):1598–1605, August 1994.

[124] Reda Merabet and Eric Laurendeau. Parametric study on the velocity sampling techniques for the actuator line method in 2D. In *AIAA Scitech 2019 Forum*. American Institute of Aeronautics and Astronautics, January 2019. doi: 10.2514/6.2019-1797. URL https://doi.org/10.2514/6.2019-1797.

[125] Alexander R. Meyer Forsting, Georg Raimund Pirrung, and Néstor Ramos-García. A vortex-based tip/smearing correction for the actuator line. *Wind Energy Science*,

4(2):369–383, June 2019. doi: 10.5194/wes-4-369-2019. URL https://doi.org/10.5194/wes-4-369-2019.

[126] D. Milano, C. Peyrard, and M. Capaldo. The effect of tendon inclination on the hydro-dynamic response of a 10 MW tension-leg platform wind turbine. In *Proceeding of the 16ème Journées de l'Hydrodynamique*, Marseille, 2018.

[127] Daniel Milano, Christophe Peyrard, Matteo Capaldo, David Ingram, Qing Xiao, and Lars Johanning. Impact of high order wave loads on a 10 MW tension-leg platform floating wind turbine at different tendon inclination angles. In *Volume 10: Ocean Renewable Energy*. American Society of Mechanical Engineers, June 2019. doi: 10.1115/omae2019-96243. URL https://doi.org/10.1115/omae2019-96243.

[128] Milton A. Miner. Cumulative damage in fatigue. *Journal of Applied Mechanics*, 12 (3):A159–A164, September 1945. doi: 10.1115/1.4009458. URL https://doi.org/10.1115/1.4009458.

[129] Anshul Mittal, Kidambi Sreenivas, Lafayette K. Taylor, and Levi Hereth. Improvements to the actuator line modeling for wind turbines. In *33rd Wind Energy Symposium*. American Institute of Aeronautics and Astronautics, January 2015. doi: 10.2514/6.2015-0216. URL https://doi.org/10.2514/6.2015-0216.

[130] Bernard Molin. *Hydrodynamique des structures offshore*. Editions Technip, 2002.

[131] J.R. Morison, J.W. Johnson, and S.A. Schaaf. The force exerted by surface waves on piles. *Journal of Petroleum Technology*, 2(05):149–154, May 1950. doi: 10.2118/950149-g. URL https://doi.org/10.2118/950149-g.

[132] Jonathan Murray and Matthew Barone. The development of CACTUS, a wind and marine turbine performance simulation code. In *49th AIAA Aerospace Sciences Meeting including the New Horizons Forum and Aerospace Exposition*. AIAA, American Institute of Aeronautics and Astronautics, January 2011. doi: 10.2514/6.2011-147. URL https://doi.org/10.2514/6.2011-147.

[133] W. Musial, S. Butterfield, and A. Boone. Feasibility fo floating platform systems for wind turbines. In *23rd ASME Wind Energy Symposium*, Reno, Nevada,USA, 2004.

[134] E. M. Nanos, C. L. Bottasso, D. I. Manolas, and V. A. Riziotis. Vertical wake deflection for floating wind turbines by differential ballast control (preprint). *Wind Energy Science Discussions*, 2021:1–30, 2021. doi: 10.5194/wes-2021-79. URL https://wes.copernicus.org/preprints/wes-2021-79/.

[135] Stefan Netzband, Christian W. Schulz, Ulf Göttsche, Daniel Ferreira González, and Moustafa Abdel-Maksoud. A panel method for floating offshore wind turbine simulations with fully integrated aero- and hydrodynamic modelling in time domain.

Ship Technology Research, 65(3):123–136, May 2018. doi: 10.1080/09377255.2018.1475710. URL https://doi.org/10.1080/09377255.2018.1475710.

[136] NREL. ROSCO. Version 2.4.1, 2021. URL https://github.com/NREL/ROSCO.

[137] Ylva Odemark and Jens H. M. Fransson. The stability and development of tip and root vortices behind a model wind turbine. *Experiments in Fluids*, 54(9), August 2013. doi: 10.1007/s00348-013-1591-6. URL https://doi.org/10.1007/s00348-013-1591-6.

[138] V. L. Okulov and J. N. Sørensen. Maximum efficiency of wind turbine rotors using Joukowsky and Betz approaches. *Journal of Fluid Mechanics*, 649:497–508, April 2010. doi: 10.1017/s0022112010000509. URL https://doi.org/10.1017/s0022112010000509.

[139] Valery L. Okulov, Jens N. Sørensen, and David H. Wood. The rotor theories by Professor Joukowsky: Vortex theories. *Progress in Aerospace Sciences*, 73:19–46, February 2015. doi: 10.1016/j.paerosci.2014.10.002. URL https://doi.org/10.1016/j.paerosci.2014.10.002.

[140] Yaşar Ostovan, M. Tuğrul Akpolat, and Oğuz Uzol. Experimental investigation of the effects of winglets on the tip vortex behavior of a model horizontal axis wind turbine using particle image velocimetry. *Journal of Solar Energy Engineering*, 141 (1), September 2019. doi: 10.1115/1.4041154. URL https://doi.org/10.1115/1.4041154.

[141] S. Øye. A simple vortex model of a turbine rotor. In *Proceedings of the Third IEA Symposium on the aerodynamics of wind turbines*, Harwell (UK), 1989. Proceedings of the Third IEA Symposium on the aerodynamics of wind turbines.

[142] S. Øye. Tjæreborg wind turbine: 4. dynamic inflow measurement. Technical report, DTH Lingby, Lyngby, 1991.

[143] A. Pegalajar-Jurad, F.J. Madsen, H. Sarlak, H. Bredmose, F. Lemmer, R. Faerron-Guzman, F. Borisade, and M. Kretschmer. Qualification of innovative floating substructures for 10MW wind turbines and water depths greater than 50m : LIFES50+ D4.8 validation of advanced models and methods for cascading into simpler models. Technical report, LIFES50+, 2019.

[144] Sebastian Perez-Becker, Francesco Papi, Joseph Saverin, David Marten, Alessandro Bianchini, and Christian Oliver Paschereit. Is the blade element momentum theory overestimating wind turbine loads? - a comparison with a lifting line free vortex wake method. October 2019. doi: 10.5194/wes-2019-70. URL https://doi.org/10.5194/wes-2019-70.

[145] W. F. Phillips and D. O. Snyder. Modern adaptation of Prandtl's classic lifting-line theory. *Journal of Aircraft*, 37(4):662–670, July 2000. doi: 10.2514/2.2649. URL https://doi.org/10.2514/2.2649.

[146] Georg Raimund Pirrung and Helge Aagaard Madsen. Dynamic inflow effects in measurements and high-fidelity computations. *Wind Energy Science*, 3(2):545–551, August 2018. doi: 10.5194/wes-3-545-2018. URL https://doi.org/10.5194/wes-3-545-2018.

[147] Dale M. Pitt and David A. Peters. Theoretical prediction of dynamic-inflow derivatives. In *SIXTH EUROPEAN ROTORCRAFT AND POWERED LIFT AIRCRAFT FORUM*, Bristol, England, 1981. Sixth European rotorcraft and powered lift aircraft forum.

[148] Ludwig Prandtl and Albert Betz. *Vier Abhandlungen zur Hydrodynamik und Aerodynamik*, volume 3. Universitätsverlag Göttingen, 2010.

[149] Sean Quallen and Tao Xing. CFD simulation of a floating offshore wind turbine system using a variable-speed generator-torque controller. *Renewable Energy*, 97:230–242, November 2016. doi: 10.1016/j.renene.2016.05.061. URL https://doi.org/10.1016/j.renene.2016.05.061.

[150] Sean Quallen, Tao Xing, Pablo Carrica, Yuwei Li, Jun Xu, et al. CFD simulation of a floating offshore wind turbine system using a quasi-static crowfoot mooring-line model. In *The Twenty-third International Offshore and Polar Engineering Conference*. International Society of Offshore and Polar Engineers, 2013.

[151] Hamid Rahimi, Andrea Martinez Garcia, Bernhard Stoevesandt, Joachim Peinke, and Gerard Schepers. An engineering model for wind turbines under yawed conditions derived from high fidelity models. *Wind Energy*, 21(8):618–633, mar 2018. doi: 10.1002/we.2182. URL https://doi.org/10.1002/we.2182.

[152] Néstor Ramos-García, Matias Sessarego, and Sergio González Horcas. Aero-hydro-servo-elastic coupling of a multi-body finite-element solver and a multi-fidelity vortex method. *Wind Energy*, November 2020. doi: 10.1002/we.2584. URL https://doi.org/10.1002/we.2584.

[153] Abdolrahim Rezaeiha, Ricardo Pereira, and Marios Kotsonis. Fluctuations of angle of attack and lift coefficient and the resultant fatigue loads for a large horizontal axis wind turbine. *Renewable Energy*, 114:904–916, December 2017. doi: 10.1016/j.renene.2017.07.101. URL https://doi.org/10.1016/j.renene.2017.07.101.

[154] Vasilis A. Riziotis and Spyros G. Voutsinas. Fatigue loads on wind turbines of different control strategies operating in complex terrain. *Journal of Wind Engineering and*

Industrial Aerodynamics, 85(3):211–240, April 2000. doi: 10.1016/s0167-6105(99)00127-0. URL https://doi.org/10.1016/s0167-6105(99)00127-0.

[155] A N Robertson, S Gueydon, E Bachynski, L Wang, J Jonkman, D Alarcón, E Amet, A Beardsell, P Bonnet, B Boudet, C Brun, Z Chen, M Féron, D Forbush, C Galinos, J Galvan, P Gilbert, J Gómez, V Harnois, F Haudin, Z Hu, J Le Dreff, M Leimeister, F Lemmer, H Li, G Mckinnon, I Mendikoa, A Moghtadaei, S Netzband, S Oh, A Pegalajar-Jurado, M Q Nguyen, K Ruehl, P Schünemann, W Shi, H Shin, Y Si, F Surmont, P Trubat, J Qwist, and S Wohlfahrt-Laymann. OC6 phase i: Investigating the underprediction of low-frequency hydrodynamic loads and responses of a floating wind turbine. *Journal of Physics: Conference Series*, 1618(3):032033, September 2020. doi: 10.1088/1742-6596/1618/3/032033. URL https://doi.org/10.1088/1742-6596/1618/3/032033.

[156] Amy Robertson, Jason Jonkman, Fabian Vorpahl, Wojciech Popko, Jacob Qvist, Lars Frøyd, Xiaohong Chen, José Azcona, Emre Uzunoglu, Carlos Guedes Soares, et al. Offshore code comparison collaboration continuation within IEA wind task 30: Phase II results regarding a floating semisubmersible wind system. In *International Conference on Offshore Mechanics and Arctic Engineering*, volume 45547, page V09BT09A012. American Society of Mechanical Engineers, 2014.

[157] Amy N. Robertson, Fabian Wendt, Jason M. Jonkman, Wojciech Popko, Habib Dagher, Sebastien Gueydon, Jacob Qvist, Felipe Vittori, José Azcona, Emre Uzunoglu, Carlos Guedes Soares, Rob Harries, Anders Yde, Christos Galinos, Koen Hermans, Jacobus Bernardus de Vaal, Pauline Bozonnet, Ludovic Bouy, Ilmas Bayati, Roger Bergua, Josean Galvan, Iñigo Mendikoa, Carlos Barrera Sanchez, Hyunkyoung Shin, Sho Oh, Climent Molins, and Yannick Debruyne. OC5 project phase II: Validation of global loads of the DeepCwind floating semisubmersible wind turbine. *Energy Procedia*, 137:38–57, oct 2017. doi: 10.1016/j.egypro.2017.10.333. URL https://doi.org/10.1016/j.egypro.2017.10.333.

[158] Dominique Roddier, Christian Cermelli, Alexia Aubault, and Alla Weinstein. WindFloat: A floating foundation for offshore wind turbines. *Journal of Renewable and Sustainable Energy*, 2(3):033104, May 2010. doi: 10.1063/1.3435339. URL https://doi.org/10.1063/1.3435339.

[159] Steven N. Rodriguez and Justin W. Jaworski. Strongly-coupled aeroelastic free-vortex wake framework for floating offshore wind turbine rotors. part 1: Numerical framework. *Renewable Energy*, 141:1127–1145, October 2019. doi: 10.1016/j.renene.2019.04.019. URL https://doi.org/10.1016/j.renene.2019.04.019.

[160] Steven N. Rodriguez and Justin W. Jaworski. Strongly-coupled aeroelastic free-vortex wake framework for floating offshore wind turbine rotors. part 2: Application.

Renewable Energy, 149:1018–1031, April 2020. doi: 10.1016/j.renene.2019.10.094. URL https://doi.org/10.1016/j.renene.2019.10.094.

[161] Tonio Sant, David Bonnici, Russell Farrugia, and Daniel Micallef. Measurements and modelling of the power performance of a model floating wind turbine under controlled conditions. *Wind Energy*, 18(5):811–834, mar 2014. doi: 10.1002/we.1730. URL https://doi.org/10.1002/we.1730.

[162] Ameya Sathe and Wim Bierbooms. Influence of different wind profiles due to varying atmospheric stability on the fatigue life of wind turbines. *Journal of Physics: Conference Series*, 75:012056, July 2007. doi: 10.1088/1742-6596/75/1/012056. URL https://doi.org/10.1088/1742-6596/75/1/012056.

[163] J. Schepers. An engineering model for yawed conditions, developed on basis of wind tunnel measurements. In *37th Aerospace Sciences Meeting and Exhibit*. American Institute of Aeronautics and Astronautics, jan 1999. doi: 10.2514/6.1999-39. URL https://doi.org/10.2514/6.1999-39.

[164] J G Schepers. IEA annex XX. dynamic inflow effects at fast pitching steps on a wind turbine placed in the NASA-Ames wind tunnel. ECN-E–07-085, Oct 2007.

[165] J.G. Schepers. *Engineering models in wind energy aerodynamics: Development, implementation and analysis using dedicated aerodynamic measurements*. PhD thesis, TU Delft, Delft, 2012.

[166] J Schijve. Fatigue of structures and materials in the 20th century and the state of the art. *International Journal of Fatigue*, 25(8):679–702, August 2003. doi: 10.1016/s0142-1123(03)00051-3. URL https://doi.org/10.1016/s0142-1123(03)00051-3.

[167] T. Sebastian and M.A. Lackner. Characterization of the unsteady aerodynamics of offshore floating wind turbines. *Wind Energy*, 16(3):339–352, mar 2013. doi: 10.1002/we.545. URL https://doi.org/10.1002/we.545.

[168] Thomas Sebastian and Matthew Lackner. Analysis of the induction and wake evolution of an offshore floating wind turbine. *Energies*, 5(4):968–1000, April 2012. doi: 10.3390/en5040968. URL https://doi.org/10.3390/en5040968.

[169] Thomas Sebastian and Matthew A Lackner. Development of a free vortex wake method code for offshore floating wind turbines. *Renewable Energy*, 46:269–275, 2012.

[170] Kelsey Shaler, Emmanuel Branlard, and Andy Platt. OLAF user's guide and theory manual. Technical report, National Renewable Energy Laboratory, 2020.

[171] R E Sheldahl and P C Klimas. Aerodynamic characteristics of seven symmetrical airfoil sections through 180-degree angle of attack for use in aerodynamic analysis of vertical axis wind turbines. Technical report, March 1981. URL https://doi.org/10.2172/6548367.

[172] Wen Zhong Shen, Robert Mikkelsen, Jens Nørkær Sørensen, and Christian Bak. Tip loss corrections for wind turbine computations. *Wind Energy*, 8(4):457–475, 2005. doi: 10.1002/we.153. URL https://doi.org/10.1002/we.153.

[173] Wen Zhong Shen, Wei Jun Zhu, and Jens Nørkaer Sørensen. Actuator line/navier-stokes computations for the MEXICO rotor: comparison with detailed measurements. *Wind Energy*, 15(5):811–825, oct 2011. doi: 10.1002/we.510. URL https://doi.org/10.1002/we.510.

[174] Xin Shen, Jinge Chen, Ping Hu, Xiaocheng Zhu, and Zhaohui Du. Study of the unsteady aerodynamics of floating wind turbines. *Energy*, 145:793–809, February 2018. doi: 10.1016/j.energy.2017.12.100. URL https://doi.org/10.1016/j.energy.2017.12.100.

[175] Michael Sherry, András Nemes, David Lo Jacono, Hugh M. Blackburn, and John Sheridan. The interaction of helical tip and root vortices in a wind turbine wake. *Physics of Fluids*, 25(11):117102, November 2013. doi: 10.1063/1.4824734. URL https://doi.org/10.1063/1.4824734.

[176] D. Simms, S. Schreck, M. Hand, and L.J. Fingersh. NREL unsteady aerodynamics experiment in the NASA-Ames wind tunnel: A comparison of predictions to measurements. Technical report, NREL, 1617 Cole Boulevard Golden, Colorado 80401-3393, 2001.

[177] Bjørn Skaare, Finn Gunnar Nielsen, Tor David Hanson, Rune Yttervik, Ole Havmøller, and Arne Rekdal. Analysis of measurements and simulations from the Hywind demo floating wind turbine. *Wind Energy*, 18(6):1105–1122, apr 2015. doi: 10.1002/we.1750. URL https://doi.org/10.1002/we.1750.

[178] H. Snel. Heuristic modelling of dynamic stall characteristics. In *European Wind Energy conference*, pages 429–433, 1997.

[179] H Snel and JG Schepers. Engineering models for dynamic inflow phenomena. In *Proceedings of the European Wind Energy Conference 1991*, Amsterdam (Netherlands), 1991. Proceedings of the European Wind Energy Conference 1991.

[180] H Snel and JG Schepers. Joule1: joint investigation of dynamic inflow effects and implementation of an engineering method. *Energy Research Center of the Netherlands, ECNC-94-107*, 1995.

[181] J. N. Sørensen, W. Z. Shen, and X. Munduate. Analysis of wake states by a full-field actuator disc model. *Wind Energy*, 1(2):73–88, dec 1998. doi: 10.1002/(sici)1099-1824(199812)1:2⟨73::aid-we12⟩3.0.co;2-l. URL https://doi.org/10.1002/(sici)1099-1824(199812)1:2<73::aid-we12>3.0.co;2-l.

[182] Jens Nørkær Sørensen and Carsten Weber Kock. A model for unsteady rotor aerodynamics. *Journal of Wind Engineering and Industrial Aerodynamics*, 58(3):259–275, dec 1995. doi: 10.1016/0167-6105(95)00027-5. URL https://doi.org/10.1016/0167-6105(95)00027-5.

[183] Jens Nørkær Sørensen and Wen Zhong Shen. Numerical modeling of wind turbine wakes. *Journal of Fluids Engineering*, 124(2):393, 2002. doi: 10.1115/1.1471361. URL https://doi.org/10.1115/1.1471361.

[184] Niels N. Sørensen, B. Méndez, A. Muñoz, G. Sieros, E. Jost, T. Lutz, G. Papadakis, S. Voutsinas, G.N. Barakos, S. Colonia, D. Baldacchino, C. Baptista, and C. Ferreira. CFD code comparison for 2D airfoil flows. *Journal of Physics: Conference Series*, 753:082019, September 2016. doi: 10.1088/1742-6596/753/8/082019. URL https://doi.org/10.1088/1742-6596/753/8/082019.

[185] Rodrigo Soto-Valle, Stefano Cioni, Sirko Bartholomay, Marinos Manolesos, Christian Navid Nayeri, Alessandro Bianchini, and Christian Oliver Paschereit. Vortex identification methods applied to wind turbine tip vortices. October 2021. doi: 10.5194/wes-2021-104. URL https://doi.org/10.5194/wes-2021-104.

[186] Charles G. Speziale, Sutanu Sarkar, and Thomas B. Gatski. Modelling the pressure-strain correlation of turbulence: an invariant dynamical systems approach. *Journal of Fluid Mechanics*, 227:245–272, June 1991. doi: 10.1017/s0022112091000101. URL https://doi.org/10.1017/s0022112091000101.

[187] Richard J.A.M. Stevens, Luis A. Martínez-Tossas, and Charles Meneveau. Comparison of wind farm large eddy simulations using actuator disk and actuator line models with wind tunnel experiments. *Renewable Energy*, 116:470–478, feb 2018. doi: 10.1016/j.renene.2017.08.072. URL https://doi.org/10.1016/j.renene.2017.08.072.

[188] Woody Stoddard. The life and work of Bill Heronemus, wind engineering pioneer. *Wind Engineering*, 26(5):335–341, September 2002. doi: 10.1260/030952402321160633. URL https://doi.org/10.1260/030952402321160633.

[189] A. Suleman, F. Afonso, J. Vale, É. Oliveira, and F. Lau. Non-linear aeroelastic analysis in the time domain of high-aspect-ratio wings: Effect of chord and taper-ratio variation. *The Aeronautical Journal*, 121(1235):21–53, September 2016. doi: 10.1017/aer.2016.94. URL https://doi.org/10.1017/aer.2016.94.

[190] Chao Sun and Vahid Jahangiri. Fatigue damage mitigation of offshore wind turbines under real wind and wave conditions. *Engineering Structures*, 178:472–483, January 2019. doi: 10.1016/j.engstruct.2018.10.053. URL https://doi.org/10.1016/j.engstruct.2018.10.053.

[191] Herbert J. Sutherland. A summary of the fatigue propoerties of wind turbine materials. *Wind Energy*, 2000.

[192] Herbert J. Sutherland and John F. Mandell. Effect of mean stress on the damage of wind turbine blades. *Journal of Solar Energy Engineering*, 126(4):1041–1049, November 2004. doi: 10.1115/1.1785160. URL https://doi.org/10.1115/1.1785160.

[193] Herbert J Sutherland and Paul S Veers. Effects of cyclic stress distribution models on fatigue life predictions. *Wind Energy*, 16:83–90, 1995.

[194] Deman Tang and Earl H. Dowell. Experimental and theoretical study of gust response for high-aspect-ratio wing. *AIAA Journal*, 40(3):419–429, March 2002. doi: 10.2514/2.1691. URL https://doi.org/10.2514/2.1691.

[195] T. Theodorsen. General theory of aerodynamic instability and the mechanism of flutter. Technical report, National Advisory Committee for Aeronautics, 1935.

[196] Kenneth Thomsen and Poul Sørensen. Fatigue loads for wind turbines operating in wakes. *Journal of Wind Engineering and Industrial Aerodynamics*, 80(1-2):121–136, March 1999. doi: 10.1016/s0167-6105(98)00194-9. URL https://doi.org/10.1016/s0167-6105(98)00194-9.

[197] Henrik Stensgaard Toft and John Dalsgaard Sørensen. Reliability-based design of wind turbine blades. *Structural Safety*, 33(6):333–342, September 2011. doi: 10.1016/j.strusafe.2011.05.003. URL https://doi.org/10.1016/j.strusafe.2011.05.003.

[198] CT Tran and D Petot. Semi-empirical model for the dynamic stall of airfoils in view of the application to the calculation of responses of a helicopter blade in forward flight. 1980.

[199] Thanh-Toan Tran and Dong-Hyun Kim. The platform pitching motion of floating offshore wind turbine: A preliminary unsteady aerodynamic analysis. *Journal of Wind Engineering and Industrial Aerodynamics*, 142:65–81, 2015.

[200] Thanh Toan Tran and Dong-Hyun Kim. A CFD study of coupled aerodynamic-hydrodynamic loads on a semisubmersible floating offshore wind turbine. *Wind Energy*, 21(1):70–85, nov 2017. doi: 10.1002/we.2145. URL https://doi.org/10.1002/we.2145.

[201] Thanhtoan Tran, Donghyun Kim, and Jinseop Song. Computational fluid dynamic analysis of a floating offshore wind turbine experiencing platform pitching motion. *Energies*, 7(8):5011–5026, aug 2014. doi: 10.3390/en7085011. URL https://doi.org/10.3390/en7085011.

[202] Niels Troldborg. *Actuator Line Modeling of Wind Turbine Wakes*. PhD thesis, Department of Mechanical Engineering, Aeroelastic Design, Wind Energy Division, Risø National Laboratory for Sustainable Energy, Technical University of Denmark, Denmark, 2008.

[203] L. B. Tuckerman. Inertia factors of ellipsoids for use in airship design. Technical report, NACA, 1925.

[204] P. Valverde. The WindFloat project - WindFloat 2MW floating offshore wind. In *10th Deep Sea Offshore Wind R&D Conference*, Trondheim, Norway, 2013.

[205] A Van Garrel. Development of a wind turbine aerodynamics simulation module. Technical Report ECN-C–03-079, ECN, 2003.

[206] Georgios H Vatistas, V Kozel, and WC Mih. A simpler model for concentrated vortices. *Experiments in Fluids*, 11(1):73–76, 1991.

[207] Pauli Virtanen, Ralf Gommers, Travis E. Oliphant, Matt Haberland, Tyler Reddy, David Cournapeau, Evgeni Burovski, Pearu Peterson, Warren Weckesser, Jonathan Bright, Stéfan J. van der Walt, Matthew Brett, Joshua Wilson, K. Jarrod Millman, Nikolay Mayorov, Andrew R. J. Nelson, Eric Jones, Robert Kern, Eric Larson, C J Carey, İlhan Polat, Yu Feng, Eric W. Moore, Jake VanderPlas, Denis Laxalde, Josef Perktold, Robert Cimrman, Ian Henriksen, E. A. Quintero, Charles R. Harris, Anne M. Archibald, Antônio H. Ribeiro, Fabian Pedregosa, Paul van Mulbregt, and SciPy 1.0 Contributors. SciPy 1.0: Fundamental Algorithms for Scientific Computing in Python. *Nature Methods*, 17:261–272, 2020. doi: 10.1038/s41592-019-0686-2.

[208] Shuaishuai Wang, Torgeir Moan, and Zhiyu Jiang. Influence of variability and uncertainty of wind and waves on fatigue damage of a floating wind turbine drivetrain. *Renewable Energy*, 181:870–897, January 2022. doi: 10.1016/j.renene.2021.09.090. URL https://doi.org/10.1016/j.renene.2021.09.090.

[209] Binrong Wen, Xinliang Tian, Xingjian Dong, Zhike Peng, and Wenming Zhang. Influences of surge motion on the power and thrust characteristics of an offshore floating wind turbine. *Energy*, 141:2054–2068, dec 2017. doi: 10.1016/j.energy.2017.11.090. URL https://doi.org/10.1016/j.energy.2017.11.090.

[210] Binrong Wen, Xingjian Dong, Xinliang Tian, Zhike Peng, Wenming Zhang, and Kexiang Wei. The power performance of an offshore floating wind turbine in platform

pitching motion. *Energy*, 154:508–521, jul 2018. doi: 10.1016/j.energy.2018.04.140. URL https://doi.org/10.1016/j.energy.2018.04.140.

[211] Binrong Wen, Xinliang Tian, Qi Zhang, Xingjian Dong, Zhike Peng, Wenming Zhang, and Kexiang Wei. Wind shear effect induced by the platform pitch motion of a spar-type floating wind turbine. *Renewable Energy*, 135:1186–1199, May 2019. doi: 10.1016/j.renene.2018.12.034. URL https://doi.org/10.1016/j.renene.2018.12.034.

[212] Binrong Wen, Qi Zhang, Haoxue Liu, Xinliang Tian, Xingjian Dong, Zhike Peng, Yongsheng Zhao, and Yufeng Kou. An experimental apparatus for investigating the unsteady aerodynamics of a floating wind turbine. In *International Conference on Offshore Mechanics and Arctic Engineering*, volume 58899, page V010T09A053. American Society of Mechanical Engineers, 2019.

[213] J Whale, C.G Anderson, R Bareiss, and S Wagner. An experimental and numerical study of the vortex structure in the wake of a wind turbine. *Journal of Wind Engineering and Industrial Aerodynamics*, 84(1):1–21, January 2000. doi: 10.1016/s0167-6105(98)00201-3. URL https://doi.org/10.1016/s0167-6105(98)00201-3.

[214] WindEurope. World's first offshore wind farm without subsidies to be built in the netherlands. https://windeurope.org/newsroom/press-releases/worlds-first-offshore-wind-farm-without-subsidies-to-be-built-in-the-netherlands/, 03 2018.

[215] D. H. Wood and J. Boersma. On the motion of multiple helical vortices. *Journal of Fluid Mechanics*, 447:149–171, October 2001. doi: 10.1017/s002211200100578x. URL https://doi.org/10.1017/s002211200100578x.

[216] Chih-Hua Keni Wu and Vinh-Tan Nguyen. Aerodynamic simulations of offshore floating wind turbine in platform-induced pitching motion. *Wind Energy*, 20(5):835–858, nov 2016. doi: 10.1002/we.2066. URL https://doi.org/10.1002/we.2066.

[217] B. F. Xu, T. G. Wang, Y. Yuan, and J. F. Cao. Unsteady aerodynamic analysis for offshore floating wind turbines under different wind conditions. *Philosophical Transactions of the Royal Society A: Mathematical, Physical and Engineering Sciences*, 373(2035):20140080, February 2015. doi: 10.1098/rsta.2014.0080. URL https://doi.org/10.1098/rsta.2014.0080.

[218] Di Yang, Charles Meneveau, and Lian Shen. Large-eddy simulation of offshore wind farm. *Physics of Fluids*, 26(2):025101, feb 2014. doi: 10.1063/1.4863096. URL https://doi.org/10.1063/1.4863096.

[219] R. Yokota, T. Narumi, R. Sakamaki, S. Kameoka, S. Obi, and K. Yasuoka. Fast multipole methods on a cluster of GPUs for the meshless simulation of turbulence. *Computer Physics Communications*, 180(11):2066–2078, November 2009. doi: 10.1016/j.cpc.2009.06.009. URL https://doi.org/10.1016/j.cpc.2009.06.009.

[220] Rio Yokota and L.A. Barba. Comparing the treecode with FMM on GPUs for vortex particle simulations of a leapfrogging vortex ring. *Computers & Fluids*, 45(1):155–161, June 2011. doi: 10.1016/j.compfluid.2010.11.029. URL https://doi.org/10.1016/j.compfluid.2010.11.029.

[221] W. Yu, V.W. Hong, C. Ferreira, and G.A.M. van Kuik. Validation of engineering dynamic inflow models by experimental and numerical approaches. *Journal of Physics: Conference Series*, 753:022024, September 2016. doi: 10.1088/1742-6596/753/2/022024. URL https://doi.org/10.1088/1742-6596/753/2/022024.

[222] W. Yu, V. W. Hong, C. Ferreira, and G.A.M. van Kuik. Experimental analysis on the dynamic wake of an actuator disc undergoing transient loads. *Experiments in Fluids*, 58(10), September 2017. doi: 10.1007/s00348-017-2432-9. URL https://doi.org/10.1007/s00348-017-2432-9.

[223] Wei Yu, Carlos Simao Ferreira, Gijs van Kuik, and Daniel Baldacchino. Verifying the blade element momentum method in unsteady, radially varied, axisymmetric loading using a vortex ring model. *Wind Energy*, 20(2):269–288, June 2017. doi: 10.1002/we.2005. URL https://doi.org/10.1002/we.2005.

[224] Wei Yu, Delphine Tavernier, Carlos Ferreira, Gijs A. M. Kuik, and Gerard Schepers. New dynamic-inflow engineering models based on linear and nonlinear actuator disc vortex models. *Wind Energy*, 22(11):1433–1450, August 2019. doi: 10.1002/we.2380. URL https://doi.org/10.1002/we.2380.

[225] Andreas Öchsner. *Classical Beam Theories of Structural Mechanics*. Springer, Cham, 2021. doi: 10.1007/978-3-030-76035-9. URL https://doi.org/10.1007/978-3-030-76035-9.